

Stratosphere–Troposphere

Dynamical Coupling

Steven Hardiman

Trinity College

Cambridge

A dissertation submitted for the degree of

Doctor of Philosophy

at the University of Cambridge

October 2006

Stratosphere–Troposphere Dynamical Coupling

Steven Hardiman

This thesis is concerned with dynamical coupling between the stratosphere and troposphere.

The first part of the thesis examines mechanisms whereby dynamical perturbations to the upper stratosphere can lead to a significant response in the lower stratosphere, looking particularly at how this response is determined by the extratropical dynamics. A one dimensional model is used to show that the response is much greater when the external parameters are such that the flow has multiple stable states. The same principle is shown to apply to a fully three dimensional flow and does not depend qualitatively on the representation of the troposphere and tropospheric wave forcing. The dependence of the response on the height of the applied dynamical perturbation, the amplitude of planetary wave forcing, and the relaxation to radiative equilibrium temperatures is considered.

In the second part of the thesis we consider the interhemispheric differences in the extratropical seasonal cycle and suggest that resonance of topographically forced waves with free travelling planetary waves could be in part responsible for these differences. The seasonal cycle in mass upwelling in the tropical lower stratosphere is also considered. In particular we look at the differences in this upwelling caused by the strength and location of tropospheric wave driving, the thermal relaxation timescale of the atmosphere, baroclinic instability, and the seasonal cycle in the tropospheric radiative equilibrium temperature field.

Finally we consider the interannual variability seen in the tropical mass upwelling. We quantify the different parts of this variability – the part that can be considered forced variability and the part that arises due to internal variability. We suggest that the high forced variability seen in the mass upwelling may be due to it being linked, via extratropical wave driving, to sea surface temperatures.

Declaration and Acknowledgements

This dissertation is the result of my own work and contains nothing that is the outcome of work done in collaboration with others or that has been submitted for any other degree, diploma or other qualification.

Huge thanks go to my supervisor Peter Haynes for his (completely) inexhaustible supply of patience, enthusiasm, and ideas. Thanks must also go to my supervisor at the UK Meteorological Office, Neal Butchart, for making work there productive and enjoyable.

Thanks are also due to Michael McIntyre and Gavin Esler for their helpful advice, and to Bjoern Hassler for his technical help.

This dissertation was supported financially by the Natural Environment Research Council, with additional support in the form of a CASE studentship from the UK Meteorological Office.

Contents

1	Introduction	7
1.1	Background	7
1.2	Downward influence: Chapters 2–3	7
1.3	Seasonal and interannual variability: Chapters 4–5	11
2	1D model experiments	13
2.1	Introduction	13
2.2	The 1D model	14
2.3	Problems with a WKB approach	15
2.4	Vacillations in the Holton–Mass model	16
2.5	Downward propagation experiments	17
2.6	Multiple state regimes	21
2.7	The non-locality of the zonal mean dynamics	26
2.8	The QBO	28
2.8.1	Downward influence experiments	30
2.9	A comparison with a new lower boundary	33
2.10	A new wave generation mechanism	35
2.11	Other details on downward propagation	38
2.11.1	Downward phase speed	39
2.11.2	Period of vacillations	42
2.11.3	Generation of vacillations	42
2.11.4	Wave transience	45
2.12	Conclusions	47
3	3D model experiments	51
3.1	Introduction	51
3.2	Holton–Mass version of Gray et al.	54
3.3	The 3D model	55
3.4	Sensitivity in the tropics	59

3.5	3D downward propagation experiments	60
3.6	Experiments with a troposphere	63
3.7	Height of applied perturbation	65
3.8	Period of vacillations revisited	70
3.9	Truncated runs	73
3.10	EP flux entering the stratosphere	75
3.11	A linear response?	85
3.12	Cold pole problem	86
3.13	Conclusions	93
4	Seasonal Cycle	97
4.1	Introduction	97
4.2	Interhemispheric differences in seasonal variation	98
4.2.1	The Lamb mode	99
4.3	Seasonal cycle in tropical upwelling	103
4.3.1	Dependence of seasonal cycle on Φ_0 and μ_0 , and relevance of downward control mechanism	106
4.3.2	Runs with constant α	112
4.3.3	Interannual variability	115
4.3.4	Baroclinic instability	116
4.3.5	2D model	119
4.3.6	Tropospheric seasonal cycle in T_e	126
4.3.7	A changing climate	132
4.4	Conclusions	133
5	SSTs and tropical upwelling	137
5.1	Introduction	137
5.2	Model and simulations	138
5.3	Diagnostics of variability	139
5.4	Results of variability diagnostics	140
5.5	Mass Upwelling	143
5.6	Effect of Sea Surface Temperatures and the QBO	148
5.7	The global temperature	151
5.8	Conclusions and Discussion	154
6	Summary and discussion	157
	Bibliography	161

Chapter 1

Introduction

1.1 Background

A traditional view is that the stratosphere responds passively to dynamical driving from the troposphere (e.g. upward propagation of planetary waves forced in the troposphere). However, there is now evidence that this is not the case and that the troposphere and stratosphere are dynamically coupled, each one affecting the other. This raises several questions: How do changes in the stratosphere affect tropospheric climate and weather? Would including more model levels in the stratosphere of dynamical general circulation models (GCMs) allow them to better predict the troposphere? Where exactly should we put these levels for the best predictions? There are also implications for medium-range weather forecasting, namely can we use the state of the stratosphere to predict change in the troposphere? It also highlights the need for a better understanding of the stratosphere–troposphere coupled system.

I do not address many of the above questions directly, but attempt to better understand the nature of the coupled stratosphere–troposphere dynamics. This thesis considers mechanisms whereby perturbations in the stratospheric circulation can propagate downward through the stratosphere to the tropopause and thus potentially alter the circulation of the troposphere. The influence of the seasonal cycle may be relevant to this in the real atmosphere. In the second part of this thesis some aspects of the seasonal cycle of the stratosphere and troposphere are considered.

1.2 Downward influence: Chapters 2–3

Can stratospheric anomalies affect surface weather and climate? It is now well known that the answer to this question is yes. What is less well known are the mechanisms

by which stratospheric anomalies propagate downward through the stratosphere and penetrate the troposphere.

Baldwin and Dunkerton (2001) showed evidence for the downward phase propagation of anomalies in the stratospheric circulation. The anomalies were seen to propagate down through the stratosphere and were followed by anomalies in the tropospheric circulation. This shows that the state of the stratosphere at a given time may be used to predict the state of the troposphere at later times.

However Plumb and Semeniuk (2003), hereafter PS, studying the dynamics of wave mean-flow interaction in the extratropical stratosphere using a Holton–Mass model, showed that the response to time-varying Rossby wave forcing at the lower boundary took the form of this downward phase propagation (i.e. downward migrating zonal wind anomalies, see figure 1.1). PS made the point that downward migration could therefore not be taken to imply any upper stratospheric forcing for such anomalies. PS also showed that the downward migration did not require downward wave reflection (which they eliminated using a WKB approximation for the waves), nor did it require vertical non-locality in the zonal mean dynamics. The QBO is a good example of this downward propagation in a flow that is forced from below (Plumb 1977).

It is therefore important to make the distinction between the downward phase propagation due to a disturbance (which implies upward group velocity for Rossby waves) and downward group propagation (in other words the downward propagation of real information, due to a disturbance in the stratosphere). The former influence on the troposphere, although important as a predictor of tropospheric change, may be influenced by conditions within the troposphere itself. The latter will not be, until the disturbance reaches the troposphere.

Figure 1.2, taken from Reichler et al. (2005), is helpful in demonstrating how easy it can be to confuse one form of downward propagation with another. How do we interpret this figure? Does it suggest a single stage where wave driving from the troposphere travels up into the stratosphere and back into the troposphere, in which case the forcing certainly comes from the troposphere? Or does it suggest two stages where wave driving from the troposphere breaks in the stratosphere causing an anomaly in the stratospheric circulation, and this anomaly then propagates downwards into the troposphere? In this case we could ignore the first stage and simply apply an equivalent anomaly directly to the stratosphere – definitely downward propagation of information. It will turn out that we interpret this figure in two stages – the downward propagation seen in our experiments (where forcing is applied in the stratosphere) looks nothing like the downward phase anomalies shown

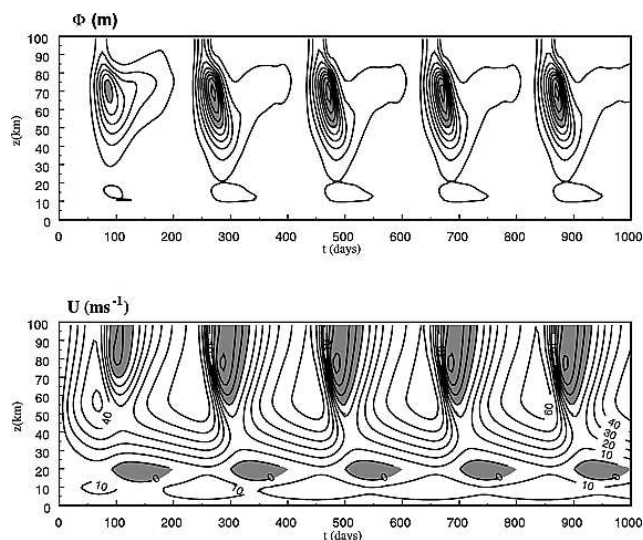


Figure 1.1:

Downward migration of geopotential height and zonal wind anomalies caused by time dependent wave forcing at the lower boundary. Figure from Plumb and Semeniuk (2003)

in PS.

PS does not rule out (or indeed say anything about) the possibility for downward propagation of disturbances imposed in the upper stratosphere (the downward propagation of information). There have, however, been several studies on the mechanisms by which these disturbances can propagate down to the troposphere. They could do so due to the non-local nature of PV inversion (Hartley et al. 1998), the physical mechanism for this being the rapid propagation of inertio-gravity waves required to maintain a state of geostrophic and hydrostatic balance (Haynes 2005). However, Charlton et al. (2005) show that the troposphere responds to changes in the stratosphere in a way that cannot be completely explained by large-scale adjustment of the tropospheric flow to the stratospheric PV distribution. Rossby wave refraction in the lower stratosphere (Hartmann et al. 2000, Limpasuvan and Hartmann 2000, Chen and Robinson 1992) and reflection from higher in the stratosphere (Perlwitz and Harnik 2003) are mechanisms by which the state of the stratosphere can affect the tropospheric flow. The waves may break in the stratosphere applying a forcing to the zonal flow (Christiansen 2003). Alternatively, the stratospheric perturbation in question could be due to solar UV heating (Kodera et al. 1990) or indeed any thermal perturbation (Polvani and Kushner 2002, Kushner and Polvani 2004) applied directly to the stratosphere.

In chapters 2 and 3 we will explain and investigate a different mechanism whereby stratospheric anomalies propagate downward through the stratosphere.

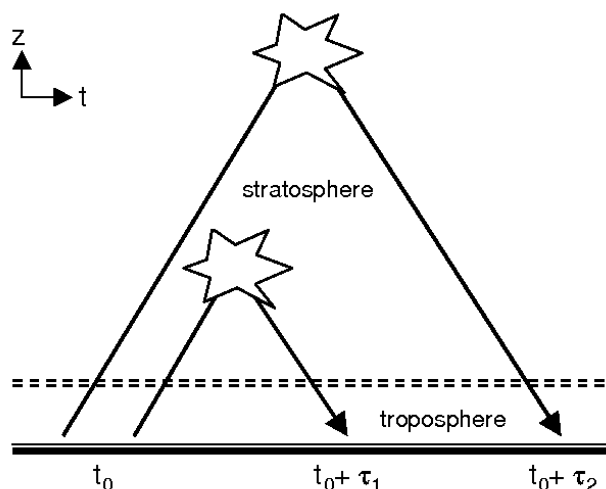


Figure 1.2:

Wave propagation into the troposphere, forced from the troposphere. One stage or two stages? Figure from Reichler et al. (2005)

We investigate this mechanism using the same 1D model as PS (chapter 2) so that it is possible to see which changes are causing which effects, and also using a 3D mechanistic model to check that our results hold in that more realistic case (chapter 3). In the experiments a perturbation is applied to the model stratosphere, and the affect of this on the flow at lower altitudes is analysed. By directly perturbing the stratosphere and watching the change below we can be sure that what we see is downward propagation of information and not simply downward phase propagation due to forcing from below. Understanding the mechanisms for the downward influence of such disturbances is directly relevant to understanding the physical effects of the solar cycle (which are largely confined to the upper stratosphere) on the circulation in the lower stratosphere and troposphere.

The way in which upper atmospheric anomalies affect the troposphere is split into two phases. First information propagates downwards through the stratosphere. There is then an interaction between the lower stratosphere and upper troposphere. In this work we focus on the first phase.

We show that indeed it is possible, in some circumstances, for a significant downward influence to occur from perturbations in the upper stratosphere, and further that the state of the stratosphere is very important to the amount of downward influence seen (contrary to the conclusions of Christiansen (2003) which instead considers the growth of stratospheric influence in the troposphere due to instability in the troposphere). We therefore conclude that the state of the stratosphere, and any perturbations to the flow in the stratosphere, cannot be ignored.

Finally it should be mentioned that the stratospheric perturbation reaching the troposphere need not be large in order for it to affect the surface weather and climate in a large way. This is because it is possible that the internal dynamics of the troposphere would amplify small dynamical signals from the stratosphere (Song and Robinson, 2004).

1.3 Seasonal and interannual variability: Chapters 4–5

Although all the experiments in chapters 2–3 ignore the effects of a seasonal cycle, the real troposphere responds to perturbations from the stratosphere under the influence of a seasonal cycle. A better understanding of the nature of the seasonal cycle and interannual variability seen in the stratosphere and troposphere is thus important. The interhemispheric differences seen in the winter stratosphere, and the seasonal cycle and interannual variability in mass upwelling in the tropical lower stratosphere are considered in chapters 4–5.

Interhemispheric differences between seasons (in particular the difference between northern hemisphere winter and southern hemisphere winter) are due to a number of factors including different surface temperatures (due to the high altitudes and high surface albedo of the Antarctic) and different amounts of dynamical wave forcing (due to the larger land mass in the northern hemisphere). Yoden (1989) simulated the difference between the cooler southern hemisphere winters and the warmer, more disturbed, northern hemisphere winters using a simple 1D model. By using different values of wave forcing, winters typical of both northern and southern hemispheres were observed. In chapter 4 we take these experiments further, and suggest that a resonance between the wave forcing and free travelling planetary waves could be the reason for some runs being more disturbed.

The global scale stratospheric meridional circulation, partially responsible for chemical distribution within the stratosphere and known as the Brewer–Dobson circulation, also displays a seasonal cycle. The mass flux upwelling in the tropical lower stratosphere is a good indication of the strength of the entire Brewer–Dobson circulation. The reason for a seasonal cycle existing on the equator is not fully understood. It is well established that the circulation is driven by ‘gyroscopic pumping’ in which wave-induced zonal forces and coriolis forces cause air to move poleward. The zonal forces are measured by the so called Eliassen–Palm flux divergence (EP flux divergence). However, in the tropics where coriolis forces are relatively weak, the way the pumping action works is less clear cut and not fully understood. In

particular the relative importance of the EP flux divergence in extratropical versus tropical latitudes is unclear. Yulaeva et al. (1994), Butchart and Scaife (2001), and Randel et al. (2002), emphasise the extratropical EP flux divergence, although Kerr-Munslow and Norton (2006) emphasise the tropical. Furthermore the mechanisms whereby northern hemisphere EP flux divergences are stronger than southern are not entirely clear. The second part of chapter 4 attempts to clarify some of these issues.

We also consider the interannual variability in this mass upwelling. A source of wave forcing contributing to this variability may be sea surface temperatures (SSTs). There is evidence to suggest that warmer SSTs might cause a stronger stratospheric circulation (Manzini et al. 2006, Zeng and Pyle 2005). There is also evidence to suggest that warmer SSTs result in a warmer stratospheric polar vortex (Braesicke and Pyle 2004). In addition, it is possible that the QBO of the zonal wind in the tropics has an effect on mass upwelling in the tropical lower stratosphere (for example, Butchart et al. 2003 shows that the QBO affects tropical ozone concentrations). In chapter 5 we will consider the impact of the QBO and SSTs on the tropical lower stratosphere and suggest a mechanism whereby warmer SSTs lead to greater mass upwelling there, thus implying that they alter the strength of the Brewer–Dobson circulation of the stratosphere. In agreement with Yulaeva et al. (1994) the mechanism described in chapter 5 shows that the predictability of the temperature in the tropical lower stratosphere is not due solely to its predictability in the tropical troposphere, but also to the global scale dynamics underlying the global scale EP flux divergence.

Chapter 2

1D model experiments

2.1 Introduction

The purpose of this chapter is to establish a basic mechanism whereby a perturbation in the stratosphere at high altitudes can affect the dynamics at lower altitudes in the stratosphere and potentially, therefore, affect the dynamics of the troposphere. We aim to understand which conditions in the real atmosphere will lead to this mechanism being important.

Although a 1D model is not physically realistic it does allow one to see exactly which changes are causing which effects. It is easy to see exactly how the downward influence of an imposed disturbance is affected by any given variable and hence to begin to understand how a mechanism works. It also runs very fast allowing many experiments and requiring limited computer power. It is also easy to change a boundary condition or method by which waves are generated in a 1D model and hence to test the robustness of a mechanism. Of course, a mechanism should then be tested using a 3D model to ensure it applies to that more physically realistic case, and this is the subject of the next chapter.

As mentioned above, it is already known that the stratosphere can affect the troposphere through a change in the PV distribution of the stratosphere, since the inversion operator giving dynamical fields from PV is non-local. It is also known that Rossby waves can be refracted or reflected by the stratosphere thus having an impact on the troposphere. The mechanism described in this chapter is distinct from both of these and it involves the non-linear two way interaction between waves and zonal mean flow.

It is suggested that, if this mechanism is important, then improved resolution in the stratosphere and improved gravity wave parametrisation schemes (with a model extending beyond the top of the stratosphere) will greatly help computer models to

predict the dynamics of the troposphere.

2.2 The 1D model

The model used is that of Holton and Mass (1976), as described in PS, to which the reader is referred for details. It is a severely truncated one-dimensional model, completely specified by evolution equations for the quasi-geostrophic potential vorticity (PV) perturbation $q(z, t)$ and the mean-shear contribution to the PV gradient $Q_y(z, t)$ (i.e. not including β). The evolution of the geopotential height $\Phi(z, t)$ and zonal mean flow $U(z, t)$ are governed by the evolution of q , Q_y , and the Eliassen–Palm flux (hereafter EP flux) $F(z, t)$. The EP flux describes the momentum flux due to planetary-scale Rossby waves, within the so-called transformed Eulerian-mean description of wave–mean flow interaction (e.g. Andrews et al. 1987). The model equations

$$\frac{\partial q}{\partial t} = -ik\gamma Uq - i\frac{gk}{f}(\beta + \gamma Q_y)\Phi - \frac{g}{\rho} \frac{\partial}{\partial z} \left(\rho \frac{\alpha f}{N^2} \frac{\partial \Phi}{\partial z} \right), \quad (2.1)$$

the wave PV equation, which is time stepped to find q ,

$$\frac{\partial Q_y}{\partial t} = \frac{\pi^2}{\rho L^2} \frac{\partial F}{\partial z} + \frac{1}{\rho} \frac{\partial}{\partial z} \left[\rho \frac{\alpha f^2}{N^2} \frac{\partial}{\partial z} (U - U_e) \right], \quad (2.2)$$

the mean PV equation, which is time stepped to find Q_y . The wave PV is related to Φ by

$$q = -\frac{g}{f} \left(k^2 + \frac{\pi^2}{L^2} - \frac{1}{\rho} \frac{\partial}{\partial z} \rho \frac{f^2}{N^2} \frac{\partial}{\partial z} \right) \Phi, \quad (2.3)$$

the EP flux is

$$F = \gamma \rho \frac{g^2 k}{2N^2} Re \left(i\Phi \frac{\partial \Phi^*}{\partial z} \right), \quad (2.4)$$

and the mean PV gradient is related to U by

$$Q_y = \frac{\pi^2}{L^2} U - \frac{C^2}{\rho} \frac{\partial}{\partial z} \left(\rho \frac{f^2}{N^2} \frac{\partial U}{\partial z} \right). \quad (2.5)$$

The coefficient C is introduced for reasons to emerge in section 2.7. However, one normally takes $C = 1$, as in Holton and Mass (1976) and PS, so that the equations conform to standard quasi-geostrophic dynamics.

Here z is log-pressure height, $\rho = \rho_0 e^{-z/H}$ is the basic state density where H is a standard nominal density scale height taken as 7km, the radiative equilibrium

profile of the zonal wind is given by $U_e = (10 + 2z) \text{ m s}^{-1}$ (z measured in nominal km), $\alpha = [1.5 + \tanh((z - 35)/7)] \times 10^{-6} \text{ s}^{-1}$ is the rate of Newtonian cooling at which the mean flow relaxes towards the radiative equilibrium profile U_e , g is acceleration due to gravity, f is the Coriolis parameter at 60°N , $\gamma = 8/(3\pi)$ is the projection of $\sin^2(\pi y/L)$ onto $\sin(\pi y/L)$ (we keep only this mode in the y direction), $L = \pi a/3$ is the latitudinal scale of the PV anomaly (the β channel width), $N = 2 \times 10^{-2} \text{ s}^{-1}$ is the buoyancy frequency, C determines the non-locality of the zonal mean dynamics, and $\beta = \partial f / \partial y$. Also

$$k = s / (a \cos(\pi/3)) \quad (2.6)$$

where a is the earth's radius ($a = 6400 \text{ km}$) and s , the zonal planetary wavenumber, is usually taken to be 2 (we keep only one wavenumber).

The model is centred at 60°N with a domain of 70 km between the upper and lower boundaries. We use a time step of 0.05 days and a vertical resolution of 0.5 km. The model is stratosphere only. We include the dynamics of the troposphere by specifying the geopotential height $\Phi = \Phi_0$ and zonal flow $U = U_0$ on the lower boundary. We take $\frac{\partial \Phi}{\partial z} \rightarrow 0$ and $\frac{\partial U}{\partial z} \rightarrow 0$ at the top boundary.

2.3 Problems with a WKB approach

Following PS any downward influence due to wave reflection can be ruled out by imposing a WKB approximation for the waves rather than by solving for them from the full equations. The ability to remove one possible source of downward influence is the motivation for attempting to use this approximation.

In the WKB approximation

$$\begin{pmatrix} \Phi \\ q \end{pmatrix} = \text{Re} \left(\begin{pmatrix} \Phi(z) \\ q(z) \end{pmatrix} \exp \left(\frac{z}{2H} + \int_0^z i m(z') dz' \right) \right) \quad (2.7)$$

with Φ and q slowly varying in z . The equation for the EP flux becomes:

$$F(z) = F(0) \exp \left[- \int_0^z \Lambda(z') dz' \right] \quad (2.8)$$

where

$$\Lambda(z) = \frac{\alpha}{\gamma k U m} \left(m^2 + \frac{1}{4H^2} \right)$$

$$m(z) = \frac{N}{f} \sqrt{\frac{\beta + \gamma Q_y}{\gamma U} - k^2 - \frac{\pi^2}{L^2} - \frac{f^2}{4N^2 H^2}}$$

The only complicated issue is what to do when the vertical wave number, m , becomes imaginary. This is dealt with in two cases. If $m \rightarrow \infty$ this means that the wave is completely attenuated, so the EP flux is set to zero above that height. If m^2 changes sign through 0, the EP flux is kept constant in height until $m^2 > 0$ again. This all follows PS.

In later sections it will become apparent that, not only can the Holton–Mass model attain a steady or a vacillating stable state (for time independent lower boundary wave forcing), but that these vacillations are crucial to any significant downward influence by the mechanism that will be described. For now it is sufficient to note that vacillations can exist in this WKB model in the same way that they exist for fully calculated waves. Waves act as a drag on the mean flow, causing U to become smaller. Once U becomes very small, $\Lambda(z)$, becomes large and the wave is attenuated (and hence trapped below that height) allowing U to relax back to a background profile U_e thus allowing waves to propagate upwards again.

Unfortunately it seems that this approximation within this 1D model is too crude to be usable. No matter how high the model resolution is increased, vacillations occur for different values of lower boundary wave forcing and not in any regular or obviously resolved way. There is no sign of the model converging as resolution is increased.

Therefore this approximation is abandoned and in what follows the waves are calculated from the full equations given in the previous section.

2.4 Vacillations in the Holton–Mass model

As mentioned in the previous section, the Holton–Mass model can attain steady and vacillating stable states when the lower boundary wave forcing is time independent. In a steady state, the two terms on the right hand side (rhs) of equation (2.2) exactly balance so that the difference between the equilibrium flow profile U_e (attained from a background temperature profile T_e by thermal wind balance) and the steady state profile U that is observed, balances the constant wave driving (due to planetary waves breaking as they propagate upwards).

Despite the lower boundary wave forcing being time independent it is also possible for vacillations to be internally generated. Their period will depend on the amplitude of the wave forcing. What occurs is the following. Breaking waves act as a drag on the mean flow, causing the zonal mean wind (U) to become weaker eastward (and sometimes westward). Due to the Charney–Drazin criteria (see Andrews et al. 1987), once U becomes westward at a certain height (or, more precisely,

becomes more westward than the phase speed of the driving waves) the forced planetary waves become trapped below this height. This allows U to relax to U_e , becoming eastward once again, and the pattern starts over.

Yoden (1987(a)) (hereafter Y87) investigated the values of lower boundary wave forcing for which these states are stable. He performed several model runs with a Holton–Mass model using many different initial profiles for the zonal wind (U). Using the amplitude of wave forcing at the lower boundary, Φ_0 (the prescribed value of the geopotential height on the lower boundary), as a bifurcation parameter, he mapped out a bifurcation diagram detailing which states (steady or vacillating) are stable for which values of Φ_0 . This diagram is shown in figure 2.1(b) in which Yoden’s HB denotes the present Φ_0 . It is important to note that for certain values of Φ_0 both steady and vacillating states are stable. The different flow profiles seen in the steady state, and the state that bifurcates to vacillations are shown in figure 2.1(a).

Since I have implemented the Holton–Mass model in a slightly different parameter regime to Y87, the bifurcation points in my model occur at different values of Φ_0 . The steady state ceases to exist when Φ_0 increases to 119m in my implementation. The vacillating state exists above $\Phi_0 \approx 50$ m. The steady state velocity field is shown in figure 2.2(a) and the vacillating state is shown in figure 2.2(b). Following Charney and DeVore (1979), we refer to the steady state velocity as that stable state close to radiative equilibrium (Yoden’s state A in figure 2.1(a)), and the vacillating state velocity field (Yoden’s state C in figure 2.1(a), and the vacillations defined in the figure caption as C’ – whichever is stable for the given value of Φ_0) as that far from radiative equilibrium.

2.5 Downward propagation experiments

To investigate the downward propagation of information through the stratosphere, a disturbance has to be introduced at high altitudes, and the response at low altitudes recorded. This disturbance can be introduced either by perturbing the velocity field (the zonal mean zonal wind) or by adding an extra forcing to the rhs of equation (2.2). In what follows we focus on the former method.

In the following experiments an initial 500 days are allowed for the model to settle to its natural state, which is either steady, or oscillatory with periodic vacillations of wave amplitude and mean flow. On day 500 of the integration the velocity field is disturbed such that $U \rightarrow (U - 20)\text{m s}^{-1}$ for z between 30 and 40 km (let ΔU be the imposed disturbance to U , so equal to 20m s^{-1} here). Results are found to be quite

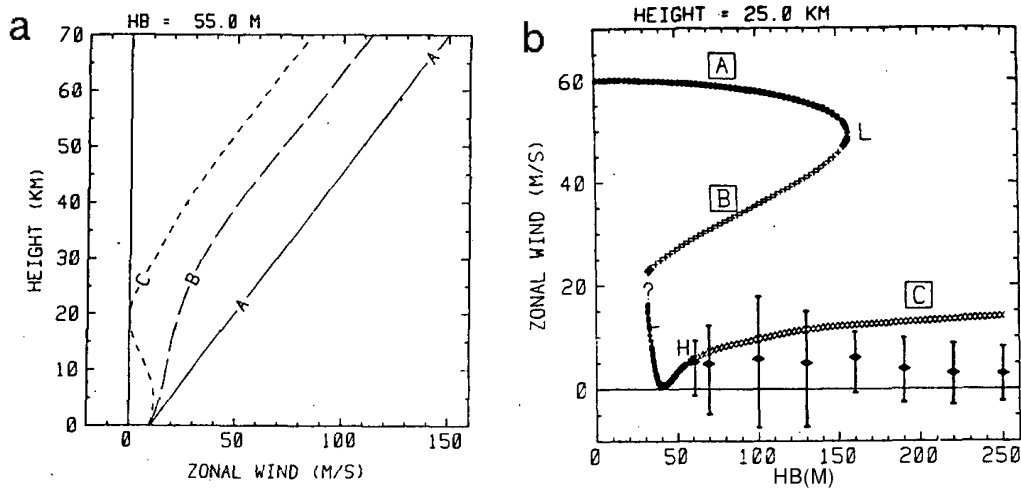


Figure 2.1:

(a) Steady zonal wind profiles and, (b) bifurcation diagram of stable states in the Holton–Mass model. Figures from Yoden (1987(a)) (using a slightly different parameter regime to the one used in this chapter). Stable state A is close to radiative equilibrium, stable state C is far from radiative equilibrium. State B is unstable. HB denotes the present Φ_0 . In (b) all the states A are stable, all the states B are unstable, and the states C for $HB > 59$ m are all unstable, the amplitude of the resulting stable vacillations (C', say) being shown by the vertical bars.

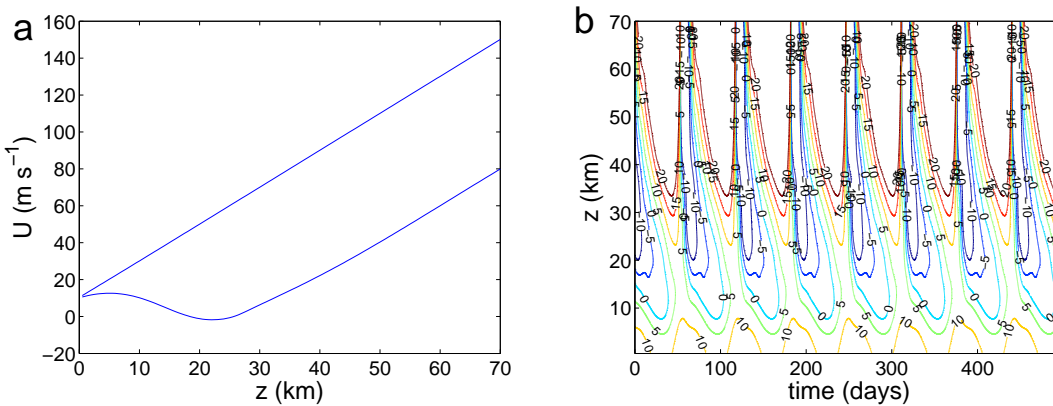


Figure 2.2:

(a) Zonal wind profile for steady regime ($\Phi_0 = 118$ m) and, (b) flow evolution for zonal wind, U (m s⁻¹), in vacillating regime ($\Phi_0 = 119$ m) in the current implementation of the Holton–Mass model. In figure (b) red contours correspond to positive values of U and blue contours to negative values.

insensitive to the height of the upper discontinuity, which can be taken to be the top boundary. (It should be mentioned that the fact that U is made discontinuous was found not to matter. Indeed the same results as we present here were found by adding a forcing in the stratosphere such that U was varied in a continuous way – see section 2.6. See also section 3.7). In each experiment the lower boundary wave forcing Φ_0 is kept constant. We consider how the response at low altitudes to the imposed disturbance changes with Φ_0 . For each chosen value of Φ_0 a second run is made with no disturbance to the velocity field, and the difference between the two runs is calculated and analysed. In all cases the initial velocity profile $U(z, 0) = U_e$ is used. The results for some chosen values of Φ_0 are shown in Figure 2.3. (Note that the height in km is not measured from the ground, but is measured from the lower boundary of this stratosphere only model).

We see from Figure 2.3(a-c) that for $0\text{m} \leq \Phi_0 < 119\text{m}$, when for our chosen initial profile of U the solution branch found is the steady state, the dynamics does not support any clear downward propagation. In this regime there is little dependence of the change the imposed disturbance causes to the zonal velocity field on the value of Φ_0 . All we see is the response of the zonally symmetric dynamics ($\Phi_0 = 0$), with some weak modification due to increased wave forcing. The zonal wind U simply relaxes, radiatively, back to its equilibrium profile. Theory for the zonally symmetric dynamics shown in figure 2.3(a) has been considered in Dickinson (1968) and Haynes et al. (1991). As we might expect, in the absence of any wave forcing (figure 2.3(a)), the time the disturbance lasts for is inversely proportional to α , the rate of Newtonian cooling. When wave forcing is present it also affects the timescale of the disturbance causing the flow to re-equilibrate to a steady state slower than in the zonally symmetric case. This wave forcing effect becomes less noticeable as α is increased, and is negligible for $\alpha \geq 2.5$.

We can determine whether or not this response (shown in figures 2.3(a)-(c)) to the applied disturbance is linear by altering the magnitude of the disturbance. Figure 2.4 shows the response (for $\Phi_0 = 118\text{m}$) with a change in U of 10m s^{-1} and 30m s^{-1} (contours plotted are 0.5 and 1.5 those used in figure 2.3(c) respectively). It can be seen that the zonally symmetric response is linear. The decay rate and period of the small vacillations due to increased wave forcing also appears linear. However, the amplitude of these vacillations is not. It increases more than a linear response would with increased disturbance magnitude (it also increases if we decrease α).

Considering further these small vacillations we look at how they alter with changing Φ_0 . It can be seen from figures 2.3(b)-(c) that the period of these small vacillations is roughly independent of Φ_0 . In fact it increases very slightly with increasing

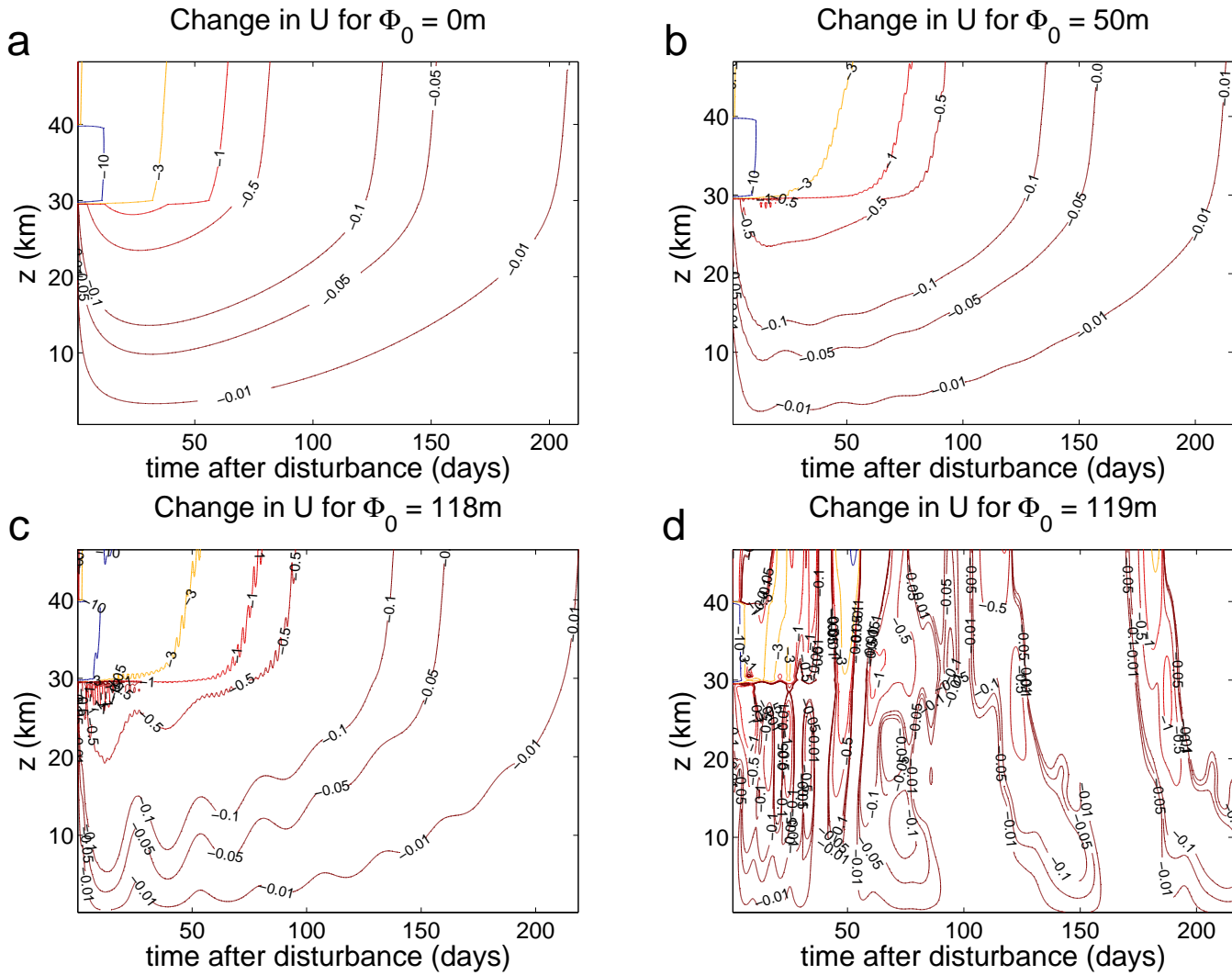


Figure 2.3:

The velocity field is perturbed such that $U \rightarrow (U - \Delta U) \text{ m s}^{-1}$ for $30 \text{ km} < z < 40 \text{ km}$ ($\Delta U = 20 \text{ m s}^{-1}$), and the change in U that this causes is shown for different values of Φ_0 . It can be seen that if the unperturbed solution is a steady state ($\Phi_0 \leq 118 \text{ m}$) then the disturbance dies out quickly, but if the unperturbed solution is vacillating ($\Phi_0 > 118 \text{ m}$) the disturbance shifts the phase of the vacillations causing the downward influence (i.e. change in U) to be greater and persist for all later times.

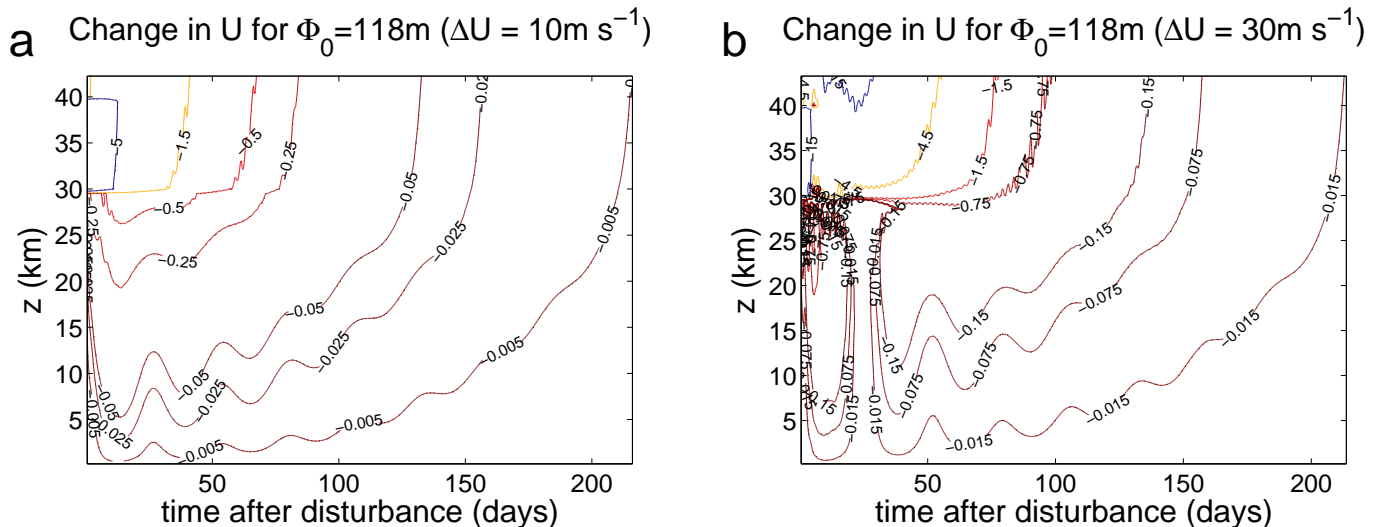


Figure 2.4:
As in figure 2.3(c), but ΔU now 10m s^{-1} and 30m s^{-1} .

Φ_0 , going from 25.0 days at $\Phi_0 = 50\text{m}$ to 25.9 days at $\Phi_0 = 100\text{m}$ and 27.2 days at $\Phi_0 = 118\text{m}$. It can also be seen that the amplitude of these vacillations increases with Φ_0 .

Similar small vacillations are seen if we look at the EP flux field, F , rather than U . We can show that these small vacillations are a wave mean-flow interaction effect, and not a wave only effect. Just after the perturbation is applied to U , we set U to be a constant value (either the value it has at the time, or the value it had before the perturbation was applied). Figure 2.5 shows that the vacillations disappear from F in both cases (compare with section 2.11.4 where we do find a wave only effect).

Increasing Φ_0 from 118m to 119m alters the stable equilibrium state from a steady state to a vacillating state. From figure 2.3(d) we see that once we are perturbing a vacillating state, the perturbation alters the phase of the underlying vacillations and this causes a much more significant downward influence, and one that lasts for longer times. By comparing figure 2.3(d) to figure 2.2(b) we see that the largest influence occurs during the most westward part of the vacillations. This response is not linear. Increasing the size of applied perturbation causes the phase shift in the vacillations to be greater, thus the response (change in U) is greatest at different times (compare figure 2.3(d) to figure 2.6).

2.6 Multiple state regimes

As already mentioned, for some values of Φ_0 multiple states (i.e. steady and vacillating) can exist for the same values of the external parameters so that choosing

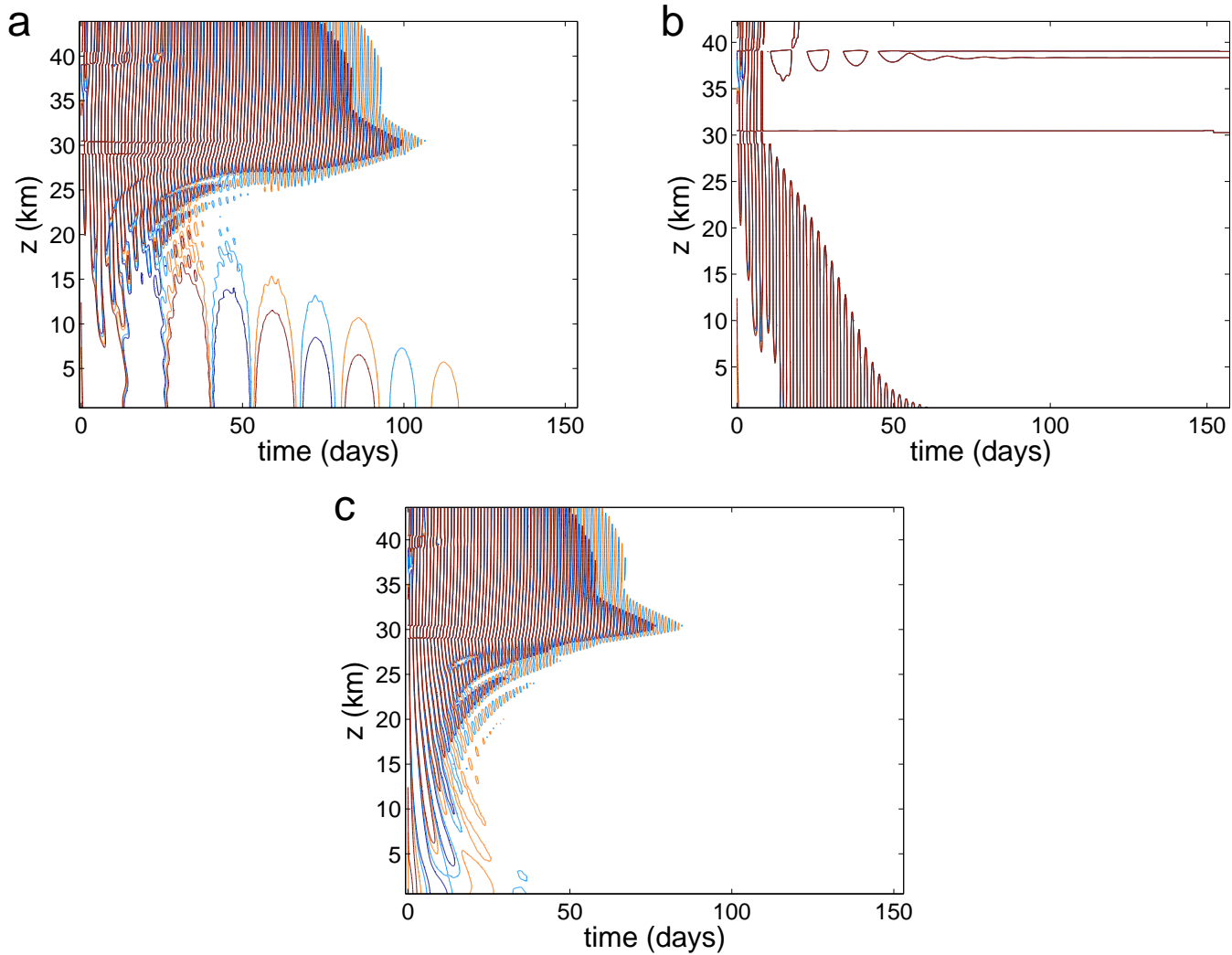


Figure 2.5:

Figures show EP flux, F . Contours used are $[-2.68, -1.34, 1.34, 2.68] 10^{-10} \text{kg s}^{-2}$. Blue contours show negative values and red contours show positive. Here $\Phi_0 = 118 \text{m}$. As before the perturbation imposed on U is $U \rightarrow (U - 20) \text{m s}^{-1}$ for $30 \text{km} < z < 40 \text{km}$.

- (a) shows normal evolution due to perturbation,
- (b) has U kept constant with perturbed value,
- (c) has U kept constant with unperturbed value.

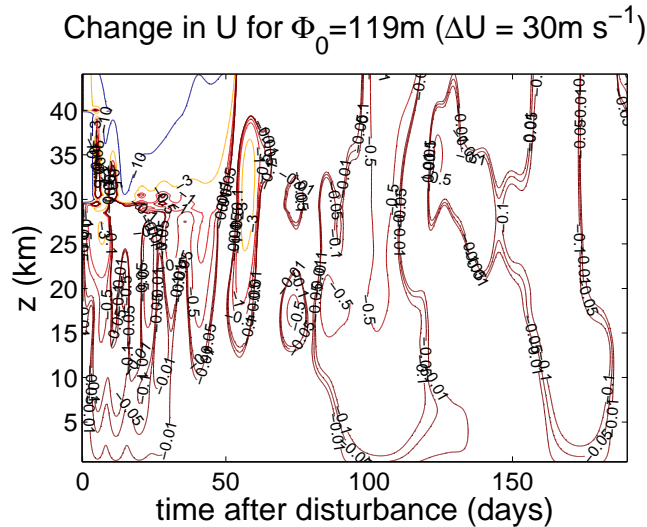


Figure 2.6:

As in figure 2.3(d), but ΔU now 30m s^{-1} . Notice that this larger perturbation has caused a more significant shift in the phase of the vacillations.

different initial profiles for the zonal wind can lead to different states being attained in a model run (Y87).

In the present model, for any value of Φ_0 such that $50\text{m} < \Phi_0 < 119\text{m}$, steady and vacillating states are both stable (note that these values are slightly different to those given in Y87 since we use slightly different values of the external parameters). By applying a perturbation at high altitudes (using a larger disturbance magnitude than that used in figure 2.3) it is found that we can force a model run from one of these states to the other. This greatly increases how much response is caused at low altitudes by the high level perturbation, and how long the response lasts.

We perform an experiment similar to that in section 2.5. Setting $U(z, 0) = U_e$ and subtracting $\Delta U\text{m s}^{-1}$ from the zonal mean velocity field from a height z_c up to the top boundary at time $t = 0$ causes such a transition between states. (The state obtained is the vacillating one, when the unperturbed system chooses the steady state. By looking at the flow profiles in figure 2.1(a) it seems plausible that for a perturbation that acts to decrease U (and so simulate wave drag) the transition caused will always be from steady state to vacillating state. This is found in all known cases.) Figure 2.7 shows an example, showing the perturbed velocity field (to make it clear what is happening, the perturbation in this figure is applied at $t = 100$ days and not $t = 0$).

It can be seen that the downward influence caused by the transition can be measured in tens of metres per second (anywhere from $\sim 20\text{m s}^{-1}$ to $\sim 60\text{m s}^{-1}$) as distinct from the fractions of metres per second caused by a disturbance that acts

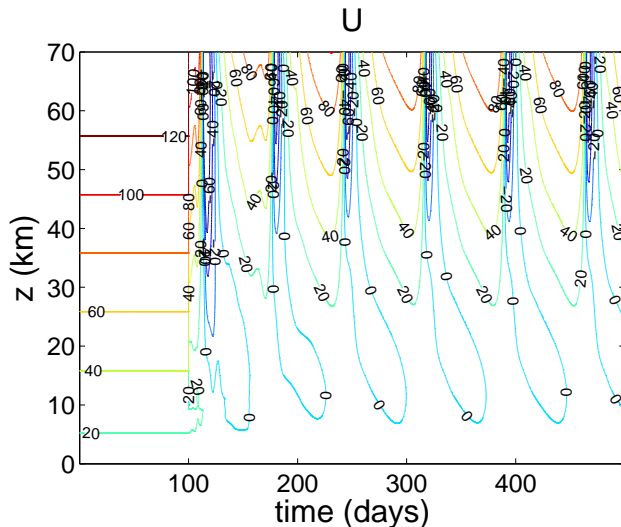


Figure 2.7:

A perturbation to the velocity field ($U \rightarrow (U - \Delta U)$) is made above a height z_c (varied). In experiments this perturbation is made at $t = 0$, but it is made at $t = 100$ days here to make it clear what is happening. As shown, disturbing the velocity field at high altitudes can cause a jump between solution branches (i.e. from steady state to vacillations). Here $\Phi_0 = 115\text{m}$.

to shift a vacillation or temporarily disturb a steady state.

We can quantify how the critical value ΔU_c of ΔU , that is the minimum amount of disturbance needed to cause the transition between states, depends on the height, z_c , above which it is applied. For $\Delta U < \Delta U_c$, the perturbation causes a weak response before the zonal wind relaxes back to a steady state. There is minimal downward influence (as in figure 2.3(a-c)).

We now consider the response for different values of z_c . Figure 2.8(a) shows ΔU_c plotted against z_c for $10\text{km} \leq z_c \leq 40\text{km}$. This curve appears roughly exponential, and this is confirmed (at least within the range of z_c considered) by figure 2.8(b) which shows $\rho \Delta U_c$ plotted against z_c . This graph is consistent with the long time limit response to a prescribed zonal force that is ‘switched on’, detailed in Haynes et al. (1991), in which $\rho \times$ change in U is constant below the level of the forcing. Thus it seems likely that, in the present experiments, a given magnitude of response $\rho \times$ change in U below the level of perturbation, z_c , characterises a transition from steady state to vacillations, regardless of the value of z_c . Thus perturbations at arbitrarily high altitudes can be effective if ΔU scales like ρ^{-1} . Another set of experiments were performed where a perturbation was applied by adding an additional forcing S to the rhs of equation (2.2), instead of perturbing the velocity field. It was found that critical values of ρS do not increase monotonically with z_c , consistent

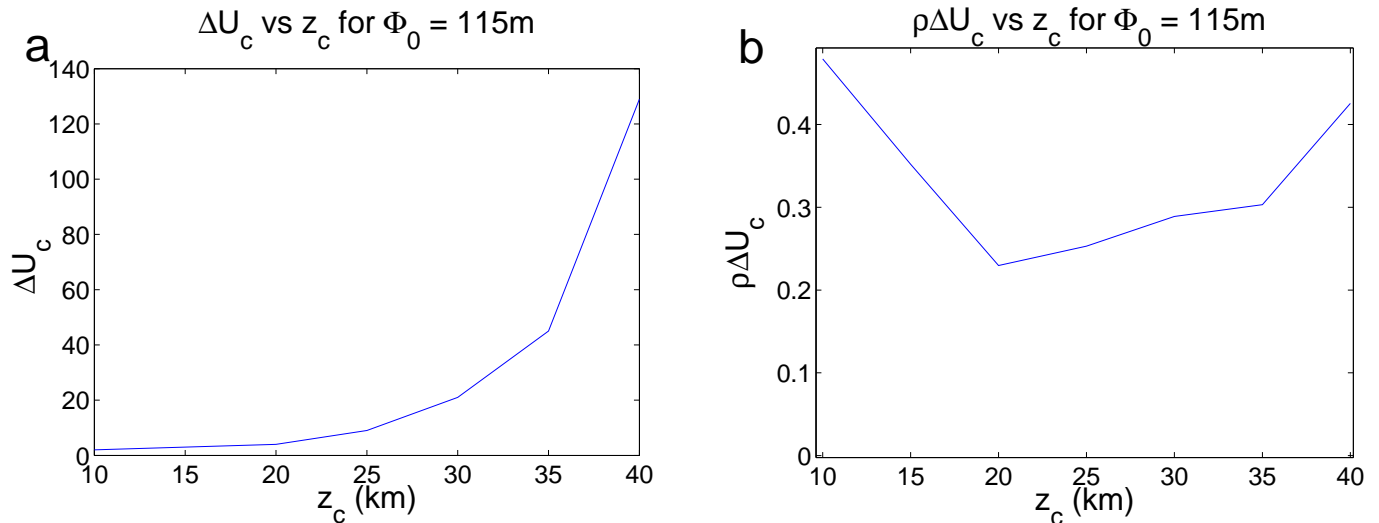


Figure 2.8:

- (a) Minimum amplitude of perturbation to U (ΔU_c in m s^{-1}) at $t = 0$ required to cause transition between solution branches plotted against height (z_c) above which it is applied,
- (b) Perturbation weighted by basic state density ($\rho\Delta U_c$) plotted against height (z_c) above which it is applied.

with figure 2.8(b). Hence this result is not dependent on how the perturbation is imposed. It should be mentioned that linear Rossby waves can only grow to a finite amplitude before deforming irreversibly, i.e. breaking, and thus cannot grow indefinitely in velocity amplitude $\propto \rho^{-1/2}$ with height. It would therefore be wrong to conclude that any given Rossby wave would affect flow evolution in the troposphere in the same way regardless of the height at which it breaks.

An important point to note from the above experiments is that, due to the non-linear nature of the dynamics, a small change in the initial conditions can mean a very large difference in the influence caused at lower altitudes by an imposed disturbance. For example, increasing Φ_0 by 1m causing the stable state to be vacillating rather than steady, or increasing the magnitude of the imposed disturbance ΔU by 1m s^{-1} such that a steady state is not regained but a transition to vacillations occurs, the downward influence our perturbation causes is changed greatly. This sensitive dependence to initial conditions has been seen in recent experiments using three dimensional models (e.g. Gray et al. 2003).

This sensitivity suggests that to accurately simulate the atmosphere in computer models (and a difference of 20m s^{-1} in the tropospheric zonal winds is significant!), a well resolved stratosphere is a necessity, and an accurate gravity wave drag parametrisation scheme and thermal relaxation profile is also important (since

breaking gravity waves will perturb U , and an incorrect value of T_e will change the bifurcation diagram as detailed in Y87, possibly changing the state of the stratosphere from steady to vacillating and causing a huge change to the zonal winds (see section 3.12)).

2.7 The non-locality of the zonal mean dynamics

In all the above we have full vertical non-locality in the zonal mean dynamics (so a change in U at one height can cause changes at other heights because of the vertical derivatives in equation 2.5). We can investigate the effect of this non-locality on the downward influence of our disturbance by artificially varying C in equation (2.5) between 1 and 0 ($C = 1$ corresponding to fully non-local dynamics and $C = 0$ corresponding to fully local dynamics). The parameter C has been included in equation (2.5) specifically for this purpose. When $C \neq 1$, for consistency we should also include a C in the second term on the rhs of equation 2.2. We take a slightly different approach and, following PS, relax to the background flow, U_e , using frictional relaxation rather than Newtonian cooling. When $C \neq 1$ neither method is actually physical, but the advantage of frictional relaxation is that we can look at the effect of just altering one term in the equations. So equation 2.2 becomes:

$$\frac{\partial Q_y}{\partial t} = \frac{\pi^2}{\rho L^2} \frac{\partial F}{\partial z} - \alpha_R \frac{\pi^2}{L^2} (U - U_e) \quad (2.9)$$

where

$$\alpha_R = \begin{cases} A_R \left[\frac{1}{200} + \frac{z}{60} \left(\frac{1}{2} - \frac{1}{200} \right) \right] & z \leq 60\text{km} \\ \frac{A_R}{2} & z > 60\text{km} \end{cases} \quad (2.10)$$

is a rate coefficient.

We repeat the experiments of taking 20ms^{-1} from U between altitudes of 30km and 40km (after 500 days of spin up time). The disturbance caused to the velocity field (i.e. the difference between the perturbed run and the control run) at a height of 15km is recorded. The root mean square (rms) of this disturbance averaged over 100 days (i.e. between days 500 and 600 of the model run) is calculated for various values of C . The results for the zonally symmetric response ($\Phi_0 = 0$) are shown in figure 2.9. In the more general case ($\Phi_0 \neq 0$) the rms value no longer decreases monotonically to zero as C is decreased, but crucially it still becomes zero as C gets small (and is still $< 10^{-3}\text{m s}^{-1}$ for $C \leq 0.2$). Results are found to be insensitive to the number of days that the rms value is averaged over. Note that for $C = 0$ no propagation of the imposed disturbance is possible above or below the height

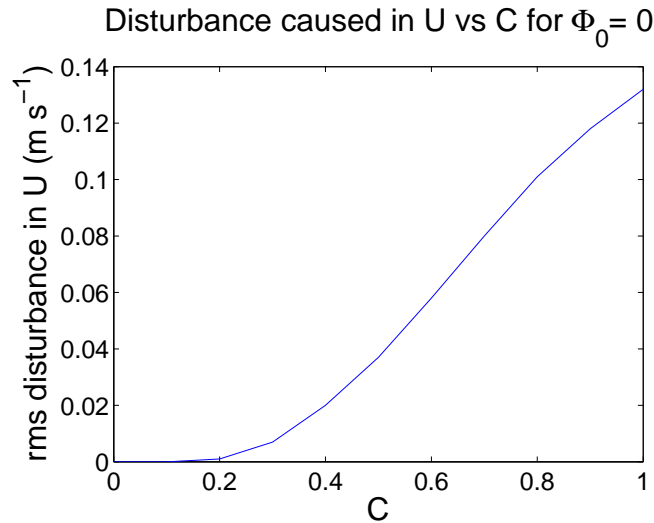


Figure 2.9:

The velocity field is perturbed between 30km and 40km and the root mean square (rms) of the disturbance caused to the velocity field at 15km, averaged over the 100 days following the perturbation, is calculated as C is varied. The zonally symmetric response ($\Phi_0 = 0$) is shown.

interval in which the disturbance is made.

We repeat the experiments of section 2.6, forcing the solution from steady state to vacillations. It is important to remember that changing C or A_R (defined in equation (2.10)) changes the value of Φ_0 for which a steady state solution ceases to exist so that comparisons (in the forcing required to cause a transition between states) must be made based on the distance of Φ_0 from the bifurcation point at which the steady state solution ceases to exist rather than on the absolute value of Φ_0 . We find that, as C decreases, it becomes harder to force a transition from steady state to vacillations, largely because the vacillations become weaker until for $C \lesssim 0.5$ they cease to exist altogether and only a single, steady, state exists. The smaller C becomes, and the further from the bifurcation point our value of Φ_0 is, for each value of C , so the smaller becomes the altitude, z_c , perturbing above which will not (for any reasonably sized perturbation) cause a transition between states.

There are two things to note here. One is that, as shown in figure 2.9, the downward influence of the imposed disturbance that is due to the zonally symmetric dynamics (cf figure 2.3(a)) tends to 0 as C tends to 0. In the case where $C = 0$ the disturbance in figure 2.3(a) would simply travel horizontally, never above or below the height at which it is applied. The other thing to note is that, as just mentioned, as C tends to 0 we no longer find vacillations (or, therefore, a bifurcation structure) in any parameter regime, and so causing a transition between two states as shown

in figure 2.7 is no longer possible. Therefore, for local zonal mean dynamics no downward influence is possible by either means. The vertical non-locality in U that we find in the extratropics is essential for any downward influence of a perturbation due to the non-linear nature of wave mean-flow interaction.

2.8 The QBO

To better understand the dynamics of downward propagation with vertically local zonal mean zonal wind, U , we next study the so called quasi-biennial oscillation (QBO), which is in fact a vacillation in almost exactly the present sense. More precisely, the QBO is a vacillation of the zonal wind in the tropics from an westward phase to a eastward phase and back again with an average period of about 28 months.

It has already been suggested that, since U becomes vertically local in the tropics, no downward influence of an applied perturbation is possible (since the disturbance itself does not travel vertically at all, and no vacillations exist). However, this is only true if we are forcing with one wave, as we have been doing up to now. The QBO exists due to forcing by more than one wave (where the waves must have different phase speeds). As we shall see, the downward propagation in the QBO due to an imposed perturbation at high altitudes is quite different to that we have seen above.

The QBO can be modelled using a 1D wave mean-flow interaction model which is very similar to the Holton–Mass model, except that internal gravity waves provide the wave driving instead of Rossby waves. The problems of using a WKB approximation for Rossby waves, discussed in section 2.3, do not arise with internal gravity waves (e.g. Plumb 1977). Thus, in what follows, we use a WKB approximation for the waves (which both follows the work of Plumb 1977 and eliminates the possibility of downward propagating waves complicating the mechanism for downward influence which we are studying).

Using the WKB approximation in a Boussinesq model, and non-dimensionalising all the variables (as in Plumb 1977) the equations solved (in the notation of Plumb 1977) are:

$$\begin{aligned}
 F_n(z) &= F_n(0) \exp \left[- \int_0^z g_n(z') dz' \right] \\
 g_n(z) &= \frac{\alpha}{k_n (U - c_n)^2} \\
 \frac{\partial U}{\partial \tau} - \Lambda \frac{\partial^2 U}{\partial z^2} &= - \sum_n \frac{\partial F_n}{\partial z}
 \end{aligned} \tag{2.11}$$

where F_n is the wave momentum flux of wave n , k_n and c_n are the wave number and

wave speed of wave n , α is buoyancy frequency multiplied by thermal dissipation rate, Λ is viscosity, and U is the horizontally averaged velocity (equivalent to zonal mean zonal wind). All quantities are scaled so as to be dimensionless, and $\alpha = k_i = F_i = 1 \forall i$. For equations of the full wave calculation (before a WKB approximation is made) see Plumb (1977).

The explanation for there being downward phase propagation in the QBO, despite the flow at all altitudes depending only on what happens below, was given by Plumb (1977). A brief summary of that explanation follows.

At least two waves are required to give vacillations, one of positive phase speed ($c_1 = 1$) and one of negative phase speed ($c_2 = -1$). (Note another difference to the case of Rossby waves which can only propagate in one direction. Also note that actually any two different phase speeds will do since a transformation to a frame moving with a speed such that the phase speeds of the two waves are in opposite directions will get us back to the case above.) Perturbing about the trivial solution to equation (2.11) and linearising, we get

$$\frac{\partial U}{\partial \tau} - \Lambda \frac{\partial^2 U}{\partial z^2} = 2 \left(U - \int_0^z U dz' \right) e^{-z} \quad (2.12)$$

The rhs of this equation is the linearised wave forcing. The dominant term at low levels is the first term on the rhs which arises due to the wave of positive phase velocity being attenuated more rapidly for $U > 0$ (due to the $1/(U - c_n)^2$ dependence of g in equation (2.11)) leading to net positive mean flow acceleration, and vice versa if $U < 0$. At upper levels the ‘shielding’ term (second term on rhs) dominates. The change of sign in the wave forcing happens at a height z_0 where these two terms balance. Below z_0 , $\partial U / \partial \tau > 0$ and $U > 0$ so that the shielding term is increasing, and to keep the balance between the wave forcing terms at z_0 , U at z_0 must increase. $\partial U(z_0) / \partial z < 0$ so z_0 must decrease. Hence the downward propagation of the change in sign of the wave forcing is dependent only on flow evolution below z_0 . As the positive U jet gets more confined to the lower boundary, the vertical viscosity Λ destroys the shear layer created and the vacillation starts over again. So to get the vacillations Λ has to be non-zero in some layer including the lower boundary. Plumb (1977) points out that there is no downward influence whatever in any layer in which $\Lambda = 0$.

Conversely, it was noted by Hampson (2000) that if $\Lambda \neq 0$ everywhere then the model does permit downward influence. In what follows we look quantitatively at how changes in Λ and α affect the downward propagation of an imposed disturbance.

2.8.1 Downward influence experiments

Experiments are carried out as in section 2.5, introducing a perturbation at high altitudes and looking at the change this has on the evolution below. In the following experiment we use $\alpha = 1$, $\Lambda = 0.02$, and initial profile

$$U(0) = \begin{cases} 0.03z & z < 10/3 \\ 0.1 & z > 10/3 \end{cases} \quad (2.13)$$

using a resolution $dz = 0.05$, $dt = 0.005$. We integrate to a height $z = 4$ and a time $\tau = 50$. Just as in Plumb (1977) we use two waves with $k_1 = k_2 = 1$, $c_1 = 1$, $c_2 = -1$, $F_1 = 0.5$, and $F_2 = -0.5$.

Between days 1 and 1.5 we introduce an extra forcing term, G , given by

$$G = \begin{cases} -4.2 \times 10^{-2} \times \frac{z-2.5}{dz} & 2.5 < z \leq 2.75 \\ -4.2 \times 10^{-2} \times \frac{3-z}{dz} & 2.75 < z \leq 3 \end{cases} \quad (2.14)$$

(This method of forcing is equivalent to what we call zonal-force perturbation in section 3.7 below.) Since we are using two waves of different phase speeds, vacillations can occur in the mean flow. The imposed perturbation thus shifts the phase of these vacillations as before (figure 2.3(d)). The vacillations in this model are strongest at lower altitudes and so most disturbance is below the point of perturbation (see figure 2.10). This is a clear example of the point made by Hampson (2000) that, given a small amount of diffusivity (which introduces a small amount of vertical non-locality into the model), a true downward influence is possible even in the tropics.

Consider figure 2.10(c). There are two obviously different speeds of downward propagation in the change in U . These are labelled c_g and c_p . We now look in more detail at the mechanisms behind each speed.

When forcing with only 1 wave (take $U(0) = 0$, $F_1 = 1$, and $F_2 = 0$) no vacillations can exist and a steady state is achieved. The change in the velocity field due to the applied disturbance (δU) is thus weak (with the zonal flow simply relaxing back to the undisturbed state, similar to the Holton–Mass model). The change in U (δU) only contains the disturbance propagating with speed c_g in figure 2.10(c).

Performing the same experiment as above (in this section) we look at how c_g depends on Λ (the diffusivity required to give vacillations, but which also introduces a small vertical non-locality into the mean flow dynamics).

In all cases (where either 1 wave or 2 waves are used to force the flow), we find

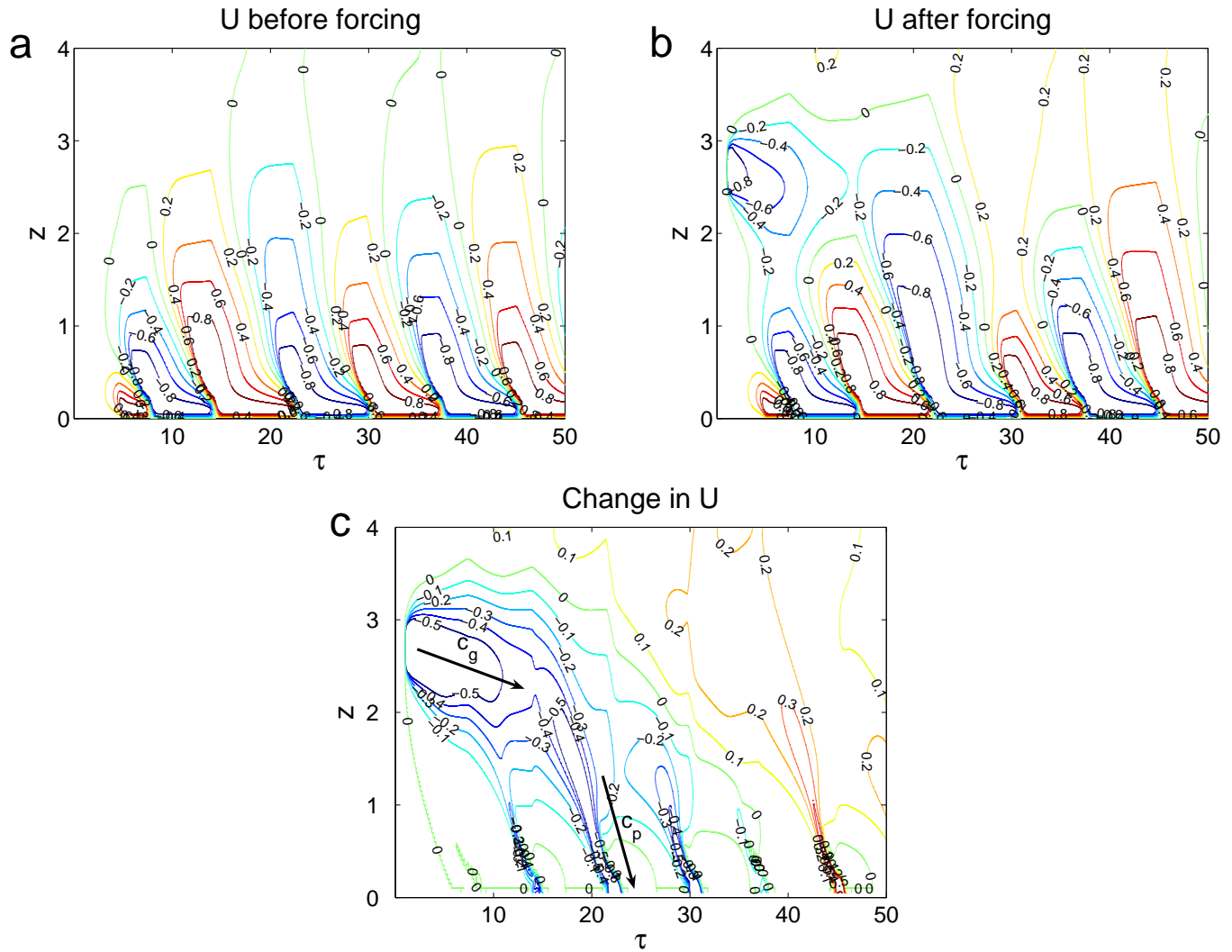


Figure 2.10:

Disturbance caused to the velocity field by perturbation at high altitudes (described in text). Notice that most of the disturbance is below the point of perturbation (imposed at heights $2.5 < z < 3$).

- (a) U before forcing
- (b) U after forcing
- (c) Change in U ((b) - (a))

that c_g^2 is proportional to Λ . This is to be expected since, at high altitudes, we essentially have zero wave driving leading to an essentially diffusive effect (where $z \sim \sqrt{\Lambda\tau}$ so that $c_g \sim \sqrt{\Lambda/\tau}$) which will not depend on the wave forcing. Note that as we approach the limit of true vertical locality $\Lambda \rightarrow 0$, we also find that $c_g \rightarrow 0$, consistent with the theory of Plumb (1977).

As already mentioned, in the 2 wave forcing case, shown in figure 2.10, an applied perturbation alters the phase of the vacillations. This gives the change in U whose downward propagation speed is denoted c_p in figure 2.10(c). c_p is directly related to the downward phase speed of the vacillations, and this will be affected by α .

We consider the various effects of α on the downward influence that we see. By altering α (in the absence of any applied perturbation) we find that the period of vacillations, T , is proportional to $1/\alpha$. As α is increased, the vacillations not only get faster, but they become more confined to the lower boundary of the model. To explain this, note from equation (2.11) that as α increases, g increases, so F undergoes a much sharper decay to zero near the bottom boundary. This gives the faster, more confined vacillations.

What this means is that, applying a disturbance at high altitudes has considerably reduced downward influence as α is increased (beyond the value of α that is used in figure 2.10). This is expected since, with $\partial F/\partial z$ virtually zero at higher altitudes, we see the weak 1 wave response to an applied perturbation (with only a diffusive type downward influence).

For values of α such that the vacillations are not too confined to the lower boundary, we find that c_p increases with α (from about 0.09 to 0.25 in non-dimensionalised units as α increases from 0.25 to 1) but then remains constant before the effect disappears due to vacillations being confined to the lower boundary (remaining at about 0.25 units as α is increased from 1 to 2.5).

Finally we should make the point that, despite similarities with the Rossby wave dynamics of the Holton–Mass model, there is a notable difference. When perturbing a vacillating state in the Holton–Mass model the response at all altitudes is almost instant (figure 2.3(d)). In the QBO model the response is much slower (consider the earliest 0 contour in figure 2.10(c)). By introducing a vertical non-locality into U , with coefficient Ω , so that the last equation (2.11) becomes

$$\frac{\partial}{\partial \tau} \left(\bar{u} - \Omega \frac{\partial^2 \bar{u}}{\partial z^2} \right) - \Lambda \frac{\partial^2 \bar{u}}{\partial z^2} = - \sum_n \frac{\partial F_n}{\partial z} \quad (2.15)$$

(similar to non-zero C in equation (2.5) in the Holton–Mass model) with Ω non-zero we recover the almost instant response at all altitudes to the applied per-

turbation (seen in figure 2.3(d) for the Holton–Mass model).

In the next section we return to considering the extratropical dynamics of the Holton–Mass model (with Rossby wave driving).

2.9 A comparison with a new lower boundary

All the experiments discussed above use a lower boundary condition where the geopotential height, Φ , and zonal mean flow, U , are given on the lower boundary. It is important to make sure that the mechanism we have outlined for the downward influence of an upper level perturbation does not depend on the artificial nature of this lower boundary condition. Therefore, we now use a more realistic lower boundary condition which allows Φ and U to evolve on the boundary with the flow. The waves in this case are produced by topography. In formulating this boundary condition it is assumed that the fluid velocity normal to the surface (w) should vanish there (i.e. a rigid lower boundary). Following Yoden (1987(c)) this new boundary condition is specified by

$$\begin{aligned} & \left(\frac{\partial}{\partial t} + ik\gamma U + \alpha \right) \frac{\partial \Phi}{\partial z} - ik\gamma \Phi \frac{\partial U}{\partial z} \\ & + ik\gamma \frac{N^2}{g} h_0 U - \left(k^2 + \frac{\pi^2}{L^2} \right) \frac{N^2}{f} D_E \Phi = 0 \end{aligned} \quad (2.16)$$

$$\begin{aligned} & \frac{\partial}{\partial t} \frac{\partial U}{\partial z} + ik \frac{\pi^2}{4L^2} \gamma \frac{N^2 g}{f^2} (\Phi h_0^* - \Phi^* h_0) - \frac{\pi^2}{L^2} \frac{N^2}{f} D_E (U - U_e) = \\ & - \alpha \frac{\partial (U - U_e)}{\partial z} + ik \frac{\pi^2}{4L^2} \gamma \frac{g^2}{f^2} \left(\Phi \frac{\partial \Phi^*}{\partial z} - \Phi^* \frac{\partial \Phi}{\partial z} \right) \end{aligned} \quad (2.17)$$

on $z = 0$. $D_E = (4/f)^{1/2}$ is the coefficient of an Ekman pumping term, and $*$ denotes a complex conjugate. To allow the topography to fit in simply with the truncated model the profile $h(x, y) = \text{Re}[h_0 e^{ikx}] \sin(\pi y/L)$ is used, where h_0 specifies the maximum height of the topography. As before, $k = s/(a \cos(\pi/3))$, where $s = 2$, and $L = \pi a/3$. $\alpha = [1.5 + \tanh((z - 35)/7)] \times 10^{-6} \text{s}^{-1}$. From now on we will keep with the notation of Wakata and Uryu (1987) and Yoden (1987(c)) and call this new topographical boundary condition the W -condition (since $\mathbf{u} \cdot \mathbf{n} = 0$ on the boundary so that $w = \mathbf{u} \cdot \nabla h$ there), and the original condition (where U and Φ are specified on the boundary) the Φ -condition.

In the following experiments a new profile could have been chosen for U_e , or the value of N^2 altered, to make the model domain act more as if it included a troposphere (since the Φ -condition can be thought to model the tropopause and the W -condition to model the ground). But the interest here is on downward influence

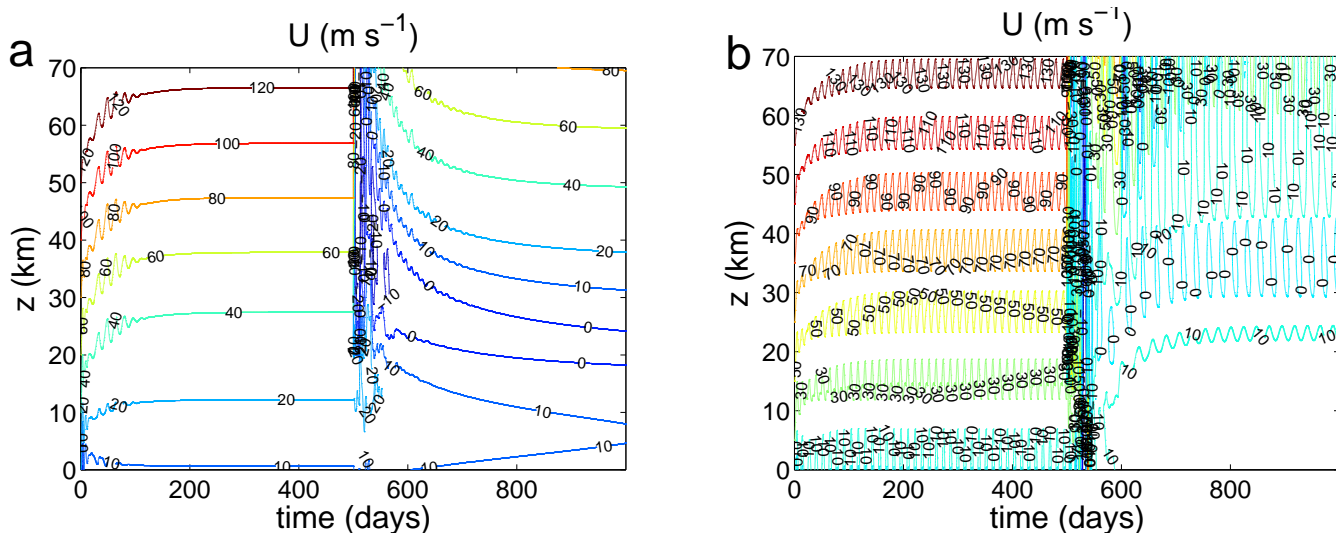


Figure 2.11:

Using the W -condition lower boundary, it is still the case that perturbing the velocity field at high altitudes can cause a transition between solution branches.

(a) shows a transition between two steady states ($h_0 = 950\text{m}$), and (b) shows a transition between two vacillating states ($h_0 = 570\text{m}$).

through the stratosphere. The purpose of checking results against a more realistic lower boundary is simply to make sure that they do not arise solely because of the non-physical nature of the Φ -condition lower boundary. So we keep the same U_e and N^2 as before.

Yoden (1987(c)) mapped out the bifurcation structure of stable solutions (steady and vacillating) with bifurcation parameter h_0 (the amplitude of the topography). He found a new type of vacillation with this W -condition where both U and Φ change significantly on the lower boundary during the model run. By choosing appropriate values of h_0 and perturbing U at high altitudes it is possible to cause a transition between solution branches (from either steady state or vacillation to either steady state or vacillation) just as with the Φ -condition. Examples are shown in figure 2.11, figure 2.11(a) showing a forced transition between two steady states ($h_0 = 950\text{m}$), and figure 2.11(b) showing a forced transition between two vacillating states ($h_0 = 570\text{m}$).

The experiment performed in section 2.5 was repeated for this W -condition and, as is shown in figure 2.12, the results obtained are qualitatively similar to those found with the Φ -condition (cf figure 2.3). As before, only a weak downward influence (essentially the zonal mean dynamics) is found whilst a steady state is the stable one for the given value of h_0 . Once vacillations are found their phase can be shifted, as before, and a stronger downward influence is seen. So the results of the previous

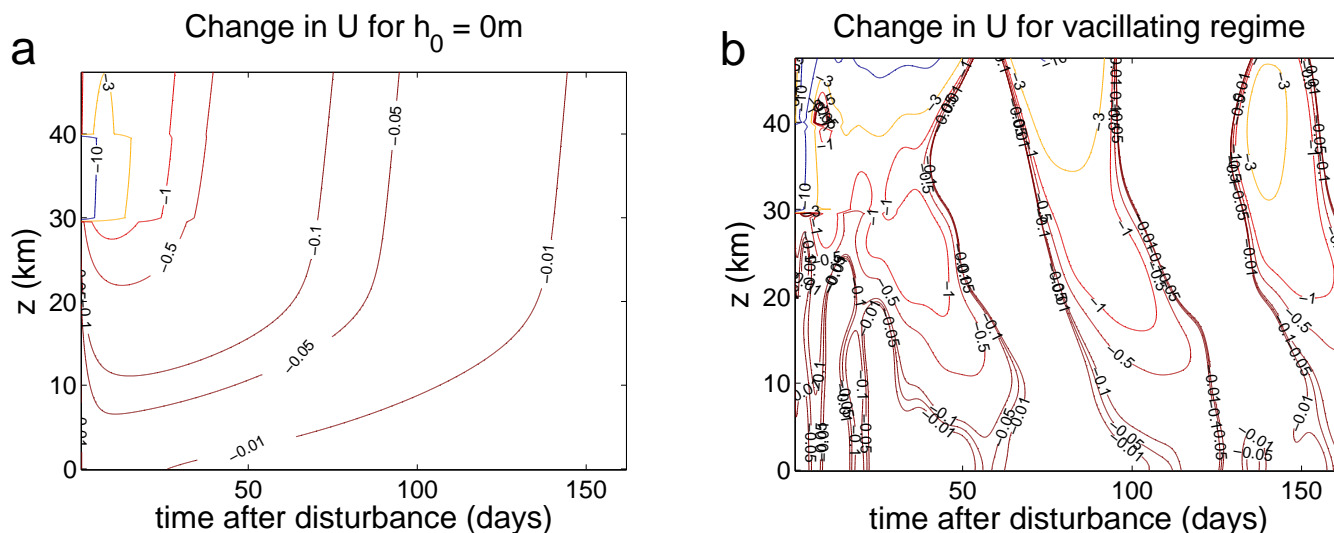


Figure 2.12:

The velocity field is perturbed such that $U \rightarrow (U-20)\text{m s}^{-1}$ for $30\text{km} < z < 40\text{km}$, and the change in U that this causes is analysed, now using the W -condition lower boundary. A comparison with figure 2.3 (a) and (d) shows that the same qualitative behaviour is observed as with the Φ -condition lower boundary.

sections do not depend on the artificial properties of the Φ -condition.

2.10 A comparison with a new wave generation mechanism

As a further test of the robustness of this mechanism, whereby the non-linear nature of the dynamics at high values of wave forcing allows significant downward influence of an upper level disturbance through wave mean-flow interaction, is to produce the wave forcing in a different way. So far we have looked at waves produced by a prescribed geopotential height anomaly, and by a simple topography.

Another way of producing waves is through tropospheric heating as was done by Scott and Polvani (2004). They use a 3D general circulation model (GCM) with mesospheric damping to keep the velocity field at a realistic size at high altitudes. They also use a tropospheric damping to prevent baroclinic instability, and impose a zonally-symmetric radiative equilibrium temperature profile, T_e , to simulate the cold polar vortex in the stratosphere. To allow waves to propagate vertically they force a weak eastward flow in the troposphere. They introduce a parameter A_0 to characterise the amplitude of the tropospheric heating which is of the form

$$Q = A_0 G(\phi) Z(z) s \cos \theta \quad (2.18)$$

where ϕ is latitude, θ is longitude, p is pressure, and s is the zonal wavenumber. $G(\phi) = \sin^2[(\phi - \pi/6)/(1/3)]$ for $\phi > \pi/6$ and zero elsewhere, $Z(z) = \cos^2(\pi z/2z_T)$ for $z < z_T$ (z_T is the tropopause height, given below) and zero elsewhere, the tropospheric weak westerlies, relaxed to at a rate $k_T Z(z)$, take the form $u_T(\phi) = U \sin^2(2\phi)$ where $U = 30 \text{ m s}^{-1}$, and the mesospheric damping takes the form $k_{sp}((p_{sp} - p)/p_{sp})^2$ for $p > p_{sp}$ and zero elsewhere, with p_{sp} the pressure at the stratopause.

To use the equivalent heating and damping (given above) and temperature profile (given below) in a Holton–Mass model, we follow Andrews et al. (1987, p.113–127) to derive the new form of equations 2.1 and 2.2 starting from the primitive equations.

Working in a quasi-geostrophic β -channel centred at 60°N we then truncate as in the Holton–Mass model, keeping one zonal wavenumber and the appropriate sinusoidal meridional profile (projecting non-linear terms onto this profile). The final equations (replacing equations (2.1) and (2.2)) are

$$\begin{aligned} \frac{\partial q}{\partial t} = & -ik\gamma Uq - i\frac{gk}{f}(\beta + \gamma Q_y)\Phi - \frac{g}{\rho} \frac{\partial}{\partial z} \left(\rho \frac{\alpha f}{N^2} \frac{\partial \Phi}{\partial z} \right) \\ & + \frac{f}{\rho} \frac{\partial}{\partial z} \left[\rho A_0 \sin^2(1/2) \cos^2(\pi z/2z_T) \frac{Re^{-\kappa z/H}}{N^2 H} \right] \\ & + k_{sp}(1 - e^{(z_{sp}-z)/H})^2 \left(k^2 + \frac{\pi^2}{L^2} \right) \frac{g}{f} \Phi \end{aligned} \quad (2.19)$$

$$\begin{aligned} \frac{\partial Q_y}{\partial t} = & \frac{\pi^2}{\rho L^2} \frac{\partial F}{\partial z} + \frac{1}{\rho} \frac{\partial}{\partial z} \left[\rho \frac{\alpha f^2}{N^2} \frac{\partial}{\partial z} (U - U_e) \right] - \frac{\pi^2}{L^2} k_T \cos^2(\pi z/2z_T) (U - U_T) \\ & - \frac{\pi^2}{L^2} k_{sp} (1 - e^{(z_{sp}-z)/H})^2 U \end{aligned} \quad (2.20)$$

with

$$\frac{f}{\rho} \frac{\partial}{\partial z} \left[\rho A_0 \sin^2(1/2) \cos^2(\pi z/2z_T) \frac{Re^{-\kappa z/H}}{N^2 H} \right]$$

from equation (2.19) and

$$-\frac{\pi^2}{L^2} k_T \cos^2(\pi z/2z_T) (U - U_T)$$

from equation (2.20) included in the troposphere ($z < z_T$) only and

$$k_{sp}(1 - e^{(z_{sp}-z)/H})^2 \left(k^2 + \frac{\pi^2}{L^2} \right) \frac{g}{f} \Phi$$

from equation (2.19) and

$$-\frac{\pi^2}{L^2}k_{sp}(1 - e^{(z_{sp}-z)/H})^2U$$

from equation (2.20) included in the mesosphere ($z > z_{sp}$) only. Suffix T relates to the troposphere (with z_T the height of the tropopause, taken to be 10km here, and k_T the coefficient of tropospheric damping) and suffix sp relates to the stratopause (with z_{sp} the height of the stratopause, taken to be 50km here, and k_{sp} the coefficient of mesospheric damping). A_0 is the amplitude of the tropospheric heating, R the gas constant for dry air, and $\kappa = R/c_p$ where c_p is the specific heat at constant pressure. We take $U_T = 22.5\text{m s}^{-1}$ (equivalent to Scott and Polvani (2004)).

A meridional temperature profile simulating the cold polar vortex in the stratosphere gives a new equilibrium profile U_e . Using the thermal wind equation

$$\frac{\partial U_e}{\partial z} = -\frac{R}{Hf_0} \frac{\partial T}{\partial y} \quad (2.21)$$

the temperature profile

$$T_e = (1 - w(\phi))T_0 + w(\phi)T_{PV}(p) \quad (2.22)$$

where

$$w(\phi) = (1 + \tanh[(\phi - \phi_0)/\delta\phi])/2$$

and

$$T_{PV}(p) = T_0 \min[1, (p/p_T)^{R\Gamma/g}]$$

gives a background equilibrium velocity profile U_e satisfying

$$\frac{\partial U_e}{\partial z} = \begin{cases} 0 & z \leq z_T \\ \frac{RT_0}{Haf} \frac{9\text{sech}^2(1/2)}{2\pi} [1 - (5e^{-z/H})^{R\Gamma/g}] & z > z_T \end{cases} \quad (2.23)$$

where we have used $\phi_0 = 50^\circ$, $\delta\phi = 20^\circ$, and we take $T_0 = 240\text{K}$, $\Gamma = 2 \times 10^{-3} \text{K m}^{-1}$, $p_T = 200\text{hPa}$, and $U_e(0) = U_T$, and we then relax to this profile using Newtonian cooling with coefficient α as before. We also have to add extra terms to the W -condition lower boundary so that boundary conditions (2.16) and (2.17) become:

$$\begin{aligned} & \left(\frac{\partial}{\partial t} + ik\gamma U + \alpha \right) \frac{\partial \Phi}{\partial z} - ik\gamma \Phi \frac{\partial U}{\partial z} + ik\gamma \frac{N^2}{g} h_0 U \\ & - \left(k^2 + \frac{\pi^2}{L^2} \right) \frac{N^2}{f} D_E \Phi = \frac{R}{gH} A_0 \sin^2(1/2) \end{aligned} \quad (2.24)$$

$$\begin{aligned} & \frac{\partial}{\partial t} \frac{\partial U}{\partial z} + ik \frac{\pi^2}{4L^2} \gamma \frac{N^2 g}{f^2} (\Phi h_0^* - \Phi^* h_0) - \frac{\pi^2}{L^2} \frac{N^2}{f} D_E (U - U_e) = \\ & - \alpha \frac{\partial (U - U_e)}{\partial z} + ik \frac{\pi^2}{4L^2} \gamma \frac{g^2}{f^2} \left(\Phi \frac{\partial \Phi^*}{\partial z} - \Phi^* \frac{\partial \Phi}{\partial z} \right) \\ & - k_T \frac{\partial}{\partial z} (U - U_T) \end{aligned} \quad (2.25)$$

It turns out that the tropospheric damping is not needed in the 1D model as no baroclinic instability is seen, and so we set $k_T = 0$. The damping seems to have a strong effect in the Holton–Mass type model and to prevent anything but a steady state from being realised. We also find that there is no need to force a weak eastward flow in a 1D model in order for waves to be able to propagate vertically – the model generates a sufficiently eastward value of U without this forcing. We set wavenumber $s = 2$ (even though Scott and Polvani (2004) use $s = 1$) which is permissible since this does not change the physics in a 1D model (wavenumber defined in equation (2.6)).

As is the case in Scott and Polvani (2004) vacillations are found to exist for certain values of A_0 , and using A_0 as a bifurcation parameter it is still the case that a bifurcation structure exists (multiple states existing for some values of A_0) and by imposing a disturbance in U at high altitudes we can cause a jump between different states creating significant downward influence as before. (Multiple states no longer exist if h_0 is used as a bifurcation parameter because of the new equilibrium profile, U_e , that is used. h_0 is kept at 0m now so that waves are solely produced by the tropospheric heating). In the case of a steady state, weak downward influence as seen in section 2.5 is still seen, although the structure of the change seen in the velocity field, is slightly different (see figure 2.13).

We now return to considering the stratosphere only version of the Holton–Mass model with Φ -condition lower boundary.

2.11 Other details on downward propagation

The following points, although not directly concerning the mechanism outlined in this chapter, do nevertheless cast some light on the dynamics of vacillations (which are crucial for large downward influence in the work detailed above).

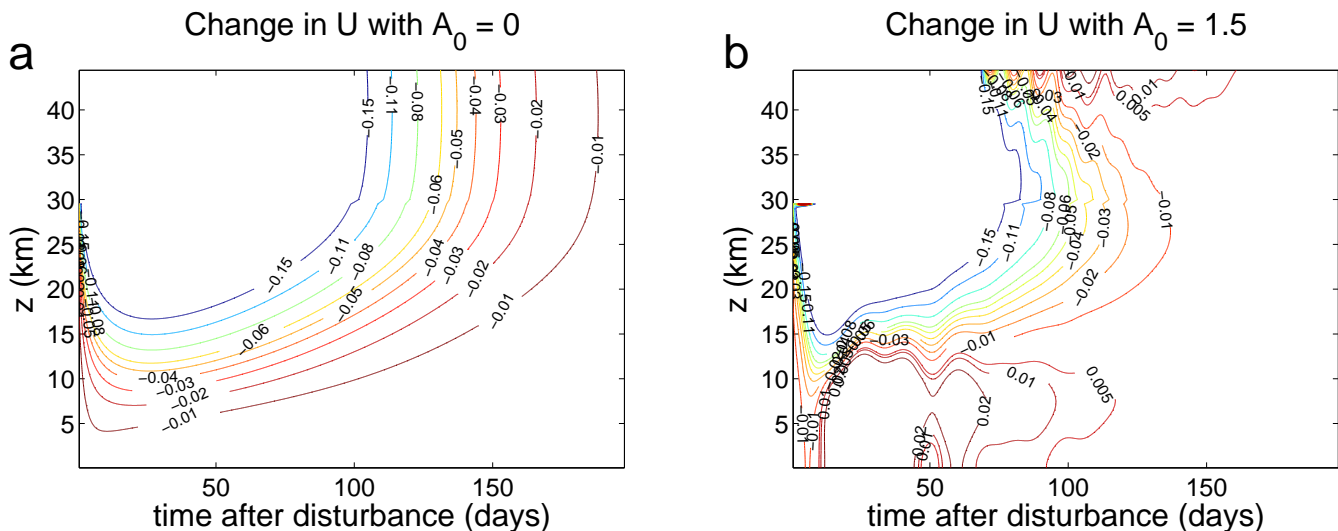


Figure 2.13:

Again, the velocity field is perturbed such that $U \rightarrow (U-20)\text{m s}^{-1}$ for $30\text{km} < z < 40\text{km}$, and the change in U that this causes is analysed. This time waves are produced by tropospheric heating, and the difference that makes is observed.

(a) shows weak downward influence with no tropospheric heating (zonal mean dynamics),

(b) shows weak downward influence with tropospheric heating.

2.11.1 Downward phase speed

So far in this chapter the impression has been given that varying Φ_0 , the lower boundary wave forcing, does not make much (if any) difference to the response at lower altitudes to a perturbation in the upper stratosphere unless we happen to cross a bifurcation point from one stable state to another (usually steady to vacillating). It may seem, therefore, that the medium-range weather forecaster has no interest (at least in this respect) in the amount of wave driving produced in an area by the mountains or land–sea temperature differences. What we shall see in this section is that the amount of wave driving, Φ_0 , *does* change the response at lower altitudes, in a different way.

PS noted that by imposing a time dependent lower boundary forcing ($\Phi_0(t)$) a downward phase propagation is seen in the mean flow anomaly, $U_{\text{anom}} = (U - \text{time average of } U)$. After several experiments we have verified that this downward phase propagation is robust to whether the vacillations are naturally present or imposed, and whether we use the Φ or W condition lower boundary. An example of U_{anom} due to natural vacillations with the Φ boundary condition ($\Phi_0 = 120\text{m}$) is shown in figure 2.14.

The interest then is in what affects the speed of this downward phase propagation

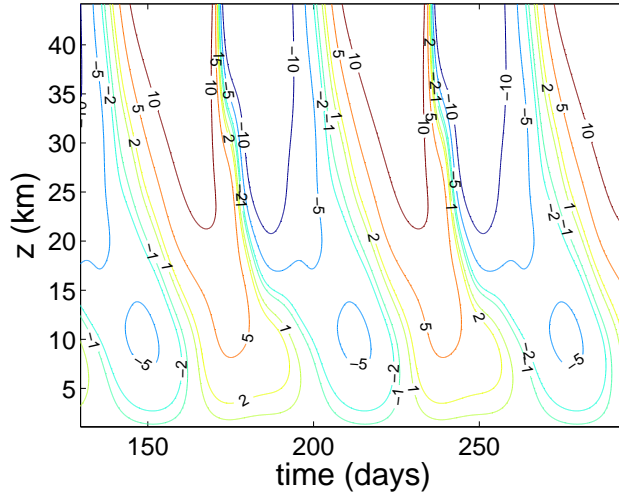


Figure 2.14:

U anomaly (U_{anom} as defined in section 2.11.1) in m s^{-1} for Φ -condition lower boundary, $\Phi_0 = 120\text{m}$.

(we saw that the non-dimensionalised buoyancy frequency \times thermal dissipation rate played a role in the case of the QBO). For a lower boundary forcing that depends on time throughout the run (i.e. periodic forcing), as used in PS, it is not obvious that the downward phase speed at any time does not depend on vacillations at an earlier time in the run. So we consider one period of time dependent forcing, as used in PS, and keep Φ_0 constant for the rest of the run. In other words, we take

$$\Phi_0 = \begin{cases} K + B[1 - \cos(2\pi t/T)] & 200 \text{ days} < t < 400 \text{ days} \\ K & \text{otherwise} \end{cases} \quad (2.26)$$

where $T = 200$ days. Thus we use a Φ condition lower boundary, and we run for 500 days. As usual, $\alpha = [1.5 + \tanh((z - 35)/7)] \times 10^{-6} \text{s}^{-1}$, and $U(0) = U_e$.

It might be expected that downward phase speed changes with K , the equilibrium value of the geopotential height on the lower boundary. B gives the amplitude of a small time-oscillatory perturbation imposed in Φ_0 . What we will call phase speed is calculated by looking at contours of U_{anom} . We look at the altitude (z) and time co-ordinates of the lowest points of the contours closest to altitudes of 13km and 2km and calculate the phase speed from them. Although the phase speed is not independent of z , using the same range of z for each calculation we can still get an indication of the dependence of phase speed on K . The results are shown in table 2.1. Note that the qualitative dependence of phase speed on K does not depend on B .

Table 2.1:
 Φ_0 defined in terms of K and B as in equation (2.26)

K (m)	Phase speed (km day ⁻¹)	
	$B = 10\text{m}$	$B = 2\text{m}$
100	8.59	7.44
80	7.75	6.79
60	7.09	6.28
40	6.56	5.87
20	6.66	6.11
0	7.02	7.23

Table 2.2:
 $\alpha = E \times 10^{-6}\text{s}^{-1}$ as defined in section 2.11.1

E	Phase speed (km day ⁻¹)		
	$K = 0\text{m}$	$K = 40\text{m}$	$K = 80\text{m}$
1	10.7	10.8	12.3
2	22.3	25.3	29.6
3	37.2	45.6	53.6
4	56.0	57.0	97.8
5	74.9	95.2	116.9

Whilst we might expect the increase of phase speed with K seen for values of $K = 40\text{m}+$ (since $|\Phi|$ is an indication of departure from the zonal mean dynamics) the fact that phase speed also increases as K decreases to 0m seems worthy of further investigation. It is worth looking at how phase speed depends on α . Set $\alpha = E \times 10^{-6}\text{s}^{-1}$, constant in height and see how phase speed depends on α by altering E . Results are given in table 2.2, where $B = 2\text{m}$ throughout. Although some of these phase speeds might seem large, we are using quite large values of α when $E = 3, 4, 5$. It is the dependence of phase speed on K and E that is really of interest.

The first thing to notice is that now phase speed increases with K . The effect seen before of phase speed increasing as K decreased to 0 was simply due to α being a function of z . The other thing to notice is that phase speed increases as α increases. This makes sense – for the dynamics to re-equilibrate faster, we might expect the phase speed to be faster.

Reichler et al. (2005) perform 3D experiments where the lower boundary wave forcing in their model is perturbed, waves travel into the stratosphere and break and the signals from that are seen again in the troposphere (see figure 1.2). They

mention that the phase speed of the linear adjustment of the zonal-mean circulation to stratospheric perturbations is proportional to α (Haynes et al. 1991) and that the eddy driving of the mean flow is stronger if α is larger. Thus they expect the rate of descent of stratospheric signals to increase as α increases (though they do not test this). Indeed, this is what we find above.

The ability to use the stratosphere as a predictor for tropospheric change depends on an understanding of the downward phase propagation. The amount of wave driving and the radiative state are therefore of great interest to the medium-range weather forecaster. It is worth again making the point, therefore, that a well resolved stratosphere with a correct radiative state is a must if we want to accurately compute what affect the stratosphere will have on the troposphere in model simulations.

2.11.2 Period of vacillations

Having considered the effect of α and Φ_0 on the downward phase speed of vacillations in this 1D model it makes sense to look at how the period of these vacillations, T , depends on these quantities. Attention is again confined to steady wave forcing ($B = 0, \Phi$ at lower boundary = $K = \Phi_0$ as previously).

The model is run with a Φ -condition lower boundary (in the same configuration as sections 2.5 and 2.6. Using $\Phi_0 = 180, 240, 300, 360,$ and 420m we measure the period of vacillations in each case.

We might expect that, since $\frac{\partial U}{\partial t} \propto \nabla \cdot \mathbf{F}$ and $\nabla \cdot \mathbf{F} \propto \Phi^2$, we would find $\Phi_0^2 \propto 1/T$. However, from figure 2.15 we see that actually $\Phi_0 \propto 1/T$.

Also, defining $\alpha = E \times 10^{-6} \text{s}^{-1}$ (as in the previous section) and setting $\Phi_0 = 400\text{m}$, the model is run for $E = 0.4, 0.6, 0.8, 1.0, 1.2,$ and 1.4 . Since $\frac{\partial U}{\partial t} \propto \alpha U$ we might expect that $\alpha \propto 1/T$. However, we find that T is essentially independent of E , increasing slightly from 19.7 to 21.0 as E increases from 0.4 to 1.4. Plumb (1977) found a similar result when, using the model of section 2.8, he considered the dependence of T on Λ (in equation (2.11)).

These results are surprising. It may be that the vacillations generated in this 1D model are rather artificial in nature. To test this we need to re-run these experiments with a more realistic model. We return to this in the next chapter.

2.11.3 Generation of vacillations

Although vacillations in a 1D model are dynamically exciting, for them to be worth studying they ought to exist also in more realistic models and in the atmosphere itself. In the next chapter we will see that a more realistic, 3D, model, run in per-

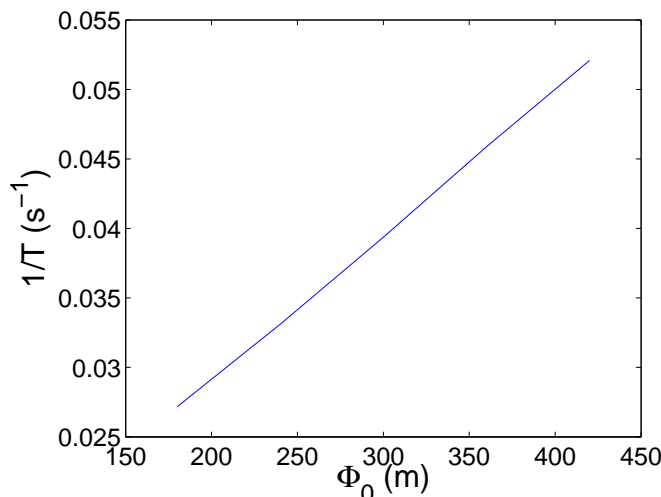


Figure 2.15:

Φ_0 (m) verses $1/T$ (s^{-1}) where T is the period of vacillations found to occur naturally for lower boundary wave forcing amplitude Φ_0 .

petual January mode, exhibits repeated vacillations that resemble sudden warmings in the real stratosphere. Thus we draw a parallel between the vacillations in a 1D model and stratospheric sudden warmings.

Stratospheric sudden warmings, major and minor, occur when the wave driving present is sufficient to significantly decrease the value of the mean wind U away from its radiative equilibrium state U_e over a short time (equivalently, as the name suggests, T in the stratosphere increases significantly over a short time). In the case of minor warmings U becomes a weaker eastward wind, but in the case of major warmings U becomes westward for a short time. Often, during northern hemisphere winter, the winter polar vortex will undergo a sudden warming (this occurs in the northern hemisphere due to the large amount of wave forcing there. Waves break on the edge of the polar vortex eroding it and causing it to deform). At the end of the winter it will undergo a final warming when the vortex disappears until the following winter.

In the Holton–Mass model, a stable steady state can be thought of as a winter in which the polar vortex does not undergo a sudden warming, and a vacillating state as one when it does (although, admittedly, in the real atmosphere stratospheric sudden warmings (SSWs) do not occur with the regular periodic nature of vacillations found in the Holton–Mass model). To cause a transition from a steady to a vacillating state by introducing a perturbation in the upper stratosphere, is for such a perturbation to have caused a sudden warming of the vortex to occur when one would not otherwise have done so. This makes clear the strong effect on the troposphere that such

perturbations can have (since the effect of a sudden warming will cause change over the whole depth of the stratosphere).

Yoden (1987(b)) investigates the dynamics of major and minor sudden warmings. The Φ condition lower boundary is used. One of the slightly surprising things found by Yoden is that generation of wave activity does not always come from the bottom boundary, but can sometimes be generated by the internal dynamics and manifested in a convergence of EP flux (actually seen as a dipole in the EP flux divergence). He suggests that the period of each vacillation is split into two parts: a dynamically active one in which the sudden warming occurs (brought about by the dipole in EP flux divergence just mentioned) and a dynamically inactive one in which the mean flow relaxes back towards the radiative equilibrium profile, the EP flux being greatest at the lower boundary during this time. This relaxation can take place since waves cannot propagate upward through westward winds due to the Charney–Drazin criterion (see Andrews et al. 1987). In the case of the Φ condition lower boundary, vacillations bifurcate from the steady solution for U that is very different from the radiative equilibrium profile as we might expect (see figure 2.1).

Yoden (1987(b)) also mentions a different type of vacillation due to wave interference which is realisable with the W condition lower boundary. This has no dynamically inactive period, and bifurcates from the steady solution close to the radiative equilibrium profile (more commonly associated with a steady state, see figure 2.1).

What Yoden’s work seems not to make clear is that, for both W condition and Φ condition lower boundaries, we can have vacillations bifurcating from the steady solution far from radiative equilibrium, which are not generated by a dipole in the EP flux divergence but where wave generation does come from the lower boundary. This implies that the dynamics of the generation of vacillations is more subtle than Yoden’s work suggests. (Indeed, Yoden’s work shows that minor warmings are found to occur for values of Φ_0 greater than, as well as less than, the required Φ_0 to give major warmings. The link between the two, then, as well as what causes the generation of these vacillations, seems complicated.)

Figure 2.16 shows examples of SSWs occurring as described above. Figures a) and b) show U and F for the Φ condition lower boundary. We have $\Phi_0 = 58\text{m}$, $\alpha = [1.5 + \tanh((z - 25)/7)] \times 10^{-6}\text{s}^{-1}$, and the initial condition

$$U(0) = \begin{cases} (30 - z)/3 + z(z - 20)(z - 30)/150 & z < 30 \text{ km} \\ 2(z - 30) & z > 30 \text{ km} \end{cases} \quad (2.27)$$

is used so that the model run follows the branch of solutions far from radiative equilibrium. Figures c) and d) show U and F for the W condition lower boundary. Here $U(0) = U_e = 20 + 2z$, $\alpha = [1.5 + \tanh((z - 35)/7)] \times 10^{-6} \text{s}^{-1}$, and $h_0 = 600 + 250(1 - \cos(2\pi t/200))$. The resolution used in both cases is $dt = 0.05$ days, $dz = 0.5$ km.

2.11.4 Wave transience – downward propagation by a different mechanism

Periods of rapid growth of extratropical planetary waves are referred to as wave transience. According to linear wave theory, the wave driving (EP flux divergence) can be split into a wave transience term and a dissipation term, the wave transience term being given by

$$W_t = -\frac{1}{2Q_y} \frac{\partial |q|^2}{\partial t} \quad (2.28)$$

Applying a disturbance at high altitudes, either to the velocity field (as done in all our experiments above) or in the form of an extra forcing term on the rhs of equation (2.2), induces a non-zero wave transience field. The exact form of the wave transience field is dependent on the type of disturbance applied, but the pattern seen near the lower boundary (see figure 2.17(a)) is always present.

We expect that this downward propagation is not due to wave-mean flow interaction (as is the case for the downward propagation seen in the U anomaly discussed in section 2.11.1), but to wave effects only. To test this hypothesis we use a value of Φ_0 such that the stable state is steady ($\Phi_0 = 90\text{m}$, $U(0) = U_e$) and allow 500 days for this state to be reached. We then impose $U \rightarrow (U - 10)\text{m s}^{-1}$ for $30 < z < 40\text{km}$ at $t = 500$ days and follow the evolution of the wave transience field thereafter. We see (figure 2.17(a)) that as time progresses the pattern in the wave transience field below 30km becomes horizontal (i.e. ceases to travel downwards) and (about 70 days after the disturbance is applied) eventually becomes positive (in other words we see an upward propagating anomaly). We know that this cannot be the phase speed of the wave we are looking at since, for Rossby waves, vertical phase and group velocities are always in opposite directions, and we know that the perturbation is imposed at upper levels, hence the phase speed should be (and must be) upwards at first, before Rossby waves reflect back up. The wave transience field simply gives an indication of the region affected directly by our imposed perturbation and we would like to know what causes this effect to spread downwards.

To this end, we impose the same perturbation but then at day 500.25 keep U constant for all time. We see a similar pattern below 30km although after a time this

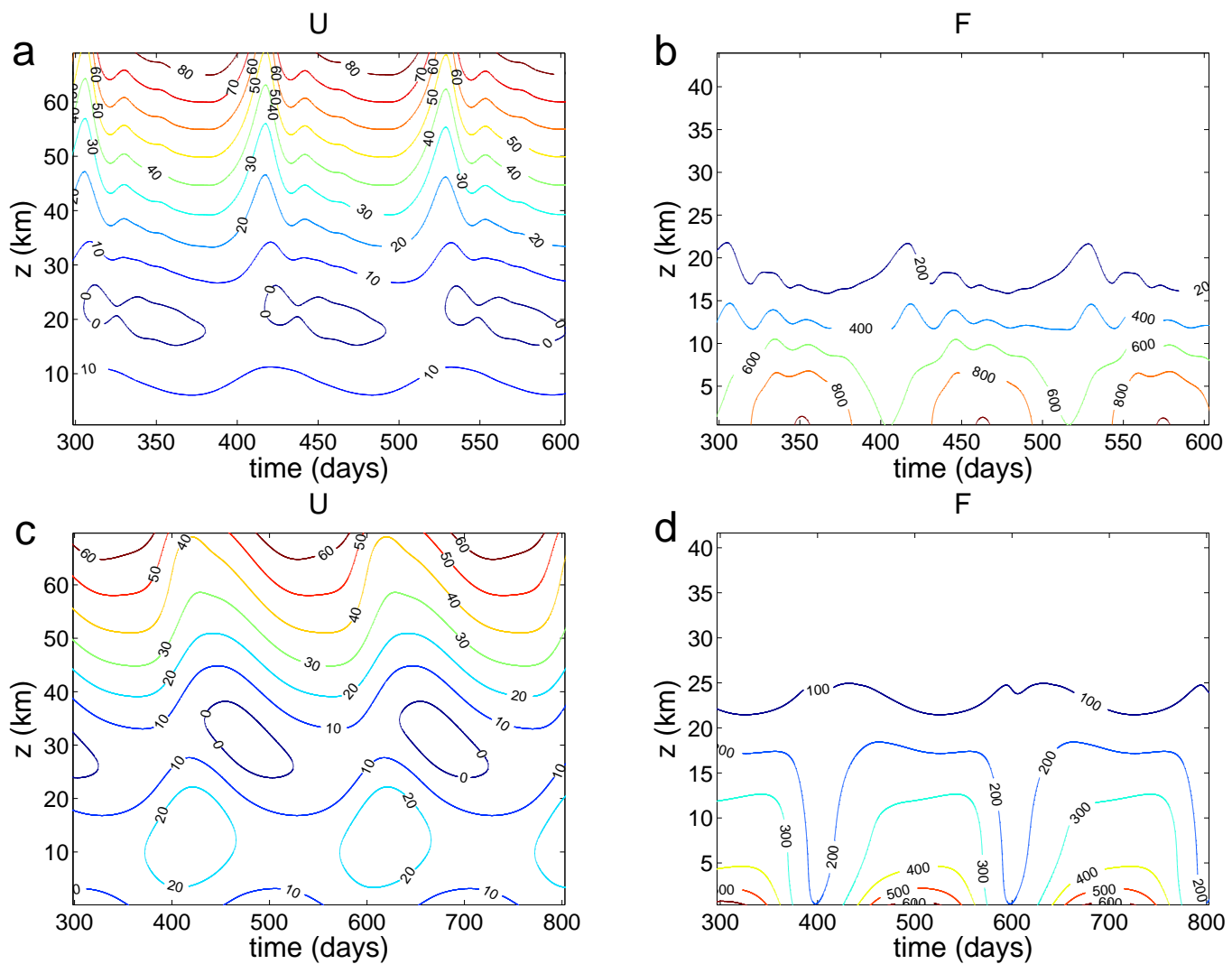


Figure 2.16:

Examples of warmings, from the steady solution far from radiative equilibrium, not generated by a dipole in the EP flux divergence. U is given in m s^{-1} and F in $\text{km}^2 \text{day}^{-2}$.

- (a) and (b) show run with Φ -condition lower boundary
- (c) and (d) show run with W -condition lower boundary

is dominated by a much more rapidly vacillating disturbance due to the continuing discontinuity in U at 30km (figure 2.17(b)). A better method of testing whether this propagation is due to wave only effects is imposing the same disturbance in U but then, at day 500.25, setting U equal to its unperturbed value (i.e. its value just before 500 days) for all time. Doing this we regain the original behaviour in the wave transience, showing that this downward phase propagation and indeed the subsequent upward phase propagation are wave only effects (figure 2.17(c)).

2.12 Conclusions

As noted by PS, downward migrating anomalies are not evidence of true downward propagation (downward propagation of information) in wave mean-flow interaction models. In this chapter we have imposed perturbations and looked at change below the height of the perturbation, so what is considered is definitely downward propagation of information. Indications from our experiments for small and moderate Φ_0 are that the vertical non-locality of the mean-flow dynamics does not allow any kind of simple downward propagation in the U and Φ fields. However, models of the extratropical wave mean-flow interaction allow strongly non-linear behaviour, with vacillations and multiple steady states. This behaviour allows a downward propagation of a perturbation at upper levels in the sense that the dynamics are sensitive to that perturbation and the resulting change occurs over the whole depth of the stratosphere. The non-linear nature of the dynamics means that a small change to the initial conditions or to the perturbation can mean large changes to the downward propagation seen. The zonal mean response to an applied perturbation ΔU is found to be potentially as significant when applied at high altitudes as at low altitudes in the sense that the amplitude of perturbation, $\rho\Delta U$, required to cause a transition from steady state to vacillations does not increase monotonically with the height at which this perturbation is applied.

The presence of vacillations and multiple steady states is dependent on having vertical non-locality in the zonal mean dynamics (as we do have in the extratropics – $C \neq 0$ in equation (2.5)), as is the weak downward influence that we see for small values of Φ_0 . We conclude that this non-locality is essential to the downward propagation seen. When two or more waves of different phase speeds are present, vacillations are present with vertically local U (although these vacillations require a small viscosity which leads to vertically non-local dynamics) and hence a large downward influence to an applied perturbation is possible. This is investigated in terms of the QBO (driven by gravity waves). We see downward influence at two

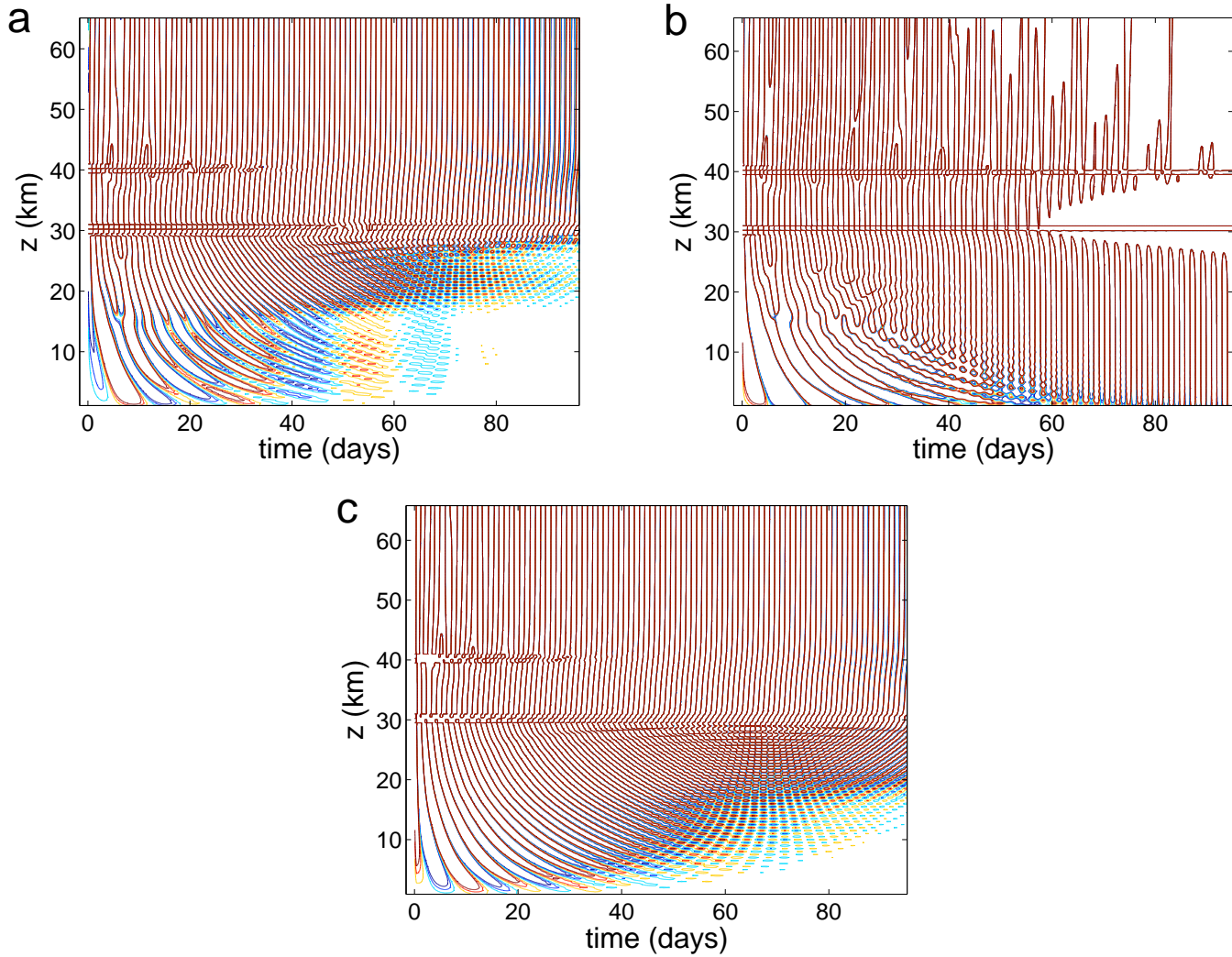


Figure 2.17:

Figures show wave transience as defined by equation (2.28). Contours used are $[-6, -4, -2, 2, 4, 6] 10^{-12} \text{m s}^{-2}$. Blue colours show negative values, red show positive.

Time axis shows time after perturbation is applied to U .

(a) shows normal evolution due to disturbance,

(b) has U kept constant after 0.25 days, and

(c) has U kept constant at its unperturbed value after 0.25 days.

different speeds, one diffusive (which becomes zero in the limit of vertically local dynamics) and one due to the fact that the perturbation alters the phase of the vacillations.

The results of the Holton–Mass model are shown not to be dependent on an artificial lower boundary or wave generation mechanism, as similar results were seen also with topographically forced waves and waves produced by tropospheric heating. Although the most significant changes to downward influence occur for specific values of Φ_0 (namely those near the bifurcation points discovered by Yoden) it should be noted that the value of Φ_0 has a separate effect, altering the downward phase speed of the disturbance through the stratosphere, and this is noticed for any value of Φ_0 . (Although untested the same is likely to be true of h_0 in section 2.9 and A_0 in section 2.10).

Chapter 3

3D model experiments

3.1 Introduction

So far we have considered the Holton–Mass model, a one dimensional quasi-geostrophic beta channel model which simulates wave mean-flow interaction in the extratropical stratosphere, the dynamics of the troposphere included as a geopotential height field prescribed on the lower boundary.

One dimensional models are very good for looking at dynamical mechanisms since it is easy to isolate the effect of a single parameter on the evolution. However, they are not physically realistic when we consider the real atmosphere. More physical are the three dimensional models used.

There are different kinds of three dimensional model. General Circulation Models (GCMs) simulate their own climate. They include a model troposphere. It is often the equilibrium state of model runs that is of interest, rather than the initial conditions, and as such GCMs are often run for several model years (and spun up from rest). A 3D mechanistic circulation model (MCM) is a more simple model used to study the dynamics of the atmosphere. It is likely to have reduced/no chemistry, a simplified radiation scheme, and will run with significantly fewer variables than a full GCM. It is models of this kind we will be most interested in here. One type of MCM is a stratosphere–mesosphere model which includes the dynamics of the troposphere only as a prescribed geopotential height field on the lower boundary (as in the Holton–Mass model).

There have been several studies performed with GCMs and MCMs concerning the dynamics of the stratosphere, and the effect of the stratosphere on the troposphere. We now consider some of these studies that are relevant to the work of this thesis.

Scaife and James (2000) use an GCM containing only a stratosphere and a mesosphere (more precisely, the UK Met Office stratosphere-mesosphere model) run un-

der perpetual January conditions. They show that 3 regimes are found for different values of wave forcing – a steady and strongly vacillating state as in the Holton – Mass model, and also a weakly vacillating state not found in the Holton – Mass model. This gives hope that multiple stable states can be found in a 3D model.

Christiansen (2003) performed similar experiments to those of section 2.5 but using a GCM. The zonal wind, or temperature field was perturbed using transient vertically confined forcings. The applied perturbation took two forms – zonal forcing and heating. A series of ensemble runs were performed, perturbing at different heights and for different lengths of time.

Christiansen found a number of interesting results. Natural variability (in the response to the applied perturbation) is found to be greater in the stratosphere than the troposphere. However, the response grows faster in the troposphere, even when the applied perturbation is in the stratosphere. Christiansen noted that, once the effects of the applied perturbation have died away, the vertical structure of all fields should be the same as before *provided the forcing does not drive the atmosphere into a different regime*. The response to the perturbations seems uncoupled from the background vacillations (when they are present) suggesting that downward propagation is a robust feature determined more by the state of the troposphere than the stratosphere.

It is encouraging that the idea of forcing the atmosphere between different stable states carries over from the Holton–Mass model to three dimensional models. This is a fact that will be demonstrated in this chapter, leaving no doubt as to the fact that the bifurcation diagram mapped out by Yoden (and detailed in the previous chapter) exists also in 3D MCMs. (Scott and Haynes 2000 also find multiple equilibria in a 3D model, although they use a severely truncated model keeping only zonal mean flow and wavenumber 1). However, there is a difference between the work in this chapter and that of Christiansen (2003). They were interested in the *growth* of a perturbation, which was largest in the troposphere (and decoupled from the stratospheric vacillations) because of baroclinic instability there. Here we shall be more concerned with the effect that a high altitude perturbation has on flow evolution at lower altitudes, rather than in the growth of the perturbation itself, and as such the state of the stratosphere will be found to matter greatly.

More evidence of steady and vacillating regimes playing a role in three dimensional models was given by the experiments of Gray et al. (2003). They use a stratosphere–mesosphere model in which, as mentioned above, the dynamics of the troposphere are included only in terms of a Φ -condition (geopotential specified on the lower boundary). A series of ensemble runs are performed under perpetual Jan-

uary radiative conditions (each using 20 integrations with initial conditions taken from different days in August such that initially U is westward and undergoes a quick readjustment due to the radiative relaxation). The only difference between the ensemble members is their initial conditions. The amplitude, Φ_0 , of the geopotential height (Φ -condition) is used as a bifurcation parameter in much the same way as in section 2.5. For low values of Φ_0 all ensemble members evolve to the same steady state solution (as is the case in the Holton–Mass model). As Φ_0 is increased the steady stable state (considered in this 3D model as a state corresponding to a cold winter containing no stratospheric sudden warmings, the polar vortex being strong throughout) no longer remains the only stable state and a sensitive dependence on initial conditions begins to appear in the ensemble runs, with approximately half of the ensemble runs undergoing a sudden warming. This will be called the intermediate behaviour. Further increase of Φ_0 and all ensemble runs show warmings, and in some cases repeated warmings, suggesting that the vacillating state is now the only stable one.

Considering the work of section 2.6 the intermediate behaviour is where we might most likely find a strong downward influence to any perturbation in the upper stratosphere, since causing an ensemble member to warm when it would not otherwise have done corresponds to causing a given ensemble member to undergo a transition between different solution branches. We might also expect a significant response at larger Φ_0 corresponding to shifting the phase of the vacillations seen in the solutions (in other words the time at which the sudden warming occurs). In short, any value of Φ_0 for which a sensitive dependence to initial conditions is seen is one in which the mechanism of chapter 2 may be important.

Gray et al. (2003) make the important point that although Φ_0 is imposed, the EP flux through lower boundary (flux of wave activity, and equivalent to the vertical flux of angular momentum across isentropic surfaces) evolves with the flow and is partly determined by flow in the mid and upper stratosphere (Gray et al. 2003 mention that this phenomenon is less surprising if it is noted that the vertical distance between the troposphere and mid-stratosphere is comparable to a vertical wavelength of the stationary waves that are considered (large-scale planetary waves)). This point was previously made by Dunkerton et al. (1981). This is a point we will return to towards the end of this chapter.

Before commencing any work with 3D models, it is of interest to redo the Gray et al. (2003) experiments using a Holton–Mass model since this makes it clear that the variability they see in their ensemble runs can also be seen in the Holton–Mass model and that it can therefore be linked to the idea of the multiple state equilibria

discovered in Yoden (1987(a)).

3.2 Holton–Mass version of Gray et al.

In the same way as Gray et al. (2003), but using a Holton–Mass model, we perform a number of ensemble runs, under perpetual January radiative conditions, using slightly different westward initial profiles of U (typical of August):

$$U(0) = \epsilon - z/(2 - \nu) \quad (3.1)$$

where $\epsilon = -2, -1, 0, 1$ and $\nu = 0, 0.2, 0.4$ so that each ensemble contains 12 members. We run at $\Phi_0 = 30, 50, 52, 55, 70, 140, 300\text{m}$ and bear in mind that for the initial U profiles chosen the stable state changes from the state very close to radiative equilibrium to the state far from radiative equilibrium at $\Phi_0 = 53\text{m}$ (vacillations set in, for this state, when $\Phi_0 \sim 50\text{m}$). In all runs we use $dz = 0.5\text{ km}$, $dt = 0.05\text{ days}$, $\alpha = [1.5 + \tanh((z - 35)/7)] \times 10^{-6}\text{s}^{-1}$ as before, and plot U at 30km . The question is whether or not we see the same sensitive dependence to initial conditions as Gray et al. (2003) do with their 3D model, and if so, whether it can be explained.

Looking at figure 3.1 we see that little difference is seen in any run up to $\Phi_0 = 70\text{m}$. Where vacillations are present the times they occur are shifted by 1 or 2 days, when a steady state is achieved ($\Phi_0 = 30\text{m}$) it is not altered at all. For $\Phi_0 = 140, 300\text{m}$ a slightly more significant shift in vacillations is found, and especially at earlier times (up to day 150 for $\Phi_0 = 300\text{m}$) the value U can take is quite variable. We also find that the frequency of vacillations increases for increased forcing. What is not seen for any value of Φ_0 is some ensemble members undergoing a warming while others do not.

Therefore it seems a more significant change in $U(0)$ is required to see any real difference within an ensemble. Choosing $\Phi_0 = 30, 52, 300$ we set $\nu = 0$ and use $\epsilon = 30, 25, 20, 15, 10, 5, 0, -5, -10, -15, -20$. We now see (figure 3.2) a significant variation in the time at which U attains a steady state when $\Phi_0 = 30\text{m}$, vacillations which occur at significantly different times when $\Phi_0 = 300\text{m}$, and the case of some ensemble members undergoing a warming while others do not when $\Phi_0 = 52\text{m}$.

This corresponds (in the case of $\Phi_0 = 52\text{m}$) to the state close to radiative equilibrium being stable for $\epsilon = 30, 25, 20$ and the state far from radiative equilibrium being stable for the other initial U profiles. Significantly different velocity profiles are not required, therefore, to see this response at $\Phi_0 = 52\text{m}$ provided that we use profiles close to (and either side of) the value of ϵ at which the stable state is changed (between 15 and 20).

Therefore, our results agree quite well with Gray et al. (2003) (sensitive dependence to initial conditions is seen) and suggest a possible reason for this sensitivity (based on the underlying bifurcation structure).

This motivates what follows in this chapter. Perturbing a 3D model in the upper stratosphere in a similar way as was done with the Holton–Mass model in section 2.5, can we find any links between dynamical sensitivity to initial conditions and the effect of perturbations in the upper stratosphere on the lower stratosphere? We would expect the greatest downward influence to such perturbations in regimes where there is large sensitivity to initial conditions.

3.3 The 3D model

The model used is the Reading IGCM spectral 3D circulation model (see Hoskins and Simmons 1975). We run the model in pressure coordinates and in mechanistic/dry mode. A resolution of T31 is used with 31 vertical levels going from $z = 16\text{km}$ to $z = 80\text{km}$ (so the model is run as a stratosphere–mesosphere model), and the model runs on a full sphere. There are 16 Gaussian latitudes in each hemisphere and 64 longitudes on the spatial grid with a jagged triangular truncation scheme used when calculating the spectral coefficients.

The reference temperature profile is given by $T_0 = 250\text{K}$, and standard basic temperature profile is calculated from the zonally symmetric radiative equilibrium wind profile of Scott and Haynes (2002), hereafter SH02, by requiring gradient wind balance (allowing the model to balance to the applied zonal wind profile and then storing the temperature profile obtained). The radiative relaxation rate to this temperature profile is given by $\alpha(z) = \{1.5 + \tanh[(z - 35)/7]\} \times 10^{-6}\text{s}^{-1}$.

The zonally symmetric radiative equilibrium wind profile of SH02 is of the form

$$U_e(\phi, z) = \cos(\phi)[u_0 \tanh(b_0(\phi - \phi_0)) + J_1 + J_2] \quad (3.2)$$

where

$$J_i = u_i \text{sech}[b_i(\phi - \phi_i)] \text{sech}[a_i(z - z_i)] \quad (i = 1, 2) \quad (3.3)$$

for constants $u_0 = 30\text{m s}^{-1}$, $b_0 = 0.01$, $\phi_0 = 20^\circ$, $u_1 = 210\text{m s}^{-1}$, $a_1 = 0.04$, $b_1 = 0.06$, $\phi_1 = 60^\circ$, $z_1 = 55\text{km}$, $u_2 = -160\text{m s}^{-1}$, $a_2 = 0.04$, $b_2 = 0.06$, $\phi_2 = -60^\circ$, $z_2 = 60\text{km}$ (similarly to SH02).

A Rayleigh friction applied above $z = 50\text{km}$ (relaxing to zero velocity at a rate $\kappa(z) = (1.02 - \exp((50 - z)/40)) \times 5 \times 10^{-6}\text{s}^{-1}$), a hyperdiffusion ∇^8 (on vorticity, divergence, and temperature), and shape of lower boundary ($z = 16\text{km}$) wave forcing

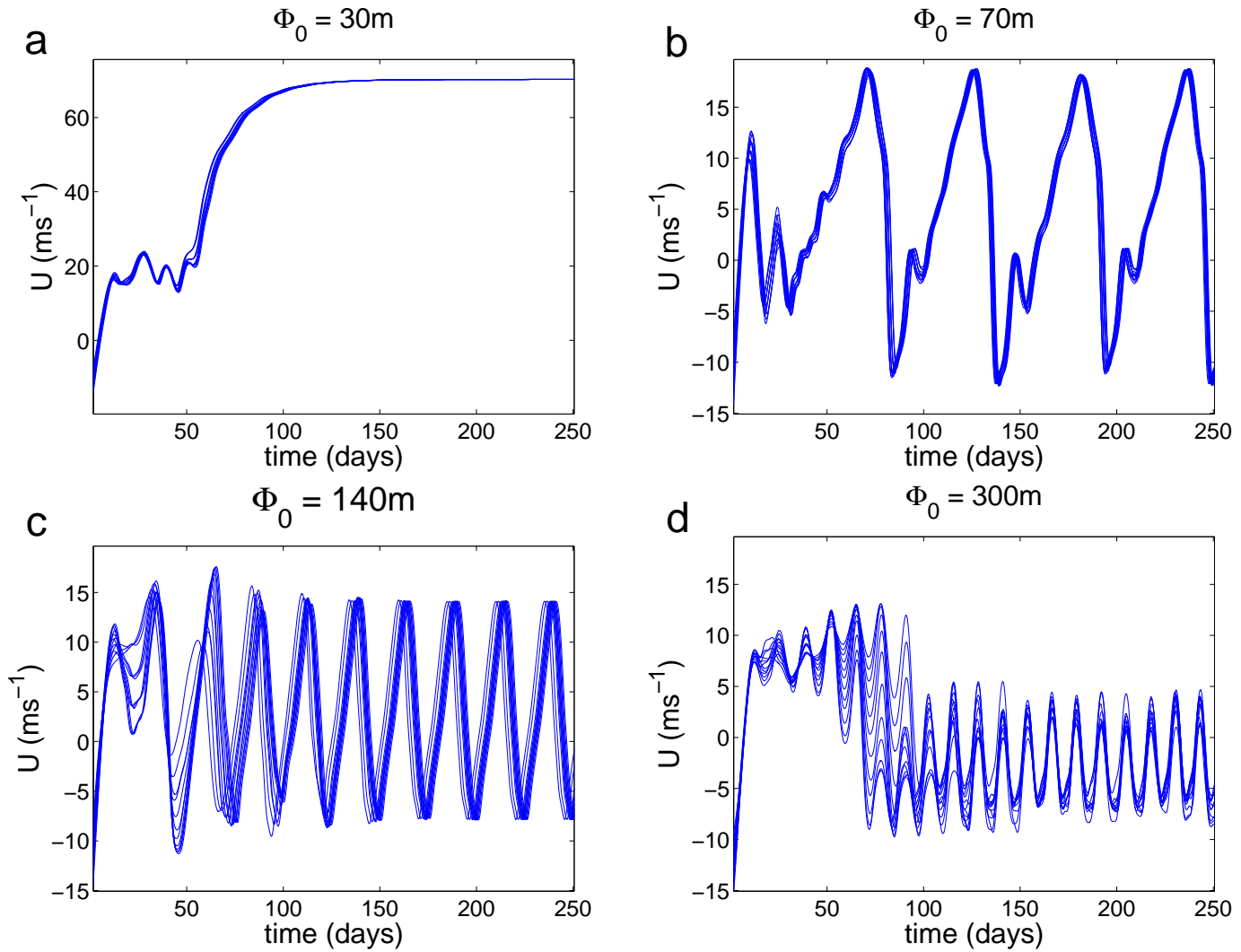


Figure 3.1:

Zonal wind, $U(\text{m s}^{-1})$, at 30km (for ensemble members with small differences in $U(0) - \epsilon$ and ν in equation (3.1) vary a small amount), for $\Phi_0 =$:

- (a) 30m
- (b) 70m
- (c) 140m
- (d) 300m

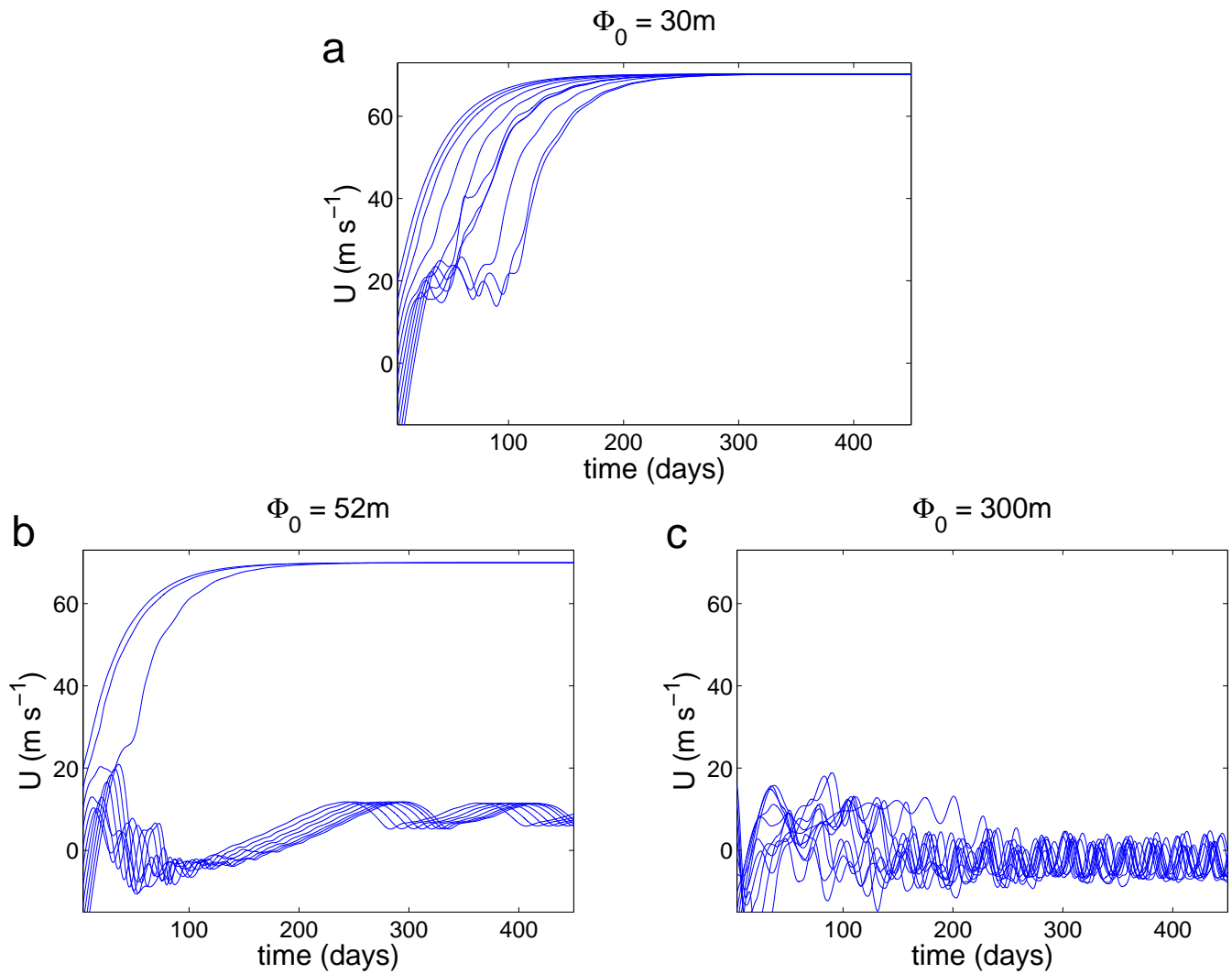


Figure 3.2:

Zonal wind, $U(\text{m s}^{-1})$, at 30km (for ensemble members with significant differences in $U(0) - \epsilon$ and ν in equation (3.1) vary a large amount), for $\Phi_0 =$:

- (a) 30m
- (b) 52m
- (c) 300m

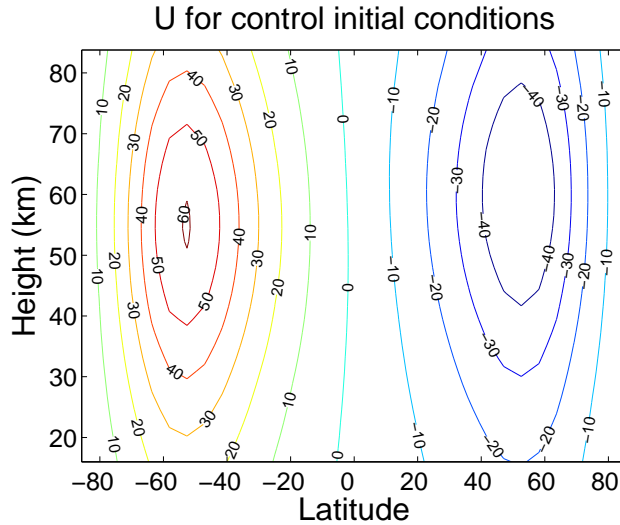


Figure 3.3:

Initial U (m s^{-1}) profile for control runs, modified slightly for each ensemble member.

Φ_0 are all as given in SH02. Thus, on the lower boundary, $\Phi = \Phi_0 E(t) G(\phi)$ where Φ_0 is a constant forcing amplitude, $E(t)$ increases smoothly from 0 to 1 over the first 10 days of the model run ($E(t) = 0.5(1 - \cos(0.1\pi t))$ for $0 < t < 10$ (t in days) and 1 otherwise), and $G(\phi) = 4\hat{\mu}^2(1 - \hat{\mu}^2)$ where $\hat{\mu} = (\mu - \mu_0)/(1 - \mu_0)$ for $\mu > \mu_0$, $\mu = \sin(\phi)$ and $\mu_0 = 0.5$. The forcing is wave 1.

One time step is taken every 7.5 minutes. Using the approach of Gray et al. (2003) the model is initialised with an August profile. Several such profiles are achieved by using the zonal wind profile (3.2) (modified slightly so we use jet strengths of 210m s^{-1} and -160m s^{-1} where they use 200m s^{-1} and -150m s^{-1}) for $\phi \rightarrow -\phi$ (causing the winter hemisphere to become the summer hemisphere, thus allowing an August initial zonal wind profile) and then adding another jet, of strength 10m s^{-1} at various heights and latitudes. The added jet is specified by

$$U_3(\phi, z, 0) \text{sech}[b_3(\phi - \phi_3)] \text{sech}[a_3(z - z_3)] \quad (3.4)$$

where $b_3 = 0.1$, $a_3 = 0.1$, $U_3 = 10\text{m s}^{-1}$ and ϕ_3 and z_3 vary (ϕ_3 chosen always in the southern hemisphere, or winter hemisphere during August). Control runs use $U_3 = 0$. Initial U profile for control runs is shown in figure (3.3).

We then relax the zonally symmetric part of the geopotential (again calculated by the model when supplied with the initial zonal wind profile), over a period of 10 days, to January conditions (although it should be noted that the model takes about 100 days to relax, by Newtonian cooling, to January conditions). The basic state temperature profile is perpetual January throughout the run. Following Gray et al.

(2003) a Rayleigh friction was imposed on the equatorial zonal winds (timescales as in Gray et al. (2003)).

3.4 Sensitivity in the tropics

Gray et al. (2003) impose different initial conditions to each member in their ensemble run by initialising the run using data from a different day in August. This gives the required small change in initial conditions but says nothing about what sort of change in the initial conditions is likely to make a difference to a model run. In fact they did find that the initial conditions should give an indication of whether a cold winter or a disturbed winter will be seen since most of the cold runs were obtained for initial conditions from consecutive days in August (Sparrow 2003). We try to look further at what changes to the initial conditions will alter the flow evolution.

(It should be mentioned that Reichler et al. (2005) gave evidence that tropospheric Rossby waves sent into the stratosphere will break and re-enter the troposphere at anomalously late times if, in the initial conditions, there is anomalously high positive EP flux divergence in the extratropical lower stratosphere and anomalously high positive geopotential in the extratropical upper stratosphere. This supports the idea that model evolution can, in some ways, be predicted from the initial conditions.)

Scott and Haynes (1998) showed from a dispersion relation for momentum anomalies that their rate of decay (assuming thermal damping but no frictional momentum damping) tends to 0 at a rate which becomes zero when the Coriolis parameter, f , is zero (i.e. on the equator). Thus in the tropics the ‘memory’ of the dynamics to such anomalies is longer.

This suggests that if initial conditions that differ in the tropics are used then members within ensemble runs are more likely to evolve showing dependence on them.

As mentioned, we define different initial conditions by adding a weak jet (of strength 10m s^{-1}) to the zonal wind at different heights and latitudes. We add the jet to the southern hemisphere where we expect to find the largest differences between different days in August.

The model is run for several values of Φ_0 to determine the cold, intermediate, and warm regimes (equivalent to those in Gray et al. 2003). We find that, as expected, when the jet is added at low latitudes (10°S) sensitivity is seen within the model runs. In figure 3.4, the two ensemble members seen to be different in the runs for $\Phi_0 = 294\text{m}$ and $\Phi_0 = 305\text{m}$ (within the intermediate regime) had initial conditions

with jets added at 10°S and 35km or 45km from the bottom boundary. (Figure 3.4 shows, as a function of time t , zonal mean zonal wind, U , at 58°N and 59km, but the same qualitative behaviour is seen at lower altitudes). Other ensemble members had initial conditions with jets added at higher latitudes (centred at 20°S and 35km, 50°S and 35km, 50°S and 45km, 70°S and 35km). $\Phi_0 = 270\text{m}$ is too small an amount of wave forcing for any sensitivity to be seen (the only stable state is a steady, cold winter). $\Phi_0 = 350\text{m}$ is a large enough value of wave forcing that every ensemble member evolves differently (and indeed every winter is warm and disturbed) – the difference in initial conditions is magnified whatever it is. The control run – with no weak jet added – is shown in black in each figure.

Taking this further, we choose just one position to add a weak jet (center 10°S and 45km) and run with jets of different strengths ($U_3 = -20, -15, -10, -5, 0$ (control run), $5, 10, 15$, and 20 m s^{-1}). The results are shown in figure 3.5 for $\Phi_0 = 294$ and 305m . It can be seen that the jet alters the flow in a predictable way, a negative (westward) jet causing the warming to occur at later times (independent of the strength of the jet) and a positive (eastward) jet causing the warming to occur at earlier times (a stronger jet causing an earlier warming). It seems odd that a westward jet should cause a later warming and an eastward jet an earlier warming. More work needs to be done to understand this result.

For completeness, taking $\Phi_0 = 294\text{m}$, we perform 6 runs with weak jets added in the northern hemisphere (at the same heights and latitudes as before – i.e. 20°S becoming 20°N). From figure 3.6 we can see that this makes the sensitivity to initial conditions that exists for $\Phi_0 = 294\text{m}$ more obvious. All runs are warmer than the control (the weak jets being eastward) and, as expected, the 3 runs that are most different from the control run correspond to the weak jet being added at low latitudes (10°N and 20°N).

Having found regimes of sensitivity in the model runs we can continue to introduce perturbations at upper levels (again in the form of weak jets) and consider their downward influence. (From now on we again use jets of strength 10m s^{-1} at the jet center, centred at the original 6 different points in the height–latitude plane (figure 3.4), to give different initial conditions.)

3.5 3D downward propagation experiments

The model is run for 365 days. Ensemble runs are performed for $\Phi_0 = 270, 294, 305$ and 350m . As mentioned above, each ensemble contains 6 members which differ only in their initial condition, and sensitivity to initial conditions is seen for values

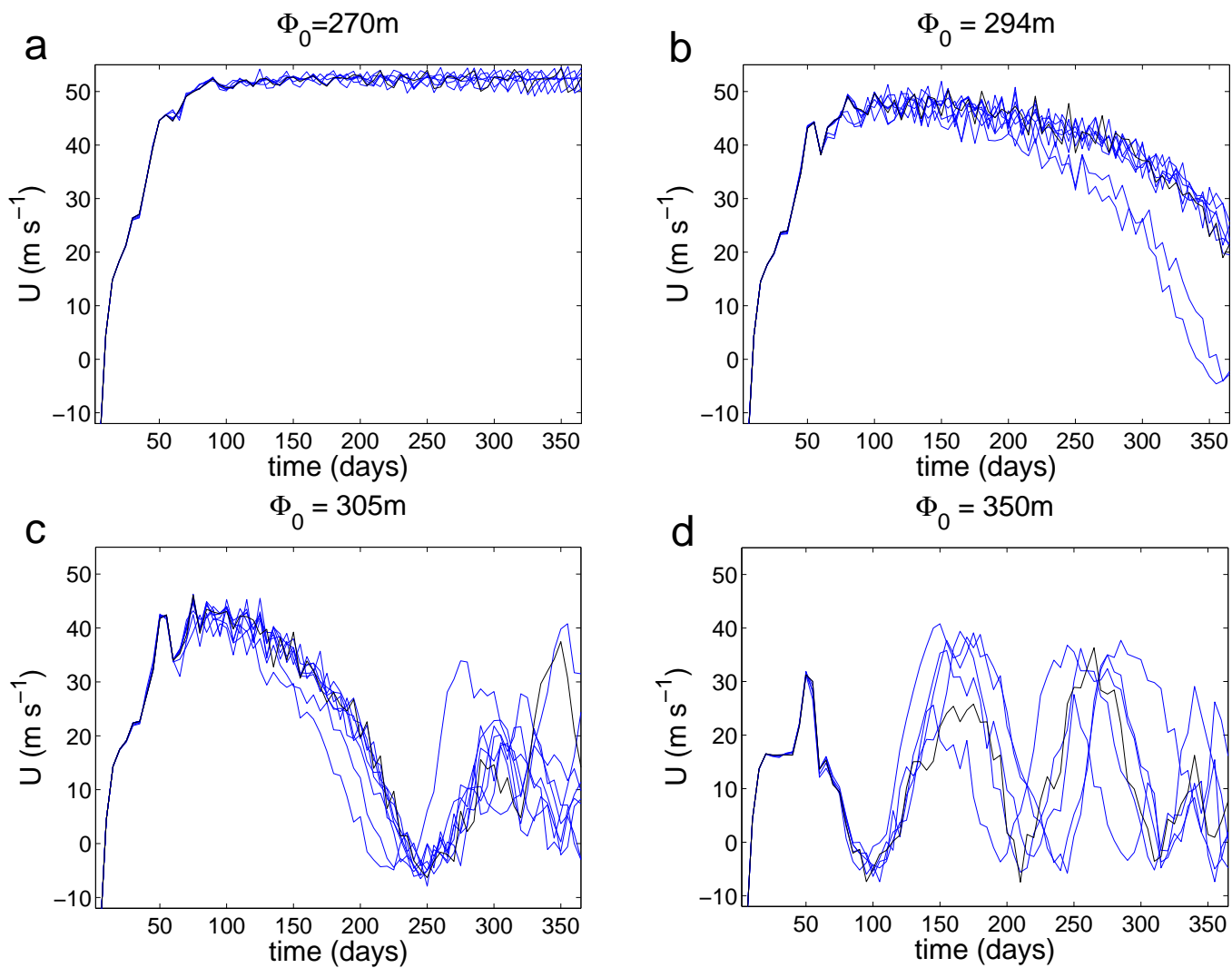


Figure 3.4:

U at 58°N and 59km .

Figures show four ensemble runs. Each ensemble member uses a different initial condition defined by adding a weak jet to the zonal wind at different heights and latitudes. Each ensemble uses a different value of wave forcing at the lower boundary, Φ_0 . In the intermediate regime ($\Phi_0 = 294\text{m}$ and 305m) differences are seen only between members whose initial conditions differ by a jet added in the tropics (i.e. 10°S). Control runs are shown in black.

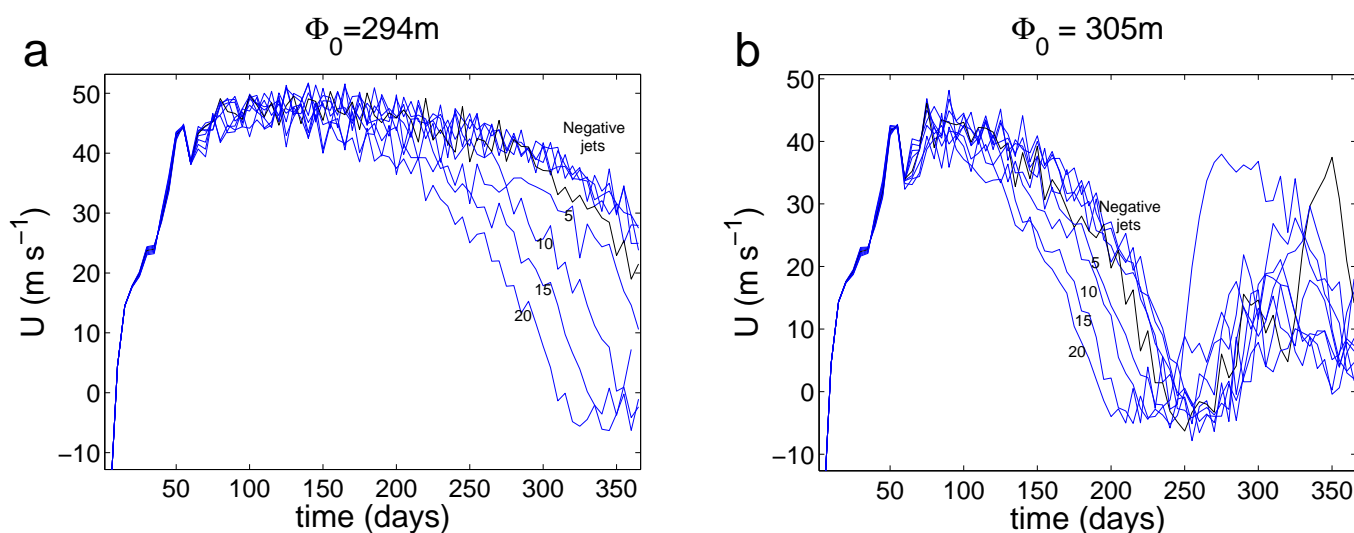


Figure 3.5:

Jets of different strengths are added to the initial conditions, centred at 10°S and 45km . We see a predictable effect on U . Control runs are shown in black. Numbers on curves give U_3 (m s^{-1}) for eastward jets.

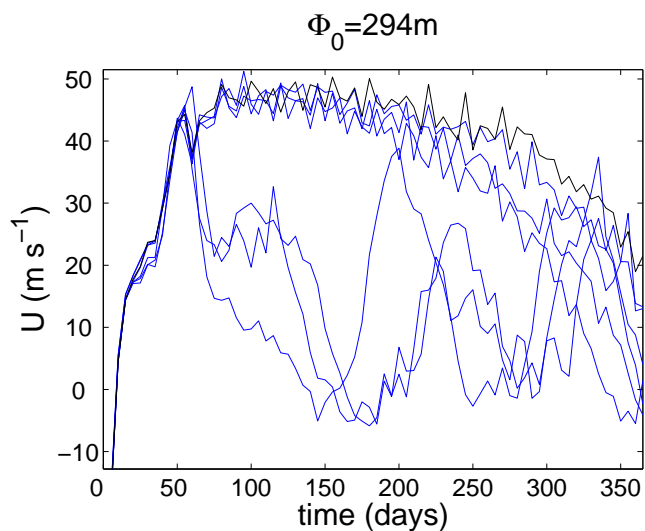


Figure 3.6:

Weak jets are added to the initial conditions, as in figure 3.4 but in the Northern Hemisphere. We again see positive jets causing earlier warmings, with the most noticeable difference when jets are added at low latitudes. The control run is shown in black. $\Phi_0 = 294\text{m}$.

Table 3.1: rms disturbance to U (m s^{-1}) at 50°N and 28km averaged from days 100-365

Jet in initial conditions	Φ_0			
	270	294	305	350
45km, 50°S	0.7059	5.2071	8.2077	8.6522
35km, 70°S	0.7073	6.1374	6.1487	
35km, 10°S	0.7180	8.7261	7.5160	8.2195
35km, 50°S	0.7032	5.7558	5.5375	5.9527
45km, 10°S	0.7072	7.3689	5.6157	6.0706
35km, 20°S	0.7101	6.9807	7.2673	7.8255

of Φ_0 greater than or equal to 294m .

Perturbations high in the stratosphere are imposed by adding a further weak jet to the velocity field of strength -20ms^{-1} centred at 50°N and 35km and having the same shape as the weak jet added to the initial conditions described above (in equations (3.2)–(3.4)). The perturbation is made 100 days into each model run (thus giving time for the model to relax to January conditions before the perturbation is applied). Taking the rms of the difference in U between perturbed and unperturbed runs at 50°N and 28km , averaged over the remaining 265 days of the runs, gives an indication of the downward influence of the applied perturbation for each value of Φ_0 . We call this the rms disturbance. The results are shown in table 3.1. A blank space indicates a run that diverges for the resolution used here.

The rms disturbance to U can be seen to be independent of the initial conditions used. As expected, this disturbance is an order of magnitude larger in runs using values of Φ_0 for which sensitivity to initial conditions is seen than it is for runs where no sensitivity is seen. Note that the disturbance is very similar for $\Phi_0 = 294, 305,$ and 350m , confirming that its magnitude is due to a sensitivity being present rather than an increasing value of Φ_0 .

3.6 Experiments with a troposphere

There is further interest in adding a troposphere to the model. The question then is what effects the perturbations introduced in the stratosphere have on the flow in the troposphere and how this depends on Φ_0 . The model containing a troposphere runs in σ coordinates so the boundary condition is similar to the W -condition of section 2.9 (the stratosphere only version of the model has a lower boundary equivalent to the Φ -condition of chapter 2). Φ_0 is now specified on σ surfaces rather than pressure

surfaces. It is important to emphasise this fact since most stratospheric modelling has been done using stratosphere–mesosphere models with artificial lower boundary conditions. Including a troposphere provides a good check that our results are not dependent on running with an artificial lower boundary condition.

Following Taguchi et al. (2001) a troposphere is included in the model as follows. The basic state temperature profile of the stratosphere is the same as before (calculated from gradient wind balance using the zonal wind profile of SH02). The basic state temperature profile of the troposphere is included by using the formula given in Akahori and Yoden (1997), and then the temperature profile is smoothed in the transition region from troposphere to stratosphere.

The temperature profile of the troposphere as specified in Akahori and Yoden (1997) is:

$$T_e(z) = T_0(z) + \frac{\Delta T(z)}{2}(\cos(2\phi) - 1/3) \quad (3.5)$$

where $T_0(z)$ is the global mean temperature at height z and $\Delta T(z)$ is the pole to equator temperature difference at height z .

Following Scott and Polvani (2004), baroclinic instability is suppressed by damping wavenumbers 2 and higher in the troposphere. The damping we use is exactly as in Scott and Polvani (2004) except that, in the notation of Scott and Polvani (2004), we damp at a rate $k_T = 3/\text{day}$. More precisely, we damp at a rate $k_T Z(z)$ where $Z(z) = \cos^2(\pi z/2z_T)$ and z_T is the tropopause height. We also, following Scott and Polvani (2004), relax to a weak eastward profile in the troposphere to allow the vertical propagation of planetary waves. The equatorial friction on U used by Gray et al. is not now included. The shape of lower boundary wave forcing described in section 3.3 now uses $\mu_0 = 0$ (following Taguchi et al 2001).

We run the model in σ -coordinates with a resolution of T42, and 41 vertical levels going from 0km to 70km. The tropopause is at 12km. There are now 32 Gaussian latitudes and 128 longitudes on the model grid. There is one model time step every 15 minutes. Again we run the model from August initial conditions relaxing to a state of rest in the first 5 days and then allowing the model to continue relaxing to the January basic state temperature profile.

Ensembles of 6 members are computed for $\Phi_0 = 1200, 1350, 1500$ and 1650m , with sensitivity to initial conditions seen for values of Φ_0 greater than about 1200m (no sensitivity to initial conditions is seen for $\Phi_0 = 1200\text{m}$). Each run is for 600 days and U at 60°N and 50km is shown for each run in figure 3.7 (the equivalent of figure 3.4 for this model including a troposphere). We see that sensitivity to initial conditions becomes noticeable after about 100 days (discounting the first 100 days taken to relax to January conditions).

As in section 3.5 we then redo each model run, allowing 200 days of spin up time before perturbing the stratosphere (again at 50°N and 35km from the lower boundary) using the same form of perturbation as before. The rms difference between perturbed and unperturbed runs, at 28km and 8km, is averaged over the remaining 400 days of the model run.

Table 3.2 gives the results of these experiments carried out with a model including a troposphere (equivalent to those shown in table 3.1 for the stratosphere only model). As before the downward influence caused by the applied perturbation is greatly increased once we are in a regime where sensitivity to initial conditions is seen in the ensemble runs (going from 0.5m s^{-1} when no sensitivity to initial conditions is seen to 5m s^{-1} or more when sensitivity is seen. Even in the troposphere a difference of 2m s^{-1} is observed (in the case where sensitivity is seen), which is significant).

Note (from table 3.2) that for two of the runs where $\Phi_0 = 1500\text{m}$ there is an even larger difference between the perturbed and unperturbed runs seen at 28km. This is because a sudden warming occurred in the unperturbed run but not the perturbed run. Note that here applying a perturbation has caused a change of state (as seen in the 1D experiments). A change of state was not seen in any of the 3D stratosphere only experiments that we performed, but it is likely to be possible given certain initial conditions and model parameters (considering that it has been observed in the 3D model running with a troposphere). Looking at the troposphere at a height of 8km (where SSWs do not occur, and hence causing a change of state will not show quite as significant a downward influence) the downward influence is still an order of magnitude greater once sensitivity to initial conditions is observed (as mentioned above). The downward influence that we observe in U is qualitatively the same as that seen in the 1D model in the previous chapter (see figure 3.9 in the following section).

The good qualitative agreement between the 1D runs of chapter 2 and the 3D runs (with and without a troposphere) in this chapter shows that our results are robust. The bifurcation structure mapped out by Yoden in the Holton Mass model is shown to exist also in this more realistic 3D model, manifested by runs choosing to undergo a stratospheric sudden warming during a winter when, in the absence of a perturbation in the upper stratosphere, they would not have done.

3.7 Height of applied perturbation

Having established the persistence of a basic mechanism for the downward influence of a perturbation in the upper stratosphere, it is of interest to investigate further

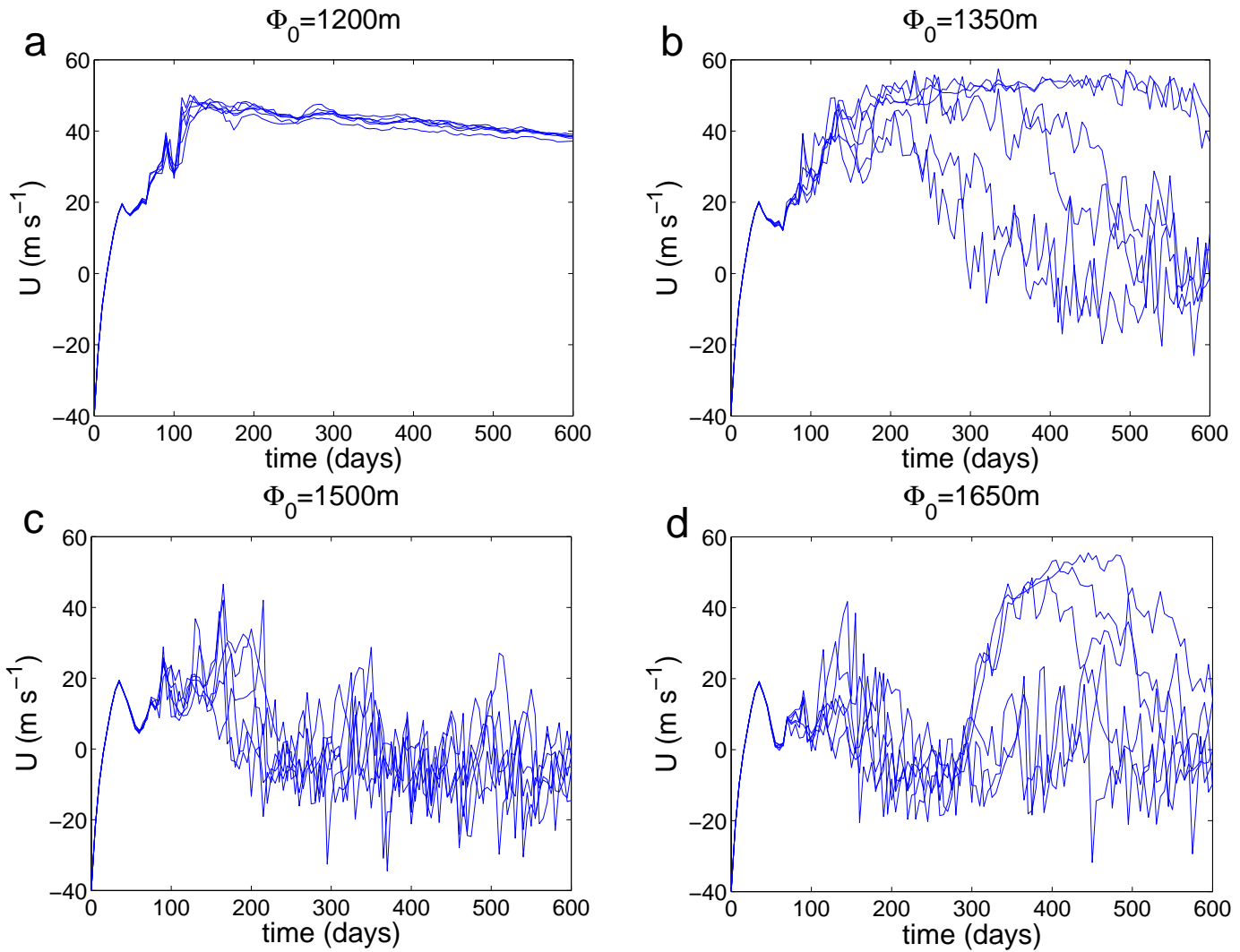


Figure 3.7:

Zonal wind, U , at 60°N and 50km . Figures show sensitivity to initial conditions in ensemble runs for $\Phi_0 = 1350, 1500$ and 1650m . Equivalent to figure 3.4 but for model including a troposphere.

Table 3.2: rms disturbance to U (m s^{-1}) at 50°N averaged from days 200-600

Jet in initial conditions	Φ_0			
	1200 (at 28km)	1350 (at 28km)	1500 (at 28km)	1650 (at 28km)
45km, 50°N	0.5139	4.4843	5.4320	24.6786
35km, 70°N	0.5062	5.2798	6.0582	16.4325
35km, 10°N	0.5167	0.7626	4.5857	10.5967
35km, 20°N	0.5211	1.1498	4.4477	14.5468
45km, 10°N	0.5021	1.8371	18.5238	15.0183
55km, 10°N	0.5360	4.6922	17.5953	19.6301
Jet in initial conditions	Φ_0			
	1200 (at 8km)	1350 (at 8km)	1500 (at 8km)	1650 (at 8km)
45km, 50°N	0.2056	1.8906	2.4463	2.3665
35km, 70°N	0.2606	1.5073	3.0268	1.6241
35km, 10°N	0.1151	0.1582	2.4156	1.6949
35km, 20°N	0.1045	0.2025	1.6294	1.5864
45km, 10°N	0.1136	0.3578	1.9591	2.4957
55km, 10°N	0.1157	1.3658	3.1271	2.8578

the nature of this downward influence. We begin by carrying out, using the 3D model containing a troposphere, an experiment similar to that of section 2.6. More specifically we consider the effect of the height above which a perturbation is applied (z_c) to its downward influence at a given reference height. The form of the perturbation we use for these experiments is a triangular jet centred at 50°N which increases linearly from 0m s^{-1} at 45°N to a strength of -20m s^{-1} at 50°N and then decreases linearly back to 0m s^{-1} at 55°N . Similarly the jet speed increases linearly from 0m s^{-1} at $z_c\text{km}$ to maximum (-20m s^{-1}) at $(z_c + 2)\text{km}$ and back to 0m s^{-1} at $(z_c + 4)\text{km}$. This profile was used rather than the profile described in previous sections since a sech profile is not actually zero anywhere (although it does become small exponentially with distance from the jet centre) and we wanted to ensure that the perturbation applied here was exactly zero below the height z_c . We refer to this as a triangular perturbation.

To ensure the robustness of the results to be presented in this section, the experiments were carried out at different values of Φ_0 . The experiments were also redone using a different form of perturbation. Instead of perturbing the velocity field, an additional forcing term was included in the U momentum equation (to simulate a force due to planetary wave breaking). This additional forcing, applied continuously from day 100 – day 101 of model runs, took the form h for $45^\circ\text{N} < \phi < 55^\circ\text{N}$ and

$z_c < z < z_c + 5\text{km}$, and zero elsewhere. h , the amplitude of the forcing, was set to 15m. We refer to this alternative method of forcing as zonal-force perturbation.

To get an indication of the downward influence of these applied perturbations two things were looked at. One was the ‘immediate effect’ measured as the difference in the velocity field 5 days after the applied perturbation (at a height of 28km, where values of 30, 35, 40, 45, 50, 55 and 60km were used for z_c). The other was the rms difference in the velocity field taken from day 200 (when the perturbation was applied) to day 600 (the end of the model run) as in section 3.6 above.

Similarly to the 1D case (section 2.6), for constant magnitude triangular perturbations applied to U at different heights z_c , we would expect, from the analysis of ‘switch on’ forcing given in Haynes et al. (1991), that the density at height z_c (where density $\rho = \rho_0 \exp(-z/H)$) divided by the response, ΔU , at a constant height of 28km, will be roughly constant.

Therefore, in figure 3.8 we plot $\log(\Delta U)$ against z_c (where, as just mentioned, z_c is the height above which a perturbation is applied, and ΔU is the ‘immediate’ change in the zonal wind due to this perturbation (measured at 28km)), and expect to find a gradient of $-1/H$, where $H = 7\text{km}$. Figure 3.8 shows examples of the results obtained, looking at the cases of an extra forcing term (zonal-force perturbation) with $\Phi_0 = 1200\text{m}$ and perturbation to the velocity field (triangular perturbation) with $\Phi_0 = 1500\text{m}$. Gradients of $-1/6$ and $-1/6.5$ are seen, sufficiently close to what we would have expected.

Thus the results of section 2.6, namely that a perturbation, $\Delta U \propto \rho^{-1}$, at high altitudes in the stratosphere can have just as much effect on flow in the troposphere as a perturbation at low altitudes in the stratosphere, as with the zonal mean response detailed in Haynes et al. (1991), carry across to this 3D model. It is worth making the point again that perturbations at all heights in the stratosphere must be captured by a model in order to accurately predict the flow in the troposphere.

There are also points to note from looking at the rms values of the disturbance to U at 28km (and 8km) (not shown). As noted in the previous section, the values increase greatly once Φ_0 is such that vacillations become the stable state. What is of interest is that the rms values do not increase or decrease monotonically with z_c as we might have expected. See Gray et al. (2004) for another example where this simple monotonic behaviour is not the case. (In that paper the equatorial winds are altered in 10km height bands in different experiments, and large differences are noticed when changes are made in the upper stratosphere). Indeed, we find the greatest rms values when the perturbation is applied in the upper stratosphere (note that, unlike the 1D experiments, where the height below which the disturbance is

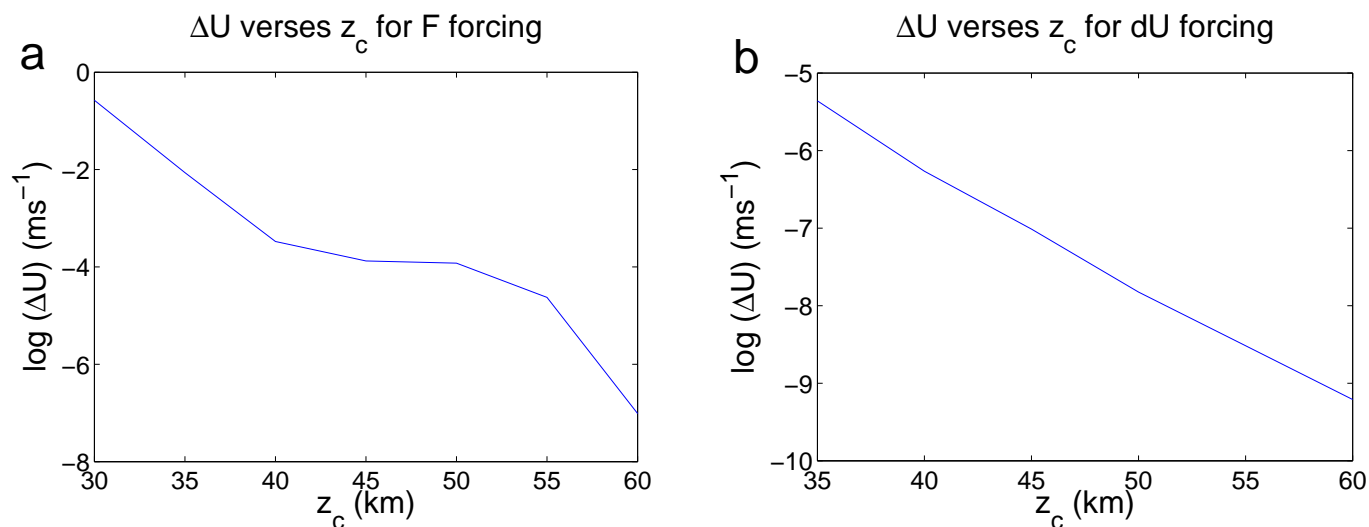


Figure 3.8:

Figures show $\log(\Delta U)$ verses z_c , where z_c is the height above which a perturbation is applied, and ΔU the change in the zonal wind at a height of 28km due to this perturbation. Since we expect $\rho/\Delta U$ to be constant, we expect a gradient of $-1/H$ ($H = 7\text{km}$).

(a) shows the result where zonal-force perturbation is used (defined in text) at $\Phi_0 = 1200\text{m}$ and has a gradient of $\sim -1/6$, and

(b) shows the result where triangular perturbation is used (defined in text) at $\Phi_0 = 1500\text{m}$ and has a gradient of $\sim -1/6.5$.

applied is found not to matter and is taken as the top boundary, in this case the disturbance is applied over a height of 4 or 5km and *not* all the way to the top boundary). This behaviour is unexpected, but consistent with the work of Gray et al. (2004).

This point is demonstrated in figure 3.9 which shows 3 cases of the change seen in the zonal mean zonal wind between perturbed and unperturbed runs (ΔU) for triangular perturbation. Figure 3.9 (a) shows a case where only weak downward influence is observed since we are in a steady state regime ($\Phi_0 = 1200\text{m}$) and no sensitivity to initial conditions is seen. Figure 3.9 (b) shows a case where sensitivity to initial conditions is present and greater downward influence is observed, and figure 3.9 (c) shows a case where applying the upper stratospheric perturbation to the zonal winds caused a considerable difference to the pattern of the sudden warming that occurred, eventually leading to a cooling at day 400 (not shown) which was not seen in the unperturbed run. Notice that the huge difference between figures 3.9 (b) and (c) is simply due to the height at which the perturbation is applied in the stratosphere ($\Phi_0 = 1500\text{m}$ in both cases). This highlights the need for a well resolved stratosphere with a good gravity wave parametrisation scheme to accurately model gravity wave breaking in the stratosphere and thus flow evolution in the troposphere (since there is a large difference in figures 3.9 (b) and (c) even in the troposphere).

3.8 Period of vacillations revisited

At the end of chapter 2 we studied the downward phase speed of an anomaly in the zonal mean zonal wind, and considered the effect of the values of Φ_0 (amplitude of lower boundary wave forcing) and α (radiative relaxation time) both on this phase speed and on the period of the vacillations leading to a downward phase propagation in U . It was noted that, whilst not directly relevant to the downward propagation of information due to a disturbance in the upper stratosphere, it is still of importance to understand this downward phase speed so that the stratosphere can be used as an indicator for change in the troposphere (see Baldwin and Dunkerton (2001)).

We found the rather surprising results that the period of vacillations, T , was almost independent of α (when we expected $\alpha \propto 1/T$) and $\Phi_0 \propto 1/T$ (when we expected $\Phi_0^2 \propto 1/T$). The suggestion was made that these results are due to the artificial nature of a 1D model. In this section we re-run these experiments to see how T depends on α and Φ_0 in the 3D model (IGCM).

First consider the effect of the rate of radiative relaxation, α , on the period of vacillations, T . Vacillations correspond to stratospheric sudden warmings and we

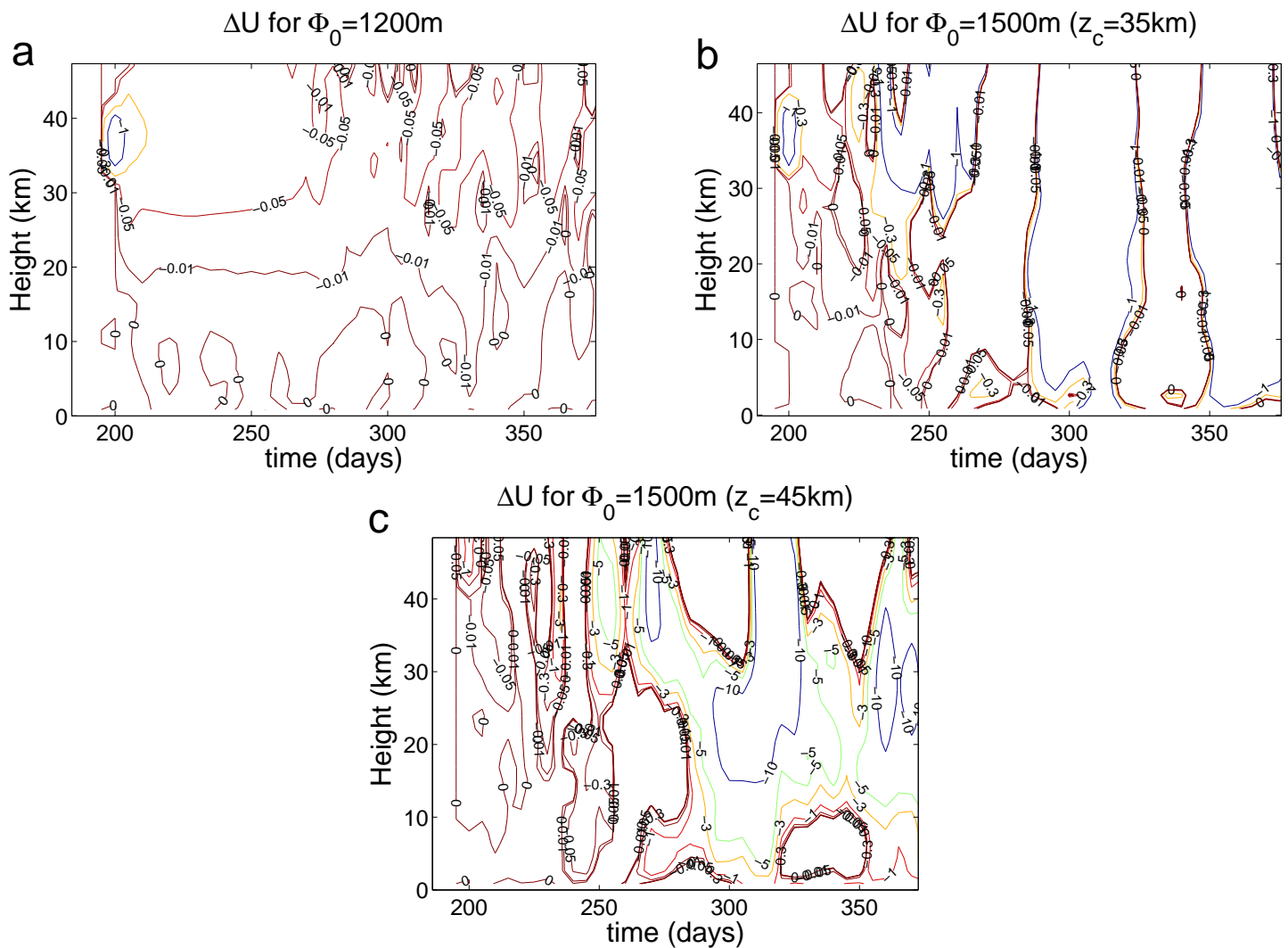


Figure 3.9:

Figures show the difference in ΔU (the change to the zonal mean zonal wind) between the steady state response (a) ($\Phi_0 = 1200\text{m}$), and the response in a vacillating regime (b) and (c). In figure (c) a sudden warming is dramatically changed by the perturbation (and the stratosphere cools at day 400 (not shown) which was not seen in the unperturbed run), hence a very large downward influence is seen. Compare with figures from 1D case (figure 2.3). Triangular perturbation is used and ΔU is shown at 48.8°N . The same initial condition is used in each run.

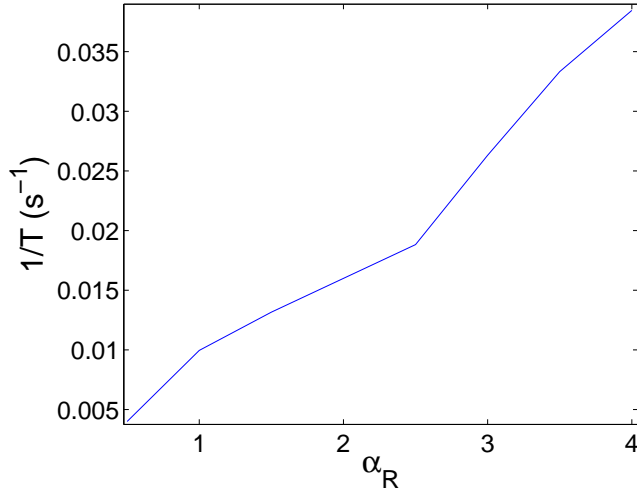


Figure 3.10:

Figure shows α_R (rate of Newtonian cooling defined in text) against $1/T$ (T is the period of vacillations in U). $\Phi_0 = 2600\text{m}$.

need to take a relatively large value of Φ_0 to obtain a suitably short period (thus enabling a large number of periods giving a good average value for T with the model still running in a reasonable amount of time). We look at the zonal mean zonal wind at $60^\circ N$ and a height of 11.5km to measure the period. Integrations are, as before, run over 600 days. It should be noted that for some values of α the period of vacillations became irregular, and in these cases an average was taken. We choose $\Phi_0 = 2600\text{m}$ which gives vacillations of a suitable period for this exercise. Write $\alpha = \alpha_R(1.5 + \tanh((z-35)/7)) \times 10^{-6}\text{s}^{-1}$. We run with $\alpha_R = 0.5, 1, 1.5, 2, 2.5, 3, 3.5$ and 4. The results are shown in figure 3.10 and it can be seen that, as expected, $\alpha \propto 1/T$. We therefore conclude that, in the 1D model, the lack of dependence of T on α is artificial.

Next consider the effect of increasing the amplitude of lower boundary wave forcing, Φ_0 , on the period of vacillations. Again we look at $60^\circ N$ and 11.5km to determine the period of vacillations. We take $\alpha = (1.5 + \tanh((z-35)/7)) \times 10^{-6}\text{s}^{-1}$ as usual and consider $\Phi_0 = 2000, 2200, 2400, 2600, 2800, 3000, 3200, 3400, 3600,$ and 3800m. As shown in figure 3.11 we find that $\Phi_0 \propto 1/T$. Fitting a straight line we find $\Phi_0 \approx 117250/T + 1500$ and 1500m is close to the transition (i.e. the bifurcation point) between steady state and vacillations. We therefore conclude that the surprising result $\Phi_0 \propto 1/T$ is not an artifact of the artificial nature of the 1D model, and further work should be done to understand this result.

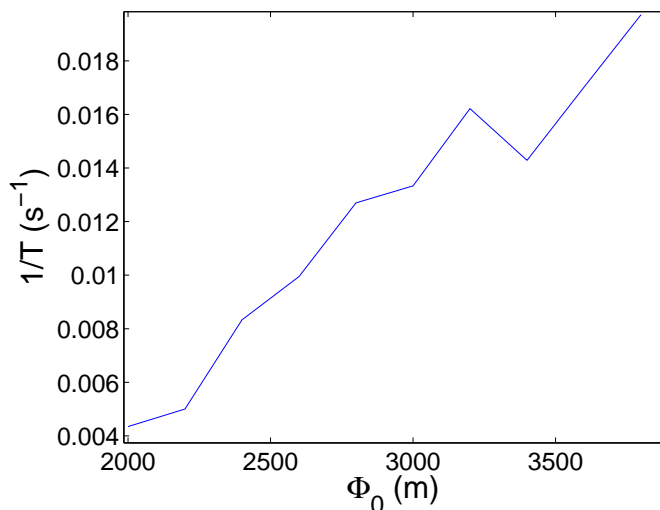


Figure 3.11:

Figure shows Φ_0 (m) versus $1/T$ (s^{-1}) where Φ_0 is the amplitude of lower boundary wave forcing, and T the period of vacillations found at this value of Φ_0 .

3.9 Truncated runs

It is suggested in Gray et al. (2003) that small scale features (travelling anticyclones) might be important in causing the sensitivity to initial conditions that is seen in their model runs. This is not easy to test with the model that they use, however it is easy to test with the Reading IGCM model which can be truncated to keep, for example, only wavenumbers 1–3 (and zonally symmetric dynamics). To this end we run the model (containing a damped troposphere) with the different initial conditions specified in section 3.5, keeping only wavenumbers 1–3. Figure 3.12 shows, for $\Phi_0 = 1350$ m, the sensitivity to initial conditions seen in the zonal wind at 60° N and 50km for the full runs (shown also in figure 3.7) and for the runs keeping only wavenumbers 1–3. It can be seen that sensitivity to initial conditions is still present, and therefore that small scale features are not necessary in causing this sensitivity. (It should be noted that sensitivity is also seen for other values of Φ_0 as before. 1350m is shown in figure 3.12 as an example.)

This result is true also in the stratosphere only version of the model (used in section 3.5). We run this model with initial conditions differing in both the southern and northern hemispheres and, in the same way as for the full model, retain only wavenumbers 1–3. We see from figure 3.13, which shows an ensemble run for $\Phi_0 = 250$ m, that although sensitivity is now seen for a slightly lower value of Φ_0 (we do not expect that truncated models will be quantitatively the same) it is still present.

If we severely truncate the model the results do change, with no sensitivity seen

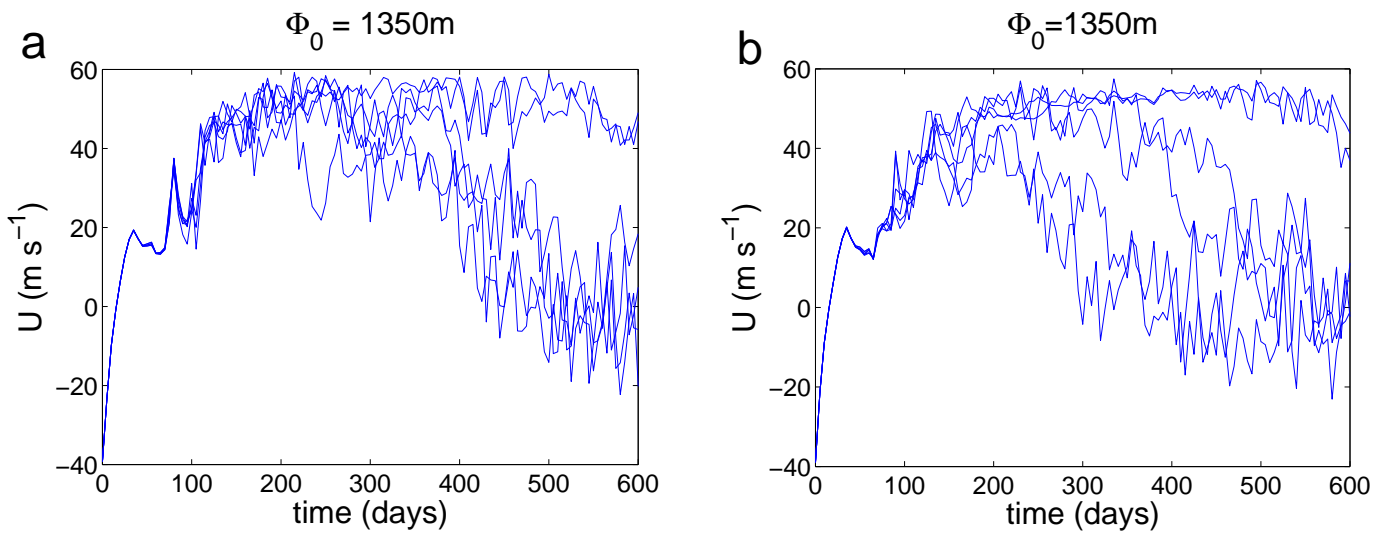


Figure 3.12:

U at 60°N and 50km . Shows sensitivity to initial conditions seen in runs that only keep wavenumbers 1–3 (figure(a)), as compared to that seen in full runs (figure(b)). $\Phi_0 = 1350\text{m}$.

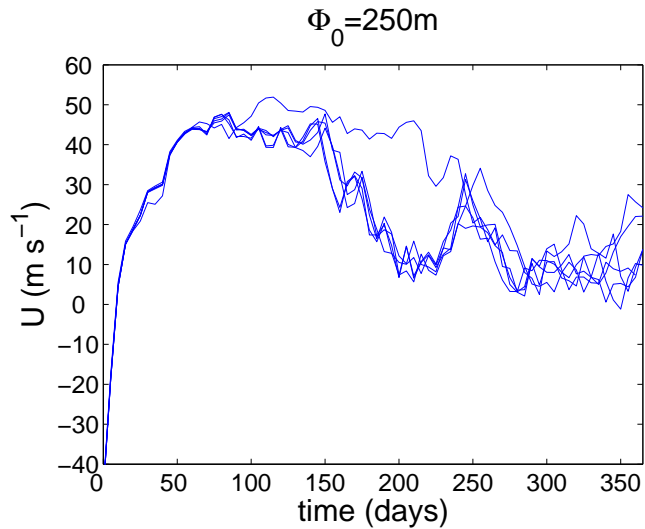


Figure 3.13:

U at 58°N and 59km . As for figure 3.4 but runs only keep wavenumbers 1–3. Sensitivity to initial conditions is still seen. $\Phi_0 = 250\text{m}$.

for the initial conditions used when only wave 1 is kept, and sensitivity to initial conditions seen at greatly reduced values of Φ_0 when only wave 2 is kept.

To try and understand the difference between these runs keeping only wave 2 and runs keeping only wave 1 we can look at PV plots centred over the north pole. It is the case that, in runs that undergo a sudden warming, the polar vortex is moved off the pole and in some cases completely destroyed. One observation that seems the same throughout the (not truncated) model runs is that the polar vortex breaks up into a wave 2 pattern before being destroyed (see figure 3.14 which shows PV on the 900K isentropic surface for days 250, 300, 350, and 400 of a run keeping all wavenumbers). This is consistent with the idea that we need to keep wave 2 in the model runs.

Previous studies have considered the wavenumbers required to generate realistic model results. Haynes and McIntyre (1987) demonstrate the great success of truncated models, keeping only wave 1, in qualitatively modelling behaviour in Rossby wave critical layers. However, they use a β -plane approximation and mention that such truncated models may not work as well on a sphere. Both Lordi et al. (1980) and Hsu (1981) suggest that keeping a small number of higher zonal harmonics (up to wavenumbers 4 and 2 respectively) and allowing some wave-wave interaction, as well as wave-mean flow interaction between wave 1 and the zonal mean flow, is crucial to modelling SSWs. They show that the inclusion of these wavenumbers leads to more rapid and intense SSWs, and that wave 2 produced by wave-wave interactions is about 60% as important as wave 1 forcing.

Certainly from our experiments above it seems that keeping a small number of higher zonal harmonics is important. However, it should be mentioned that Scott and Haynes (1998, 2000 and 2002) demonstrate realistic behaviour using only wave 1 and zonal mean dynamics in a spherical model.

In any case, we conclude from our brief experiments here that no disturbance smaller than planetary scale is required to produce SSWs or sensitivity to initial conditions in the model runs, despite what is suggested in Gray et al. (2003).

3.10 EP flux entering the stratosphere and baroclinic instability

We have seen that the influence of a perturbation in the upper stratosphere can reach the troposphere, relaying to the troposphere the current state of the stratosphere (whether no sensitivity is present, so that a small influence is felt, or sensitivity is seen, when a large influence is felt). Further, Scott and Polvani (2004) made the

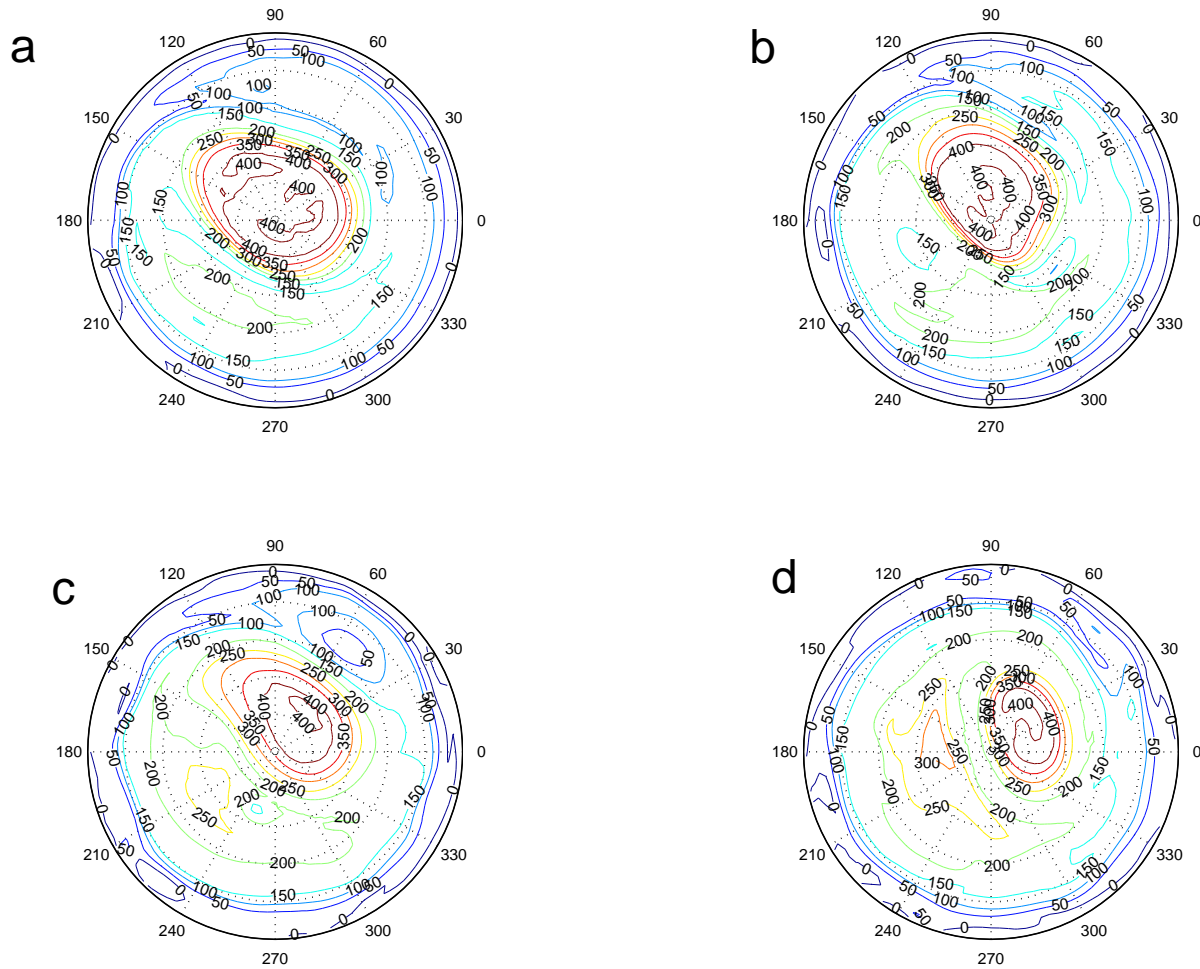


Figure 3.14:

PV ($10^{-6} \text{ K m}^{-1} \text{ s}^{-1}$) on the 900K isentropic surface at days 250, 300, 350, and 400 for a model run keeping all wavenumbers ($\Phi_0 = 1350\text{m}$). Notice that the polar vortex breaks up into a wave 2 pattern. This seems to be a consistent behaviour when the vortex warms.

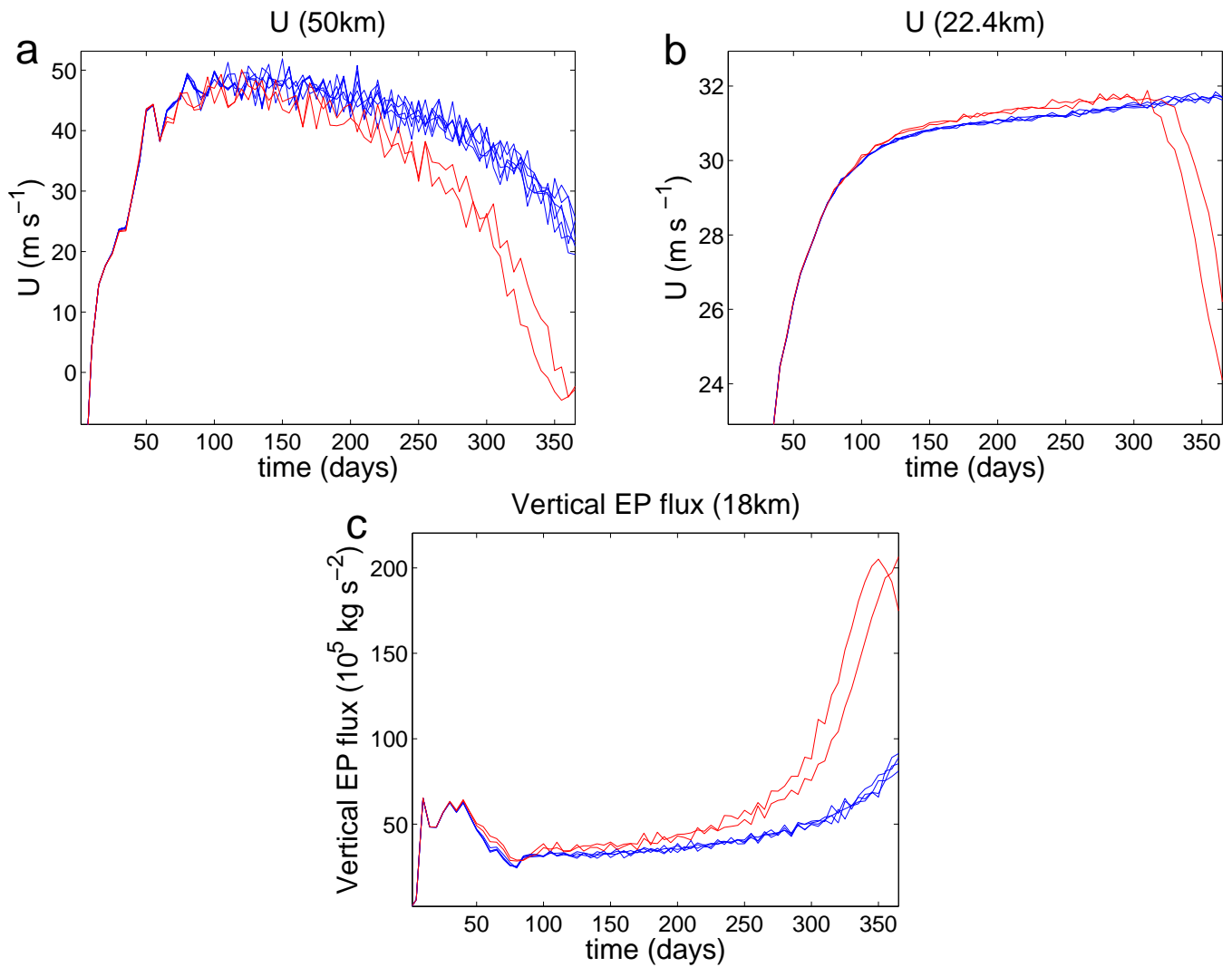


Figure 3.15:

Figures show U at 50km and 22.4km and vertical EP flux at 18km (all at 60°N) for $\Phi_0 = 294\text{m}$, stratosphere only model. Warm runs are shown in red and cool runs in blue. The signal of an SSW occurring at 50km is clearly transmitted down to near the tropopause.

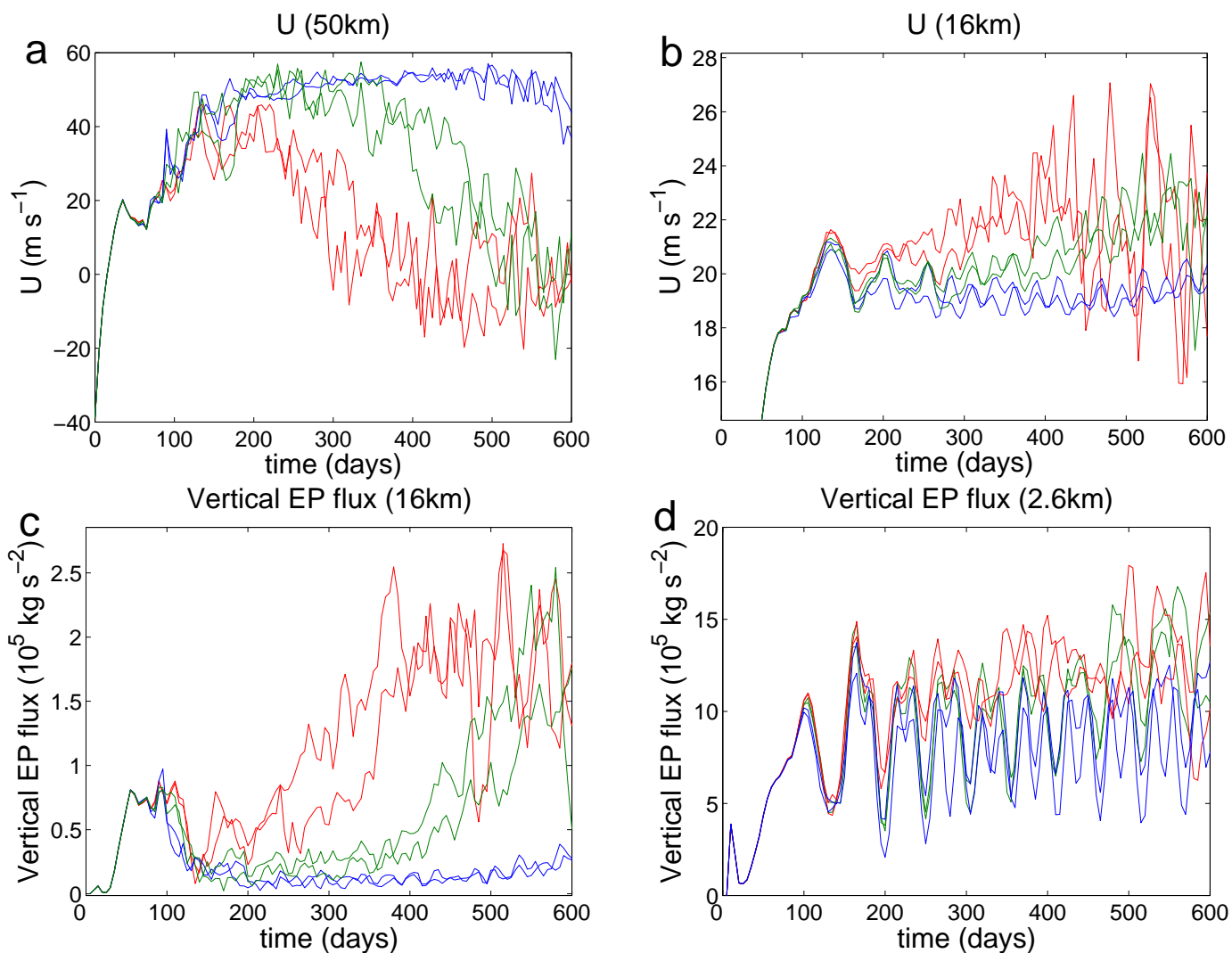


Figure 3.16:

Figures (a)-(c) show U at 50km and 16km and vertical EP flux at 16km (60°N) for $\Phi_0 = 1350\text{m}$, full atmosphere model. Warm runs are shown in red, intermediate runs in green and cool runs in blue. Figures show that the signal of an SSW occurring at 50km is clearly transmitted down to the tropopause. Figure (d) shows latitudinally averaged vertical EP flux in the northern hemisphere at 2.6km. This shows that in warm runs greater EP flux is generated at the lower boundary (in agreement with Scott and Polvani 2004).

point that the EP flux entering the stratosphere is not simply a function of how much EP flux is generated in the troposphere, but rather it is a function of how much EP flux the stratosphere chooses to accept from the troposphere, and this depends on the state of the stratosphere (this point was also made in Gray et al. 2003). It should be noted that the EP flux entering the stratosphere is equivalent to the EP flux leaving the troposphere and thus has a direct effect on the tropospheric flow.

Scott and Polvani (2004) run with a model that includes a troposphere. The troposphere is relaxed to a thermal equilibrium that is baroclinically stable, and contains a Rayleigh drag to ensure weak westerlies allowing waves to propagate upward into the stratosphere. The IGCM model containing a troposphere that we use (section 3.6) is similar to that of Scott and Polvani (2004) in that the troposphere is damped to prevent baroclinic instability. In our model this is achieved by damping wave numbers 2 and higher.

Considering the work of section 2.11.3 (which follows that of Yoden 1987(b)) we might expect that, in the stratosphere only version of IGCM used earlier in this chapter, the same behaviour would be observed (namely that the EP flux generated at the lower boundary would be a function of the stratospheric flow). We would expect warmer runs to show greater generation of EP flux at the lower boundary even with Φ_0 kept constant there. Figure 3.15 shows that this is indeed the case.

The same holds in the full atmosphere version of IGCM used earlier, with baroclinic instability damped in the troposphere. This is shown in figures 3.16(a)-(c) which show U at 50km and 16km, and the vertical EP flux at 16km (all at 60°N). Thus the difference in runs already shown at 50km does persist all the way down through the stratosphere to the tropopause. An interpretation of figure 3.16 is that greater EP flux into the stratosphere means greater EP flux divergence at the tropopause, thus stronger eastward flow there, and a greater EP flux convergence in the upper stratosphere, thus more westward flow there.

However this is not the whole story since, in agreement with Scott and Polvani (2004), warmer runs show greater EP flux generation at the lower boundary. This is shown in figure 3.16(d) which shows latitudinally averaged vertical EP flux at 2.6km in the northern hemisphere. Hence the effect of the stratospheric flow seems to be felt down to the lower boundary. (It is important to look at latitudinally averaged vertical EP flux. In all runs the EP flux on the lower boundary is similar at 60°N, but it is greater towards the equator in warmer runs with a larger poleward transport of EP flux at low altitudes and larger vertical transport of EP flux in the extratropics. This agrees with Yoden et al. (1996) (their figure 9) who look

at composite maps, over runs with cold, moderate and warm polar stratospheres, of EP flux, and also mention that a composite map of the planetary waves in the troposphere shows a wave train pattern at high latitudes in the warm case giving evidence of a vertical link between the troposphere and the stratosphere in this case). Scott and Polvani (2004) form their conclusions from a single model run looking at several model years. Here we extend that by showing that their conclusions carry over to the case of separate model runs, some with cool and some with warm polar stratospheres, in the way that we would expect.

It should be emphasised again that baroclinic instability is damped in the troposphere for these model runs, and it is worth considering the EP flux entering the stratosphere in a model in which baroclinic instability is allowed to develop. In such a run we would expect this to be governed by both the state of the stratosphere (how much EP flux the stratosphere chooses to accept from the troposphere) and also how much EP flux is produced in the troposphere due to baroclinicity.

Due to the latter, when baroclinic instability is allowed to develop a steady state is no longer attained in any model run (no matter how small a value of Φ_0 is used). We can no longer distinguish between cool and warm runs – such a clear cut difference no longer exists (see figure 3.17). Even when strong westerlies are observed in a run, there is no obvious decrease in the EP flux entering the stratosphere. It is no longer clear if there is any relation between the available EP flux and U in the stratosphere. However, as we will demonstrate below in this section, there is indeed still a link between the EP flux entering the stratosphere and U in the stratosphere. The idea of Scott and Polvani (2004) that the flow in the stratosphere can influence the EP flux entering the stratosphere will be shown still to apply.

We proceed as follows, asking the question as to how the amplitude of lower boundary wave forcing, internal variability in the troposphere (sometimes generated by baroclinic instability) and internal variability in the stratosphere (sometimes concerning the dynamical state of the stratosphere (steady or vacillating)), affect the total amount of (vertical) EP flux, Fz_{tot} , that enters the stratosphere during a model run. To this end we evaluate (using the model with a troposphere included):

$$Fz_{tot} = 2\pi a \int_{-\pi/2}^{\pi/2} f_z \cos\phi a d\phi$$

where f_z is vertical EP flux, ϕ is latitude, and a is the radius of the earth.

Running with a troposphere damped to prevent baroclinic instability (as in section 3.6 but for a more extended range of Φ_0) we consider Fz_{tot} at a height of 16.8km averaged from days 200 to 600 of the model runs (we look also at 13.3km to check

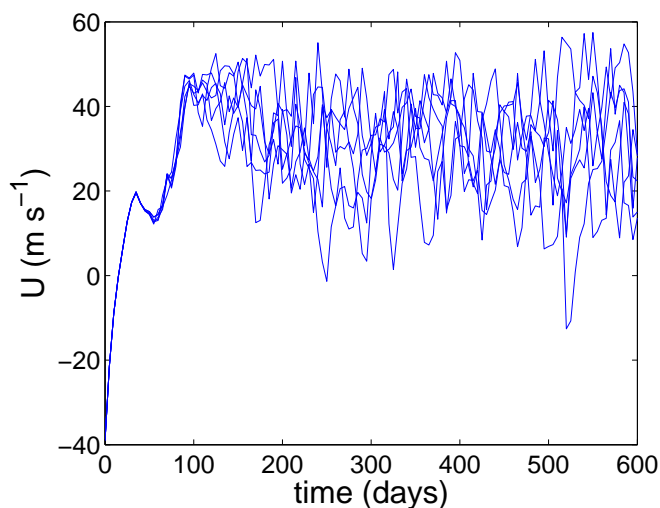


Figure 3.17:

When baroclinic instability is allowed to develop, we no longer see runs which are definitely ‘cool’ or definitely ‘warm’. Here we look at U at 60°N and 50km for $\Phi_0 = 1350\text{m}$.

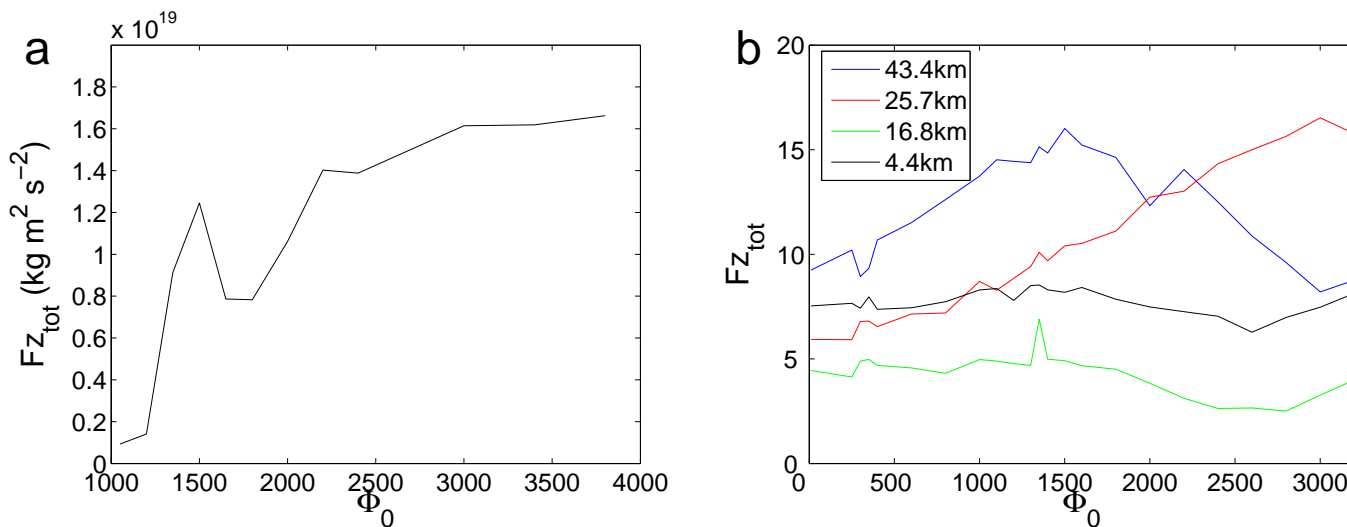


Figure 3.18:

Figure (a) shows total upward EP flux through 16.8km as a function of Φ_0 for runs with baroclinic instability damped in the troposphere. Figure (b) shows total upward EP flux through 4.4km ($10^{20} \text{ kg m}^2 \text{ s}^{-2}$), 16.8km ($10^{18} \text{ kg m}^2 \text{ s}^{-2}$), 25.7km ($10^{17} \text{ kg m}^2 \text{ s}^{-2}$) and 43.4km ($10^{15} \text{ kg m}^2 \text{ s}^{-2}$) for runs with baroclinic instability allowed to develop.

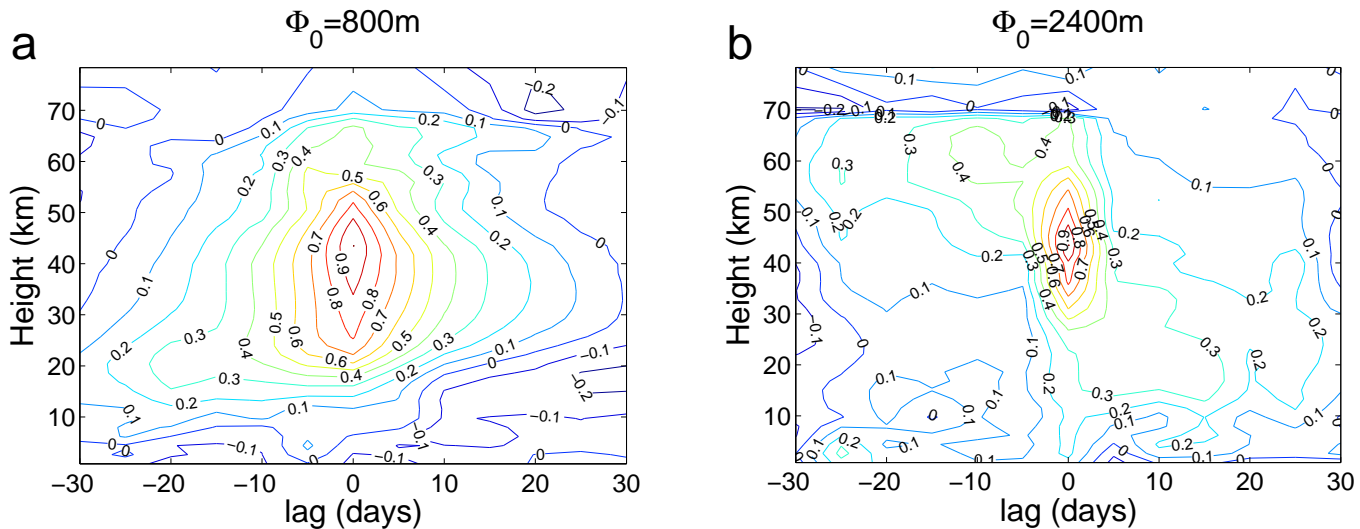


Figure 3.19:

Figures show lag-correlation coefficients, in lag-height sections, for the vertical EP flux using a reference point of 85°N and 43.4km . (This follows Taguchi et al., 2001, who show similar figures for T , U , and wave amplitude). Figure (a) shows run with $\Phi_0 = 800\text{m}$ where the influence in the vertical EP flux is largely upward and figure (b) shows run with $\Phi_0 = 2400\text{m}$ where the influence is largely downward.

that the same results are found at both heights – not shown). See figure 3.18(a). In the absence of baroclinic instability the amount of EP flux entering the stratosphere is found to be around $10^{18} \text{ kg m}^{-2} \text{ s}^{-2}$ when the stratosphere is in a steady state and around $10^{19} \text{ kg m}^{-2} \text{ s}^{-2}$ when it is vacillating. In general there appears to be only a small increase in $F_{z_{tot}}$ with Φ_0 – the largest difference is seen either side of the bifurcation point from steady state to vacillations.

In the presence of baroclinic instability no steady state is ever achieved (as is mentioned above). We run without damping in the troposphere and consider the vertical EP flux crossing the 4.4km , 16.8km , 25.7km , and 43.4km surfaces as a function of Φ_0 . The results are shown in figure 3.18(b). In what follows in this section we consider carefully what is shown in figure 3.18(b).

Scinocca and Haynes (1998) show that, in the presence of baroclinic instability and no other form of wave driving in the troposphere, the instability gives rise to small scale disturbances which in turn give rise to planetary scale wave forcing which propagates upwards into the stratosphere. We consider the largest wave number components (from 1 to 7) of the zonal wind at 60°N in our model runs and find that the amplitudes of the wave 5–7 components decrease with height and the amplitudes of the wave 1–4 components increase with height. This is true for all values of Φ_0 even though for large values of Φ_0 (greater than 1800m) wave 1 dominates the zonal

wind even in the troposphere. It is worth remembering that the wave forcing we impose is wave 1, so these results suggest that the mechanism discussed in Scinocca and Haynes (1998) is relevant here. This mechanism may well be the cause of all model runs being disturbed (even for small Φ_0), and hence the distinction between ‘cool’ and ‘warm’ runs which we found with a damped troposphere being no longer present.

Taguchi et al. (2001) run a spectral primitive equation model the set up for which we follow closely in our model including a troposphere (allowing baroclinic instability to develop) as was mentioned in section 3.6. They considered (as we do) lower boundary forcing Φ_0 with values from 0m to 3000m and discovered that the dynamical behaviour, as Φ_0 was increased, split into 4 different regimes. Considering time series for T at 86°N and 2.6hPa (43km), they found that in regime 1 (small Φ_0) the polar vortex is basically undisturbed, in regime 2 small undulations in T were observed, in regime 3 SSWs occur intermittently and in regime 4 the vortex is usually weak and warm.

Taguchi et al. (2001) used two further means of classifying these regimes the first of which we follow to ensure that we are finding the same classification. For each value of Φ_0 they plot the values of T in the time series (mentioned above) as a histogram and note qualitative differences between the regimes. For our runs we don’t observe regime 1 (the runs are always slightly disturbed – our model is not identical to theirs, and certainly T_e will be slightly different (see section 3.12)) but the transition from regime 2 to regime 3 (using the histograms just mentioned) is found to occur at $\Phi_0 = 1200\text{m}$ and the transition from regime 3 to regime 4 occurs at $\Phi_0 = 1800\text{m}$.

The other means they use is to look at time lag correlations, correlating time series for T at 86°N and 43km to time series for T at 86°N and all heights shifted in time by up to ± 30 days. The upward propagating correlations that they find in regime 2 (confined to the stratosphere) and the downward propagating correlations in regimes 3 and 4 (over both stratosphere and troposphere) lead them to suggest that vertical linkage between the stratosphere and troposphere in regimes 3 and 4 is two way (and that this is not the case in regimes 1 and 2).

We perform the same lag correlation analysis but using the vertical EP flux at 85°N rather than T . It appears that in regime 2 the influence is largely upward – we see the largest correlations below the reference point for negative lag times (figure 3.19(a)). In regime 3 these positive correlations still appear largely confined to the stratosphere although they do not obviously show an effect that is mainly upward or downward. There is a big change in regime 4 ($\Phi_0 \geq 1800\text{m}$) where the influence

of wave driving appears to be downward – the largest correlations appearing above the reference point for negative lag times and below the reference point for positive lag times, and positive correlations extend also into the troposphere (figure 3.19(b)).

We can therefore interpret figure 3.18(b) in terms of these regimes. We can see that the upward EP flux crossing the 4.4km and 16.8km surfaces is largely independent of Φ_0 (this suggests that the amount of EP flux in the troposphere and the amount of EP flux entering the stratosphere is largely independent of Φ_0 in the presence of baroclinic instability). However, the EP flux crossing the 25.7km surface increases with Φ_0 suggesting that less wave breaking occurs in the lower stratosphere as Φ_0 increases, and the EP flux crossing the 43.4km surface increases through regimes 2 and 3 and then decreases through regime 4 suggesting that significantly more wave breaking occurs between 25.7km and 43.4km in regime 4 (which will lead to a usually warm and disturbed polar vortex). Note that the vertical axis in figure 3.18(b) uses a different scale for each curve.

Further, if instead of looking at the time averaged EP flux entering the stratosphere we look at the amplitude of the vacillations in the time series of $F^{z_{tot}}$ at 16.8km, we find that this amplitude is set by the regime. In regime 2 the amplitude falls somewhere in the range of $6\text{--}8.5 \times 10^{18} \text{ kg m}^2 \text{ s}^{-2}$, in regime 3 it lies within the range of $8.5\text{--}10 \times 10^{18} \text{ kg m}^2 \text{ s}^{-2}$, and in regime 4 is between $10\text{--}13 \times 10^{18} \text{ kg m}^2 \text{ s}^{-2}$ (in no regime does the amplitude increase monotonically with Φ_0 so it is clearly different in the different regimes). Again this agrees with the idea of Scott and Polvani (2004), namely that the flow in the stratosphere helps determine the EP flux into it, since the vacillations in the mean flow also increase as the dynamics move from regime 2 to 3 and 3 to 4 (as described in Taguchi et al. 2001 and above in this section).

Thus, in the sense we have described, the results of Scott and Polvani (2004) carry over to the case where baroclinic instability is allowed to develop, provided we consider the different regimes detailed in Taguchi et al. (2001). It is worth also carrying out the lag correlation analysis mentioned above for runs in which the troposphere is damped to prevent baroclinic instability. Figure 3.20 shows the results of doing so. We find that the influence in the vertical EP flux at 85°N is largely upward in the steady state regime for any value of Φ_0 (an example is shown in figure 3.20(a)) and is largely downward for any value of Φ_0 in the vacillating regime (an example is shown in figure 3.20(b)).

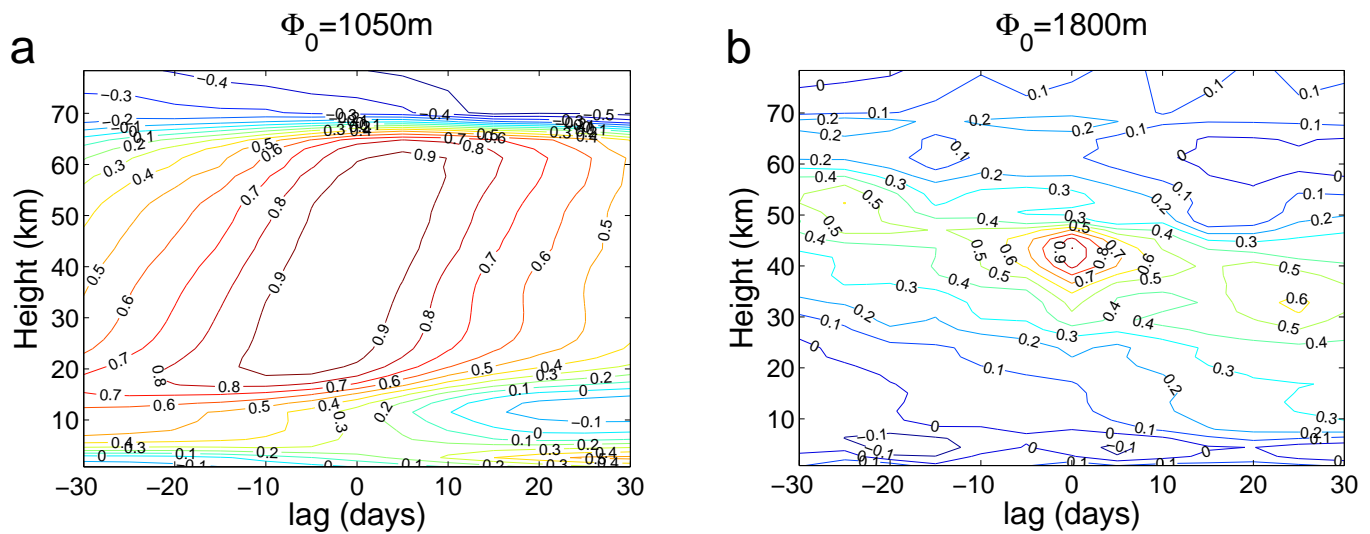


Figure 3.20:

As for figure 3.19 but for runs with troposphere damped to prevent baroclinic instability. Figure (a) shows run with $\Phi_0 = 1050\text{m}$ where the influence is largely upward and figure (b) shows run with $\Phi_0 = 1800\text{m}$ where the influence is largely downward.

3.11 A linear response?

In the last section we argued that the amount of EP flux entering the stratosphere is not simply due to how much wave activity is generated in the troposphere, but it is significantly affected by the state of the stratosphere. If linear theory holds then it might be thought that the fact that the refractive index contains vertical derivatives (see Chen and Robinson 1992) makes this obvious. The question is whether or not linear theory does hold for values of Φ_0 that we are interested in.

A way of testing whether it does is the following. Run the 3D model (both with a troposphere (which we call a full atmosphere model), and in stratosphere only mode) with a given value of Φ_0 . Then, in a separate run, impose the same zonal wind (by reading in the zonally symmetric spectral coefficients from the original run) whilst running with a smaller value of Φ_0 . From equation (2.4) we would expect the vertical EP flux to scale with Φ_0^2 if linear theory holds. So, for example, for an initial run using $\Phi_0 = 10\text{m}$, and a following run using the same U but $\Phi_0 = 1\text{m}$, we expect the EP flux of the first run to be 100 times that of the second.

The vertical EP flux at about 50km and 40°N is shown for each model run in figure 3.21. Figure 3.21(a) shows results for the full atmosphere model. The black curves show EP flux for runs with U corresponding to $\Phi_0 = 1\text{m}$. The three curves are for runs with $\Phi_0 = 0.1\text{m}$ (multiplied by 10^2), $\Phi_0 = 0.02\text{m}$ (multiplied by 50^2) and $\Phi_0 = 0.01\text{m}$ (multiplied by 100^2). The blue curves are for runs with U

corresponding to $\Phi_0 = 10\text{m}$. They show the EP flux for $\Phi_0 = 1\text{m}$ (multiplied by 10^2) and $\Phi_0 = 0.1\text{m}$ (multiplied by 100^2). The red curves are similarly scaled, U corresponding to $\Phi_0 = 100\text{m}$, with $\Phi_0 = 1\text{m}$ and 10m used. Notice that, although the EP flux scales correctly between different runs for the same U , it does not scale like Φ_0^2 for runs with different U (i.e. the blue curves are not 100 times the black curves). Also 100m is a value of Φ_0 considerably smaller than that which we are interested in. It can be seen in figure 3.21(c) that when realistic values of Φ_0 are used (specifically $\Phi_0 = 1000\text{m}$) the response is certainly not linear. The two curves in figure 3.21(c) show runs for $\Phi_0 = 10\text{m}$ and 100m using U corresponding to $\Phi_0 = 1000\text{m}$ (not scaled).

The stratosphere only model, however, is essentially linear (though notice, from figure 3.21(b), that the amount of vertical EP flux is significantly smaller than that found in the full atmosphere model). Figure 3.21(b) is scaled in the same way as figure 3.21(a) except that between different runs (i.e. different colours of curve) the EP flux is scaled by $1/(\Phi_0^2)$. In other words, the curve for the run with lower boundary wave forcing $\Phi_0 = 10\text{m}$ using U corresponding to the $\Phi_0 = 100\text{m}$ run has the EP flux scaled by $10^2/100^2$ (whereas in figure 3.21(a) it would just be scaled by 10^2). Thus, EP flux scales as Φ_0^2 for the same value of U and also for different values of U .

In conclusion, linear theory holds with a stratosphere only model. However, it cannot be used to claim that the stratosphere obviously significantly influences the amount of EP flux it accepts from the troposphere (as was shown in Scott and Polvani 2004 and extended in the previous section) since linear theory does not hold in a full atmosphere model running with realistic values of Φ_0 .

3.12 Cold pole problem

It is well known that some GCMs suffer from a ‘cold pole problem’, the temperature in high latitudes in the model stratosphere being colder than observations suggest it should be. It is important, therefore, to know if the effect of the stratospheric temperature profile on tropospheric flow can be large. By simulating a ‘cold pole’ in our model (in other words changing the stratospheric temperature profile) we will answer the question (raised in section 2.6) as to whether gravity wave breaking or solar heating in the stratosphere, as well as Rossby wave forcing from the troposphere, can alter what regime the stratosphere is in (steady or vacillating). Although the bifurcation parameter is lower boundary Rossby wave forcing (Φ_0) it is possible that a different radiative state in the stratosphere will alter this bifurcation diagram and,

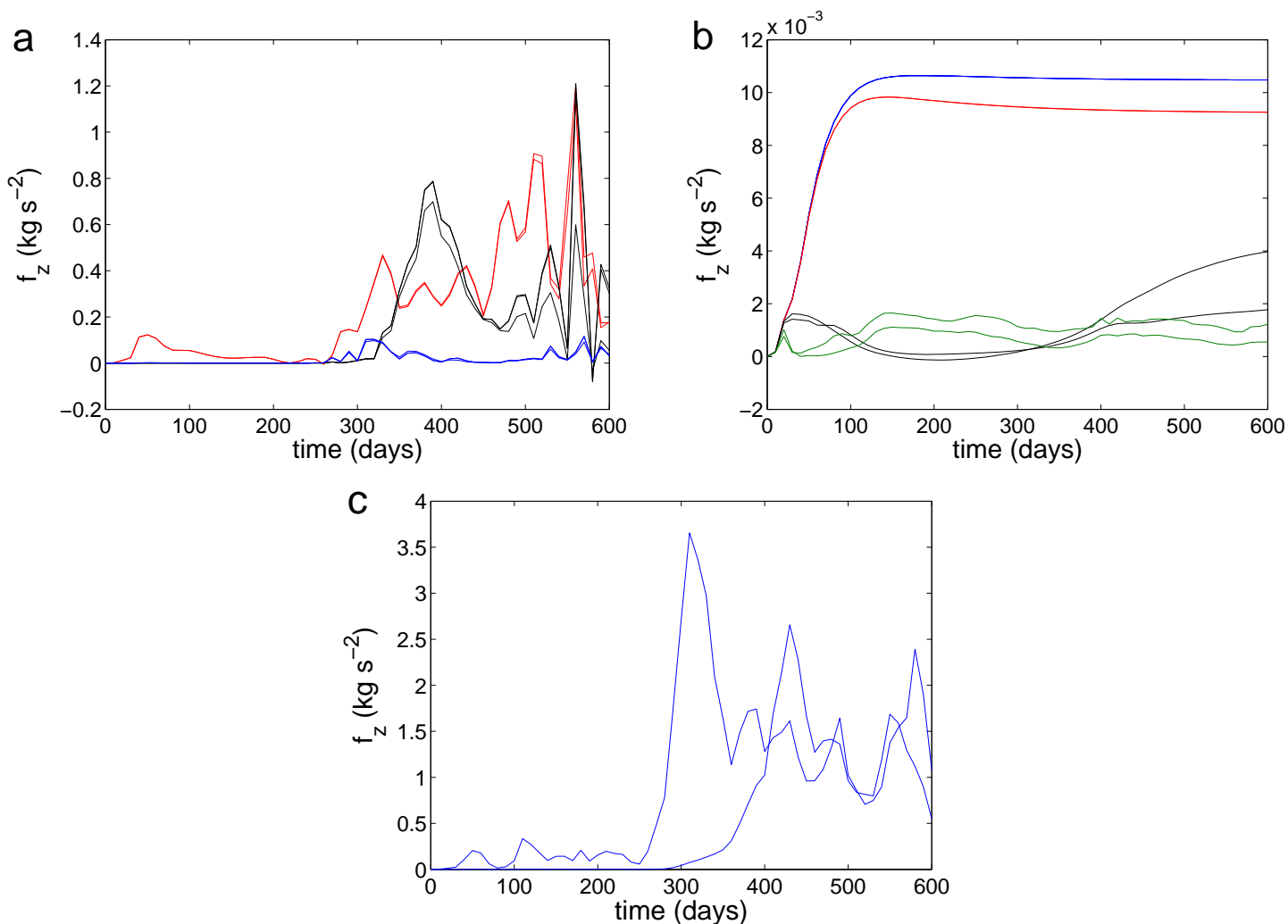


Figure 3.21:

Vertical EP flux at 50km, 40°N for full atmosphere model, and 54km, 40°N for stratosphere only model. Full details of scaling given in the text.

(a) Full atmosphere model. Black lines correspond to U for $\Phi_0 = 1\text{m}$, blue lines to $\Phi_0 = 10\text{m}$, and red lines to $\Phi_0 = 100\text{m}$.

(b) Stratosphere only model. Blue lines correspond to U for $\Phi_0 = 1\text{m}$, red lines to $\Phi_0 = 10\text{m}$, black lines to $\Phi_0 = 100\text{m}$, and green lines to $\Phi_0 = 300\text{m}$.

(c) Full atmosphere model. EP flux for runs corresponding to U for $\Phi_0 = 1000\text{m}$.

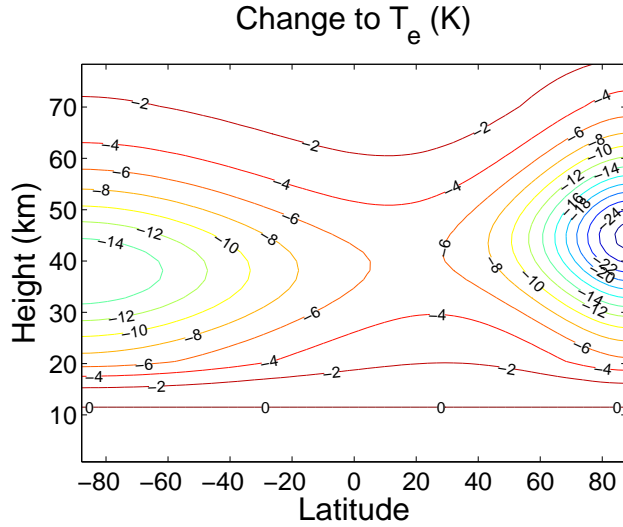


Figure 3.22:

Change applied to radiative equilibrium temperature field (T_e).

in particular, the value of Φ_0 at which the bifurcation point lies. If this is the case, then it follows from the work of this chapter that a cold pole problem could cause a significant error in the simulated tropospheric dynamics.

Butchart and Austin (1998) compared UK Meteorological Office Unified Model (UKMO UM) simulated temperatures with the 5 year mean temperature field from UKMO stratospheric data assimilation for 1992–1996. The difference between these temperature profiles showed the cold pole problem appearing in the UM (their figure 3(c)). We simulate a cold pole problem in our model by adding the following perturbation (given in Kelvin, with z in km) to the radiative relaxation temperature profile T_e (the perturbation matches closely figure 3(c) of Butchart and Austin 1998):

$$C(z)[-26\text{sech}(0.046941(\phi - 90^\circ))\text{sech}(0.093883(z - 45)) \\ - 16\text{sech}(0.018814(\phi + 90^\circ))\text{sech}(0.0823(z - 38))]$$

where

$$C(z) = \begin{cases} 1 & 20 < z \\ (z - 12)/8 & 12 < z \leq 20 \\ 0 & z \leq 12 \end{cases}$$

Figure 3.22 shows this perturbation.

We run the model with troposphere included, using the same T_e profile as in

sections 3.6 to 3.8. The model is spun up from rest to simulate early winter, but thereafter we maintain perpetual January conditions in order for multiple states to be established (it is not clear whether the Yoden bifurcation diagram would persist in the case of a seasonal cycle being applied). We also heavily damp baroclinic instability in the troposphere (using $k_T = 9/\text{day}$ in the notation of section 3.6). The model is run for 600 days.

Figure 3.23 shows U at 60°N and 50km for $\Phi_0 = 1050, 1100, 1175,$ and 1250m for runs with both normal and cold pole relaxation temperature profiles. It can be seen that without adding a cold pole to the radiative temperature profile, a cool winter is seen for values of Φ_0 above 1175m but when using a temperature profile with the cold pole perturbation added a warm winter is already seen when $\Phi_0 = 1100\text{m}$. It seems odd that the colder poles have caused a weaker value of wave forcing to be necessary to produce a warming.

Looking at the zonal wind and EP flux divergence at days 400 (figure 3.24) and 500 (figure 3.25) of runs both with and without a cold pole (using $\Phi_0 = 1175\text{m}$) we can see more clearly what is happening. At day 400 it can be seen that the cold pole has caused the zonal jet (at a height of about 40km) to move poleward from about 50°N to 70°N . By day 500 the change in EP flux divergence (a poleward shift of EP flux convergence at high altitudes, and increased EP flux divergence at high latitudes and low altitudes) has caused U to become more westward at high latitudes (around 40–50km) and more eastward at low latitudes (at the same height).

The important point to note here is that altering the stratospheric temperature profile can alter the tropospheric dynamics by shifting the bifurcation point marking transition from cool to warm run and thus causing/preventing an SSW. From figure 3.26 we can see that $\Phi_0 = 1175\text{m}$ is in the intermediate regime where both cool and warm runs are stable when T_e has a cold pole added, whereas it is in the cool regime (with no sudden warmings observed) in the absence of a cold pole.

Investigating further, we apply the cold pole temperature perturbation to the model stratosphere only in certain regions to try and understand which areas of the change in T_e applied in this section are important. We find that applying the temperature perturbation just in the northern hemisphere (so set SH jet to 0, which we refer to as ‘cp-nh’), or just above 20km (so alter $C(z)$ above to increase linearly from 0 to 1 between 20km and 30km, ‘cp-20’), makes little difference to the case of applying the whole perturbation. U still becomes very strong and eastward and then the stratosphere warms whereas with no temperature perturbation it does not warm (see figure 3.27). Thus it is change to T_e in the northern hemisphere stratosphere that is found to be important.

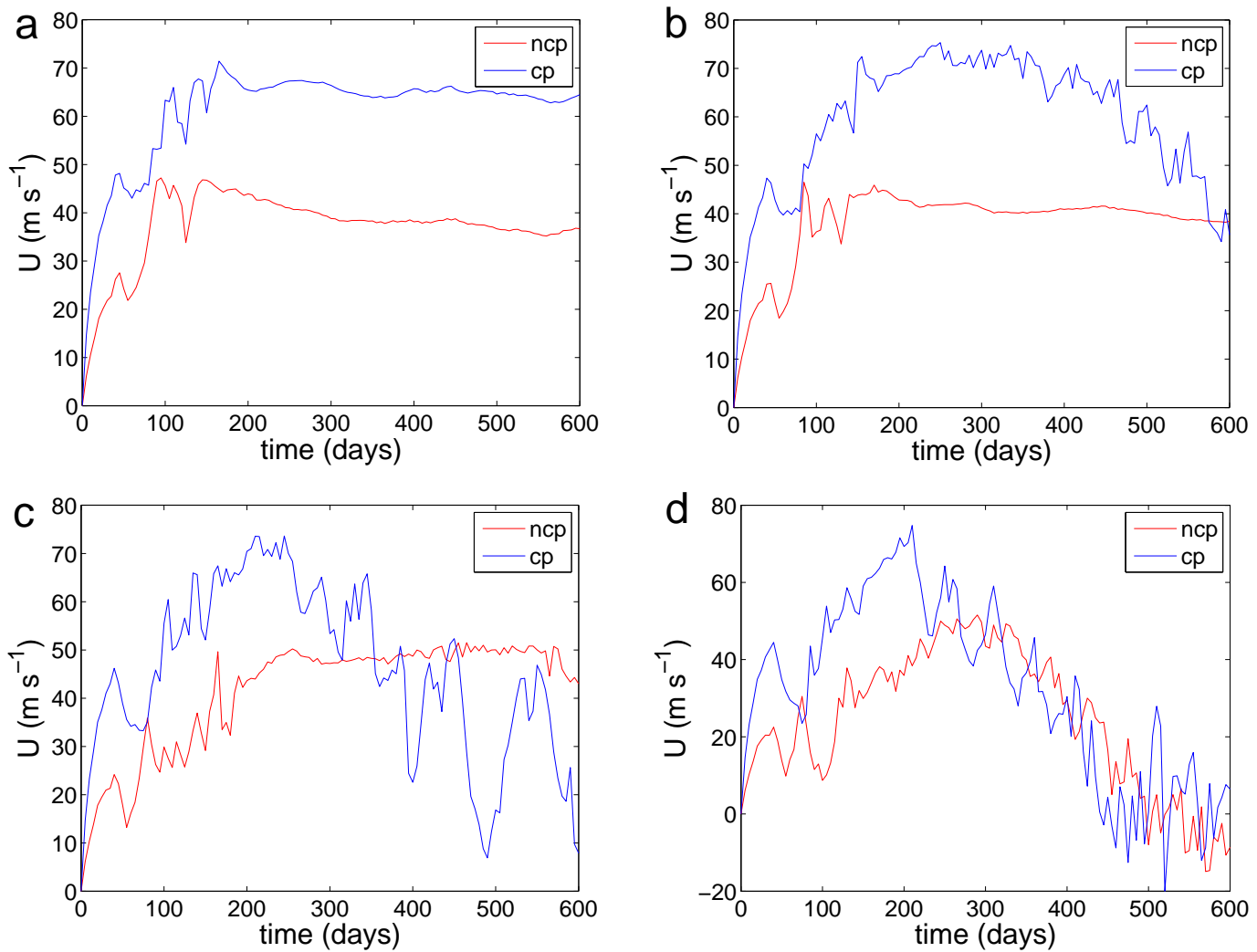


Figure 3.23:

U at 60°N and 50km for $\Phi_0 = 1050, 1100, 1175, 1250\text{m}$ for runs with both normal (or 'no cold pole' – ncp) and 'cold pole' (cp) radiative equilibrium temperature profiles.

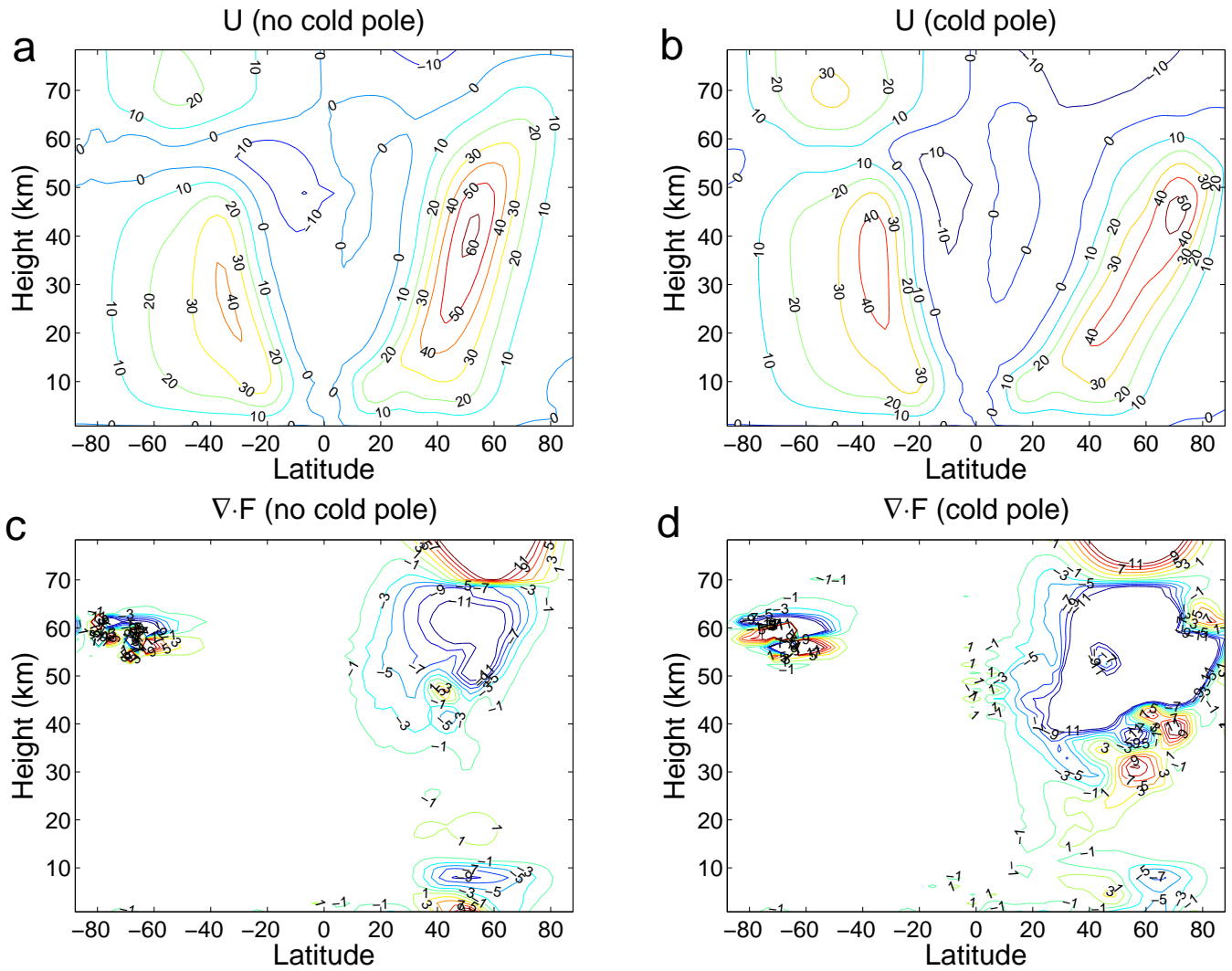


Figure 3.24:

Figures (a) and (b) show U (m s^{-1}). Figures (c) and (d) show total EP flux divergence (i.e. zonally averaged $\nabla \cdot \mathbf{F} \times 2\pi a$, where a is the earth's radius) (10^9 kg s^{-2}).

Figures (a) and (c) show run with no simulated cold pole, and figures (b) and (d) show run including a simulated cold pole.

All figures show day 400 of model runs.

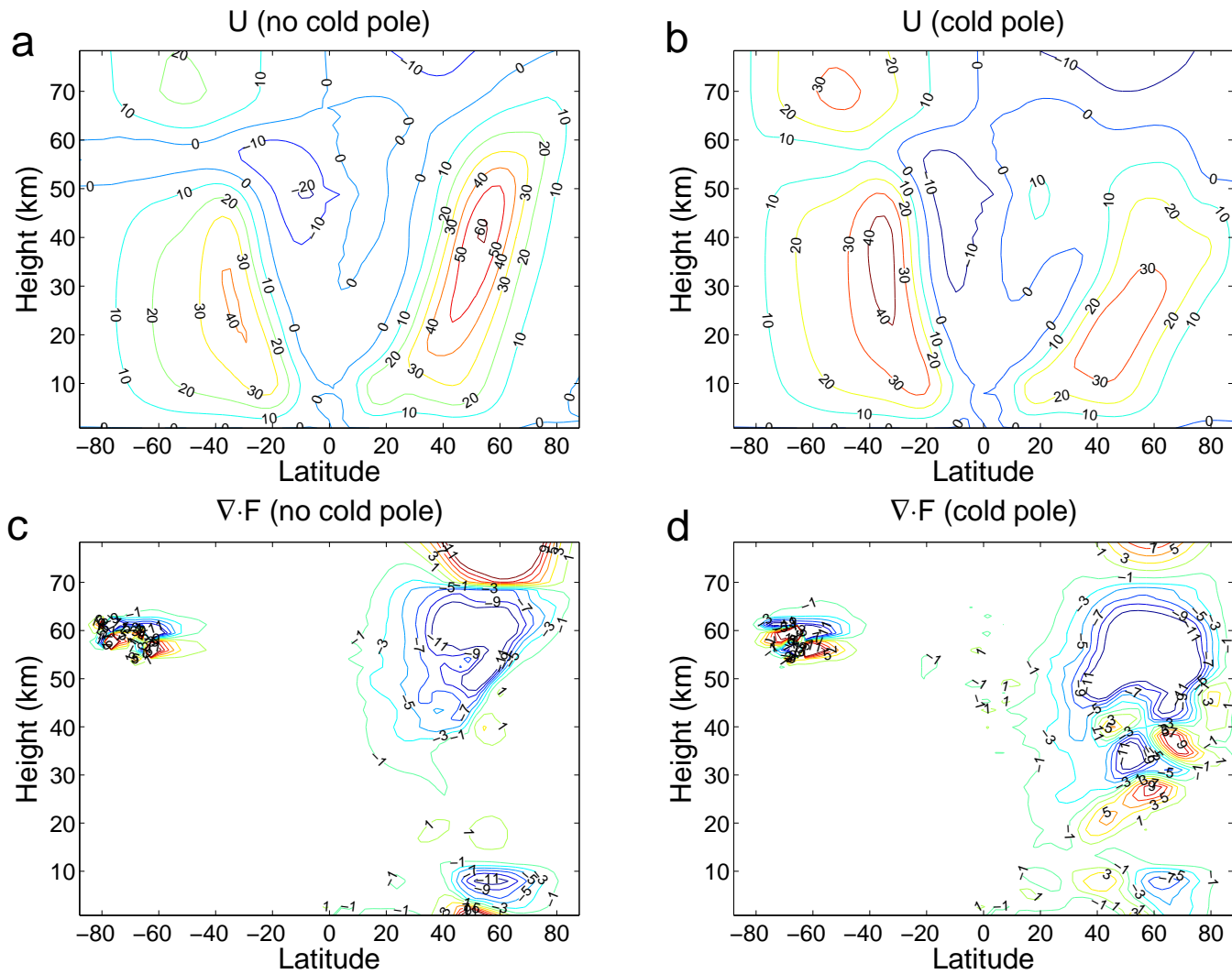


Figure 3.25:

As for figure 3.24 but at day 500 of model runs.

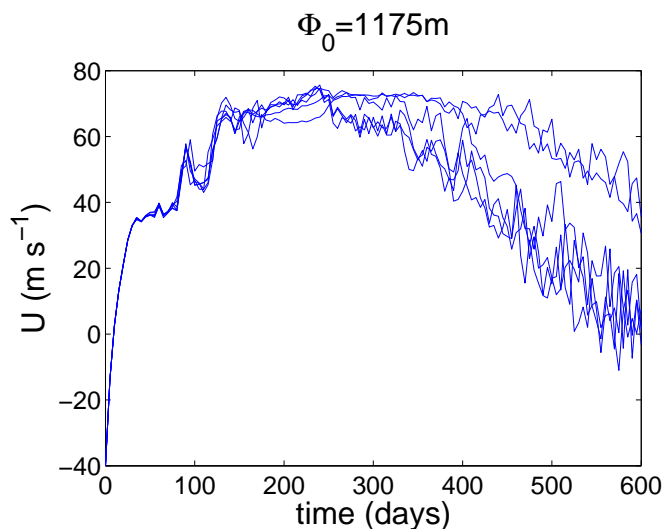


Figure 3.26:

Zonal wind, U , at 60°N and 50km . As for figure 3.7 but for run with simulated cold pole.

In conclusion, what we have shown is that altering T_e in the stratosphere can alter whether or not a stratospheric sudden warming will occur in a particular winter. It will alter the underlying bifurcation structure mapped out by Yoden for 1D models and shown in this chapter to persist in 3D models. Including a T_e in the stratosphere that is correct is therefore essential, given the ability of small perturbations to move the stratosphere from a steady/cool state to a vacillating/warm state detailed above, to correctly model flow evolution in the troposphere. It is worth noting again that even a small change induced in the tropospheric flow could be amplified by the internal dynamics of the troposphere thus causing a large change (Song and Robinson, 2004).

3.13 Conclusions

The conclusions of chapter 2, where a 1D model was used to investigate a mechanism for the downward propagation of dynamical signals in the upper stratosphere, have been found to apply also to experiments performed using a more physically realistic 3D mechanistic circulation model. The fact that the mechanism described persists in different models makes it more credible.

Sensitivity to initial conditions is found for suitably high values of lower boundary wave forcing. This sensitivity is greatest when the difference in the initial conditions occurs in low latitudes. A stratospheric perturbation at high altitudes will have the greatest downward influence for conditions in which sensitivity to initial

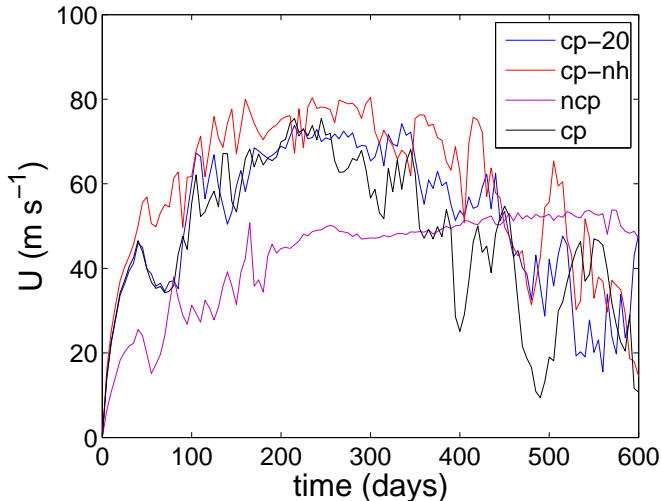


Figure 3.27:

U at 60°N and 50km shown for runs using various radiative equilibrium temperature profiles (described in text). $\Phi_0 = 1175\text{m}$.

conditions is possible and, in these cases, we see the largest downward influence where the perturbation prevents an SSW from occurring (when one would otherwise have done so) or causes an SSW (when, without a perturbation, a cold winter would have been seen). This downward influence is shown to extend significantly into the troposphere. (We draw a parallel between these conclusions and those for the 1D model by suggesting that a steady state in a 1D model is equivalent to a cold winter and a vacillating state in a 1D model is equivalent to a winter in which an SSW occurs.)

It has been shown that the downward influence of a perturbation to the zonal wind, $\Delta U \propto \rho^{-1}$, is significant at whatever height the perturbation is applied (consistent with the analysis of Haynes et al. 1991). Thus, to capture the effects of perturbations on the flow throughout the stratosphere, a model top boundary should not lie below the top of the stratosphere. The sensitivity to initial conditions that we see (which allows a perturbation, ΔU , to have a significant downward influence) can be accounted for by dynamics on planetary scales without considering smaller scales.

Scott and Polvani (2004) show that the amount of EP flux that enters the stratosphere is dependent on the state of the stratosphere (and thus can be time dependent even for time independent external forcing). We have shown that this result carries across to the case of multiple runs (rather than one long run) and (using the work of Taguchi et al. 2001) to the case where baroclinic instability is allowed to develop

in the troposphere. We have also demonstrated that this result is true in the case of stratosphere only models (where the lower boundary on which Φ_0 is kept constant can be thought to be the tropopause).

It is not only Rossby and gravity waves that can affect the state of the stratosphere (by causing a transition from one branch of the equivalent Yoden bifurcation diagram in this 3D model to another), but also the stratospheric radiative relaxation temperature profile, T_e (by altering the bifurcation diagram).

The implications of the last two chapters for climate modellers are that sufficient resolution is required in model stratospheres to accurately resolve planetary wave breaking throughout the stratosphere (since wave breaking at high altitudes can have just as much effect on the model as wave breaking at lower altitudes, and indeed the altitude at which a perturbation is made has been shown to significantly alter its effect on the flow), an accurate radiative state needs to be maintained, and a good gravity wave parametrisation scheme needs to be employed. Without these things it is possible that a model will not, for the tropospheric wave driving available, correctly simulate whether or not a sudden warming should occur in the winter hemisphere (manifested in 1D models by a transition from steady to vacillating state) and thus the model may predict the state of the troposphere completely incorrectly. It is not only the case that the correct perturbation entering the troposphere from the stratosphere must be simulated, but also that the correct vertical EP flux leaving the troposphere must be simulated, and this is driven in part by the state of the stratosphere. The sort of perturbations we have applied could equally be caused by wave breaking or solar heating highlighting the need for a realistic ozone distribution in model stratospheres.

Although it would be good to use ERA-40 data to show the mechanism explored in the last two chapters at work in the real world, the complications of baroclinic instability being present (discussed in section 3.10) are likely to make this very difficult.

Chapter 4

Seasonal Cycle

4.1 Introduction

All investigations so far have been run in a state of perpetual winter. However, the influence of the stratosphere on the troposphere in the real atmosphere occurs under the influence of a seasonal cycle. It is therefore important to understand more about the seasonal cycle seen in dynamical fields in the stratosphere and what causes it. The interhemispheric differences seen in the winter stratosphere, and the seasonal cycle in the mass upwelling in the tropical lower stratosphere are the aspects of this seasonal cycle we will focus on in this chapter.

There are large interhemispheric differences in the winter stratosphere. In the southern hemisphere the polar vortex almost never warms during winter, strong eastward flow being observed throughout. In the northern hemisphere, however, stratospheric sudden warmings in which the polar vortex can be severely distorted during winter are common. Using the language of the previous chapters, it may be that the northern hemisphere is close to the bifurcation point between a steady state and vacillating state (in other words a cool or warm state), whilst the southern hemisphere is within the regime where the steady state is stable. If this is the case then the work of the previous chapter shows that only a small change in the stratosphere would be required to cause or prevent a stratospheric sudden warming in the northern hemisphere. Yoden (1989) showed that this interhemispheric difference could be reproduced in a simple (Holton–Mass) 1D model simply by altering the amount of lower boundary wave forcing applied (their work followed that of Plumb 1989). This is consistent with the hypothesis just suggested. For a lower boundary condition, Yoden used the Φ -condition (described in section 2.9). We ensure that the conclusions of Yoden (1989) persist when using the more physically realistic W -condition lower boundary. We go on to show evidence that a resonance between the

topographically forced waves and free travelling planetary waves could be the reason for large disturbances being seen in the geopotential height field of some runs.

What causes the seasonal cycle in mass upwelling in the tropical lower stratosphere is largely an open question, and it is an important one since it is related to the strength of the Brewer–Dobson circulation of the stratosphere (discussed further in chapter 5) which is responsible for chemical transport within the stratosphere. Yulaeva et al. (1994) suggested that extratropical wave driving is the cause of this equatorial seasonal cycle. However, Kerr-Munslow and Norton (2006) suggest that wave driving in the tropical troposphere may be important. We look further into the causes of this seasonal cycle, investigating the effects of: the strength and location of lower boundary wave forcing, the radiative relaxation time scale, α , adding a seasonal cycle to the tropospheric part of the radiative relaxation temperature profile, T_e , and allowing baroclinic instability to develop. We consider how well downward control appears to apply since showing that it works well would be consistent with the findings of Yulaeva et al. (1994).

4.2 Interhemispheric differences in seasonal variation

There are notable differences in the seasonal variation between the Northern and Southern hemispheres. In the Southern hemisphere winter an uninterrupted strong eastward flow is observed, whereas in the middle of Northern hemisphere winter a stratospheric sudden warming often occurs where the zonal flow becomes westward for a short time. One factor contributing to these differences is the temperature of the surface. The Antarctic is significantly colder because snow reflects much of the sun’s radiation that falls on it. Another explanation for these differences is greater land masses and greater land–sea temperature contrast in the Northern hemisphere causing greater wave formation there, and consequent greater wave propagation into the stratosphere. Yoden (1989) ran some experiments with a Holton–Mass model (as used in chapter 2) to test the effect of this greater topography on seasonal variation. A seasonal cycle was introduced into the radiative equilibrium profile (defined below) and the Φ lower boundary condition (defined in section 2.9) was used. Yoden found that a greater value of Φ_0 gave behaviour typical of Northern hemisphere winter (with a mid winter stratospheric warming), and a lesser value of Φ_0 gave behaviour typical of Southern hemisphere winter (with strong eastward flow), as expected. This is an interesting result, but the Φ lower boundary condition is unrealistic. The question addressed here is whether such behaviour found was

dependent on the artificial nature of this Φ lower boundary condition or whether it can also be found if the W lower boundary condition (defined in section 2.9) is used.

Experiments are run with the Holton–Mass model using the same parameters as Yoden (1989), namely the radiative equilibrium profile U_e is specified by $U_e(z = 0) = 20 \text{ m s}^{-1}$ with $dU_e/dz = 0.75 - 2.25 \cos(\omega t) \text{ m s}^{-1} \text{ km}^{-1}$ and $\omega = 2\pi \text{ year}^{-1}$, $U(t = 0) = U_e$ (although the initial condition is found to be unimportant), $\alpha = [1.5 + \tanh((z - 25)/7)] \times 10^{-6} \text{ s}^{-1}$, and resolution $dt = 0.05 \text{ days}$, $dz = 0.5 \text{ km}$ (with a vertical range of 70 km). However, as mentioned above, we use the W lower boundary condition. We do find, just as for the Φ condition, that a greater value of h_0 ($h_0 = 1250 \text{ m}$) gives behaviour typical of Northern hemisphere winter, and a lesser value of h_0 ($h_0 = 30 \text{ m}$) gives behaviour typical of Southern hemisphere winter. Figure 4.1 shows U and $|\Phi|$ for both values of h_0 .

4.2.1 The Lamb mode

The question then arises – what is it that causes this variation in the model runs? With an imposed seasonal cycle in U_e it is not simply the difference between a steady state and vacillating state since we are being forced away from these natural states by the imposed time dependence in U_e . Something is producing large values of geopotential height at certain times during model runs. One possibility is that a resonance is occurring between the (stationary) topographical forcing and free travelling planetary waves whose phase speed has very small real part. Whether using the Φ -condition or W -condition lower boundary, free travelling planetary waves exist. These are waves not maintained by travelling forcing effects. However, with the W -condition lower boundary a free travelling mode called the Lamb mode exists which is more realistic than any mode obtained for the Φ -condition lower boundary in that a very similar looking mode is observed in the real atmosphere (see Andrews et al. 1987). The Lamb mode is therefore of more interest than other modes.

In fact, the W -condition is not quite the right lower boundary to use. It assumes that the material derivative of pressure vanishes on the boundary which neglects mass redistribution. The correct condition is that the material derivative of the geopotential vanishes on the boundary (see Haynes and Shepherd 1989). Following Tung (1983) this yields

$$w = \mathbf{u} \cdot \nabla h - \left(\frac{\partial}{\partial t} + \mathbf{u} \cdot \nabla \right) \Phi_{\text{tot}}$$

where recall we always use Φ for geopotential height rather than geopotential, and in fact it is geopotential height without the zonal mean so that here $\Phi_{\text{tot}} = \bar{\Phi} + \Phi$

(where overbar denotes zonal mean). The second term on the rhs is additional to the W -condition used before, and is a consequence of mass redistribution on the lower boundary. The calculation proceeds (still following Tung (1983)) by using the thermodynamic equation

$$g \left(\frac{\partial}{\partial t} + \mathbf{u} \cdot \nabla \right) \Phi_{\text{tot}z} + N^2 w = 0$$

along with the geostrophic approximation that

$$\mathbf{u} = \frac{g}{f} \mathbf{k} \times \nabla \Phi_{\text{tot}}$$

where \mathbf{k} is a unit vector in the vertical (in log-pressure coordinates). Thus equation (2.16) becomes

$$\begin{aligned} & -\frac{N^2}{g} \frac{\partial \Phi}{\partial t} + \left(\frac{\partial}{\partial t} + ik\gamma U + \alpha \right) \frac{\partial \Phi}{\partial z} \\ & - ik\gamma \Phi \frac{\partial U}{\partial z} + ik\gamma N^2 h_0 U g^{-1} - \left(k^2 + \frac{\pi^2}{L^2} \right) \frac{N^2}{f} D_E \Phi = 0 \end{aligned} \quad (4.1)$$

and equation (2.17) becomes

$$\begin{aligned} & -\frac{N^2}{g} \frac{\partial U}{\partial t} + \frac{\partial}{\partial t} \frac{\partial U}{\partial z} + ik \frac{\pi^2}{4L^2} \gamma \frac{N^2 g}{f^2} (\Phi h_0^* - \Phi^* h_0) - \frac{\pi^2}{L^2} \frac{N^2}{f} D_E (U - U_e) = \\ & -\alpha \frac{\partial (U - U_e)}{\partial z} + ik \frac{\pi^2}{4L^2} \gamma \frac{g^2}{f^2} \left(\Phi \frac{\partial \Phi^*}{\partial z} - \Phi^* \frac{\partial \Phi}{\partial z} \right) \end{aligned} \quad (4.2)$$

(It is found that the only real difference these extra terms (the $\frac{N^2}{g} \frac{\partial}{\partial t}$ terms) make is to the vertical structure of the Lamb mode at lower levels).

To make analytic progress on the Lamb mode we must linearise about an atmosphere at rest (see Andrews et al. 1987, p.169 for details). A transformation allows a velocity field that is constant in height, but we would like to deal with a general velocity field. Therefore we proceed computationally, solving equations (2.1) and (2.3) as an eigenvalue problem at time t using the value of U at that time. In the lower boundary condition 4.1 we set $h_0 = 0$ else we have a forced problem and do not find free modes (although the model runs that we take U from still use $h_0 \neq 0$ of course). This gives as many eigenvalues, and corresponding eigenmodes, as there are vertical levels in the model (141 here). The mode corresponding to the velocity at $z = 0$ is the Lamb mode. We find this mode by solving for it analytically in the case where U is independent of z and then gradually altering U , and tracking the small changes in the eigenvalue of the Lamb mode for such small changes in U ,

until we are applying the value of U we require (taken from the Holton–Mass model runs). In matrix form the equations we are solving are

$$\begin{aligned}
 c\mathbf{Q}\Phi_i &= \mathbf{P}\Phi_i \\
 \text{where} \\
 \mathbf{P} &= \gamma U_i \mathbf{Q} + \frac{g}{f} \mathbf{K} - \frac{igf}{kN^2} \mathbf{D} \\
 \mathbf{Q} &= -\frac{g}{f} \left(k^2 + \frac{\pi^2}{L^2} \right) \mathbf{I} + \frac{gf}{N^2} \mathbf{M}
 \end{aligned} \tag{4.3}$$

where \mathbf{I} is the identity matrix, \mathbf{K} is the matrix form of $\beta + \gamma Q_y$, \mathbf{M} is the matrix form of $(1/\rho)(\partial/\partial z)(\rho\partial/\partial z)$, and \mathbf{D} is the matrix form of $(1/\rho)(\partial/\partial z)(\rho\alpha\partial/\partial z)$.

Although the vertical structure of the Lamb mode seems to bear little resemblance to $|\Phi|$, the important thing is where $\text{Re}(c)$ (the real part of the phase speed of the Lamb mode (i.e. the real part of the eigenvalue of the Lamb mode)) vanishes. If it is small at times when the geopotential height and EP flux are large, then there may be a resonance between the Lamb mode and stationary planetary wave forcing.

The model is run for 2000 days (allowing 1000 days spin up time, so considering day 1000 of the model run to be day 0) for both $h_0 = 30\text{m}$ and $h_0 = 1250\text{m}$. To eliminate transient effects, we examine the EP flux both in the time evolving case (using radiative equilibrium velocity profile $U_e(t)$ defined above) and also by evolving to a steady state. (In other words we take the values of U_e and U at several different points of the time evolving run and, for each point, run with them constant at these values until a steady state is achieved. Combining the values of a dynamical field at each of these points gives a time evolution for that field without transient behaviour. We refer to this as the steady state run.)

Consider first $h_0 = 1250\text{m}$. Looking at figure 4.3(a) we see that the phase speed of the Lamb mode is fairly constant throughout the run, and far from zero. So no resonance is possible in this case. The (linear) case where $h_0 = 30\text{m}$ is more interesting. Now from figure 4.3(a) we see that the real part of the phase speed ($\text{Re}(c)$) gets small at two times during the run. This happens on days 479 and 667. Looking at the EP flux through the lower boundary, $F(z=0)$, (figure 4.2(a)) we see an increase in F during these times – the first time being around day 450, when $\text{Re}(c)$ is fairly small. At the second of these times F appears to go large and negative – behaviour that is not seen in the steady state run (figure 4.2(a)). As we plot F further from the bottom boundary it becomes clear exactly which contributions lead to greater $|\Phi|$ (figure 4.2(b)). It also becomes clear that the negative F is due to topographical contributions from the lower boundary. The maxima in $|\Phi|$ are

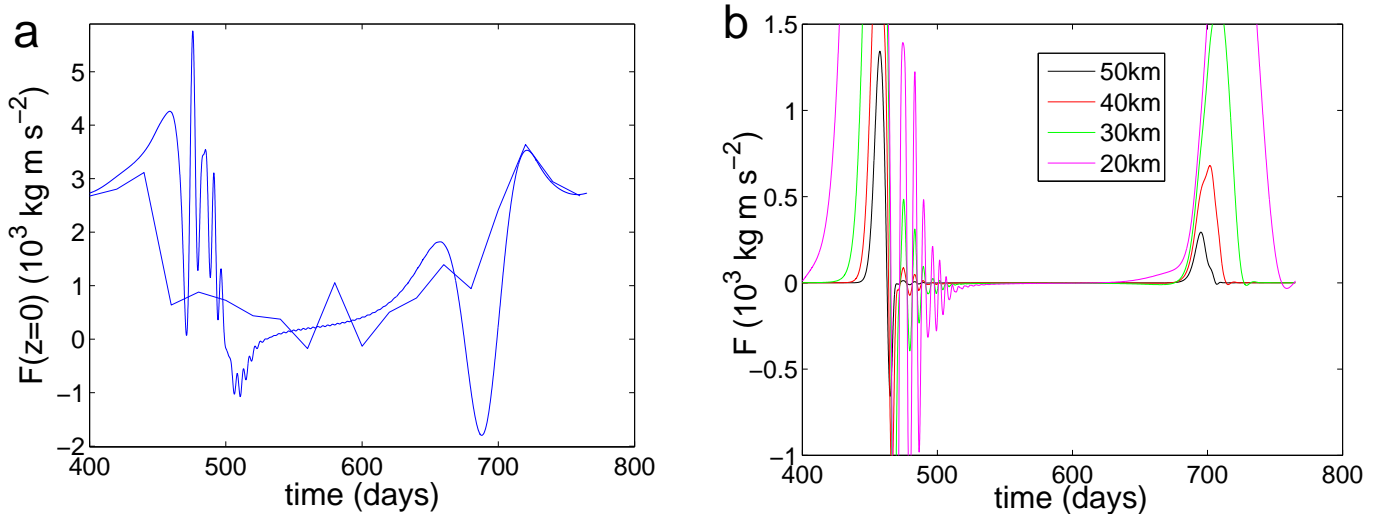


Figure 4.2:

- a) Vertical EP flux on bottom boundary, $F(z=0)$ (10^3 kg m s^{-2}) in time-evolving and steady state runs (defined in text) for $h_0 = 30\text{m}$.
 b) Vertical EP flux (10^3 kg m s^{-2}) at various altitudes (time-evolving case) for $h_0 = 30\text{m}$.

realised on days 461 and 692 (figure 4.1(b)). The fact that these times closely agree with the times when the Lamb mode has negligible real phase speed suggests that resonance may be occurring.

The question that then arises is what aspect of the flow causes such a difference in the eigenvalues of the Lamb mode when $h_0 = 30\text{m}$ and $h_0 = 1250\text{m}$ leading to a possible resonance at $h_0 = 30\text{m}$ when none is seen at $h_0 = 1250\text{m}$. This is answered by looking at $U(z=0)$, the velocity at the bottom boundary, for both values of h_0 . We see (figure 4.3(b)) that $\text{Re}(c)$ appears to be strongly influenced by the flow near the surface. It remains to discover the reason for the large difference in the flow near the surface between the linear and non-linear regimes (this is a point for further work). Once understood this should help explain why a resonance might occur in the linear regime ($h_0 = 30\text{m}$) but not the non-linear one ($h_0 = 1250\text{m}$).

4.3 Seasonal Cycle in Mass Upwelling in the tropical lower stratosphere

In this section we consider what affects the seasonal cycle in the mass upwelling in the tropical lower stratosphere. It was suggested by Yulaeva et al. (1994) that the seasonal cycle at the equator is largely due to extratropical wave forcing in the stratosphere. More recently Kerr-Munslow and Norton (2006) suggested that it may

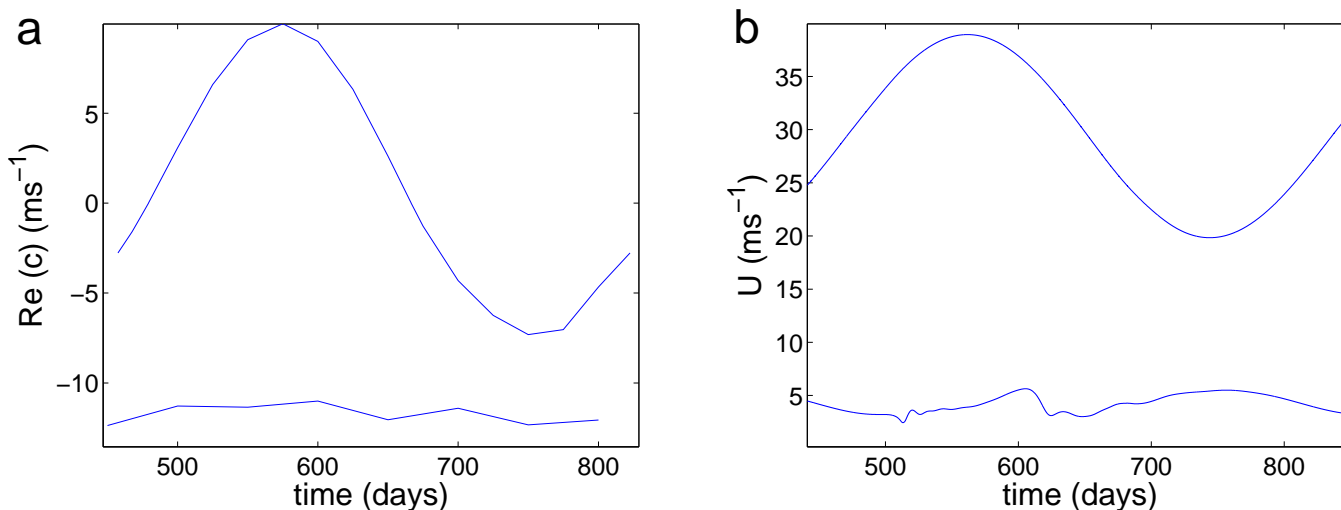


Figure 4.3:

a) Phase speed of Lamb mode ($\text{Re}(c)$) for $h_0 = 30\text{m}$ and $h_0 = 1250\text{m}$.

b) $U(z = 0)$ (velocity on lower boundary) for $h_0 = 30\text{m}$ and $h_0 = 1250\text{m}$.

The curves showing strongly varying Lamb mode phase speed ($\text{Re}(c)$) and zonal wind at the surface (U) correspond to the linear regime ($h_0 = 30\text{m}$) and the curves where these quantities are almost constant correspond to the non-linear regime ($h_0 = 1250\text{m}$)

be due, in some significant part, to wave propagation in the tropical troposphere.

We investigate the cause of this seasonal cycle and we will show that, consistent with Yulaeva et al. (1994), wave forcing in the midlatitude lower stratosphere plays a crucial role (via the downward control mechanism (Haynes et al. 1991)).

The model set up described below is similar to that used by Scott (2002). In that paper a modified version of the downward control integral including transient effects was used to investigate the mean tropical upwelling in the lower stratosphere. The main result of the paper was that the transient effects of the seasonal cycle in thermal and mechanical forcing contributed more to the mean upwelling than the nonlinear redistribution of angular momentum contours by the forcing. The paper uses forcing centred at different latitudes, and a zonal mean (2D) version of the model (with EP flux prescribed) – ideas that we shall also use to further explore the seasonal cycle in mass upwelling in the tropical lower stratosphere.

The model used is the 3D mechanistic circulation model (IGCM) used in chapter 3 above. We run with T42, 41 vertical levels, and one time step every 15 minutes. The model is run in sigma-coordinates with lower boundary at the ground and top boundary at 68km. The model is spun up from rest.

To achieve a reasonable seasonal cycle in model runs, a more realistic T_e profile than that used in chapter 3 was required. To achieve this new T_e profile, the old

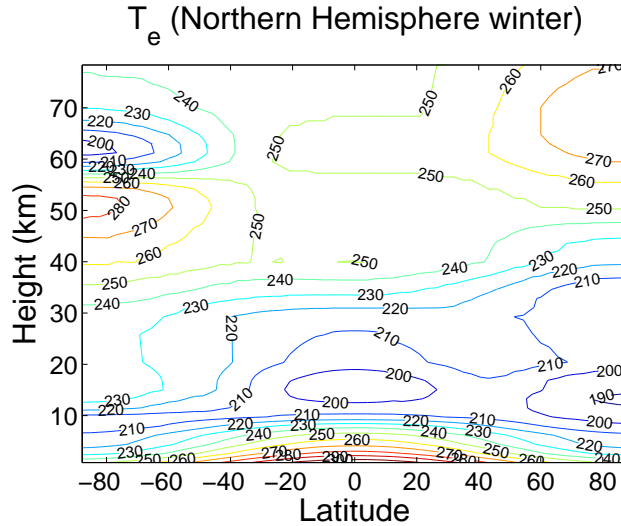


Figure 4.4:

New version of T_e (described in text)

profile was modified in the following ways:

The stratospheric profile (obtained from gradient wind balance as in SH02) was altered in the summer hemisphere to take the temperature maximum (at the pole) from 45km to 50km. The temperature in the troposphere was increased at the equator giving an enhanced pole to equator temperature gradient. The difference in temperature between the two poles was increased, at the tropopause, from virtually no difference to a difference of 30K. An increased pole to equator temperature gradient in the lower stratosphere in the summer hemisphere gives a lower zero wind line there. A temperature low was included in the tropical lower stratosphere to produce well defined tropospheric jets in the wind profile. The new T_e profile is shown in figure 4.4.

Everything else is set as described in section 3.3. In particular we set $\Phi = \Phi_0 E(t) G(\phi)$ where Φ_0 is a constant forcing amplitude, $E(t)$ increases smoothly from 0 to 1 over the first 10 days of the model run, and $G(\phi) = 4\hat{\mu}^2(1 - \hat{\mu}^2)$ for $\mu > \mu_0$ and 0 otherwise, where $\hat{\mu} = (\mu - \mu_0)/(1 - \mu_0)$, $\mu = \sin(\phi)$, all as before (forcing is wave 1). Initially baroclinic instability is damped in the troposphere (as in section 3.6, using $k_T = 9/\text{day}$). We will investigate the effect of Φ_0 (magnitude of lower boundary wave forcing) and μ_0 (location of lower boundary wave forcing) on the seasonal cycle.

Each run has a year length of 360 days, and we run for 6 years (analysing only the final 5 years of each run, so allowing 1 year of spin up time). The lower boundary

wave forcing is constant (as given in section 3.3) with a seasonal cycle being imposed by setting

$$T_e = rT_{\text{summer}} + (1 - r)T_{\text{winter}} \quad (4.4)$$

with

$$r = \frac{1}{2} \left(1 + \cos \frac{2\pi t}{360 \text{ days}} \right) \quad (4.5)$$

as was done in Scott (2002). T_{summer} is the same as T_{winter} (shown in figure 4.4) with the poles reversed in the stratosphere and the (symmetric) troposphere remaining constant. Thus all runs start in the middle of northern hemisphere summer.

We will also consider the effects of the radiative relaxation timescale, baroclinic instability, and adding a seasonal cycle to the relaxation temperature profile in the troposphere on the seasonal cycle of mass upwelling in the tropical lower stratosphere.

4.3.1 Dependence of seasonal cycle on Φ_0 and μ_0 , and relevance of downward control mechanism

First we try to determine the effect of Φ_0 (magnitude of lower boundary wave forcing) and μ_0 (location of lower boundary wave forcing) on the annual average mass upwelling in the tropical lower stratosphere, M , and the amplitude of the seasonal cycle in M . Mass upwelling is calculated as

$$M = \int_{\phi_-}^{\phi_+} \rho w^d a \cos \phi d\phi \quad (4.6)$$

where a is the radius of the earth, ρ the density at the height at which the upwelling is measured (here 100hPa), ϕ is latitude, and we take $\phi_- = 30^\circ\text{S}$ and $\phi_+ = 30^\circ\text{N}$. w^d (used also in Scott 2002) is a measure of the vertical velocity (due to diabatic effects) and is given by

$$w^d = \frac{\alpha(\bar{\theta}_e - \bar{\theta})}{\theta_{0z}} = \frac{\alpha H(\bar{T}_e - \bar{T})}{\kappa T_0} \quad (4.7)$$

where overbar represents a zonal average, and T_0 is the basic state temperature profile (here 250K at all heights). So it can be seen that w^d is a zonal average, and the units of M are $\text{kg m}^{-1} \text{s}^{-1}$. We will use this definition of M throughout to represent mass upwelling (since it is directly comparable to the downward control streamfunction described below). However, it should be remembered that to give an average upwelling mass flux (in kg s^{-1}) all values given in this section should be

multiplied by $2\pi a$.

As just suggested, we also calculate the mass upwelling by using the downward control streamfunction, ψ , as given in Haynes et al. (1991). $M = \psi(\phi_+) - \psi(\phi_-)$. Again $\phi_- = 30^\circ\text{S}$ and $\phi_+ = 30^\circ\text{N}$. (All calculations are repeated using $\phi_- = 20^\circ\text{S}$ and $\phi_+ = 20^\circ\text{N}$ to check the robustness of the relevance of the downward control mechanism.) The downward control streamfunction is approximated by

$$\psi(\phi, z) = \int_z^\infty \left(\frac{\rho a^2 \bar{\mathcal{F}} \cos^2(\phi)}{\bar{m}_\phi} \right)_{\phi=\text{const}} dz' \quad (4.8)$$

where

$$\mathcal{F} = \frac{\nabla \cdot \mathbf{F}}{\rho a \cos \phi}$$

and

$$\bar{m} = a \cos \phi (U + a \Omega \cos \phi)$$

18 model runs are computed using the values $\Phi_0 = 200, 400, 600, 800, 1000, 1200\text{m}$ and $\mu_0 = 0, 0.2, 0.5$ (giving forcing centred at approximately 45°N , 50°N and 59°N (respectively) where forcing is zero south of 0°N , 11.5°N and 30°N (respectively)). Figure 4.5 shows latitude–time plots giving an example of w^d (mm s^{-1}) and the vertical component of the EP flux, f_z , at 100hPa, and also the mass streamfunctions as calculated using w^d and the downward control integral (using time averaged data) for the run where $\Phi_0 = 800\text{m}$ and $\mu_0 = 0$.

Figure 4.6 shows height–latitude plots for U and T from the same run averaged over winter months (DJF) and summer months (JJA). (A 30 day lag behind T_e is used in all fields (i.e. U , T , ...) when dividing the data into seasons for reasons to be explained in the next section).

The annual average value of M and magnitude of seasonal cycle in M for each run is shown in table 4.1. Average upwelling was calculated (using both w^d with equation (4.6) and downward control (referred to as DC) using equation (4.8)) by time averaging the upwelling calculated at each individual time, allowing 1 year of spin up time. An alternative approach would be to time average the U , T , and $\nabla \cdot \mathbf{F}$ fields before calculating the upwelling, but this is found to be little different to what is done here (indeed – one would only expect the downward control estimate (which is nonlinear in U) to be any different). We remove the upwelling seen in the absence of any lower boundary wave forcing, denoted w_0^d , from our average upwelling calculated using w^d so that we just compare the wave driven part of the circulation with the downward control calculation. The size of the seasonal cycle (again in $\text{kg m}^{-1} \text{s}^{-1}$) was calculated as the difference between mass upwelling averaged over DJF

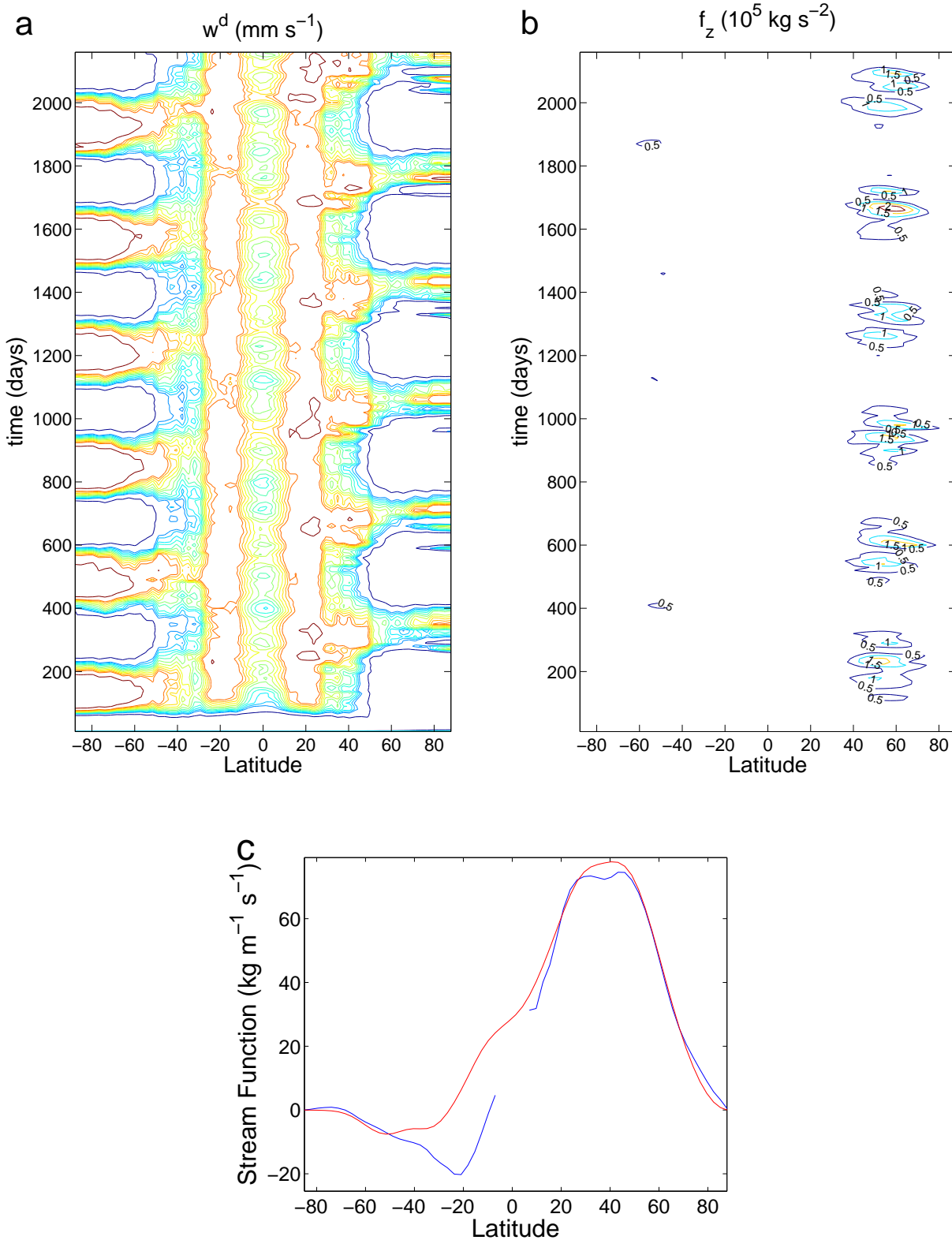


Figure 4.5:

All figures are for the run using $\Phi_0 = 800\text{m}$ and $\mu_0 = 0$ and show the following at 100hPa:

a) w^d , contours are $[-0.2, -0.1, -0.08, -0.06, -0.04, -0.02, 0, 0.02, 0.04, 0.06, 0.08, 0.1, 0.2]$ (mm s⁻¹).

b) f_z (10⁵ kg s⁻²)

c) Average mass streamfunction calculated from w^d (red) and the downward control integral (blue) (kg m⁻¹ s⁻¹).

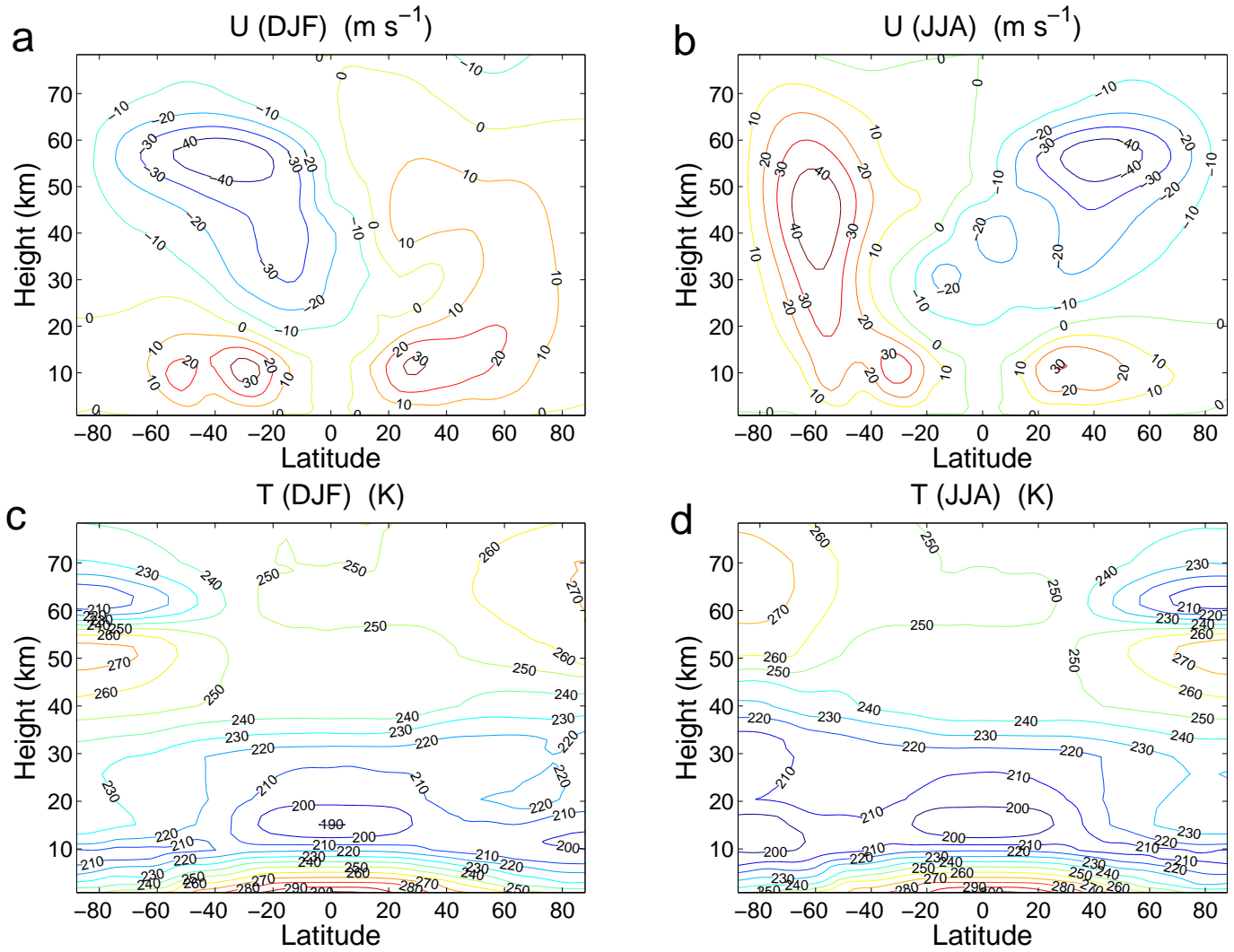


Figure 4.6:

Figures show U and T averaged over DJF and JJA for run using $\Phi_0 = 800\text{m}$ and $\mu_0 = 0$.

Table 4.1:
 M ($\text{kg m}^{-1} \text{s}^{-1}$)

	μ_0		
	0	0.2	0.5
$\Phi_0 = 1200$			
Average upwelling ($w^d - w_0^d$)	70.7	62.9	52.8
Average upwelling (DC)	73.5	62.1	52.0
Size of SC	32.3	27.2	28.0
$\Phi_0 = 1000$			
Average upwelling ($w^d - w_0^d$)	68.0	61.5	46.2
Average upwelling (DC)	70.4	62.4	45.4
Size of SC	29.6	23.6	17.2
$\Phi_0 = 800$			
Average upwelling ($w^d - w_0^d$)	62.1	57.9	50.9
Average upwelling (DC)	64.3	58.1	50.4
Size of SC	34.6	26.7	17.1
$\Phi_0 = 600$			
Average upwelling ($w^d - w_0^d$)	56.5	49.6	43.6
Average upwelling (DC)	56.0	48.7	41.5
Size of SC	33.3	18.0	-8.8
$\Phi_0 = 400$			
Average upwelling ($w^d - w_0^d$)	50.9	45.6	37.4
Average upwelling (DC)	49.8	45.2	34.6
Size of SC	18.6	14.0	8.3
$\Phi_0 = 200$			
Average upwelling ($w^d - w_0^d$)	43.4	37.4	38.5
Average upwelling (DC)	41.9	34.8	36.2
Size of SC	0.5	3.8	1.1

and mass upwelling averaged over JJA (where a 30 day lag was used in defining DJF and JJA as mentioned above). (Note – in some cases where the seasonal cycle is not well defined, the upwelling in JJA is stronger than in DJF leading to a negative value for the size of the seasonal cycle.)

Looking at table 4.1 we see that upwelling increases with Φ_0 roughly linearly. Upwelling also appears to increase as μ_0 decreases (i.e. as the forcing moves equatorward). However, consider the fact that, given the shape of forcing $G(\phi)$ described above, the total (integrated) forcing applied will alter with μ_0 . We must adjust the size of the upwelling accordingly by assuming a linear relationship of size of upwelling with Φ_0 :

Suppose we are comparing two results, one for $\mu_0 = a$ and one for $\mu_0 = b$.

Assume $a < b$ and we are scaling the result for $\mu_0 = b$. Using $y = mx + c$ we have (size of upwelling) = $m\Phi_0 + c$. Now, if Φ_0 becomes $r\Phi_0$ where r is I_a/I_b given by

$$I_{\mu_0} = \int_{\mu_0}^1 G(\mu) d\mu$$

then we must scale (size of upwelling) to become (size of upwelling) + $m\Phi_0(r-1)$, where m is the gradient of the (size of upwelling) vs Φ_0 curve for $\mu_0 = b$ calculated from table 4.1. Scaling in this way, we find upwelling to be roughly independent of μ_0 .

The size of the seasonal cycle in M appears not to depend on Φ_0 , as long as Φ_0 is above a certain value required to see a reasonable seasonal cycle. Here that value is found to be about 400m. However, the size of the seasonal cycle does depend on μ_0 . That is the seasonal cycle becomes better defined as the forcing is centred closer to the equator.

In conclusion mass upwelling increases with Φ_0 but is independent of μ_0 (after appropriate scaling) and the magnitude of the seasonal cycle in M is independent of Φ_0 but increases with decreasing μ_0 .

As might be expected from table 4.1, if we look at the time averaged EP flux entering the stratosphere (time averaged over years 2–6 of model run, allowing 1 year of spin up time as before), we find that it increases with increasing Φ_0 (and decreasing μ_0 before scaling as above).

This is relevant to considering whether or not the downward control mechanism is important to the mass upwelling. We have already seen from table 4.1 that it does a very good job of calculating the annual average mass upwelling (the correlation between the annual average mass upwelling as calculated from w^d and by downward control (i.e. the correlation of 18 pairs of points) is 0.9960). Since downward control is valid in the steady state limit we might expect that it will more accurately calculate the upwelling of annual averages than it will the seasonal cycle.

To demonstrate that downward control will also calculate the magnitude of the seasonal cycle (and so provide a reasonable estimate of the upwelling even when not in the steady state limit) we calculate the average mass upwelling (between 30°S and 30°N), using both w^d (considering only the wave driven part of the circulation) and downward control, for DJF, MAM, JJA, and SON. This gives 72 values (from the 18 model runs) which are plotted in figure 4.7. For reasons to be explained in the next section, we use time lags when dividing the data up into seasons. A 30 day lag behind T_e is used when calculating M using downward control, and a 60 day lag is used when calculating M from w^d . The good correlation shown in this figure

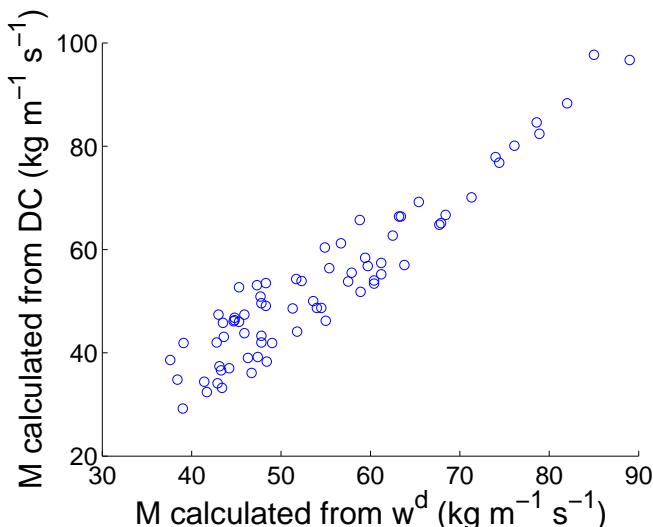


Figure 4.7:

M at 100hPa calculated for each season in each model run using w^d and downward control. The good correlation shows that extratropical eddy forcing is a significant cause of the seasonal cycle in M .

suggests that downward control is relevant to the seasonal cycle in M .

To get a more quantitative feel for how well the downward control principle works, table 4.2 gives the correlations between different sets of points in the scatter plot figure 4.7. The correlation is seen to improve for increasing Φ_0 , improve for decreasing μ_0 , and it is best in DJF and worst in JJA. It is to be expected that the correlation with downward control will improve as the wave driving increases which is the case with all 3 points just made. Computing M between 20°S and 20°N and redoing these correlations gives the same conclusions. Therefore we suggest that the seasonal cycle seen in these runs is largely due to extratropical/subtropical eddy forcing. In later sections we will try to pin down which points of the height–latitude plane are responsible for the most important contributions of eddy forcing to the seasonal cycle, and also consider the effects (on the conclusion that extratropical/subtropical eddy forcing dominates the seasonal cycle in M) of adding baroclinic instability to the model and adding a seasonal cycle to the tropospheric relaxation temperature profile.

4.3.2 Runs with constant α

We now explain the time lags, behind T_e , of mass upwelling, M . As mentioned above, the seasonal cycle in mass upwelling calculated from 30°S to 30°N is found (by graphing M as a function of time) to lag T_e by 60 days if calculated from w^d and by 30 days if calculated from downward control. Consider a simplified form of

Table 4.2:
Correlations of M calculated using w^d with M calculated using downward control

All Φ_0 and μ_0	
All seasons	0.9468
DJF only	0.9898
MAM only	0.9816
JJA only	0.9421
SON only	0.9879
All seasons	
$\Phi_0=1200$ or 1000 , all μ_0	0.9477
$\Phi_0=800$ or 600 , all μ_0	0.9319
$\Phi_0=400$ or 200 , all μ_0	0.8390
$\mu_0 = 0$, all Φ_0	0.9685
$\mu_0 = 0.2$, all Φ_0	0.9240
$\mu_0 = 0.5$, all Φ_0	0.8950

the primitive equations similar to that used by Sankey (1998):

$$i\omega u - 2\Omega \sin(\phi)v = F \quad (4.9)$$

$$2\Omega \sin(\phi)u = -\frac{1}{a} \frac{\partial \Phi}{\partial \phi} \quad (4.10)$$

$$\frac{\partial \Phi}{\partial z} = \frac{RT}{H} \quad (4.11)$$

$$i\omega T + \frac{HN^2}{R}w = -\alpha T \quad (4.12)$$

$$\frac{1}{a \cos(\phi)} \frac{\partial}{\partial \phi} (v \cos(\phi)) + \frac{1}{\rho} \frac{\partial (w\rho)}{\partial z} = 0 \quad (4.13)$$

where \mathcal{F} denotes the EP flux divergence forcing term (see equation (4.8)), and we have assumed an $e^{i\omega t}$ time dependence in all variables ($\omega = 2\pi/360$ days). a is the radius of the earth, Ω the angular velocity of the earth, R the ideal gas constant, and N the buoyancy frequency. From equation (4.12) we expect that the phase of T will lag that of w by

$$\tan^{-1}\left(\frac{\omega}{\alpha}\right) \quad (4.14)$$

(Sankey 1998). Further, equations (4.13) and (4.9) suggest that w , v , and \mathcal{F} will be in phase. We know from equation (4.7) that w^d is calculated from T , and we also know that downward control is calculated from \mathcal{F} , so, for the value of α that we are using (given in section 3.3), this would seem to explain the difference in phase between M calculated with w^d and M calculated using downward control (a lag of

about 25 days). However, after further investigation we don't believe this to be the case. The rest of this section explains why, and suggests an alternative explanation.

We run the model as before, taking $\Phi_0 = 1000\text{m}$ and $\mu_0 = 0$, but with α independent of height. 6 runs were computed using $\alpha = 1/(10 \text{ days})$, $1/(15 \text{ days})$, $1/(20 \text{ days})$, $1/(25 \text{ days})$, $1/(30 \text{ days})$, and $1/(35 \text{ days})$. The lags behind T_e of T , U , and $\nabla \cdot \mathbf{F}$ were considered for each run (by graphing them as a function of time, at various heights and latitudes) and the following observations were made:

The differences in time lag behind T_e of either T and $\nabla \cdot \mathbf{F}$ or T and U do *not* change as α changes. This rules out equation (4.14). Time lags in all variables increase, roughly linearly, as $1/\alpha$ is increased. For the value of α that we use in the runs of the previous section, the time lag in all fields is approximately 30 days. (This is approximate since the lag is dependent on height and latitude. Also no clear seasonal cycle is seen in $\nabla \cdot \mathbf{F}$ below the middle stratosphere.)

Thus *all* variables have, on average, a 30 day lag behind T_e (and the lag appears independent of Φ_0 and μ_0 provided that Φ_0 is large enough for a seasonal cycle to be observed). This explains the time lag of 30 days seen in M (from 30°S to 30°N) when computed using the downward control integral. It now remains to suggest why M is found to lag T_e by 60 days when computed from w^d .

Consider figure 4.8(a) showing U , T , and T_e at 100hPa and 30°N for the model run using $\Phi_0 = 800\text{m}$ and $\mu_0 = 0$. We see that, as already mentioned, U and T lag T_e by 30 days. From equation (4.7), $w^d = \alpha H(\bar{T}_e - \bar{T})/\kappa T_0$. It can be seen from figure 4.8(a) that this will lag T_e by approximately 120 days. The lag would be exactly 120 days were T a perfect sine wave (see figure 4.8(b), bearing in mind that a maximum in T corresponds to a minimum in w).

It is also the case that T_e has no seasonal cycle on the equator, thus w^d will be in phase with T here, lagging the seasonal cycle by approximately 30 days. Thus averaging from 30°S to 30°N gives a lag in M of 60 days, since the lag in w^d increases from 30 days to 120 days as we go from the equator to 30°N (or 30°S).

Finally in this section, we consider the effect of α on the size of annual average upwelling and the amplitude of the seasonal cycle in this upwelling. The results are shown at the start of table 4.3 and are calculated in the same way as those in table 4.1. We can see that upwelling appears to increase with $1/\alpha$, downward control works well in all cases, and the seasonal cycle is destroyed for too large a value of $1/\alpha$ (but until that point its magnitude is independent of α). However, this interpretation forgets the fact that altering α will alter $\nabla \cdot \mathbf{F}$. This turns out to be important. Ideally we would like to change *only* the value of α (keeping $\nabla \cdot \mathbf{F}$ fixed). We return to this in a later section.

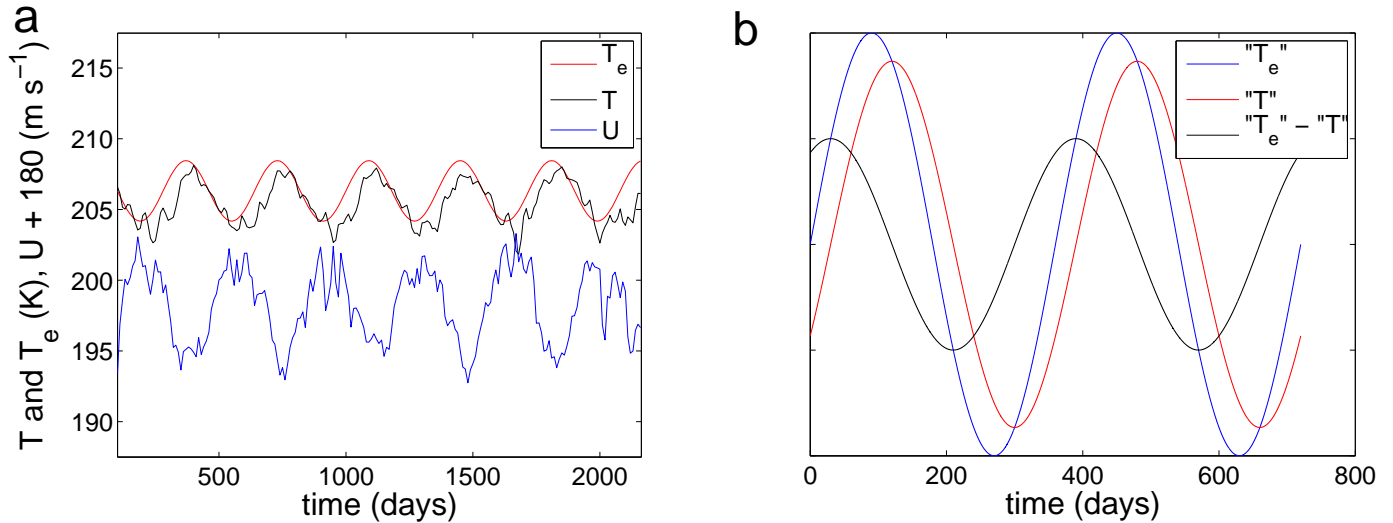


Figure 4.8:

- (a) U , T , and T_e at 100hPa and 30°N for run with $\Phi_0 = 800m$ and $\mu_0 = 0$.
 (b) Example of lag in w^d assuming T were a perfect sine wave.

4.3.3 Interannual variability

In all the above, we have only considered data averaged over all the years of a model run. However, it is important when checking that downward control does apply to make sure that it calculates the correct interannual variability in the upwelling. To this end we calculate M between 30°N and 30°S, using both downward control and w^d , for each season for years 3–6 of the model runs (i.e. 16 values for each run).

Figure 4.9(a) shows this upwelling for the run using $\Phi_0 = 800m$ and $\mu_0 = 0$. We can see that there is good agreement between M calculated with w^d and downward control. (We have used a 30 day lag for downward control and a 60 day lag for w^d , as explained above). Thus downward control (although only valid in the steady state limit) does a good job of predicting the interannual variability in the mass upwelling in the tropical lower stratosphere. Notice (from figure 4.9(b)) that when baroclinic instability is added to the troposphere (i.e. the damping of higher wave numbers is removed) downward control does not work nearly as well, and the upwelling is greatly increased. Both observations might be expected since baroclinic instability allows wave driving other than that due to Φ_0 . This motivates looking more closely at the effect of baroclinic instability on the seasonal cycle. We do this in the next section.

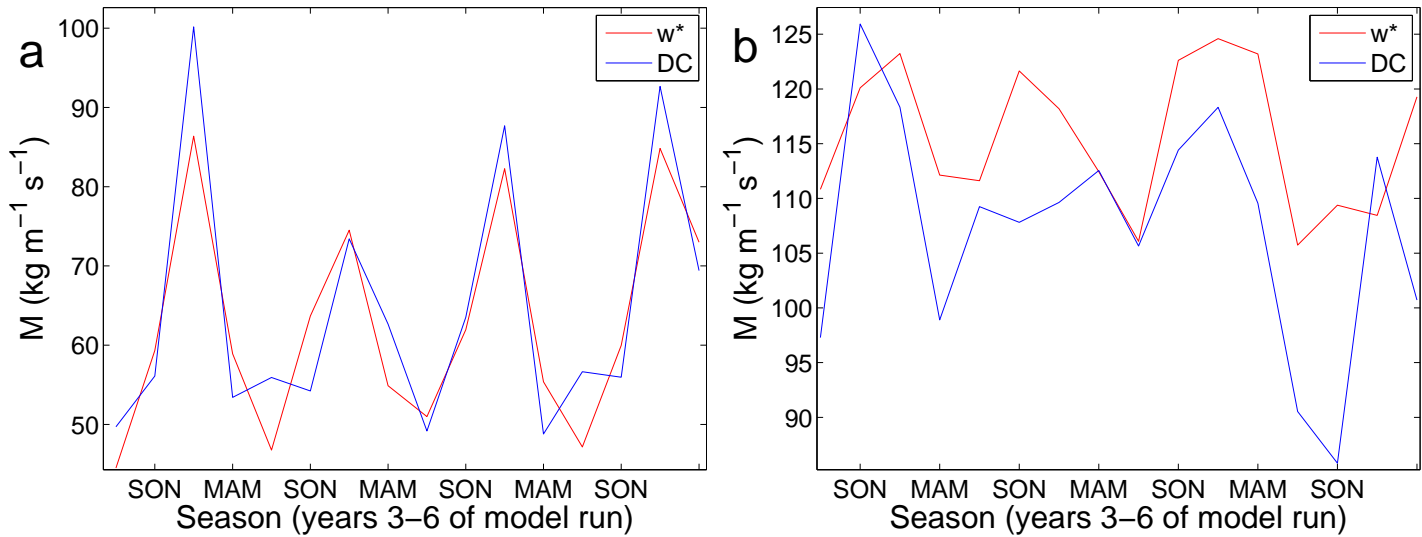


Figure 4.9:

M for the run with $\Phi_0 = 800\text{m}$ and $\mu_0 = 0$ calculated from w^d and using downward control.

(a) shows a run without baroclinic instability and

(b) shows a run with the same external parameters but including baroclinic instability.

4.3.4 Baroclinic instability

In the same way as the previous sections, but now allowing baroclinic instability to develop, model runs are computed for six 360 day years. Six runs are performed, using $\mu_0 = 0$, and $\Phi_0 = 2, 400, 600, 800, 1000,$ and 1200m . The results are shown at the start of table 4.4. (Note that the size of seasonal cycle found in the $\Phi_0 = 600\text{m}$ run is very small. There seems no good reason for this since a reasonable seasonal cycle is found for all other values of Φ_0 that were used.) The equivalent results for 3D runs with no instability (from table 4.1) are reproduced at the start of table 4.4. Comparing these two sets of results (for runs with/without instability) there are a few things to notice.

There is a large increase in the annual average upwelling. The strength of the meridional circulation has been increased by extra forcing arising due to the instability. There is a decrease in the magnitude of the seasonal cycle. This could be due to the fact that the extra forcing arising due to the instability is not restricted to the northern hemisphere. Looking at the vertical component of the EP flux entering the stratosphere (not shown), we find that it is now significantly non-zero in the southern hemisphere (with maximum values (in SH winter) about 1/3 the size of the maximum values in the northern hemisphere (in NH winter)). As in the case with no instability, the magnitude of the seasonal cycle does not depend on

Φ_0 (except in the unusual case of $\Phi_0 = 600\text{m}$ where the instability seemed to cause as much vertical EP flux generation in the southern hemisphere as in the northern hemisphere. Note that this did not happen in other runs including the run in which $\Phi_0 = 2\text{m}$ (see below)).

Running with $\Phi_0 = 0\text{m}$ the dynamics stay zonally symmetric and there is nothing to trigger the instability (thus we calculate $w^d - w_0^d$ in table 4.4 as before). However, running with $\Phi_0 = 2\text{m}$ we find the same annual average upwelling as we do with any other value of Φ_0 considered (although the magnitude of the seasonal cycle for $\Phi_0 = 2\text{m}$ is lower).

It seems odd that running with $\Phi_0 = 2\text{m}$ can produce enough difference between the hemispheres for any seasonal cycle to be seen in M . To investigate this we run the model as above but with $\Phi_0 = 400\text{m}$ in the northern hemisphere and 2m in the southern hemisphere. We also run using $\Phi_0 = 400\text{m}$ in both hemispheres. The same shape of lower boundary wave forcing is used in both hemispheres. We find no seasonal cycle in M in either run (more specifically, in the notation of table 4.4, we find a seasonal cycle of $2.7 \text{ kg m}^{-1} \text{ s}^{-1}$ and $3.5 \text{ kg m}^{-1} \text{ s}^{-1}$ respectively). Looking at the time series in M there is evidence of a semiannual cycle (not shown). This suggests that a lower boundary wave forcing of 2m is, due to causing instability, generating as much EP flux as a lower boundary wave forcing of 400m . What is perhaps more surprising is that if we run with non-zero lower boundary wave forcing (now non-zero only in the northern hemisphere) for only the first 20 days of a run (so redefining $E(t)$ given in section 3.3 such that now $E(t) = 0.5(1 - \cos(0.1\pi t))$ for $0 < t < 20$ (t in days) and 0 otherwise) we find no seasonal cycle in M either (in the notation of table 4.4, we find a seasonal cycle of $3.8 \text{ kg m}^{-1} \text{ s}^{-1}$ for $\Phi_0 = 2\text{m}$ and $-3.6 \text{ kg m}^{-1} \text{ s}^{-1}$ for $\Phi_0 = 100\text{m}$). Again a weak semiannual cycle is seen in both cases (due to the time dependence in the stratospheric part of T_e). Thus a small amount of lower boundary wave forcing must be required to cause the instability to generate larger amounts of EP flux when this is allowed by the stratospheric T_e profile (we know from section 3.10 that EP flux generation is influenced by the stratospheric T_e profile). Further work is required to properly understand this.

Considering again the original 6 runs described in this section, figure 4.10 shows the change in w^d due to baroclinic instability time averaged over the final 5 years of each 6 year run. The $\Phi_0 = 0\text{m}$ curve compares the $\Phi_0 = 2\text{m}$ run with instability to the $\Phi_0 = 0\text{m}$ run without. Here we can clearly see the increase in circulation (greater positive w^d at the equator and negative w^d at the pole) due to the instability, and also the shift poleward in the northern hemisphere, as Φ_0 increases, of the upwelling (corresponding to a poleward shift in $\nabla \cdot \mathbf{F}$). Also notice the double peak in w^d (not

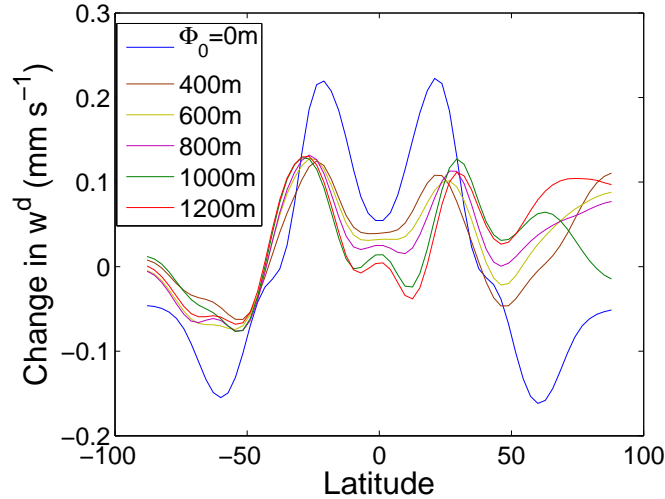


Figure 4.10:

Change in w^d due to baroclinic instability (time averaged). Line for $\Phi_0 = 0\text{m}$ compares $\Phi_0 = 2\text{m}$ run with instability to $\Phi_0 = 0\text{m}$ run without instability.

observed in the equivalent figures in Scott 2002) due to the non-zero vertical EP flux in the southern hemisphere.

The suggestion (confirmed in the next section) that, although no longer dominated by Φ_0 , the seasonal cycle is still driven by $\nabla \cdot \mathbf{F}$, suggests that downward control should still hold (although only approximately since this is not steady state). We see from figure 4.11, calculated in the same way as figure 4.7, that there is still a reasonable correlation between M calculated with w^d and M calculated using downward control. However, it is not as high as it was in the absence of instability. It is likely that, with baroclinic instability included in the runs, the extratropical stratospheric $\nabla \cdot \mathbf{F}$ is not the only wave forcing contributing to the seasonal cycle (although forcing is wave 1, instability will produce higher wavenumbers which will not propagate in the vertical so much). Kerr-Munslow and Norton (2006) suggest that tropical tropospheric forcing may be important. Although we suggest a dominant contribution from extratropical stratospheric wave forcing (exactly where will be discussed in the next section), tropospheric contributions could explain the lower correlation seen in figure 4.11. (Here we use 30 day lags in M calculated from downward control, and 60 day lags in M calculated from w^d as before, since the addition of baroclinic instability does not alter these time lags).

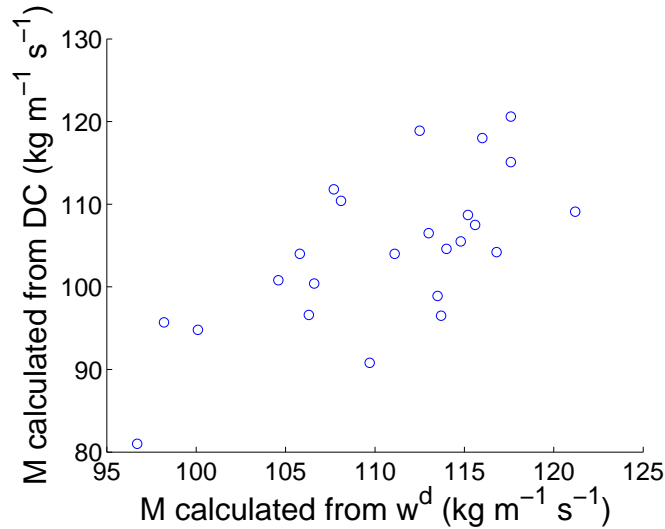


Figure 4.11:

Same as figure 4.7 but for runs including baroclinic instability.

4.3.5 2D model

In order to analyse further the effect of wave forcing, baroclinic instability, the seasonal cycle in the temperature field, and the radiative relaxation time, $1/\alpha$, on the seasonal cycle in M , we need the ability to alter parameters in the model without the indirect changes to $\nabla \cdot \mathbf{F}$ that such alterations will inevitably cause in a fully 3D mechanistic circulation model. To this end the model is run in zonally symmetric mode – in other words we truncate everything from wave 1 upwards, only keeping the zonally symmetric dynamics. Thus the model cannot generate EP flux (and we set the wave 1 forcing amplitude, Φ_0 to 0). The EP flux divergence field from a 3D model run is added to the rhs of the horizontal momentum equation for U . Thus we can run this zonally symmetric model with the same $\nabla \cdot \mathbf{F}$ forcing as that in the 3D models and consider other effects, for example the value of α , on the seasonal cycle in M . We refer to this zonally symmetric setup as the 2D model. Relaxation to the same time varying T_e profile as above is included in the model. Model runs are, again, over six 360 day years. From now on we always use $\mu_0 = 0$ in the lower boundary wave forcing.

There were a couple of technical points about applying $\nabla \cdot \mathbf{F}$ to the 2D model that needed to be dealt with. The 3D model was set to output diagnostic fields every 10 days (although running with a time step of 15 minutes). Thus these fields had to be interpolated (at 15 minute intervals between each 10 day time interval) for use in the 2D runs. It is also the case that the vertical gradient of potential temperature fluctuates close to 0 in the lower model levels causing sharp spikes in

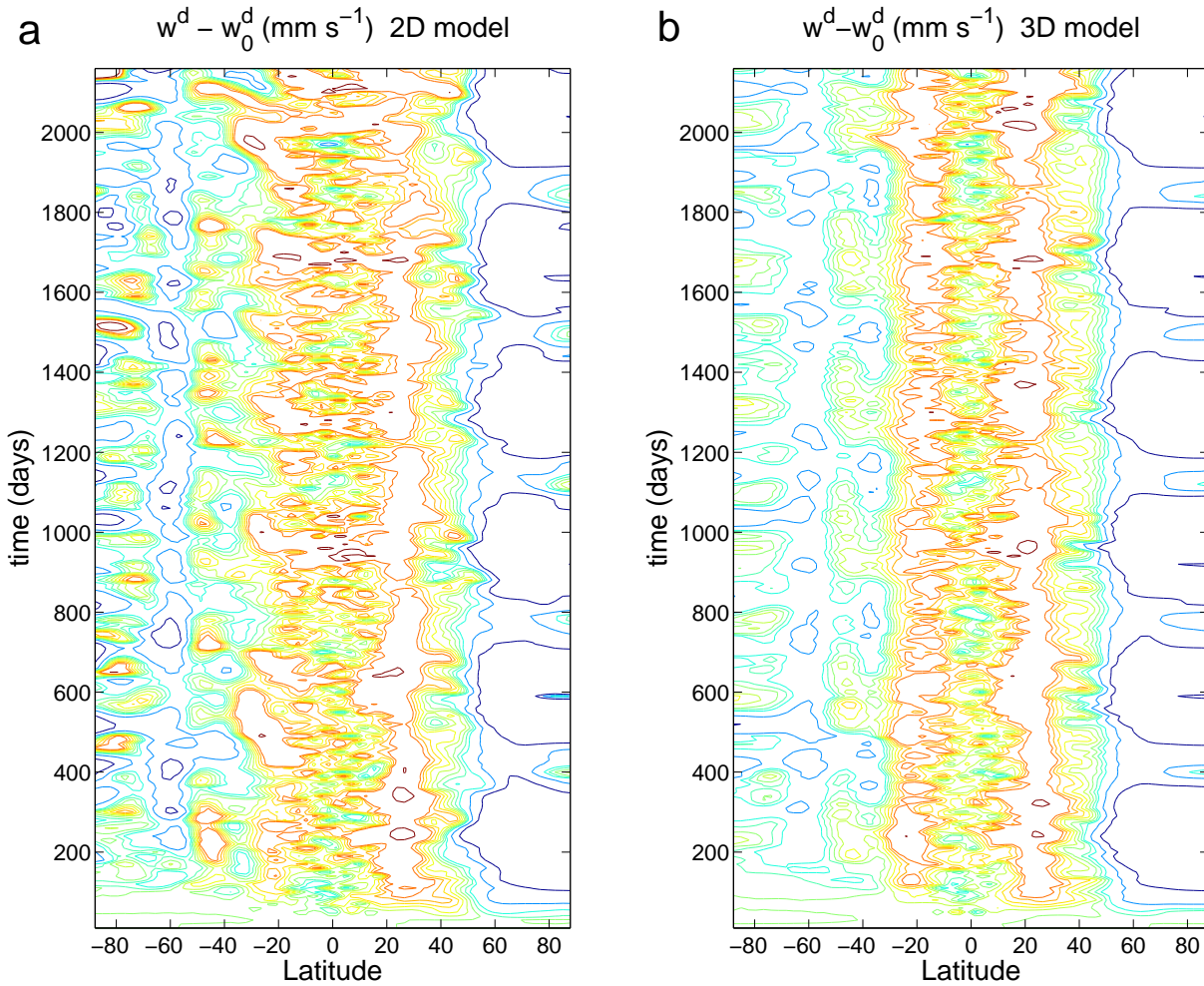


Figure 4.12:

The wave driven part of w^d (given by $w^d - w_0^d$) (mm s^{-1}) at 100hPa for both (a) 2D, and (b) 3D runs using $\Phi_0 = 800\text{m}$ (2D run (a) uses EP flux from 3D run (b)). Contours are $[-0.2, -0.1, -0.04, -0.02, 0, 0.02, 0.04, 0.06, 0.08, 0.1, 0.2]\text{mm s}^{-1}$

$\nabla \cdot \mathbf{F}$ which had to be smoothed using time and space averaging. Even so, tests were done comparing the wave driven part of the circulation in 2D model runs with that of the corresponding 3D run, and the 2D model circulation was found to be close to that of the 3D model (see figure 4.12).

A series of experiments were run with this 2D model. The first experiment concerns discovering in which area, in a height–latitude plane, $\nabla \cdot \mathbf{F}$ contributes most importantly to the seasonal cycle in M . This involved running the 2D model using the EP flux divergence of a 3D model, interpolated and smoothed as described above, to carry out two sets of runs. In the first, the EP flux divergence was set to zero poleward of a certain latitude, ϕ_c , and in the second it was set to zero

Table 4.3:
 M ($\text{kg m}^{-1} \text{s}^{-1}$)

	$1/\alpha$ (days)					
	5	10	15	20	25	30
3D runs						
Average upwelling ($w^d - w_0^d$)		61.7	63.9	69.9	72.5	74.4
Average upwelling (DC)		62.2	64.4	70.6	77.2	82.1
Size of SC		47.3	42.5	48.5	21.8	0.3
2D runs						
$\Phi_0 = 1200\text{m}$						
Average upwelling ($w^d - w_0^d$)	87.2	77.9	75.6	74.8	73.3	72.0
Size of SC	39.9	41.9	37.8	36.1	34.3	30.4
$\Phi_0 = 800\text{m}$						
Average upwelling ($w^d - w_0^d$)	78.7	69.2	66.3	64.4	62.7	60.9
Size of SC	30.6	32.7	35.1	35.2	35.3	34.6

above a certain height, z_c . We used $\nabla \cdot \mathbf{F}$ from 3D runs with $\Phi_0 = 1200\text{m}$ and $\Phi_0 = 800\text{m}$ to check that the same results were obtained in both cases. We compute the annual average upwelling and magnitude of the seasonal cycle, from the w^d of the 2D model runs, in the same way as before. The results are shown in table 4.5. We can quite clearly see that both the magnitude (and well defined cycle (pictures not shown)) of the seasonal cycle and the size of mean upwelling increase dramatically when including forcing between 20° – 40° in the first set of runs, and 15 – 30km in the second set of runs. Thus we conclude that it is the EP flux divergence in the subtropical lower stratosphere that has the most important influence on the seasonal cycle of mass upwelling in the tropics (via the downward control mechanism, already shown to apply).

Consider now the beginning of table 4.4 (comparing the results from the 3D runs to those of the 2D runs using the EP flux divergence field of the 3D runs (the 2D ‘normal runs’)). We can see that all the conclusions about runs with baroclinic instability made in the previous section carry over to the 2D case in which the *only* difference in the model runs is the EP flux divergence field supplied. The average upwelling increases, the magnitude of the seasonal cycle decreases, and both are independent of Φ_0 for runs including baroclinic instability. Thus the change seen in the seasonal cycle is due to the contribution to the EP flux divergence arising from the instability.

How large is the contribution of the seasonal cycle in the relaxation temperature field, T_e , to the seasonal cycle seen in M ? To answer this question the 2D model

Table 4.4:
 M (kg m⁻¹ s⁻¹)

	Φ_0 (m)					
	2	400	600	800	1000	1200
3D runs						
No instability						
Average upwelling ($w^d - w_0^d$)		50.9	56.5	62.1	68.0	70.7
Size of SC		18.6	33.3	34.6	29.6	32.3
Baroclinic instability						
Average upwelling ($w^d - w_0^d$)	109.3	111.4	113.6	111.6	104.8	103.8
Size of SC	8.1	13.8	2.0	10.1	18.3	13.3
2D runs						
Normal runs						
No instability						
Average upwelling ($w^d - w_0^d$)		51.0	55.4	63.4	70.9	73.8
Size of SC		15.7	24.7	36.3	38.2	34.4
Baroclinic instability						
Average upwelling ($w^d - w_0^d$)	100.7	103.8	107.5	105.8	101.4	100.5
Size of SC	7.9	11.6	1.7	10.6	17.4	14.2
Global T						
No instability						
Average upwelling ($w^d - w_0^d$)		49.8	54.7	62.7	69.9	73.0
Size of SC		15.6	24.4	35.2	36.6	32.9
Baroclinic instability						
Average upwelling ($w^d - w_0^d$)		102.9	105.9	104.7	100.3	99.1
Size of SC		11.6	1.1	10.1	14.8	13.2
No friction						
No instability						
Average upwelling ($w^d - w_0^d$)		52.2	57.5	65.3	72.5	75.9
Size of SC		15.4	25.4	36.4	38.7	35.3
Baroclinic instability						
Average upwelling ($w^d - w_0^d$)		105.7	108.4	107.6	103.5	102.8
Size of SC		12.9	1.7	10.7	17.5	15.3
New α						
No instability						
Average upwelling ($w^d - w_0^d$)		40.4	44.2	50.8	57.0	60.2
Size of SC		8.6	19.0	27.6	26.4	22.7
Baroclinic instability						
Average upwelling ($w^d - w_0^d$)		89.5	92.2	89.6	84.3	83.9
Size of SC		10.4	-0.5	6.7	12.3	9.4
New climate T_e (direct)						
No instability						
Average upwelling ($w^d - w_0^d$)		50.9	55.6	63.3	70.6	74.1
Size of SC		14.4	24.0	36.2	35.9	34.2
New climate T_e (indirect)						
No instability						
Average upwelling ($w^d - w_0^d$)		45.6	52.6	60.4	65.8	71.3
Size of SC		6.8	21.8	12.5	36.6	32.2

Table 4.5:
 M ($\text{kg m}^{-1} \text{s}^{-1}$)

ϕ_c	20°	30°	40°	50°	60°	70°
$\Phi_0 = 1200\text{m}$						
Average upwelling ($w^d - w_0^d$)	12.9	39.2	65.6	72.0	73.3	74.1
Size of SC	0.6	5.6	25.2	32.4	34.3	34.2
$\Phi_0 = 800\text{m}$						
Average upwelling ($w^d - w_0^d$)	11.2	34.3	56.7	60.4	62.8	63.3
Size of SC	2.2	8.7	22.4	31.7	35.6	36.4
z_c	10km	15km	20km	30km	40km	50km
$\Phi_0 = 1200\text{m}$						
Average upwelling ($w^d - w_0^d$)	2.5	3.5	47.8	66.1	71.2	73.8
Size of SC	1.8	0.9	14.3	27.4	33.5	34.7
$\Phi_0 = 800\text{m}$						
Average upwelling ($w^d - w_0^d$)	1.9	2.3	40.2	56.2	60.5	63.3
Size of SC	-1.1	1.7	13.9	27.1	35.0	36.3

is run using the same EP flux divergence fields as before, but now relaxing to a time independent T_e given by the annually averaged temperature field, T_{global} . By computing

$$T_{\text{global}} = \frac{1}{\pi} \int_0^\pi T_{\text{summer}} \frac{1 + \cos 2\theta}{2} + T_{\text{winter}} \frac{1 - \cos 2\theta}{2} d\theta$$

(see equations (4.4) and (4.5)) we find that $T_{\text{global}} = (T_{\text{summer}} + T_{\text{winter}})/2$. The results from running with $T_e = T_{\text{global}}$ are shown under the heading ‘Global T’ in table 4.4. It can be seen from the results given (and is clear by looking at the time series for M , not shown) that there is very little difference, either with instability or not, in the upwelling or magnitude of the seasonal cycle caused by running with time independent T_e . This shows that, with the T_e profile we are currently using, the upwelling is driven almost completely by $\nabla \cdot \mathbf{F}$.

This is to be expected since, in both cases ($T_e(t)$ and $T_e = T_{\text{global}}$), T_e has no seasonal cycle on the equator. A difference in T is seen between the runs off the equator (which is considerable by a latitude of 30°) but M is calculated from w^d with a $\cos(\phi)$ weighting. Adding a realistic seasonal cycle to T_e in the troposphere would mean that T_e *did* have a seasonal cycle on the equator and thus we would expect to see a difference in the seasonal cycle of M in this case. We return to this point later.

As mentioned in section 3.3 a Rayleigh friction is added to the model (acting on both zonal mean and all higher wave numbers) above a height of 50km. It is

possible that this may be affecting the circulation and, due to the seasonal cycle in the stratospheric T_e profile, adding to the seasonal cycle in the upwelling mass flux in the tropical lower stratosphere. To determine what effect it is having we run the 2D model again, prescribing the same EP flux divergence as before, but with no Rayleigh friction. The results are shown in table 4.4 under ‘No friction’. We can see that setting the Rayleigh friction to zero has virtually no effect on the average upwelling (which increases by about $2 \text{ kg m}^{-1} \text{ s}^{-1}$) or the magnitude of the seasonal cycle in upwelling in the tropical lower stratosphere.

We return now to considering the effect of the radiative relaxation time scale, α , on the seasonal cycle seen in M . Recall that, in section 4.3.2, increasing the value of $1/\alpha$ appeared to increase the annual average upwelling but not affect the magnitude of the seasonal cycle (until one was no longer seen). The point was made that these experiments did not take into account the fact that changing $1/\alpha$ was inevitably changing $\nabla \cdot \mathbf{F}$ also. Using the 2D model, 12 runs are computed using the EP flux divergence taken from 3D runs in which $\Phi_0 = 800\text{m}$ or 1200m with no baroclinic instability. Values of 5, 10, 15, 20, 25, and 30 days are used for $1/\alpha$ which is taken to be constant (independent of height and latitude) as in section 4.3.2. This enables us to look at the effect of the value of $1/\alpha$ on M without altering $\nabla \cdot \mathbf{F}$ (2 values of Φ_0 are used to ensure that the conclusions are robust).

The results are shown in table 4.3. As $1/\alpha$ increases the average upwelling decreases. To explain this decrease in the upwelling we follow Haynes et al. 1991 (their equation (3.2)) and eliminate u , v , and Φ from equations (4.9) to (4.13) to give

$$\frac{\partial}{\partial \phi} \left[\frac{\partial(N^2 w)}{\partial \phi} \frac{\cos \phi}{\sin^2 \phi} \right] + 4a^2 \Omega^2 \cos \phi \frac{\partial}{\partial z} \left[\frac{1}{\rho} \frac{\partial(w\rho)}{\partial z} \right] = 2a\Omega \frac{\partial}{\partial \phi} \left[\frac{\cos \phi}{\sin \phi} \frac{\partial F}{\partial z} \right] - \frac{R}{H} \frac{\partial}{\partial \phi} \left[\frac{\cos \phi}{\sin^2 \phi} \frac{\partial(\alpha T)}{\partial \phi} \right] \quad (4.15)$$

(this holds for general $\partial/\partial t$ without assuming $e^{i\omega t}$ time dependence.)

Hence we can view the forcing on w as split into two parts – one due to the EP flux divergence, and one due to radiative cooling which is proportional to α . This second contribution will become small as $1/\alpha$ becomes large. Hence, as $1/\alpha$ increases, the size of upwelling will decrease like α , tending to a value due to the EP flux divergence forcing term (for α independent of ϕ). This is indeed what we see. (Note that in the limit of $\alpha = 0$ the solution cannot be steady.)

Consider now a more realistic value for α . The value $\alpha = [1.5 + \tanh((z - 35)/7)] \times 0.0864 \text{ days}^{-1}$ has been used in all the above (except cases of constant α). Considering the profile for α shown in Randel et al. (2002) and Kiehl and

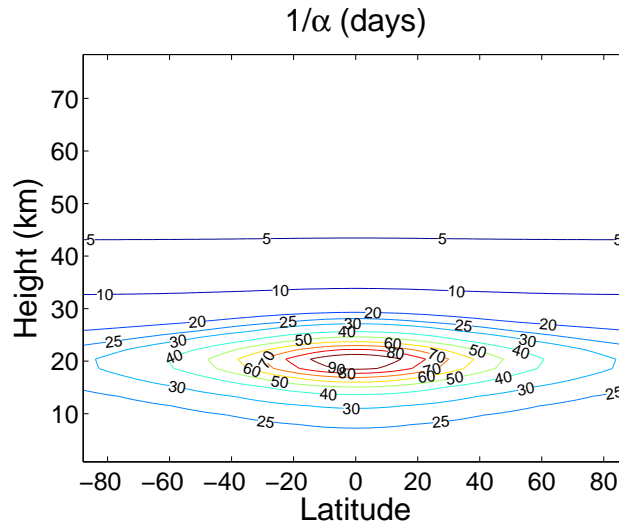


Figure 4.13:

New, more realistic, profile for $1/\alpha$, allowing for the long radiative time scales observed in the tropical lower stratosphere.

Solomon (1986), modify this so that now $\alpha = 1/(1/(0.0864[1.5 + \tanh((z - 35)/7)]) + 78\text{sech}(0.35(z - 20))\text{sech}((0.035\pi/180)\phi))\text{days}^{-1}$ (where units for z are km and units for ϕ are radians). This new profile for α is shown in figure 4.13. It simulates an increased relaxation time in the tropical lower stratosphere.

The 2D code is run with this value of α using EP flux divergence fields from 3D runs, with and without instability, using $\Phi_0 = 400, 600, 800, 1000,$ and 1200m (again using the original 3D runs so that only α will change and not $\nabla \cdot \mathbf{F}$). The results are shown in table 4.4 under the heading ‘New α ’. In both cases where instability is damped and allowed to develop we find the same behaviour. It can be seen that the average upwelling is slightly reduced, but that the magnitude of the seasonal cycle in M is greatly reduced (roughly from $35 \text{ kg m}^{-1} \text{ s}^{-1}$ to $25 \text{ kg m}^{-1} \text{ s}^{-1}$ in the case of no instability, and $15 \text{ kg m}^{-1} \text{ s}^{-1}$ to $10 \text{ kg m}^{-1} \text{ s}^{-1}$ in the case of instability).

However, if we look at the seasonal cycle in the tropical temperature perturbation we see an *enhanced* seasonal cycle. (The tropical temperature perturbation is calculated by (using the final 5 years of a 6 year run) removing the time averaged temperature from T at each height and latitude, to give T' , and then calculating $\int_{-30^\circ}^{+30^\circ} T' \cos(\phi) d\phi / \int_{-30^\circ}^{+30^\circ} \cos(\phi) d\phi$). Figure 4.14 shows this for the run using $\Phi_0 = 1200\text{m}$ and no baroclinic instability. Notice that the seasonal cycle in the tropical temperature perturbation penetrates to lower altitudes with the new, increased, value of $1/\alpha$ (this is not true for the seasonal cycle in M). Averaging T' from -10° to 10° rather than -30° to 30° gives the same results.

The decrease in the seasonal cycle for w^d even though the seasonal cycle in T

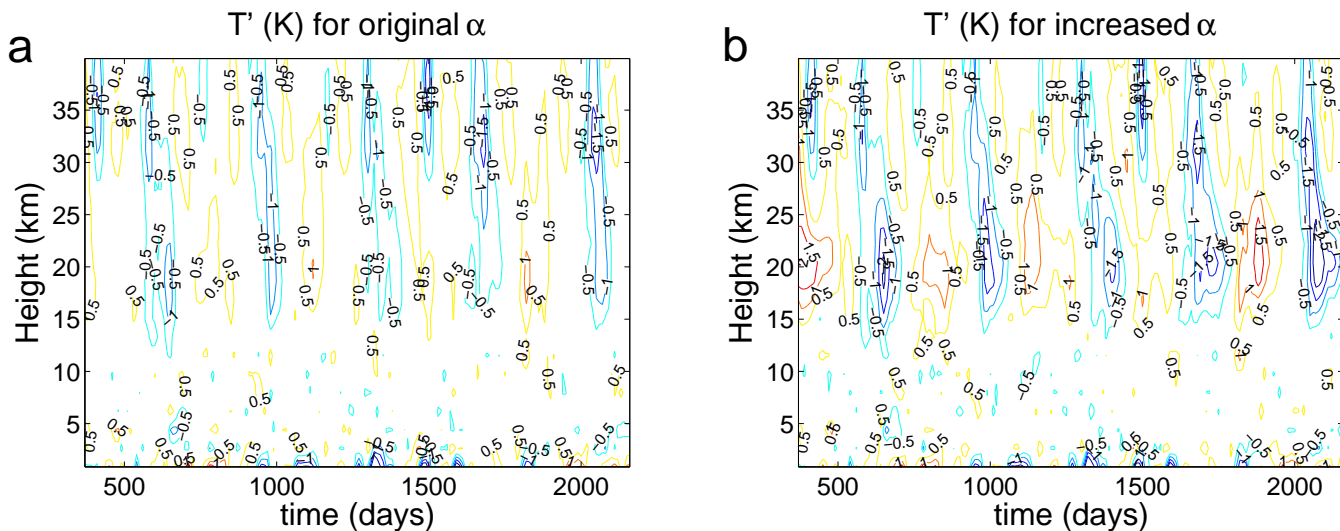


Figure 4.14:

Seasonal cycle in tropical temperature perturbation (defined in text) with (a) original value of α and, (b) increased value of α shown in figure (4.13).

is enhanced can be explained by the fact that $w^d = \alpha H(\bar{T}_e - \bar{T})/\kappa T_0$ (equation (4.7)). The new value of α is considerably smaller in the tropical lower stratosphere (and is proportionally smaller than the new seasonal cycle in the temperature field is larger). This is demonstrated in figure 4.15 where w^d is shown (again using the 2D run in which the EP flux from the 3D code where $\Phi_0 = 1200\text{m}$ and instability is damped is used) for the last 5 years of a 6 year model run. We see that the seasonal cycle in w^d does have smaller amplitude for the new value of α (curves labelled ‘New α ’ and ‘Original α ’) but if we calculate w^d using the new temperature field (T from the run with new α) and the original value of α (curve labelled ‘New α (weighted)’), then the seasonal cycle is enhanced. (Figure 4.15 does not show M but, equivalently, shows w^d averaged from -30° to 30° in the same way as T' was above. The curve for ‘New α (weighted)’ has had $1.5 \times 10^{-4} \text{ m s}^{-1}$ removed from all values so that it overlies the other curves and the magnitude of the seasonal cycle can be easily compared.)

Note that in the steady state limit we expect upwelling to be independent of α (Haynes et al. 1991) thus it is reasonable to suppose that the decrease in the seasonal cycle of upwelling which we see with this ‘New α ’ is due to time dependent effects.

4.3.6 Tropospheric seasonal cycle in T_e

In all work so far, there has been a seasonal cycle in T_e only in the stratosphere. However, in the real atmosphere there is a seasonal cycle in T in the troposphere.

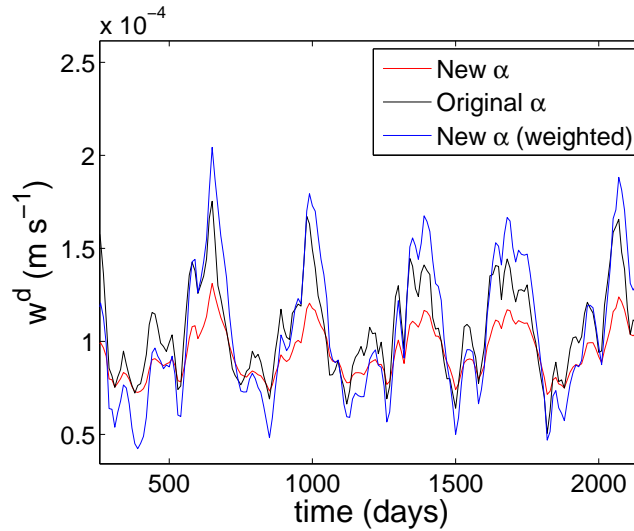


Figure 4.15:

Seasonal cycle in w^d (averaged from 30°S to 30°N) at 100hPa. Run shown uses $\Phi_0 = 1200\text{m}$ and has no baroclinic instability. Figure shows why an increased value of $1/\alpha$ in the tropics will give an increased seasonal cycle in the tropical temperature, but *not* in the mass upwelling. Full details given in the text.

Hence it is of interest to know what effect adding a seasonal cycle to T_e in the troposphere will have on the seasonal cycle in M .

We do this by modifying equation (3.5) in section 3.6, which specifies T_e in the troposphere, so that it now reads

$$T_e = T_0(z) + \frac{\Delta T(z)}{2} (\cos(2(\phi - \phi_0)) - \cos(2\phi_0)/3) \quad (4.16)$$

where

$$\phi_0 = 7.5(1 + \cos(2\pi t/360))$$

t is time in days (recall that we use 360 day years), and ϕ is measured in degrees.

This profile gives a maximum temperature at the ground centred on the equator at mid winter and at 15°N at mid summer (this follows the figures given in Randel 1992). As before, T_0 is the global mean temperature at height z .

It is the case that the magnitude of the seasonal cycle in M shown in the previous sections is not as large as that seen in Scott (2002) or in observations. This is largely because there is a very small interhemispheric difference in U and T in the troposphere leading to smaller interhemispheric difference in U and T in the lower stratosphere than is seen in Scott 2002. (Running with a stratosphere only version of the model we do find a seasonal cycle in M comparable to that in Scott 2002). We would expect a larger seasonal cycle in M using this new T_e profile.

Including this seasonal cycle in the tropospheric part of T_e will have two separate effects on the meridional circulation. One is the effect of time dependent heating which we call the direct effect. The other is the effect of a time dependent pole to equator temperature gradient which will alter the generation of EP flux, and thus alter the EP flux divergence in the stratosphere. We call this the indirect effect.

In order to separate the direct effects from the indirect effects on the annual average upwelling and the magnitude of the seasonal cycle in M we do the following in both the case of no instability and the case where baroclinic instability is allowed to develop. The full 3D code is run with the new T_e for $\Phi_0 = 400, 600, 800, 1000,$ and 1200m . Then the 2D code is run twice for each value of Φ_0 . It is run with T_e having a tropospheric seasonal cycle (hereafter denoted tsc) using the EP flux from 3D runs with no tsc, and it is run with no tsc using the EP flux from 3D runs with tsc.

We consider the direct effect to be the difference between results obtained by running the 2D model with and without tsc, in both cases using the EP flux from the 3D model with no tsc. Similarly the indirect effect is taken to be the difference between results obtained by running the 2D model with no tsc using the EP flux from the 3D model running with and without tsc. These two effects should add up to give a total effect equal to the difference between results obtained using the 3D model running with and without tsc.

The results are shown in table 4.6. Results of runs without any tsc are repeated from table 4.4 to allow easy comparison with new results but note that we now show upwelling as calculated from w^d rather than $w^d - w_0^d$ (in other words the entire upwelling rather than just the wave driven part of the upwelling). As explained above we compare the original 2D runs (under the main heading of ‘Runs without tsc’) to the 2D runs under the heading ‘Runs with tsc (3D no tsc)’ for the direct effect and ‘Runs with no tsc (3D tsc)’ for the indirect effect.

It can be seen that the direct effect of the tsc in T_e in the absence of instability is to increase the annual average upwelling by $10\text{--}15 \text{ kg m}^{-1} \text{ s}^{-1}$ (an amount which increases with Φ_0) and increase the magnitude of the seasonal cycle in M by about $13 \text{ kg m}^{-1} \text{ s}^{-1}$. The indirect effect is to increase the upwelling by about $15 \text{ kg m}^{-1} \text{ s}^{-1}$ and the magnitude of the seasonal cycle by about $20 \text{ kg m}^{-1} \text{ s}^{-1}$. These agree with the total change seen (in the 3D runs) in the average upwelling which is an increase of about $30 \text{ kg m}^{-1} \text{ s}^{-1}$ and slightly underestimate the increase of about $47 \text{ kg m}^{-1} \text{ s}^{-1}$ in the seasonal cycle.

With baroclinic instability allowed to develop the direct effect of the tsc in T_e is to increase the upwelling by about $10 \text{ kg m}^{-1} \text{ s}^{-1}$ and increase the magnitude of

Table 4.6:
 M ($\text{kg m}^{-1} \text{s}^{-1}$)

	$\Phi_0(\text{m})$				
	400	600	800	1000	1200
Runs without tsc					
3D runs					
No instability					
Average upwelling (w^d)	52.8	58.4	64.0	69.9	72.6
Size of SC	18.6	33.3	34.6	29.6	32.3
Baroclinic instability					
Average upwelling (w^d)	113.3	115.5	113.5	106.7	105.7
Size of SC	13.8	2.0	10.1	18.3	13.3
2D runs					
No instability					
Average upwelling (w^d)	52.9	57.3	65.3	72.8	75.7
Size of SC	15.7	24.7	36.3	38.2	34.4
Baroclinic instability					
Average upwelling (w^d)	105.7	109.4	107.7	103.3	102.4
Size of SC	11.6	1.7	10.6	17.4	14.2
Runs with tsc					
3D runs					
No instability					
Average upwelling (w^d)	86.9	90.9	96.1	100.8	100.6
Size of SC	84.6	76.9	83.8	75.6	65.7
Baroclinic instability					
Average upwelling (w^d)	111.8	112.8	112.7	114.6	110.3
Size of SC	19.2	21.7	33.4	23.1	36.0
2D runs					
Runs with tsc (3D no tsc) No instability					
Average upwelling (w^d)	61.2	67.5	76.4	86.1	89.2
Size of SC	17.4	33.7	56.7	52.6	53.4
Baroclinic instability					
Average upwelling (w^d)	119.2	124.8	119.0	112.2	111.2
Size of SC	39.3	37.7	27.7	27.1	22.9
Runs with no tsc (3D tsc) No instability					
Average upwelling (w^d)	68.7	74.9	81.3	87.1	88.3
Size of SC	44.3	42.0	57.4	54.0	48.7
Baroclinic instability					
Average upwelling (w^d)	88.5	89.7	89.4	91.5	88.6
Size of SC	11.4	10.2	27.5	15.6	29.9

the seasonal cycle in M by about $15 \text{ kg m}^{-1} \text{ s}^{-1}$. The indirect effect is to decrease the upwelling by about $15 \text{ kg m}^{-1} \text{ s}^{-1}$ and increase the magnitude of the seasonal cycle by about $8 \text{ kg m}^{-1} \text{ s}^{-1}$. These roughly agree with the total change seen (in the 3D runs) in the average upwelling, which is no change, and slightly overestimate the increase of about $15 \text{ kg m}^{-1} \text{ s}^{-1}$ in the seasonal cycle.

Thus whilst the average upwelling seems well accounted for by the separate direct and indirect effects it may be that the magnitude of the seasonal cycle in M relies on some interaction between the two effects. Further work is needed to understand this.

It seems odd that the indirect effect of including a tsc should be to decrease the upwelling in the presence of baroclinic instability. To try and understand this we consider the streamfunctions of runs (using $\Phi_0 = 800\text{m}$) with and without tsc and with and without baroclinic instability (shown in figure 4.16(a)). Key points to note are as follows: In the absence of baroclinic instability, including a tsc greatly increases the circulation in the southern hemisphere. When baroclinic instability is present, this is already large even without a tsc. The effect of the tsc, in both cases, is a northward shifting of the upwelling (also seen in $\nabla \cdot \mathbf{F}$), and a decrease in upwelling at the equator. This is possibly due to a northward shifting of the baroclinicity by the inclusion of a tsc. Thus, looking at the difference in the mass streamfunctions between runs with and without tsc in the case of baroclinic instability (figure 4.16(b)) there is a large decrease in upwelling seen between 30°S and 30°N although there is a far smaller decrease in the overall circulation. It can be seen from figure 4.16(b) that this effect is confined to the lower stratosphere in the case of baroclinic instability (the tropopause height is 12km).

In conclusion, in the absence of instability the direct and indirect effects of including a tsc both act to increase the annual average M and the magnitude of the seasonal cycle in M . The indirect effect is slightly larger than the direct effect. In the presence of baroclinic instability, the upwelling remains roughly constant. The magnitude of the seasonal cycle does increase, largely due to the direct effect.

There is another change brought about by the tsc in T_e and that is to the time lag (behind T_e) seen in M . This is because T_e is now warmest on the equator in DJF and warmest at 15°N in JJA. We find that T is out of phase (by almost half a year) with T_e on the equator and that T lags T_e by 50–60 days at 30°N . There is a semiannual cycle in T at about 20°N (at the tropopause). (The semiannual cycle at ground level is at 7.5°N since it is imposed there. By the tropopause, the semiannual cycle in T is found at 20°N). This further complicates the lag in M (which is averaged from the equator to 30°N). $\nabla \cdot \mathbf{F}$ is affected by the lags in U and T and thus also lags

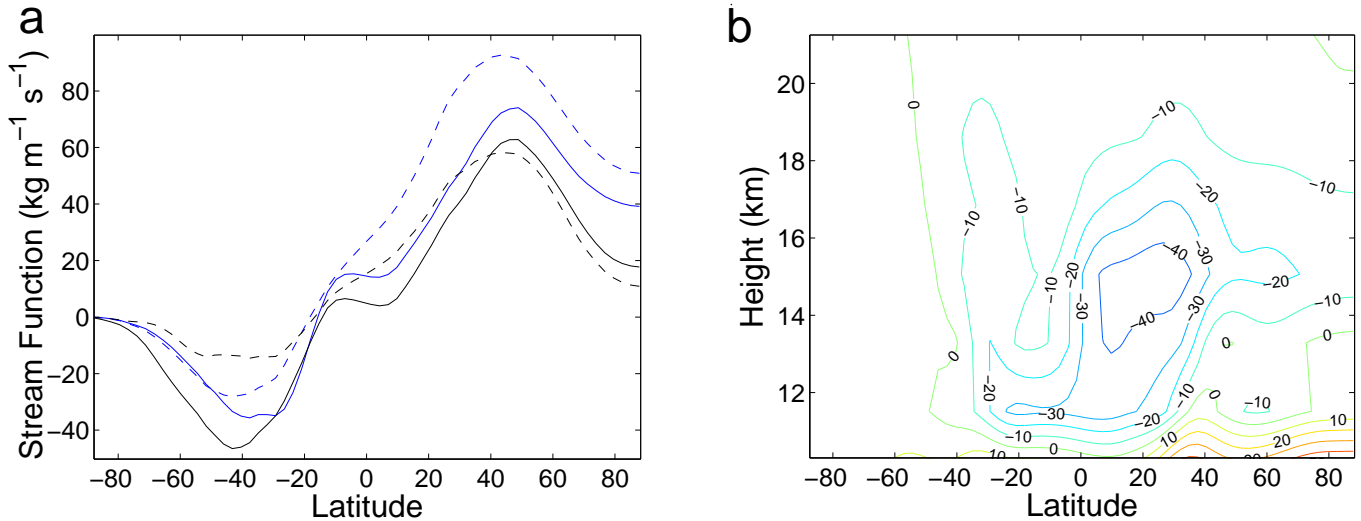


Figure 4.16:

(a) Streamfunctions at 100hPa for runs with $\Phi_0 = 800\text{m}$. Runs with baroclinic instability are shown in blue and those without are shown in black. Dashed lines are for runs with no tsc, solid lines are for runs with tsc.

(b) Difference between streamfunctions for runs with and without tsc (running with baroclinic instability allowed). Units are $\text{kg m}^{-1} \text{s}^{-1}$

T_e by a different amount than it does when there is no tsc in T_e . In the absence of instability, we find the lag in M to be about -30 days when calculated from w^d and about -70 days when calculated from downward control. The results for ‘Runs with tsc’ in table 4.6 were calculated using these lags. Further work needs to be done to properly understand these time lags, but note that M calculated from w^d still lags M calculated using downward control by about the same amount.

It is suggested in Kerr-Munslow and Norton (2006) that the annual cycle in tropical tropopause temperatures is driven by wave dissipation due in some significant part to equatorial waves. It is therefore relevant to check whether or not downward control (suggesting sub/extra tropical lower stratospheric wave driving) still predicts upwelling correctly when T_e has a seasonal cycle in the troposphere. Using the time lags just described we compute the average upwelling in separate seasons (DJF, MAM, JJA, SON) as before, for each of the 5 model runs not including instability. The 20 pairs of values obtained are shown in figure 4.17. Only the wave driven part of the circulation is considered in this figure. It can be seen that downward control still does a good job at predicting both the correct magnitude of upwelling and the correct magnitude of seasonal cycle in M despite our conclusion above that the direct effect of adding a seasonal cycle to T_e in the troposphere is significant. The fact that downward control works so well is contrary to the suggestion of Kerr-Munslow

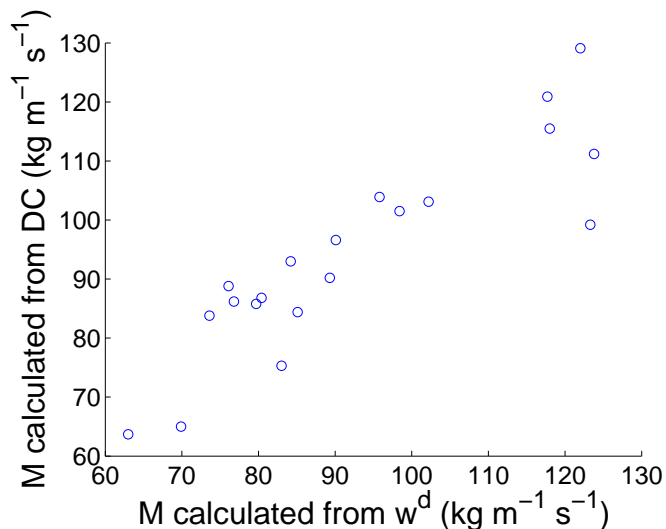


Figure 4.17:

M at 100hPa calculated for each season in each model run using w^d and downward control (as in figure 4.7 but now runs include tsc).

and Norton (2006).

4.3.7 A changing climate

At the moment our climate is changing in such a way that the tropospheric temperatures are likely to increase, and the stratospheric temperatures are likely to decrease. It is of interest to know what effect this might have on the strength of the stratospheric circulation. To this end we alter T_e by everywhere adding to it $10.5e^{-z/18} - 5.5$. This increases T_e by an amount which is 5K at the ground, decreases to 0K at the tropopause and is -5K by a height of 55km. We run the 3D code for $\Phi_0 = 400, 600, 800, 1000, 1200\text{m}$ in the absence of baroclinic instability (we run without instability throughout this section). Although the change to the circulation that this alteration to T_e has seems different for different values of Φ_0 (with the exception of U always becoming more eastward in the tropical troposphere and lower stratosphere), the annual average upwelling is always decreased by about $6 \text{ kg m}^{-1} \text{ s}^{-1}$, and the size of the seasonal cycle in M is unchanged. Thus it seems that a warming troposphere and cooling stratosphere will act to weaken the strength of the stratospheric circulation.

Cagnazzo et al. (2006) study stratospheric changes induced by ozone depletion and find decreasing ozone leads to a decrease in the strength of the stratospheric circulation. As they mention, this will lead to less ozone being transported to the high latitude lower stratosphere and thus a further cooling there giving a positive

feedback. Butchart et al. (2006) find an increase in the strength of the stratospheric circulation in response to growing greenhouse gas concentrations. Thus the response to climate change of the stratospheric circulation is complex. Here we run a dry, mechanistic model and so do not account for changes in moisture, for example, which will be brought about by a warming troposphere. We study only the effect of T_e being warmer in the troposphere and cooler in the stratosphere, in a way which is independent of latitude, and find that this leads to a decrease in the strength of the stratospheric circulation.

Using the 2D code (as in the previous two sections) we are able to separate this effect, as before, into a direct effect (caused simply by a different T_e profile, keeping the EP flux divergence fixed) and an indirect effect (using the old T_e profile in the 2D model so that only the EP flux divergence, now taken from 3D runs with the new T_e profile, is different). The results are shown at the bottom of table 4.4 under ‘New climate T_e ’ direct for runs with new T_e and old EP flux divergence field, and indirect for runs with old T_e and using new EP flux divergence field (compare to 2D ‘Normal runs’ without instability in the same table). We find that the direct effect makes no change to the annual average upwelling. The indirect effect causes the upwelling to decrease by about $4 \text{ kg m}^{-1} \text{ s}^{-1}$. Both effects cause the magnitude of the seasonal cycle in M to decrease slightly.

We conclude that a changing T_e , simulating a warming troposphere and cooling stratosphere, will decrease the strength of the stratospheric circulation due only to the change in the EP flux that this new T_e profile causes.

4.4 Conclusions

The influence of the stratosphere on the troposphere in the real atmosphere occurs under the influence of a seasonal cycle. In this chapter we have looked at the seasonal cycle of the extratropical stratosphere and also that of mass upwelling in the tropical lower stratosphere.

In the extratropical stratosphere, Yoden (1989) showed that interhemispheric differences to seasonal variability (the fact that SH winter is usually cool and undisturbed and NH winter is warmer and the polar vortex often undergoes a stratospheric sudden warming) seem reproducible by using different amounts of wave driving in the troposphere. We have shown that this remains true when using a more realistic lower boundary condition (using waves produced by topography) than was used by Yoden (1989). In the linear regime (small wave amplitude), the peaks in geopotential and EP flux seen at the beginning and end of winter could be due to a resonance

between a free travelling mode (the Lamb mode) and wave forcing from topography on the ground. In the non-linear regime it is not obvious what may be causing the resonance that gives large peaks in the geopotential and EP flux.

The cause of a seasonal cycle in the upwelling mass flux in the tropical lower stratosphere is not well understood. We have shown that the downward control mechanism seems to predict this upwelling well (in agreement with Yulaeva et al. 1994), even when used to look at interannual variability that is far from the steady state limit in which downward control is known to apply. Downward control continues to apply even when adding a seasonal cycle to the tropospheric radiative temperature profile, T_e . Further it seems that the EP flux divergence most important to this seasonal cycle is that in the subtropical lower stratosphere.

The amplitude of the seasonal cycle in M appears independent of the magnitude of lower boundary wave forcing (above a certain value of wave forcing found to be about 400m). However, the amplitude of the seasonal cycle increases as the forcing is located nearer to the equator. The annual average upwelling (an indication of the strength of the stratospheric circulation) increases with greater lower boundary wave forcing if we damp baroclinic instability. If we allow baroclinic instability to develop then the EP flux divergence is dominated by this instability and no longer depends on the amplitude of the lower boundary wave forcing.

There is a 60 day lag (behind T_e) seen in the upwelling mass flux (calculated from w^d), even though all other dynamical fields lag T_e by 30 days. The reason for this is shown to be due to how w^d is calculated. This becomes more complicated when we add a seasonal cycle to T_e in the troposphere (since this introduces semiannual cycles in T) and the lag becomes negative.

Increasing the radiative relaxation timescale ($1/\alpha$) to a more realistic value in the tropical lower stratosphere increases the seasonal cycle seen in T and the depth to which this seasonal cycle penetrates the troposphere. However the same is not true for the seasonal cycle in mass upwelling, and in fact the opposite is seen, due to the fact that w^d is proportional to α (where we expect this difference to be due to time dependent effects). Rayleigh friction (above 50km) is found to have little effect on the seasonal cycle in mass upwelling. The seasonal cycle in stratospheric temperature is also found to have little effect. However adding a seasonal cycle to T_e in the troposphere enhances both the average upwelling (when baroclinic instability is damped) and the magnitude of seasonal cycle seen.

A T_e profile that is warmer in the troposphere and cooler in the stratosphere causes a decrease in the annual average upwelling, and thus a decrease in the strength of the stratospheric circulation, due only to the change in the EP flux that this new

T_e profile causes.

In the next chapter we consider the interannual variability of mass upwelling in the tropical lower stratosphere, M , and demonstrate how that can be affected, again due to remote wave forcing, by sea surface temperatures.

Chapter 5

Links between sea surface temperatures and tropical mass upwelling

5.1 Introduction

There have been many studies on the idea that sea surface temperatures in the tropics can affect climate. For example:

Braesicke and Pyle (2004) show that sea surface temperatures (SSTs) can have an effect on the stratospheric circulation (in particular the amount of polar ozone that is present). They demonstrate that SST interannual variability leads to weakening of the winter stratospheric polar vortex, and show with simple correlations that SSTs affect UT/LS heat fluxes and hence LS temperature and stratospheric circulation.

Scaife et al. (2003) show that ENSO affects the amount of water vapour entering the stratosphere.

Manzini et al. (2006) suggests that ENSO produces persistent eddies in the troposphere which induce stationary wave 1 forcing there. This propagates vertically in the extratropics into the stratosphere, where it weakens the zonal wind and can cause the final warming of the polar vortex to occur earlier.

In this chapter we consider an ensemble of runs, described in the next section, each run differing only in the initial conditions used and, in particular, each run having the same prescribed SSTs (which are the only time dependent forcing in the model). It is discovered, by comparing runs in this ensemble, that the interannual variability in mass upwelling in the tropical lower stratosphere is fairly predictable.

This raises the question as to whether the model is artificially lacking in internal variability and, if not, why it should be predictable in the tropical lower stratosphere.

This motivates looking more carefully at the variability we see in the model runs.

In other studies there has been strong evidence to suggest that the stratosphere and troposphere exhibit significant internal variability which would be present even if all external forcings were time independent and which has long characteristic time scales (and so cannot be averaged over in any single run of only a few years length). For example Butchart et al. (2000) show that two integrations of a troposphere–stratosphere general circulation model, identical except for initial conditions, show significant differences in high-latitude wintertime temperatures on decadal timescales. One method of overcoming this problem is to use ensembles of runs to distinguish between forced and internal variability.

In this chapter we introduce a new diagnostic to quantify the importance of forced versus internal variability and show how this depends on height, latitude, and season. We present some features that are brought to light by this diagnostic and then focus on the tropical lower stratosphere.

Mass upwelling in the tropics is important since it gives perhaps the best indication of the strength of the Brewer–Dobson Circulation (BDC) of the stratosphere (responsible for the distribution of chemicals within the stratosphere). Understanding interannual and longer term variations in the BDC are important for understanding changes in the stratosphere associated with increasing greenhouse gases, and assessing the ‘recovery’ of the ozone layer as the concentration of chlorofluorocarbons starts to decrease.

We make the point, in this chapter, that the predictability seen in the tropical lower stratosphere is not simply a vertical extension of the predictability seen in the tropical troposphere but rather is due to remote forcing effected by the prescribed SSTs. We will show some diagnostics which, using the downward control principle, demonstrate a dynamic link between SSTs and the strength of the BDC.

We also consider the effect of the QBO on both mass upwelling and the difference between tropical and global temperatures in the lower stratosphere.

5.2 Model and simulations

Two five member ensembles were carried out by Reading University using the UK Met Office Unified Model (UM). The 64 level version of the UM was used with a top boundary at 0.01 hPa and horizontal resolution of 2.5° (latitude) by 3.75° (longitude). The simulations are used in Cagnazzo et al. (2006) and described in detail in Hare et al. (2004).

As is explained in Cagnazzo et al. (2006) both ensembles use sea ice and sea sur-

face temperature fields as given by the Atmospheric Model Intercomparison Project (AMIP) (Gates 1992). The SSTs are the only time dependent external forcing in the model (apart from imposed secular trends in ozone) and are the same in every run. One ensemble (the control ensemble) uses AMIPII ozone climatology, the other (the ozone ensemble) uses AMIPII ozone climatology with an imposed zonal mean linear ozone trend. The model is run for the period 1980–1999. The data we use is monthly averaged data. Usually we will annually average over the months.

Within the ensembles, the runs differ only in their initial conditions. We discard the first 3 years of each model run to allow this as spin up time, and also discard one of the control ensemble runs (leaving 4) due to an error in the data available to us.

5.3 Diagnostics of variability

In this section we develop a diagnostic to distinguish between forced variability and internal variability in any quantity. Consider a general quantity $\chi(t)$ say. We will consider data that has, for any given year, one value for each height, latitude, and quantity. This value may be averaged over a particular month, a particular season, or the whole year. Therefore t is a discrete quantity that represents the year. We denote an average over time (i.e. many time periods) by $\overline{(\)}$ and an average over all ensemble runs by $\langle(\)\rangle$.

A natural measure of total variability in time, e.g. of interannual variability, for a single realisation $\chi(t)$ is the variance $\overline{(\chi - \bar{\chi})^2}$.

We define forced variability to be that appearing in the ensemble mean $\langle\chi(t)\rangle = \phi(t)$, say. (Thus care must be taken in interpreting the word forced, since any imposed trends, or any fields which are initialised with the same value and take time to decorrelate, will add to our definition of forced variability). Hence the forced variability is measured by $\overline{(\phi - \bar{\phi})^2}$. A natural definition of the internal variability is the ensemble average total variability minus the forced variability. It is useful to note the identity

$$\overline{(\chi - \bar{\chi})^2} = \overline{(\phi - \bar{\phi})^2} + \overline{(\chi - \phi - \bar{\chi} + \bar{\phi})^2}$$

The left-hand side is the total variability and the first term on the right-hand side is the forced variability. The second term on the right-hand side is what is defined above to be the internal variability and the identity implies that this is equal to the ensemble average variability of the difference between each realisation and the ensemble mean.

The ratio

$$\mu = \overline{(\phi - \bar{\phi})^2} / \langle \overline{(\chi - \bar{\chi})^2} \rangle$$

is used as an indicator of the proportional contribution of forced variability to the total variability of χ . If there is no forced variability, i.e. if there is no variability in the ensemble mean, then $\mu = 0$. If there is no internal variability, i.e. if all realisations are identical (and hence equal to the ensemble mean), then $\mu = 1$.

5.4 Results of variability diagnostics

To get a clear picture of which parts of the atmosphere are dominated by internal variability and which are more predictable we now apply these diagnostics to the zonally averaged temperature field over the height–latitude plane. We consider annually averaged data.

Figure 5.1 (a), (b), and (c) show μ for both ensembles separately, and an ensemble average (equal to $(4/9) \times \mu$ for control ensemble + $(5/9) \times \mu$ for ozone ensemble). Notice the large difference in the ratio between the two ensembles at about 50km. This is due to the fact that temperature trends (the same in all runs) will be considered (under the definitions of the previous section) as forced variability. By fitting linear least squares lines at each height and latitude we can find the gradient (in K/month) of the temperature trend in each ensemble. This is shown in figure 5.2 and we see that, as expected, it is greatest at a height of about 50km, and considerably greater in the ozone trend ensemble. Detrending the data using these least squares lines we find that the large value of the ratio at 50km in the ozone trend ensemble no longer appears (figure 5.1 (d)). Using the detrended data, the essential features in the ratio are the same in both ensembles (not shown).

Consider figure 5.1 (a) (μ for the ensemble average of the original (i.e. not detrended) data). There are a number of points that this ratio raises:

There is a local minimum in the tropics at a height of about 35km. This might be expected due to the QBO. However when the detrended data is considered (figure 5.1 (d)), μ is fairly uniform in the tropical stratosphere. This observation may seem surprising, but is explained by figure 5.3 (which shows the square root of total variability for both the original and detrended ensemble averaged data). The total variability is much larger around the equator and at a height of about 40km. This is true of both the original and the detrended data. Thus the QBO does generate more internal variability, but appears to generate more ‘forced’ variability also. The reason for this ‘forced’ variability is that each run starts from very similar initial

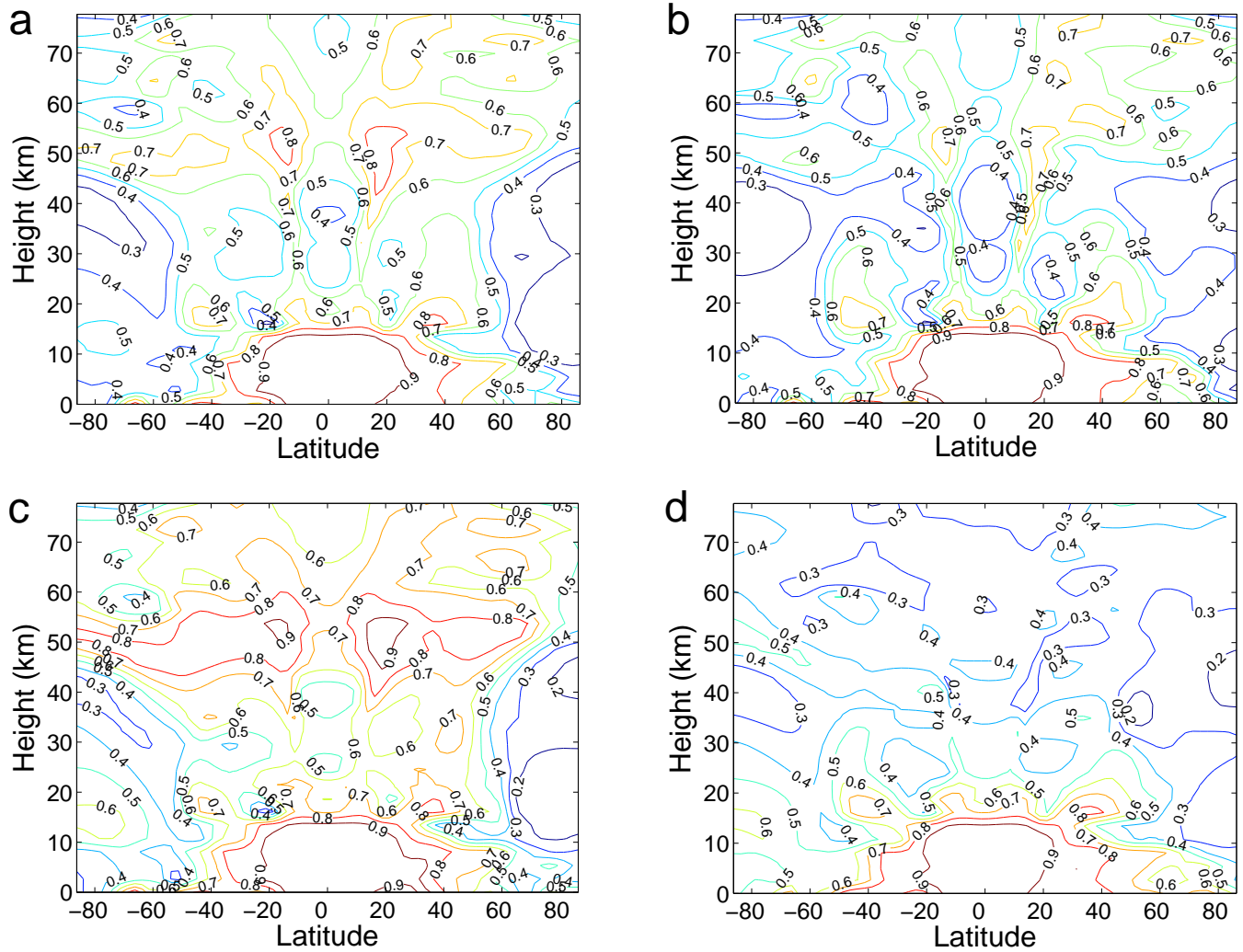


Figure 5.1:

μ , ratio of forced to total variability, showing which regions in the stratosphere are dominated by internal variability (low values) and which are more predictable (high values), applied to temperature.

- (a) Ensemble averaged data
- (b) Control ensemble
- (c) Ozone ensemble
- (d) Ensemble averaged, detrended data

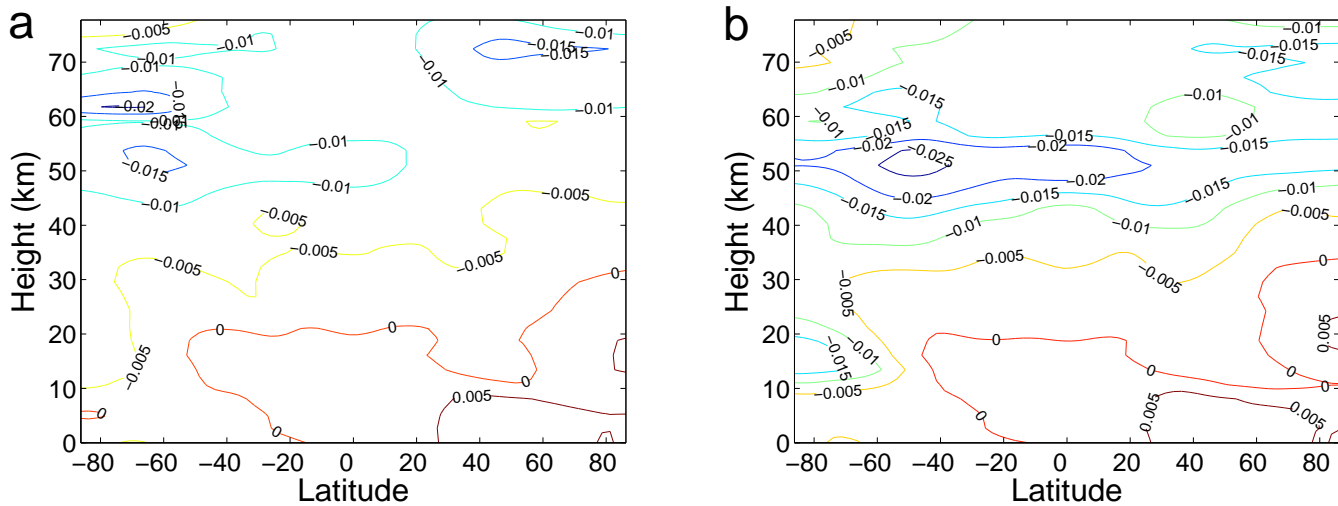


Figure 5.2:

Gradient of linear least squares fitting to temperature (K/month). Shows size of secular trend in temperature as a function of height and latitude.

- (a) Control ensemble
- (b) Ozone ensemble

conditions and, as will be seen later in the chapter, the phase of the QBO remains very predictable for the first 6 years of the runs (not counting spin up time) (i.e. it takes this long for the ensemble members to diverge from one another).

Caution should be taken, then, when interpreting our definition for ‘forced’ variability since the QBO is certainly not forced in the normal sense. It is forced in the sense that the equatorial zonal wind is set at time 0 (the same for every ensemble member) and it takes time for the ensemble members to diverge from one another.

Care must also be taken, when considering ratios, for the following reason. The signal from an imposed forcing in a given region may, for example, decay exponentially across the whole height–latitude plane. Therefore it will appear important in any region where there is very little total variability giving an unrealistically high value of μ there. This is not an issue here, however, since from figure 5.3 it can be seen that there are no regions in which the total variability is small.

Figures 5.4 and 5.5 show, respectively, μ and the square root of the total variability (in Kelvin) as applied to seasonally averaged temperature data (both figures use original data and show ensemble averaged quantities). The greatest value of total variability is, as expected, in the NH extratropics in NH winter. In the northern hemisphere, the seasonal cycle in both μ and the total variability shows that when the total variability is large, the forced variability is small, and vice versa. In the southern hemisphere things are more complicated.

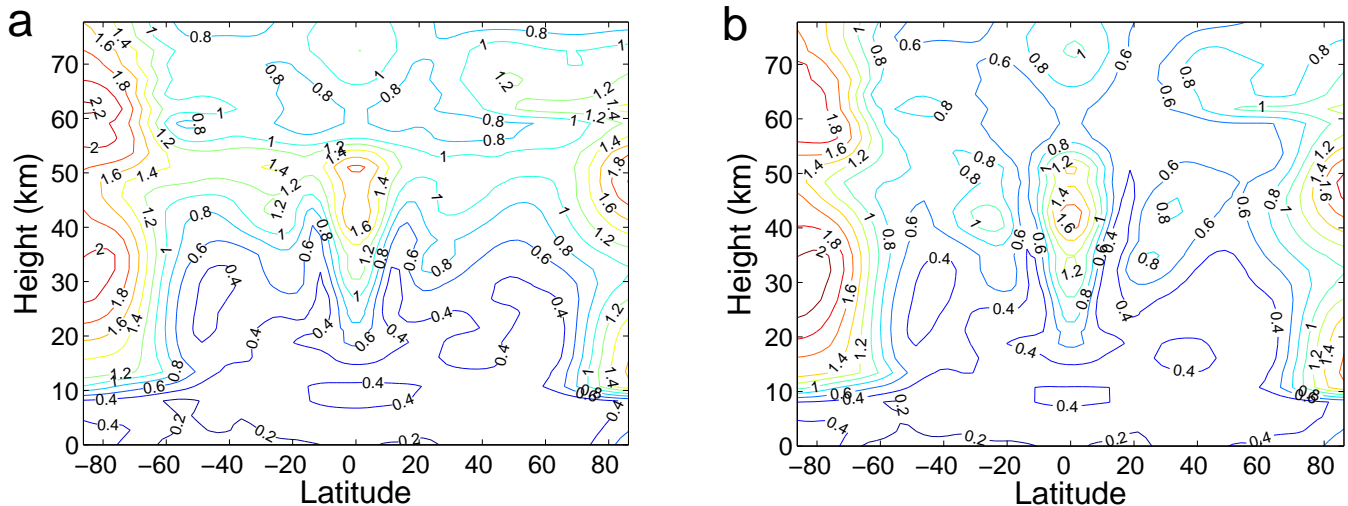


Figure 5.3:

Square root of total variability in temperature (K), ensemble averaged data.

(a) Original data

(b) Detrended data

Examining μ more closely (figure 5.1 (a)) in the lower stratosphere at a height of, say 20km, it can be seen that within the tropics the local variability is the same as the variability averaged between the turnaround latitudes (defined as the latitudes where the residual vertical velocity changes sign). This is clearly not the case in the extratropics (and the variability is less forced in the extratropics) although this seems to contradict continuity (which states that mass upwelling in the tropics is equal to mass downwelling in the extratropics). A possible explanation for this is that there is little small scale structure to the tropical upwelling but there is lots of small scale structure to the extratropical downwelling. If we integrated over the extratropics then this small scale structure would be removed.

Finally, it is important to re-emphasise the idea that the high forced variability in the tropical lower stratosphere is not simply a vertical continuation of the high forced variability in the tropical troposphere. In the next section we go on to suggest evidence that this is the case. It should be noted that this predictability is a real feature – the low values of the ratio in the extratropics show that it is not the case that the model is artificially lacking in internal variability.

5.5 Mass Upwelling

By comparing figures 5.1 (a) - (d) we can see that, focusing on the tropical lower stratosphere (the area which we shall be interested in from this point onwards),

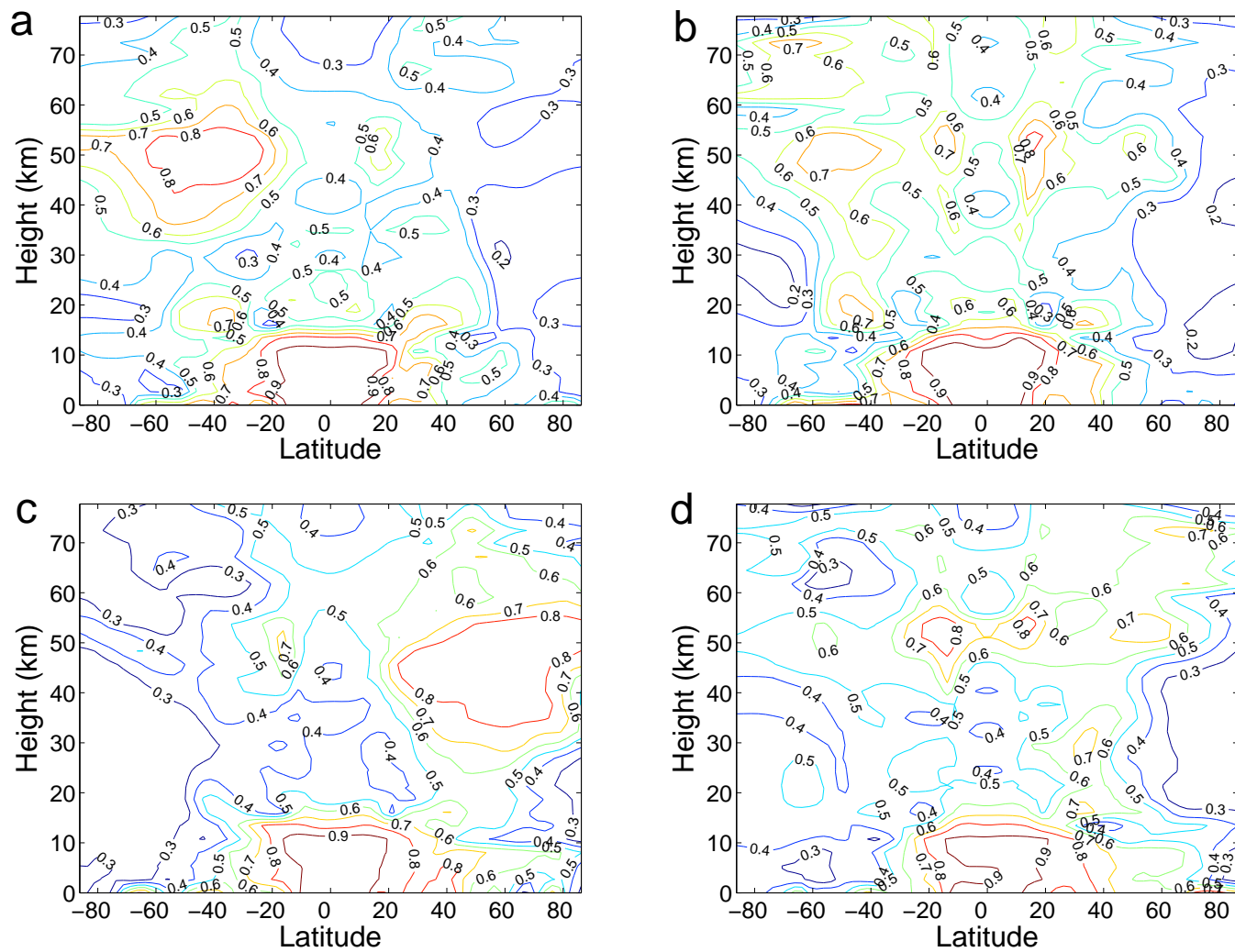


Figure 5.4:

μ applied to seasonally averaged temperature data. (Uses original ensemble averaged data).

- (a) DJF
- (b) MAM
- (c) JJA
- (d) SON

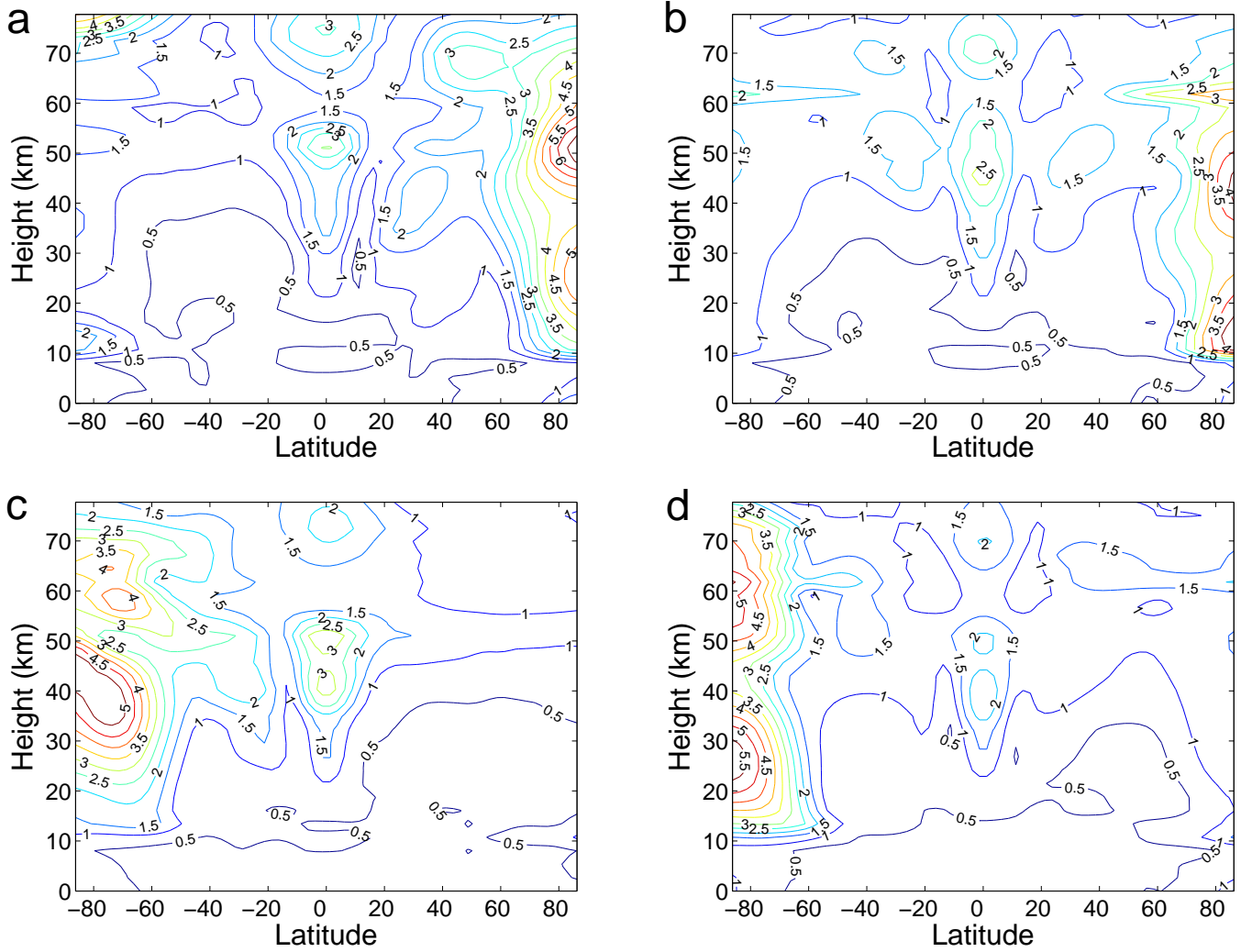


Figure 5.5:

Square root of total variability in temperature (K) for seasonally averaged data.
(Uses original ensemble averaged data).

- (a) DJF
- (b) MAM
- (c) JJA
- (d) SON

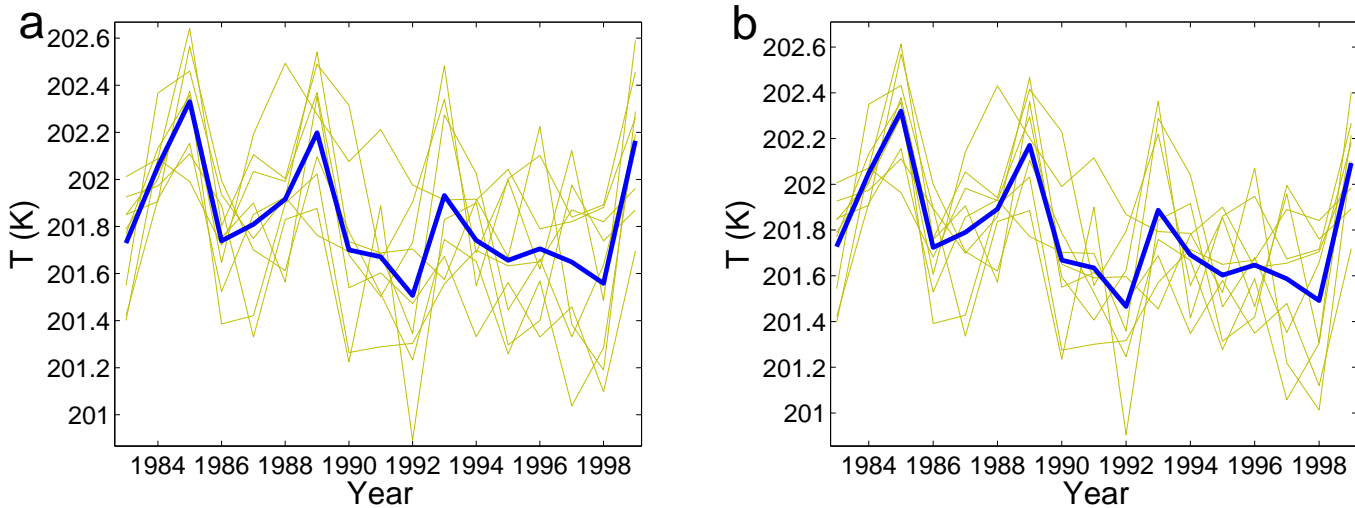


Figure 5.6:

Annual averages of area weighted temperature from 30°S to 30°N at 68hPa. Shown for all runs (yellow) and the ensemble mean (blue).

(a) Original data

(b) Detrended data

there is little difference in μ between the different ensembles or between the original and detrended data. This is made clear in figure 5.6 which shows the temperature at 68hPa, area averaged from 30°S to 30°N, for every run (the ensemble mean, i.e. ‘forced’ part of the data, is shown in blue) for both the original data (figure 5.6 (a)) and the detrended data (figure 5.6 (b)). μ applied to this data is 0.5746 for the original data and 0.5863 for the detrended data. Since there is such a small difference here, both between individual runs and between the original and detrended data, from this point onwards we deal with the ensemble averaged original data.

We consider the mass upwelling at the tropical tropopause. We are particularly interested in what affects this mass upwelling since, as mentioned above, it is perhaps the best indicator that we have of the strength of the BDC.

As already mentioned, by the BDC we mean the chemical transport circulation of the stratosphere. (By the strength of the BDC we mean the strength of this diabatic circulation, neglecting the effects of two-way mixing occurring. This strength is important to the distribution of, for example, ozone and methane within the stratosphere). By mass continuity the upwelling in the tropics that is part of this circulation will be balanced by downwelling in the extratropics, although there is small scale structure in the extratropics which must be integrated over to properly show this, as mentioned above. In particular, secondary circulations (e.g. during SSWs) can cause this downwelling to be weaker in mid-latitudes and stronger in

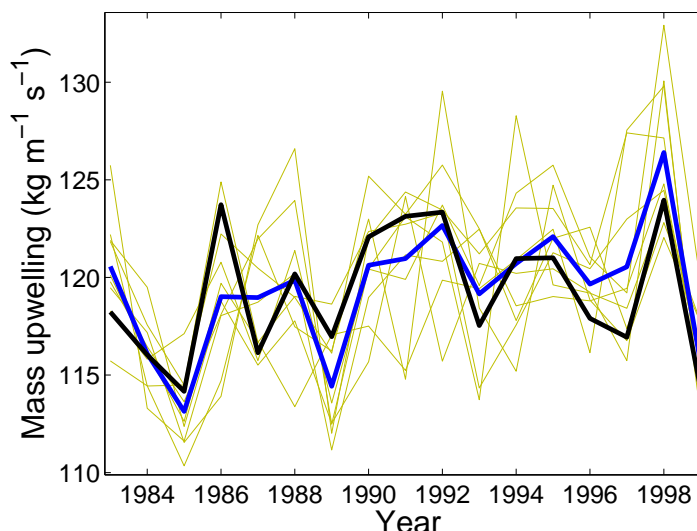


Figure 5.7:

Annual averages of total mass upwelling at the tropical tropopause shown for each of the model runs (yellow), the ensemble mean (blue), and downward control calculation (black), at 68hPa.

high latitudes. We consider this as secondary to the strength of the main BDC (and looking at seasonal means will average over this).

Mass upwelling, M , is defined (similarly to equation (4.6) in the previous chapter) as

$$M = \int \rho w^* a \cos(\phi) d\phi \quad (5.1)$$

Here, ϕ is latitude, ρ is density, a is the radius of the earth, and w^* is the TEM residual vertical velocity.

Annual averages of total mass upwelling (at the tropical tropopause) for each of the model runs are shown (yellow) in figure 5.7 (similar to figure 5.6) along with the ensemble mean mass upwelling (blue) and downward control calculation of mass upwelling (black) at 68hPa.

The important thing to notice at this stage is that the mass upwelling is indeed coherent (the value of μ applied to this data is 0.6193). The downward control curve, and its similarity with the ensemble mean, will be explained in the next section.

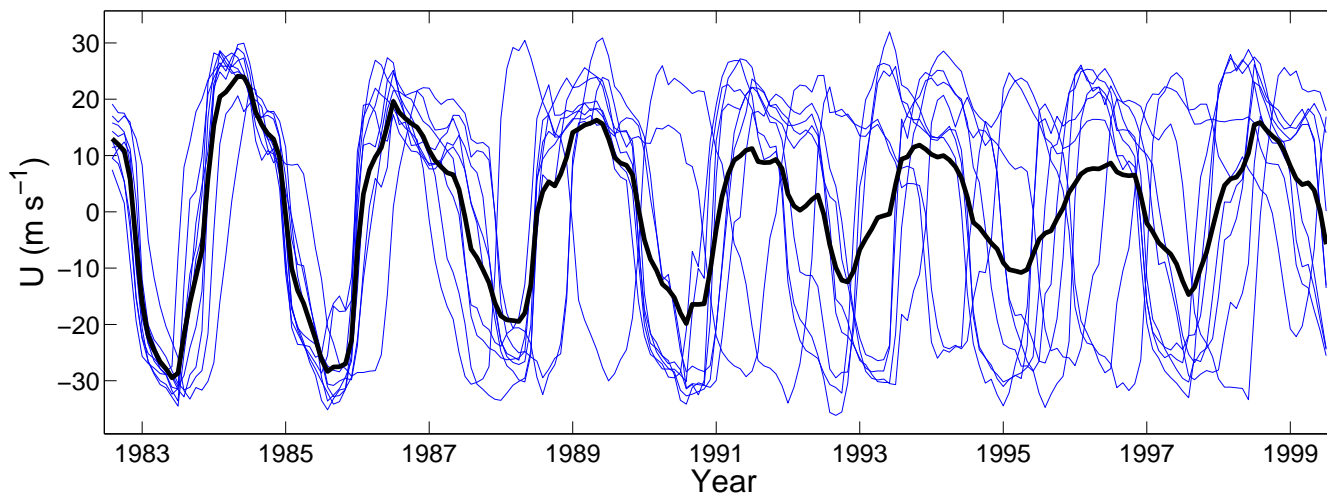


Figure 5.8:

QBO – equatorial zonal wind at 14.7hPa (individual runs shown in blue, ensemble mean shown in black)

5.6 Effect of Sea Surface Temperatures and the QBO

Having demonstrated the dominance of forced variability in the tropical lower stratosphere and the coherence of mass upwelling there, we now consider the causes of this predictability. We have already hinted that the only time dependent external forcing, the SSTs, play a role. We have also mentioned that another type of ‘forced’ (in our sense) variability is possible – the case where fields are set at day 0 and ensemble members take a long time to diverge. In the runs used here this is seen in the QBO.

It is well known that the QBO affects the upwelling in the tropics. This is because the wave-induced changes in the vertical shear $\partial U/\partial z$ must be balanced, in the thermal wind sense, by T anomalies. These in turn imply anomalies in radiative heating rates and hence in upwelling rates (Baldwin et al. 2001). For a warm temperature anomaly we get less upwelling than for a cold temperature anomaly. Figure 5.8 shows the equatorial zonal wind, U , at 14.7hPa for each of the model runs. Here the deseasoned monthly means of U are shown. Individual runs are shown in blue and the ensemble mean is shown in black.

It can be seen (as mentioned earlier), that the phase of the QBO is the same in all runs until about 6 years into the run. After that time the runs diverge although it can be seen from the ensemble mean that the phase of the QBO never becomes

completely unpredictable. (The qualitative behaviour shown in figure 5.8 persists over different model heights down to 70hPa).

It may be thought to be the case that the coherence in mass upwelling at the tropical tropopause is in part due to effects of this predictability in the QBO. After 6 years, however, the phase of the QBO is less predictable so we would expect the interannual variability in the mass upwelling to become more dominated by internal variability after that time, and this is not observed. We conclude that the QBO has a negligible effect on the upwelling. (It should be mentioned that in other studies (Hamilton 1993, Baldwin and O’Sullivan 1995) the QBO was thought to have an effect, although this effect could not be separated from that of ENSO. Although we find no obvious influence due to the QBO here it should not necessarily be discounted as unimportant.)

To be more sure that the QBO has little effect on the predictability of the mass upwelling we should compute longer runs and start all our diagnostics at year 6 once the QBO has become unpredictable. With long enough runs it is likely that any mode of low frequency variability will become unpredictable and hence have no net effect on results. This is a point for further work.

Improvements in gravity wave parametrisation schemes will also mean the need for further runs. Models without a QBO show no interannual variability in the tropics, whereas the real atmosphere has comparable interannual variability in the tropics as it does at the poles. It is believed that the gravity wave parametrisation scheme accounts for more of the QBO (and hence also the tropical internal variability) than is due to resolved wave driving (e.g. EP fluxes). It is therefore possible that the QBO may be less predictable in the real atmosphere than is suggested here (where it is predictable for 6 years). On the other hand, if gravity waves are largely driven by SSTs, which we will claim to cause a predictable response in the stratosphere, then the QBO may be more predictable than we suggest here. Again this is a point for further work.

Having ruled out the effect of the QBO in these runs, this leaves SSTs as the likely cause of coherent mass upwelling in the tropical lower stratosphere. We now suggest a mechanism by which the SSTs affect this mass upwelling. It is shown by Manzini et al. (2006) that during ENSO events, increased wave activity is seen in the extratropical stratosphere. The vertical EP flux entering the stratosphere in the extratropics is increased.

Via the downward control mechanism (Haynes et al. 1991) an increase in EP flux divergence means an increase in the meridional circulation at that latitude. Thus greater EP flux divergence will lead to a stronger circulation in the stratosphere, and

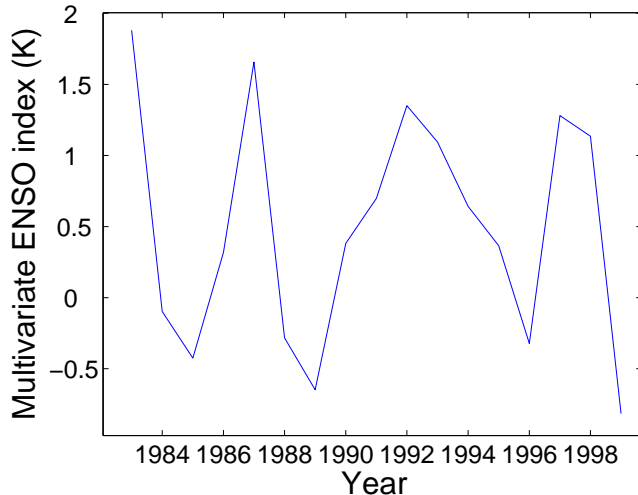


Figure 5.9:
Annually averaged multivariate ENSO index from 1983–2000

stronger mass upwelling in the tropics. We have already shown, in figure 5.7, that downward control approximates mass upwelling in the tropical lower stratosphere very well.

Evidence of the good correlation between ENSO and mass upwelling can be seen by comparing the ensemble mean mass upwelling (blue curve in figure 5.7) to figure 5.9 which shows the annually averaged multivariate ENSO index (data from the NOAA Climate Diagnostics Center website). The correlation between these two curves is 0.6350.

Since we have shown the extratropical EP flux to be crucial to mass upwelling in the tropics (via the downward control mechanism), it is of interest to know up to what altitude we must integrate the EP flux in our models to correctly calculate this mass upwelling. One way of discovering this is to look at the downward control streamfunction produced by integrating up to different altitudes and ask below what altitude the streamfunction starts to significantly change.

Working with annually averaged data we calculate the downward control streamfunction (integrated up to various heights z_c) for each year of each run, and then, for each height z_c , average over all of the streamfunctions for each year. The resulting averages for each value of z_c are shown in figure 5.10 which suggests that the EP flux up to a height of about 50km is important.

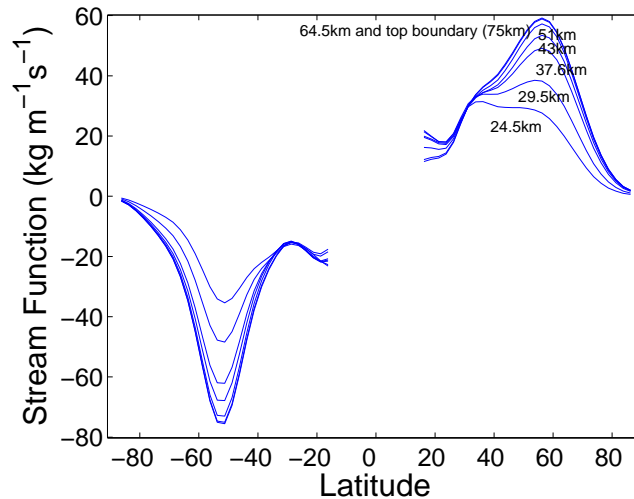


Figure 5.10:

Ensemble averaged downward control mass streamfunction (at 70hPa) calculated by integrating to different heights. The streamfunction significantly changes if we integrate only to a height below about 50km.

5.7 The global temperature

The imposed SSTs not only affect the mass upwelling, but also the global temperature at 100hPa. The global temperature is not linked to the strength of the BDC since mass continuity implies that a stronger upwelling (hence cooling) at one latitude will lead to an equally increased downwelling (hence warming) at another. This is therefore a separate effect.

We can show that the SSTs affect the global temperature since one of the ensemble runs we are using was actually run for 40 years, the SSTs prescribed in the first 20 years being identical to the SSTs prescribed in the second 20 years and taken from data for 1980–1999. Figure 5.11 shows the global temperature at 100hPa for both the first and second 20 years of this run. It is clear that SSTs are affecting the global temperature since there is good agreement between this temperature in the first and second 20 years of the model run, and it is reiterated that the only time dependent external forcing in these runs is the imposed SSTs.

We claim that the difference between global temperature which we will write as $T[-90^\circ, 90^\circ]$, and tropical temperature (i.e. between 10°N and 10°S) here written as $T[-10^\circ, 10^\circ]$, can be attributed to a combination of the phase of the equatorial zonal wind and the mean mass upwelling, M (or equivalently the residual vertical velocity w^*).

The difference between the global and tropical temperatures is split into two

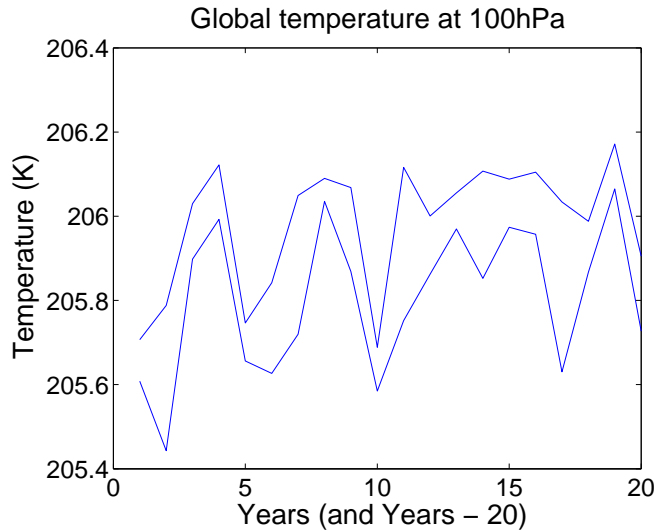


Figure 5.11:

Global temperature at 100hPa for first and last 20 years of the 40 year run. It can be clearly seen that the SSTs are affecting the 100hPa temperature field.

parts: $T[-10^\circ, 10^\circ] - T[-30^\circ, 30^\circ]$, and $T[-30^\circ, 30^\circ] - T[-90^\circ, 90^\circ]$. We suggest that the phase of the equatorial zonal wind is partly responsible for the $T[-10^\circ, 10^\circ] - T[-30^\circ, 30^\circ]$ temperature difference, and that the $T[-30^\circ, 30^\circ] - T[-90^\circ, 90^\circ]$ temperature difference can be partly explained by the size of w^* .

Here we look at temperatures, the equatorial zonal wind, and w^* all at 100hPa. We are, again, only concerned with ensemble averages (to try to eliminate internal variability).

The annual averages of $T[-30^\circ, 30^\circ] - T[-90^\circ, 90^\circ]$ and w^* are shown in figure 5.12(a). There is a clear link between the two fields. From the thermodynamic equation, assuming a steady state and Newtonian cooling, it can be seen that

$$wN^2 \frac{H}{R} \sim -\alpha(T - T_R) \quad (5.2)$$

explaining the negative correlation seen.

Figure 5.12(b) shows the equatorial zonal wind at 100hPa, and $T[-10^\circ, 10^\circ] - T[-30^\circ, 30^\circ]$. Removing the seasonal cycle from both these fields leaves just the interannual signature. This is shown in figure 5.12(c). It can be seen that there is definite agreement in the interannual variation of both fields.

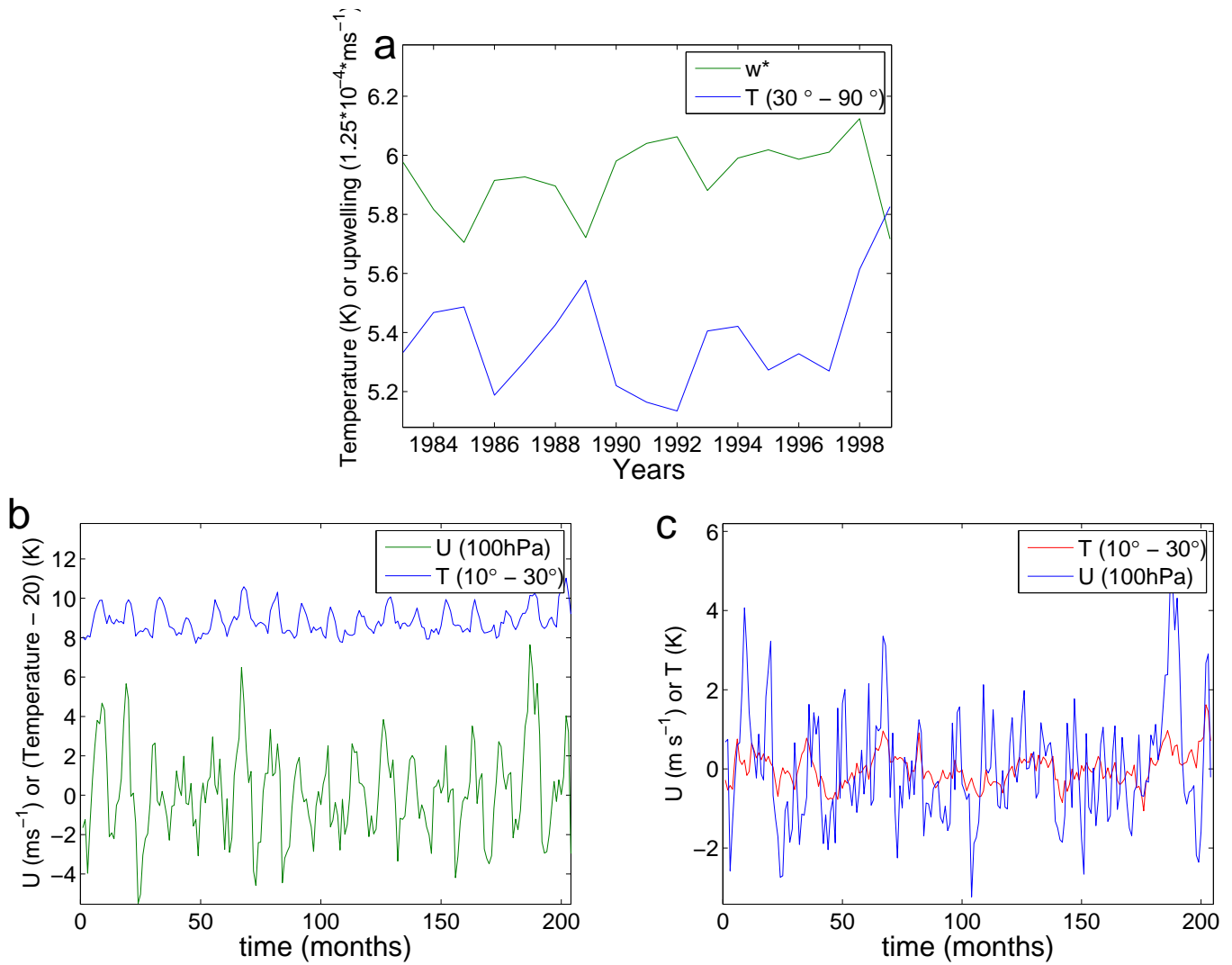


Figure 5.12:

Using ensemble and annually averaged data, figures show:

- (a) Comparison of extratropical temperature difference with w^*
- (b) Comparison of tropical temperature difference with equatorial zonal mean zonal wind
- (c) As in (b) but with seasonal cycle removed

5.8 Conclusions and Discussion

In this chapter we have considered a ratio of forced variability to total variability to show which parts of the height–latitude plane can be considered in some sense predictable, and which are dominated by internal variability. Large total variability is seen on the equator, due to the QBO, and also in the extratropical winter hemispheres. In the NH extratropics large total variability suggests small forced variability, and vice versa. Where a temperature trend was present this showed high predictability. The most noticeable feature, which we focused on, was the high predictability of the tropical troposphere and lower stratosphere. This implied a high predictability in the interannual variation of tropical upwelling and hence the strength of the stratospheric circulation.

We here make the important point that the predictability of the tropical lower stratosphere is not simply a vertical extension of the predictability of the tropical troposphere but is largely due to remote forcing. It has been shown (Manzini et al. 2006) that, during El Niño events, there is more wave activity in the extratropical stratosphere (greater vertical EP flux entering from the extratropical troposphere).

We have provided evidence to suggest that this increase in extratropical vertical EP flux drives a stronger mass upwelling in the tropics via the downward control principle. Hence we suggest that, in this way, ENSO affects the strength of the BDC of the stratosphere.

We have also suggested that the globally averaged temperature is affected by SSTs and that the difference between this globally averaged temperature and tropical temperature is related to a combination of the strength of mass upwelling and the strength of the equatorial zonal wind.

As mentioned above, further work is needed to fully understand the influence of the QBO. For the purposes of this study, however, we have shown that the QBO is predictable for the first 6 years of the model runs and thereafter is less so. No difference is seen in the predictability of the mass upwelling just above the tropical tropopause if we look only at the first 6 years of model runs, or only at the final 6 years. Therefore we conclude that the QBO has no noticeable influence here although make the comment that further runs will be necessary (perhaps over longer times and with more precise gravity wave parametrisation) before we can be certain about this.

Downward control is only exact in the steady state limit (although we have further approximated in this chapter by integrating at constant latitude). Further work could be done to check that an even better correlation between mass upwelling in the tropics and stratospheric EP flux divergence is given, for each individual

run, when using a time dependent wave solver rather than the downward control approximation.

Chapter 6

Summary and discussion

There is now plenty of evidence to suggest that the stratosphere is not passive, being driven by the troposphere, but that the stratosphere and troposphere are dynamically coupled, each influencing the other.

This leads to the need to better understand the coupled nature of the stratosphere and troposphere. In this thesis we have attempted to look at some aspects of this by considering the following questions. What are the mechanisms whereby a dynamical perturbation in the stratosphere can influence surface weather and climate? When and how would we expect to see a stratospheric perturbation have a large downward influence? What are the causes of the interhemispheric differences in the seasonal cycle, the seasonal cycle in tropical upwelling, and the interannual variability in the strength of the stratospheric circulation?

In chapters 2 and 3 we focused on the downward propagation of information through the stratosphere due to a dynamical perturbation introduced there. We suggested and investigated a new mechanism whereby dynamical perturbations introduced in the stratosphere can influence the flow lower down in the stratosphere, and thus affect the troposphere.

A perturbation, ΔU , was introduced to the zonal wind field in experiments. Using a simple 1D model it was found that the amount of downward influence from the perturbation depended on the state of the stratosphere, being greater in a vacillating than in a steady regime. The greatest downward influence was seen when the perturbation caused a transition from steady to vacillating stable states. The change, ΔU , to the mean flow required to cause such a transition scales inversely with density over the range of altitudes, z_c , at which the perturbation is applied. Non-locality of the zonal mean flow (non-zero C in equation 2.5) was found to be essential to this downward influence, and this was investigated further using a model of the QBO (in which a “group speed” was found proportional to the square root

of vertical viscosity, and a “phase speed” dependent on the buoyancy frequency \times thermal dissipation rate). The results were found not to depend qualitatively on the lower boundary or wave generation mechanism used in the 1D model.

Multiple stable states (and hence an underlying bifurcation diagram) were found to persist in a, more realistic, 3D mechanistic circulation model. Multiple states were noticeable due to a large sensitivity to initial conditions (most sensitive when initial conditions differed in the tropics) and the mechanism whereby perturbations caused a transition between stable states was manifested by their causing or preventing a stratospheric sudden warming. In agreement with the findings of Scott and Polvani (2004) it was also found that the vertical EP flux accepted by the stratosphere (and hence leaving the troposphere) depended largely on the state of the stratosphere (disturbed or undisturbed) in any particular run (true with baroclinic instability both damped and allowed to develop).

In general the experiments brought to light the sensitivity of the models and hence the need to be more precise in modelling stratospheric flow. For example: increasing the lower boundary wave forcing by 1m could cause the stable state to be vacillating rather than steady, or sensitivity to initial conditions to be seen. Increasing the magnitude of the imposed stratospheric disturbance by 1m s^{-1} , or altering the height at which this disturbance is applied, could cause a transition between states, or cause a stratospheric sudden warming when one would not otherwise have occurred. Altering the stratospheric T_e profile was shown to change the underlying bifurcation diagram. Thus the Rossby wave generation, gravity wave parametrisation scheme, and radiative equilibrium profile all have to be accurate to correctly simulate the flow in the stratosphere and hence its affect on the troposphere.

Chapters 2 and 3 consider runs under perpetual January radiative conditions. In chapters 4 and 5 we go on to consider how the stratosphere and troposphere affect each other under the influence of a seasonal cycle.

The observed interhemispheric difference in the seasonal cycle (of, for example, the evolution of the zonal wind during winter) has already been shown to be largely attributable to the difference in lower boundary wave forcing in the two hemispheres (Plumb 1989, Yoden 1989). In chapter 4 we showed that the large build up in the geopotential height anomaly which leads to SSWs (often in midwinter in the northern hemisphere) could be due to resonance between the topographically forced and the free travelling planetary waves, at least for low wave amplitudes. There appeared not to be this kind of resonance for larger wave amplitudes.

The downward control mechanism was shown to work well in predicting the seasonal cycle in tropical upwelling and, further, wave forcing between 20° and 40° at

a height of 15–30km was shown to be the most important in driving this seasonal cycle. The strength of lower boundary wave forcing was shown to be unimportant to the seasonal cycle in tropical upwelling. A larger seasonal cycle was seen for forcing centred nearer the equator. The time lag in the upwelling behind T_e (the radiative equilibrium temperature profile) was attributed to the phase difference between T_e and the tropical temperature. A more realistic radiative time scale in the tropics showed an increased seasonal cycle in the temperature, but not in the upwelling. A seasonal cycle imposed in the tropospheric radiative equilibrium temperature profile did increase both the annual average upwelling and the seasonal cycle in the upwelling. This was shown to be due both to a direct, time dependent, heating effect and to the indirect effect of altering wave generation in the troposphere. The decrease in the strength of the stratospheric circulation due to altering T_e to simulate a warming troposphere and cooling stratosphere was found to be due mainly to the indirect effect of altering wave generation in the troposphere.

The interannual variability in tropical upwelling was considered in chapter 5. A new ratio was constructed to show which parts of the height–latitude plane can be considered in some sense predictable, and which are dominated by internal variability. High internal variability was seen in the extratropics, and also in the low latitude stratosphere due to the effects of the QBO. Where a temperature trend was present this showed high predictability. The most striking feature, though, was the high predictability of the tropical troposphere and lower stratosphere. This implied a high predictability in the interannual variation of tropical upwelling and hence the strength of the stratospheric circulation. This predictability was confirmed and shown to be due to imposed sea surface temperatures, with warm temperatures causing greater planetary wave forcing in the extratropics and this, via the downward control mechanism, driving a stronger circulation. The difference between the tropical temperature and global average temperature was shown to be in part due to both the equatorial zonal wind and the strength of tropical upwelling.

The QBO appeared not to have any direct effect on the strength of tropical upwelling that we could determine. It would be useful to be able to confirm this lack of influence of the QBO on tropical upwelling with the aid of longer model runs and perhaps improved gravity wave parametrisation schemes.

The consideration of the effects of the stratosphere and troposphere on each other, and in particular how stratospheric perturbations affect flow in the troposphere once they have crossed the tropopause, especially in a world where the climate is changing, is something that merits a great deal of further attention.

Bibliography

Akahori K., and S. Yoden, 1997: Zonal Flow Vacillation and Bimodality of Baroclinic Eddy Life Cycles in a Simple Global Circulation Model. *J. Atmos. Sci.*, **54**, 2349–2361.

Andrews, D. G., J. R. Holton, and C. B. Leovy, 1987: *Middle Atmosphere Dynamics*. Academic Press, Inc., 489pp.

Baldwin, M. P., and D. O’Sullivan, 1995: Stratospheric effects of ENSO related tropospheric circulation anomalies. *J. Climate*, **8**, 649–667.

Baldwin, M. P., and T. J. Dunkerton, 2001: Stratospheric Harbingers of Anomalous Weather Regimes. *Science*, **294**, 581–584.

Baldwin, M. P., L. J. Gray, T. J. Dunkerton, K. Hamilton, P. H. Haynes, W. J. Randel, J. R. Holton, M. J. Alexander, I. Hirota, T. Horinouchi, D. B. A. Jones, J. S. Kinnerson, C. Marquardt, K. Sato, and M. Takahashi, 2001: The Quasi-Biennial Oscillation. *Rev. Geophys.*, **39**, 179–229.

Braesicke, P., and J. A. Pyle, 2003: Changing ozone and changing circulation in northern mid-latitudes: Possible feedbacks? *Geophys. Res. Lett.*, **30(2)**, 1059, doi:10.1029/2002GL015973.

Braesicke, P., and J. A. Pyle, 2004: Sensitivity of dynamics and ozone to different representations of SSTs in the Unified Model. *Quart. J. Roy. Meteor. Soc.*, **130**, 2033–2045.

Butchart, N., and J. Austin, 1998: Middle Atmosphere Climatologies from the Troposphere–Stratosphere Configuration of the UKMO’s Unified Model. *J. Atmos. Sci.*, **55**, 2782–2809.

Butchart, N., J. Austin, J. R. Knight, A. A. Scaife, and M. L. Gallani, 2000: The Response of the Stratospheric Climate to Projected Changes in the Concentrations of Well-Mixed Greenhouse Gases from 1992 to 2051. *J. Climate*, **13**, 2142–2159.

Butchart, N., and A. A. Scaife, 2001: Removal of CFCs by increased mass exchange between the stratosphere and troposphere in a changing climate. *Nature*, **410**, 799–802. doi:10.1038/35071047

- Butchart, N., A. A. Scaife, J. Austin, S. H. E. Hare, and J. R. Knight, 2003: Quasi-biennial oscillation in ozone in a coupled chemistry–climate model. *J. Geophys. Res.*, **108(D15)**, 4486, doi:10.1029/2002JD003004.
- Butchart, N., A. A. Scaife, M. Bourqui, J. de Grandpré, S. H. E. Hare, J. Kettleborough, U. Langematz, E. Manzini, F. Sassi, K. Shibata, D. Shindell, and M. Sigmond, 2006: A multi-model study of climate change in the Brewer–Dobson circulation. To appear.
- Cagnazzo, C., C. Claud, and S. Hare, 2006: Aspects of stratospheric long-term changes induced by ozone depletion. *Climate Dyn.*, **27**, 101–111. doi:10.1007/s00382-006-0120-1
- Charlton, A. J., A. O’Neill, P. Berrisford, and W. A. Lahoz, 2005: Can the dynamical impact of the stratosphere on the troposphere be described by large-scale adjustment to the stratospheric PV distribution? *QJRMS*, **131**, 525–543.
- Charney, J. G., and J. G. Devore, 1979: Multiple Flow Equilibria in the Atmosphere and Blocking. *J. Atmos. Sci.*, **36**, 1205–1216.
- Chen, P., and W. A. Robinson, 1992: Propagation of Planetary Waves between the Troposphere and Stratosphere. *J. Atmos. Sci.*, **49**, 2533–2545.
- Christiansen, B., 2003: Temporal growth and vertical propagation of perturbations in the winter atmosphere. *QJRMS*, **129**, 1589–1605.
- Dickinson, R. E., 1968: On the Excitation and Propagation of Zonal Winds in an Atmosphere with Newtonian Cooling. *J. Atmos. Sci.*, **25**, 269–279.
- Dunkerton, T. J., C.-P. F. Hsu, and M. E. McIntyre, 1981: Some Eulerian and Lagrangian diagnostics for a model stratospheric warming. *J. Atmos. Sci.*, **38**, 819–843.
- Gates, W. L., 1992: AMIP: the atmospheric model intercomparison project. *Bull. Am. Meteorol. Soc.*, **73**, 1962–1970.
- Gray, L. J., S. Sparrow, M. Juckes, A. O’Neill and D. G. Andrews, 2003: Flow regimes in the winter Stratosphere of the northern hemisphere. *QJRMS*, **129**, 925–945.
- Gray, L. J., 2003: The influence of the equatorial upper Stratosphere on stratospheric sudden warmings. *Geophys. Res. Lett.*, **30(4)**, 1166, doi:10.1029/2002GL016430.
- Gray, L. J., S. Crooks, C. Pascoe, S. Sparrow, and M. Palmer, 2004: Solar and QBO Influences on the Timing of Stratospheric Sudden Warmings. *J. Atmos. Sci.*, **61**, 2777–2796.
- Hamilton, K., 1993: An explanation of observed Southern oscillation effects in

the Northern hemisphere stratosphere. *J. Atmos. Sci.*, **50**, 3468–3473.

Hampson, J., 2000: *Interannual Variability in Stratospheric Dynamics: Interaction Between the QBO and the Extratropics*, PhD thesis, Cambridge University.

Hare S. H. E., L. J. Gray, W. A. Lahoz, A. O'Neill, and L. Steenman-Clark, 2004: Can stratospheric temperature trends be attributed to ozone depletion? *J. Geophys. Res.*, **109**, doi:10.1029/2003JD003897

Hartley, D. E., J. T. Villarín, R. X. Black, and C. A. Davis, 1998: A new perspective on the dynamical link between the stratosphere and troposphere. *Nature*, **391**, 471–474.

Hartmann, D. L., J. M. Wallace, V. Limpasuvan, D. W. J. Thompson, and J. R. Holton, 2000: Can ozone depletion and global warming interact to produce rapid climate change? *Proc. Nat. Acad. Sci. (Wash. DC)*, **97**, 1412–1417.

Haynes, P. H., and M. E. McIntyre, 1987: On the representation of Rossby wave critical layers and wave breaking in zonally truncated models. *J. Atmos. Sci.*, **44**, 2359–2382.

Haynes, P. H., and T. G. Shepherd, 1989: The importance of surface pressure changes in the response of the atmosphere to zonally-symmetric thermal and mechanical forcing. *QJRMS*, **115**, 1181–1208.

Haynes, P. H., C. J. Marks, M. E. McIntyre, T. G. Shepherd, and K. P. Shine, 1991: On the “Downward Control” of Extratropical Diabatic Circulations by Eddy-Induced Mean Zonal Forces. *J. Atmos. Sci.*, **48**, 651–678.

Haynes, P. H., 2005: *Stratosphere–Troposphere Dynamical Coupling*. SPARC Newsletter N° 25.

Holton, J. R. and C. Mass, 1976: Stratospheric Vacillation Cycles. *J. Atmos. Sci.*, **33**, 2218–2225.

Holton, J. R., P. H. Haynes, M. E. McIntyre, A. R. Douglass, R. B. Rood, and L. Pfister, 1995: Stratosphere–Troposphere Exchange. *Rev. Geophys.*, **33(4)**, 403–439.

Hoskins, B. J., and A. J. Simmons, 1975: A multi-layer spectral model and the semi-implicit method. *QJRMS*, **101**, 637–655.

Hsu, C.-P. F., 1981: A numerical study of the role of wave-wave interactions during sudden stratospheric warmings. *J. Atmos. Sci.*, **38**, 189–214.

Kerr-Munslow A. M., and W. A. Norton, 2006: Tropical Wave Driving of the Annual Cycle in Tropical Tropopause Temperatures. Part I: ECMWF Analyses. *J. Atmos. Sci.*, **63**, 1410–1419.

Kiehl, J. T., and S. Solomon, 1986: On the radiative balance of the

stratosphere. *J. Atmos. Sci.*, **43**, 1525–1534

Kodera K., K. Yamazaki, M. Chiba, and K. Shibata, 1990: Downward Propagation of Upper Stratospheric Mean Zonal Wind Perturbation to the Troposphere. *Geophys. Res. Lett.*, **17(9)**, 1263–1266.

Kushner, P. J., and L. M. Polvani, 2004: Stratosphere–Troposphere Coupling in a Relatively Simple AGCM: The Role of Eddies. *J. Climate*, **17**, 629–639.

Limpasuvan, V., and D. L. Hartmann, 2000: Wave-maintained annular modes of climate variability. *J. Climate*, **13**, 4414–4429.

Lordi, N. J., A. Kasahara, and S. K. Kao, 1980: Numerical simulations of sudden warmings with a primitive equation spectral model. *J. Atmos. Sci.*, **37**, 2746–2767.

Manzini, E., M. A. Giorgetta, M. Esch, L. Kornblueh, and E. Roeckner, 2006: The influence of sea surface temperatures on the Northern winter stratosphere: Ensemble simulations with the MAECHAM5 model. *J. Climate*, **19(16)**, 3863–3881.

Norton, W. A., 2006: Tropical Wave Driving of the Annual Cycle in Tropical Tropopause Temperatures. Part II: Model Results. *J. Atmos. Sci.*, **63**, 1420–1431.

Perlwitz, J., and N. Harnik, 2003: Observational Evidence of a Stratospheric Influence on the Troposphere by Planetary Wave Reflection. *J. Climate*, **16**, 3011–3026.

Plumb, R. A., 1977: The Interaction of Two Internal Waves with the Mean Flow: Implications for the Theory of the Quasi-Biennial Oscillation. *J. Atmos. Sci.*, **34**, 1847–1858.

Plumb, R. A., 1989: On the Seasonal Cycle of Stratospheric Planetary Waves. *PAGEOPH*, **130**, 233–242.

Plumb, R. A. and K. Semeniuk, 2003: Downward migration of extratropical zonal wind anomalies. *J. Geophys. Res.*, **108 (D7)**, 4223, doi:10.1029/2002JD002773.

Polvani, L. M., and P. J. Kushner, 2002: Tropospheric response to stratospheric perturbations in a relatively simple general circulation model. *Geophys. Res. Lett.*, **29(7)**, 1114, doi:10.1029/2001GL014284.

Randel, W. J., 1992: *Global Atmospheric Circulation Statistics, 1000–1 mb*. NCAR Technical Note, NCAR/TN-366+STR.

Randel, W. J., R. R. Garcia, and F. Wu, 2002: Time-Dependent Upwelling in the Tropical Lower Stratosphere Estimated from the Zonal-Mean Momentum Budget. *J. Atmos. Sci.*, **59**, 2141–2152.

Randel, W. J., F. Wu, S. J. Oltmans, K. Rosenlof, and G. E. Nedoluha, 2004:

Interannual Changes of Stratospheric Water Vapor and Correlations with Tropical Tropopause Temperatures. *J. Atmos. Sci.*, **61**, 2133–2148.

doi:10.1175/1520-0469(2004)061<2133:ICOSWV>2.0.CO;2

Reichler, T., P. J. Kushner, and L. M. Polvani, 2005: The Coupled Stratosphere–Troposphere Response to Impulsive Forcing from the Troposphere. *J. Atmos. Sci.*, **62**, 3337–3352.

Sankey, D., 1998: *Dynamics of Upwelling in the Equatorial Lower Stratosphere*, PhD thesis, Cambridge University.

Scaife, A. A., 1998: *Interannual Variability of the Stratosphere*, PhD thesis, Reading University.

Scaife, A. A., N. Butchart, C. D. Warner, D. Stainforth, W. Norton, and J. Austin, 2000: Realistic Quasi-Biennial Oscillations in a simulation of the global climate. *Geophys. Res. Lett.*, **27(1)**, 3481–3484.

Scaife, A.A., N. Butchart, D. R. Jackson, and R. Swinbank, 2003: Can changes in ENSO activity help to explain increasing stratospheric water vapor? *Geophys. Res. Lett.*, **30(17)**, 1880, doi:10.1029/2003GL017591.

Scinocca, J. F., and P. H. Haynes, 1998: Dynamical Forcing of Stratospheric Planetary Waves by Tropospheric Baroclinic Eddies. *J. Atmos. Sci.*, **55**, 2361–2392.

Scott, R. K. and P. H. Haynes, 1998: Internal interannual variability of the extratropical stratospheric circulation: The low-latitude flywheel. *QJRMS*, **124**, 2149–2173.

Scott, R. K. and P. H. Haynes, 2000: Internal Vacillations in Stratosphere-Only Models. *J. Atmos. Sci.*, **57**, 3233–3250.

Scott, R. K. and P. H. Haynes, 2002: The Seasonal Cycle of Planetary Waves in the Winter Stratosphere. *J. Atmos. Sci.*, **59**, 803–822.

Scott, R. K., 2002: Wave-Driven Mean Tropical Upwelling in the Lower Stratosphere. *J. Atmos. Sci.*, **59**, 2745–2759.

Scott, R. K. and L. M. Polvani, 2004: Stratospheric control of upward wave flux near the tropopause. *Geophys. Res. Lett.*, **31**, LO2115, doi:10.1029/2003GLO17965.

Song, Y., and W. A. Robinson, 2004: Dynamical Mechanisms for Stratospheric Influences on the Troposphere. *J. Atmos. Sci.*, **61**, 1711–1725.

Sparrow, S. N., 2003: *Model studies of winter hemisphere stratospheric flow regimes*, PhD thesis, Oxford University.

Taguchi M., T. Yamaga, S. Yoden, 2001: Internal Variability of the Troposphere–Stratosphere Coupled System Simulated in a Simple Global

Circulation Model. *J. Atmos. Sci.*, **58**, 3184–3203.

Tung, K. K., 1983: On the Nonlinear Versus Linearized Lower Boundary Conditions for Topographically Forced Stationary Long Waves. *Mon. Wea. Rev.*, **111**, 60–66.

Wakata, Y. and M. Uryu, 1987: Stratospheric Multiple Equilibria and Seasonal Variations. *J. Meteor. Soc. Japan*, **65**, 27–41.

Yoden, S., 1987(a): Bifurcation Properties of a Stratospheric Vacillation Model. *J. Atmos. Sci.*, **44**, 1723–1733.

Yoden, S., 1987(b): Dynamical Aspects of Stratospheric Vacillations in a Highly Truncated Model. *J. Atmos. Sci.*, **44**, 3683–3695.

Yoden, S., 1987(c): A New Class of Stratospheric Vacillations in a Highly Truncated Model Due to Wave Interference. *J. Atmos. Sci.*, **44**, 3696–3709.

Yoden, S., 1989: An Illustrative Model of Seasonal and Interannual Variations of the Stratospheric Circulation. *J. Atmos. Sci.*, **47**, 1845–1853.

Yoden, S., Y. Naito, and S. Pawson, 1996: A further analysis of internal variability in a perpetual January integration of a troposphere–stratosphere–mesosphere GCM. *J. Meteor. Soc. Japan*, **74**, 175–188.

Yulaeva, E., J. R. Holton, and J. M. Wallace, 1994: On the Cause of the Annual Cycle in Tropical Lower-Stratospheric Temperatures. *J. Atmos. Sci.*, **51**, 169–174.

Zeng, G., and J. A. Pyle, 2005: Influence of El Niño Southern Oscillation on stratosphere/troposphere exchange and the global tropospheric ozone budget. *Geophys. Res. Lett.*, **32**, L01814, doi:10.1029/2004GL021353.